

Tumour Grading and Discrimination based on Class Assignment and Quantitative Texture Analysis Techniques

by

Omar Sultan Al-Kadi

June 2009

Department of Informatics,
School of Science and Technology,
University of Sussex,
Brighton BN1 9QJ UK.

A thesis submitted for the degree of
Doctor of Philosophy in Engineering at the University of Sussex

Declaration

I hereby declare that this thesis has not been and will not be, submitted in whole or in part to another university for the award of any other degree.

Omar Sultan Al-Kadi

Signature:

To my family

Abstract

Medical imaging represents the utilisation of technology in biology for the purpose of noninvasively revealing the internal structure of the organs of the human body. It is a way to improve the quality of the patient's life through a more precise and rapid diagnosis, and with limited side-effects, leading to an effective overall treatment procedure. The main objective of this thesis is to propose novel tumour discrimination techniques that cover both micro and macro-scale textures encountered in computed tomography (CT) and digital microscopy (DM) modalities, respectively. Image texture can provide significant information on the (ab)normality of tissue, and this thesis expands this idea to tumour texture grading and classification. The fractal dimension (FD) as a texture measure was applied to contrast enhanced CT lung tumour images in an aim to improve tumour grading accuracy from conventional CT modality, and quantitative performance analysis showed an accuracy of 83.30% in distinguishing between advanced (aggressive) and early stage (non-aggressive) malignant tumours. A different approach was adopted for subtype discrimination of brain tumour DM images via a set of statistical and model-based texture analysis algorithms. The combined Gaussian Markov random field and run-length matrix texture measures outperformed all other combinations, achieving an overall class assignment classification accuracy of 92.50%. Also two new histopathological multiresolution approaches based on applying the FD as the best bases selection for discrete wavelet packet transform, and when fused with the Gabor filters' energy output improved the accuracy to 91.25% and 95.00%, respectively. While noise is quite common in all medical imaging modalities, the impact of noise on the applied texture measures was assessed as well. The developed lung and brain texture analysis techniques can improve the physician's ability to detect and analyse pathologies leading for a more reliable diagnosis and treatment of disease.

This work has been cited in [1-3].

بِسْمِ اللَّهِ الرَّحْمَنِ الرَّحِيمِ

وَقَالُوا الْحَمْدُ لِلَّهِ الَّذِي هَدَانَا لِهَذَا وَمَا كُنَّا لِنَهْتَدِيَ لَوْلَا أَنْ هَدَانَا اللَّهُ

صدق الله العظيم سورة الأعراف (اية 43)

Acknowledgments

...and they shall say: "Praise be to Allah, who hath guided us to this: never could we have found guidance, had it not been for the guidance of Allah"

The Holy Quran (The Heights - verse 43)

All praise and thanks be to Allah, the Cherisher and Sustainer of the worlds, for guiding me to this.

First of all, I would like to express my sincerest thanks to my father and mother for all their effort, dedication and inspiration since the time I came to this world till this very moment, for me to become a man that they can really rely upon, a man that will try always to deliver every effort to seek their satisfaction and happiness, and who will strive to do good to serve his family, society and country. Thanks to my brothers and sister for their support which always gave me the determination to finish this work.

I would like to express my gratitude to Dr. Mohammad Bilal Al-Zoubi and Dr. Rifat Al-Shunnak for their guidance and encouragement for me to continue for this PhD.

Finally, thanks to my lab mate Marcos Rosetti for his encouragement in the early times when we were trying to get the grasp of our research, and to the rest of my lab mates whom I spent with all an enjoyable time.

Contents

1 WHAT IS TEXTURE?	1
1.1 Sense of texture	2
1.2 Our perception of texture	5
1.3 Texture analysis and its applications	7
1.3.1 Classification	8
1.3.2 Segmentation	9
1.3.3 Texture synthesis	9
1.3.4 Shape from texture	10
1.4 Summary	10
2 OVERVIEW OF CT LUNG AND DM BRAIN TUMOUR IMAGING TECHNIQUES	11
2.1 Texture characterisation	12
2.2 Biomedical imaging modalities	12
2.3 Tumours	13
2.3.1 Defining and identifying tumours	16
2.3.2 Lung tumours	17
2.3.3 Brain tumours	18
2.4 CT lung tumour imaging	20
2.5 DM brain tumour imaging	23
2.5.1 Meningioma-related work	23
2.5.2 Other types of brain histopathologies	24
2.6 Summary	25
3 FRACTAL DIMENSION AS A LUNG TUMOUR QUANTITATIVE CLASSIFIER	26
3.1 Introduction	26
3.2 Theoretical concepts of fractal dimension	28
3.3 Methodology	33
3.3.1 Image Acquisition	33
3.3.2 FD transformation	34

3.3.3 Region of Interest & Feature extraction.....	35
3.3.4 Impact of CT tube voltage and current on FD_{avg} and Lacunarity.....	37
3.4 Experimental results and evaluation.....	38
3.4.1 Fractal Analysis	38
3.4.2 Statistical tests.....	40
3.4.3 Phantom tests	40
3.5 Discussion.....	41
3.6 Conclusion	44
4 NOISE IMPACT ON LUNG TUMOUR TEXTURE MEASURES	45
4.1 Introduction.....	45
4.2 Material and methods.....	47
4.2.1 Image acquisition	48
4.2.2 Noise evaluation.....	48
4.2.3 CT image reconstruction.....	51
4.2.4 Texture feature extraction	52
4.2.5 Measuring separability quality.....	54
4.3 Results and discussion	55
4.4 Conclusion	58
5 MULTI-FEATURE CLASS ASSIGNMENT FOR HISTOPATHOLOGICAL MENINGIOMA TUMOUR IMAGES	59
5.1 Introduction.....	59
5.2 Methodology	61
5.2.1 Image acquisition and preparation	62
5.2.2 RGB space colour segmentation	63
5.2.3 Morphological processing.....	64
5.2.4 Feature extraction approaches.....	65
5.2.5 Features selection by correlation thresholding.....	80
5.2.6 Pattern classification technique.....	83
5.3 Experimental results	84

5.3.1 Colour channel selection.....	84
5.3.2 Individual and combined classification accuracies	84
5.3.3 Morphological processing.....	86
5.4 Texture measures behaviour analysis	87
5.4.1 Relevance to histopathological texture	87
5.4.2 Simulation of noise impact on extracted features	88
5.5 Discussion.....	90
5.6 Conclusion	92
6 MULTIREOLUTION VIA WAVELET TRANSFORM AND GABOR FILTERS	93
6.1 Introduction.....	93
6.2 Foundation of wavelet multiresolution representation.....	96
6.3 Image pre-processing.....	101
6.4 Subband selection optimisation	101
6.4.1 Fractal signature approach	103
6.4.2 Other texture signatures	106
6.5 Texture signature classification	106
6.6 Wavelet packet results.....	106
6.7 Interpretation of wavelet packet results	108
6.8 Gabor filter	110
6.9 Gabor filter results.....	113
6.10 Interpretation of Gabor filter results	114
6.11 Conclusion	116
7 CONCLUDING DISCUSSION	117
7.1 Challenges in medical texture characterisation	117
7.1.1 Fine structure texture (CT Lung tumours)	117
7.1.2 Coarse structure texture (DM brain tumours)	118
7.2 Classification approach	120
APPENDIX	122
BIBLIOGRAPHY	129

List of Figures

Fig. 1.1 The Royal Pavilion palace in Brighton.....	4
Fig. 1.2 Real tissue texture.....	5
Fig. 1.3 An example of preattentive discrimination.....	7
Fig. 1.4 Stages of a typical computer vision system.....	8
Fig. 1.5 Example of segmenting five types of textures using co-occurrence features.	9
Fig. 3.1 Sierpinski triangle fragmented up to six scales.	29
Fig. 3.2 Obtaining an array of row vectors from a multidimensional array.....	31
Fig. 3.3 Different texture patterns selected from the Brodatz album.	32
Fig. 3.4 Surface of the selected ROI shown in Fig 3.7.	35
Fig. 3.5 Scaling factor vs required number of boxes in log-log scale.....	35
Fig. 3.6 Original, windowed and fractally transformed baseline DICOM images.	36
Fig. 3.7 Original, windowed and fractally transformed maximum contrast DICOM images.....	36
Fig. 3.8 Selected FD tumour ROI enlarged to show texture.	37
Fig. 3.9 Eleven ROIs extracted from eleven successive CT scans	37
Fig. 3.10 Fractally transformed image of early stage non-aggressive lung tumour.....	39
Fig. 3.11 Sequence of FD ROIs representing normal and abnormal cases.	39
Fig. 3.12 Correlation between standard tumour uptake of fluorodeoxyglucose with maximum FD _{avg} and baseline FD _{avg}	42
Fig. 3.13 Standard deviation of fractal features for groups of similar phantom slices acquired under specific CT parameters.	42
Fig. 4.1 Two images selected from a CE CT and a NCE CT image data sets.	47
Fig. 4.2 Methodology used to assess texture measures' susceptibility to noise for lung tumour CT images.	47
Fig. 4.3 Histograms of transverse section of scanning table in CT images followed by corres- ponding generated Gaussian, Rayleigh and Erlang noises.....	50
Fig. 4.4 Noise suppression after adaptive filtering.	53
Fig. 4.5 Horizontal grey-level profile along the middle of an extracted ROI from the backgro- und area in the CT image.	53
Fig. 4.6 Two level wavelet packet transform decomposition for an extracted lung tumor ROI of case 56 in the NCE CT data set	54
Fig. 4.7 Subband energy values for the tumour ROI decomposition in Fig. 4.6	54
Fig. 5.1 Diagram explaining the process followed in classification of the histopathological meningioma images	61
Fig. 5.2 Four types of grade I meningioma.	62

Fig. 5.3 Selected sample cell nucleus used for segmenting all relevant meningothelial subtypes.	64
Fig. 5.4 Segmented and reference image for transitional meningioma subtype	64
Fig. 5.5 Blue colour channel image and its corresponding morphological gradient.....	65
Fig. 5.6 Third order Markov neighbourhood for a sample image pixel.....	66
Fig. 5.7 Blue channel image of meningioma subtypes and their corresponding fractal dimension images computed using fBm and DBC algorithms.	68
Fig. 5.8 A 5 X 5 pixel image and its corresponding co-occurrence matrix.	69
Fig. 5.9 Co-occurrence matrices of the blue colour channel for fibroblastic subtype in Fig. 5.2.	71
Fig. 5.10 Entropy vs energy and homogeneity vs correlation co-occurrence matrix features.	73
Fig. 5.11 An example of run-length matrices for five grey levels and four different directions.	74
Fig. 5.12 Run-length matrices in four directions of fibroblastic subtype image in Fig. 5.2 after quantisation to 32 grey levels.....	75
Fig. 5.13 Surface plot of the normalised auto-covariance functions referring to meningioma fibroblastic, meningothelial, psammomatous and transitional subtypes.....	79
Fig. 5.14 Individual texture measures' classification accuracy for morphologically and non-morphologically processed meningioma images	86
Fig. 5.15 Initial and final images of the 15 generated pseudo-cell nuclei images and the corresponding distorted versions.	88
Fig. 5.16 Susceptibility of RLM, GMRF and FD texture measures to 15 morphologically processed pseudo-cell nuclei images with increasing shape frequency.	88
Fig. 5.17 Horizontal gray-level profile along the first pseudo-cell nuclei image.	89
Fig. 5.18 Effect of noise distortion on texture measures applied to images in Fig. 5.2.	90
Fig. 6.1 Decomposition filter bank for a 2-D wavelet transform.....	99
Fig. 6.2 Time-frequency tiling	100
Fig. 6.3 Comparing tiling covering of the time-frequency domain	101
Fig. 6.4 Meningioma fibroblastic, meningothelial, psammomatous and transitional subtypes and the corresponding grey-level segmented cell nuclei general structure.....	102
Fig. 6.5 First level of decomposition showing the LL, LH, HL and HH bands for fibroblastic, meningothelial, psammomatous and transitional subtypes.	102
Fig. 6.6 Fibroblastic meningioma power spectrum of LL, LH, HL and HH wavelet bands for the first and third level of resolution.....	103
Fig. 6.7 Wavelet quad-tree structure for first three decomposition levels of transitional subtype appearing in Fig. 6.5 and its corresponding channel decomposition.....	105
Fig. 6.8 Multiresolution level wavelet packet comparison of meningioma classification accuracy based on fractal dimension, energy and co-occurrence texture signatures	108
Fig. 6.9 Gabor filter having response.....	111
Fig. 6.10 Gabor filter defined in the spatial-frequency domain	113

List of Tables

Table 1.1 Texture surface pattern	3
Table 1.2 Tactility of selected textures	3
Table 2.1 Main biomedical imaging modalities used for disease detection and diagnosis.....	14
Table 2.2 Lung tumour staging based on TNM system	18
Table 3.1 Some studies which used FD for texture analysis and classification.....	28
Table 3.2 Fractal dimension and its corresponding lacunarity for each of the patterns in Fig.3.3	32
Table 3.3 Slices for phantom group 3 showing corresponding CT acquisition parameters for fractal features.....	38
Table 3.4 Number of cases greater than set threshold	38
Table 3.5 FD texture analysis data for all 15 cases.....	43
Table 4.1 PDFs for three different types of noise and their corresponding mean and variance	49
Table 4.2 Matusita distance between original extracted uniform lung tumour ROIs from data set 1 and three types of noise distributions.....	51
Table 4.3 Matusita distance between the original extracted uniform lung tumour ROIs from the NCE data set	51
Table 4.4 Fisher's distance between original and reconstructed clean and noisy CT images	58
Table 4.5 Sorted texture measures in Table 4.4 according to class separability.....	58
Table 5.1 Main histological features for the four meningioma subtypes in Fig. 5.2	62
Table 5.2 Estimated GMRF parameters using 3 rd order Markov neighbours for the subtypes shown in Fig. 5.2.....	67
Table 5.3 First order statistics derived from a fractal dimension generated image using fractal Brownian motion and differential box counting algorithms	67
Table 5.4 Autocovariance function least squares exponential fittings.....	77
Table 5.5 Labeled grey level co-occurrence matrix and fractal dimension texture features.....	81
Table 5.6 Sorted texture features of Table 5.5 in descending order according to corresponding divergence	81
Table 5.7 Correlation matrix for the 37 different texture features listed in Table 5.6.....	82
Table 5.8 Assessing classification quality for each colour channel.....	84
Table 5.9 The RGB colour channels classification accuracies for the RLM texture measure.....	84
Table 5.10 Individual texture features testing classification accuracy of the blue colour component of meningioma images	85
Table 5.11 Classification accuracy of extracted texture features in different combinations ranked in descending order	85
Table 5.12 Optimum features for the top four texture combination features in Table 5.11 which	

improved the classification accuracy beyond the set threshold	85
Table 5.13 Four class meningioma classification confusion matrix for the combined GMRF and RLM texture measures	86
Table 6.1 Wavelet transform 8-tap Daubechies filter coefficients.....	103
Table 6.2 Fractal dimensions for each corresponding fibroblastic wavelet subband.....	105
Table 6.3 Optimum decomposition levels for meningioma subtypes' FD signature absolute difference values	107
Table 6.4 Wavelet packet decomposition using maximum fractal dimension signature for best basis selection	107
Table 6.5 Classification accuracy comparison of Gabor filtered meningioma images after extraction of the energy and in combination with the fractal dimension, Gaussian Markov random fields, grey level co-occurrence and run-length matrices texture measures	114

Chapter 1

WHAT IS TEXTURE?

Image texture is an enormous field of research and is perceived as a fundamental component in computer vision. With over a half a century of digital image processing, texture still remains a very fertile field of research attracting numerous mathematical algorithms and techniques developed for the purpose of improving object surface characterisation. The exploitation of image textural properties has led to new opportunities for researchers to solve problems where simulation of human vision for automated object recognition was required, taking advantage of the exponential increase in computer processing power and storage capacity. This has opened the door wide open for establishing new solutions to many problems that were deemed unfeasible and computationally demanding.

Despite that, texture is regarded as a "fuzzy" concept with no mathematical or comprehensive definition agreed upon yet. This may be due to the vague concept that texture may actually hold resulting in the many interpretations related to human perception. The Oxford dictionary defines texture with three different meanings [4]: “the way a surface, substrate or fabric looks or feels to the touch, i.e. whether it is rough, smooth, hard, soft, etc; the way food or drink tastes or appears; the way in which a piece of music or literature is constructed, with regard to the way in which its parts are combined”. Consequently, we understand the term “texture” is interchangeably used to describe various patterns arising from different substrates that interact with our senses. For instance our eye deploys its retina cones (photopic vision) and rods (scotopic vision) photoreceptors to convert incident light energy into signals carried to the brain by the optic nerve to discern the different patterns in an image. Similarly the sensory receptors in our fingers translate the feeling of objects; the chemoreceptors in the nose detect different odour molecules in the air; the hair cells in the inner ear cochlea convert the sound vibrations; and the receptor cells that form the tongue’s taste buds, all transform the different sensations electrically to the brain via the nervous system. Therefore, each object we sense would initiate a unique feeling in our brain ranging from pleasant to unpleasant, e.g. roughness is usually associated with pain and discomfort, unpleasant smell or bitter taste does not promote your appetite, and a squeaking chalk sound on a chalkboard is unlike a singing bird. This explains the wide use of texture to describe the feeling in many fields, naming a few, such as in music, food, paintings and visual arts, textile fabrics, geology, cosmology and computer animation. In this thesis, we are concerned with visually sensed textures in the field of medical imaging and how disease alters the tissue structure of healthy tissue, so whenever the word texture is mentioned it refers to the appearance of organ tissue in a digital image.

After specifying the type of texture that we are concerned with, we can then simply conceive texture as the variation or arrangement of elementary elements which jointly compose the surface pattern. For any picture element (i.e. pixel) in a digital image $I(x, y)$, where x and y are the spatial coordinates and I is the amplitude representing the intensity at any pair of co-ordinates (x, y) , the elementary elements can be composed from virtually one to a set of pixels, and the unique arrangement of the finite set of discrete values of x, y and I characterise the texture, which will give the sense of the surface.

1.1 Sense of texture

Sensation in its *tactile* and *non-tactile or visual* sense plays a major role in defining this concept. That is, we can recognise image texture based on its intrinsic properties either by using our tangible senses, such as the direct feeling of an observed object, or intangibly through perception as when viewing an object from a distance which will be then translated to a texture feeling in our mind. In either case the brain associates previously learnt sensation experiences with the different objects or substance properties as colour, surface orientation, luminance or brightness, material nature, etc. For example before picking an apple or a kiwi fruit our brain gives us a preconceived idea on the smoothness or roughness of the fruit peel surface, and it would be quite odd if the rough kiwi's peel feel comes to our mind when seeing a glossy apple. This is maybe due to using the same neural pathways of actual sensation for imaginative sensations.

The experience of human sensation perception takes into account the amount of variation of pixels in an image, in the form of edges, which will assist in determining the type of surface under observation. Image edges are recognised when a discontinuity occurs in a gradient across a straight line. Given that not all imaging applications have high quality coloured images, hence the orientation, shape and density of these texture edges becomes significant in object description; especially when dealing with grey scale images where discrimination capability is reduced. These edges assist in differentiating texture into *deterministic* and *stochastic* textures where the edges in the former occur in an equally spaced repetitive pattern unlike the latter being more random. Also two other kinds can be deduced as *hybrid* where the image is composed of mixtures of both deterministic and stochastic textures, and *fractal* having a self-similar deterministic pattern at various scales such as mathematical fractals (e.g. Sierpinski triangle, Koch snowflake, etc.), or even having a stochastic self-similar pattern such as natural fractals (e.g. tree branching, clouds, mountains, etc.). Depending on the specification of these edges, textures can be further categorised into fine, rough and glossy, and their opposites, coarse, smooth and matt. However, other words exist which can give a descriptive meaning in our daily life according to the material type, as instead of coarse or rough we might use grainy, furrowed, bumpy, cracked, fuzzy, prickly; or silky, soft, furry, slippery, slick for fine or smooth. The main difference between the previous textures is how image pixels form their spatial relationship to define the edges, which takes into account besides the pixels grey levels, the size or number of pixels used to compose

the texture's elementary elements, their directionality or shape, and frequency or separating distance in-between showing the rapidity of fluctuation in texture. These sets of properties used to characterise a specific texture may not be the same if the same texture was viewed at a different scale, which makes all texture types scale dependent except for fractal textures where the zoomed-in view should resemble the overall initial texture view.

To show the level of sophistication that our brain deals with in our daily life and how much texture with various patterns can be found in just one glimpse, let's take a real-world digital image, such as the Brighton Royal Pavilion depicted in Fig. 1.1, and see how texture could represent the necessary details to understand the context. The difference in texture properties defines the border between the palace domes and minarets on one hand and the sky above, and between the green fields in front on the other. Also the variation in the texture itself can add more description to the scene, where the sky in Fig. 1.1 varies from clear to cloudy and even grainy with the little flying birds to the upper left; a similar analogy applies to other objects in the image. All of these texture variations result in different textures which gives us the ability to distinguish the objects. In order to show how texture can be diverse in a single image, seven distinct textures are selected from Fig. 1.1 for identification. Although we can select numerous types of textures depending on which part of the image attracts our attention, the most distinct textures were selected for clarity. Table 1.1 lists the selected textures into three different categories based on their surface patterns, while Table 1.2 sorts textures in a more general way based on their tactility, with the perceived feeling – which was restricted to fine and coarse for simplicity – given between brackets.

Table 1.1 Texture surface pattern



Deterministic	Stochastic	Fractal
Stone fence	Clouds	Tree
Engraved wall	Flying birds	
Tower wall	Grass field	

Table 1.2 Tactility of selected textures

Tactile	Visual
Tree (coarse)	Clouds (fine)
Grass field (fine)	Flying birds (coarse)
Tower wall (fine)	
Stone fence (coarse)	
Engraved wall (coarse)	

Real images of tissue – or sometimes called medical – texture, unlike the situation in Fig. 1.1, usually have a single pattern as the acquisition modality focuses on a specific area of an organ. The way the tissue pattern appears can reflect its healthiness state; yet, unfortunately tissue structure is not identical in all image samples and varies from one patient to another, since disease might alter the tissue structure unequally. This tissue heterogeneity places tissue patterns commonly in the category of stochastic or possibly fractal textures – such as the lung's tissue structure or the folds of the brain – which can exhibit *fractal-like* characteristics.

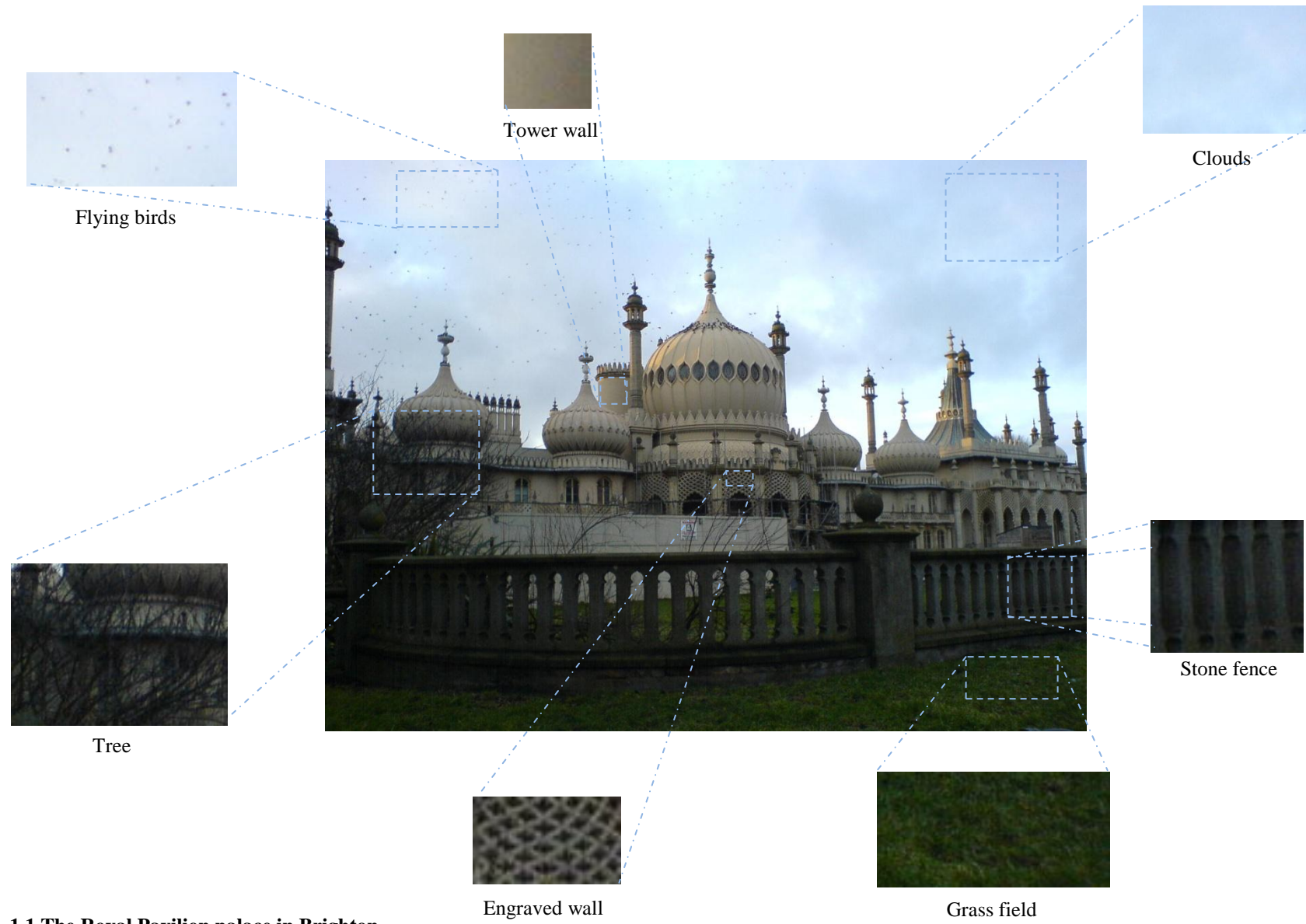


Fig. 1.1 The Royal Pavilion palace in Brighton.

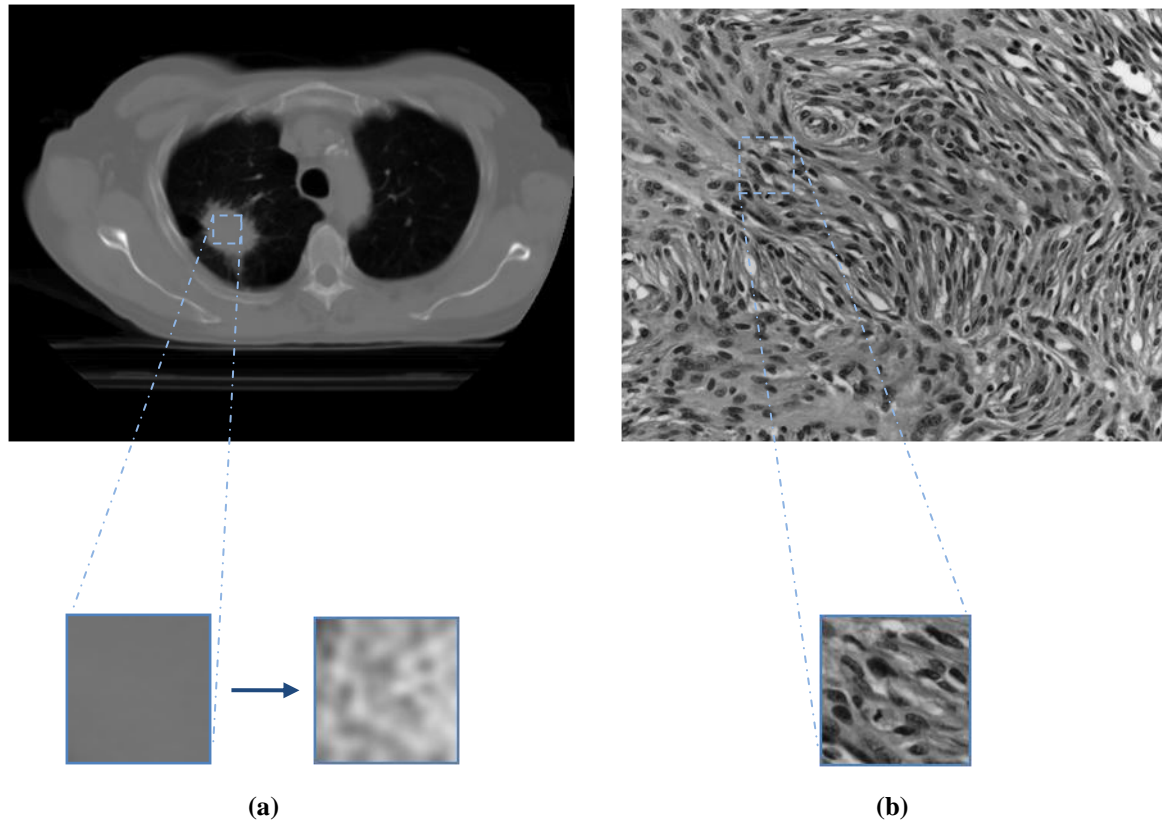


Fig. 1.2 Real tissue texture (a) extracted lung tumour tissue and its corresponding fractal dimension version to reveal structure, and (b) extracted meningioma brain tissue.

Two different examples of the type of fine and coarse tissue that this thesis will deal with are shown in Fig. 1.2. The two medical images represent the type of texture encountered when using non-invasive and invasive modalities, where Fig. 1.2(a) is a lung tumour region acquired at a *micro-scale* and Fig. 1.2(b) is a brain tumour acquired at a *macro-scale*. Sometimes fine texture, as the case with lung tissue image, might need processing such as transforming to the fractal dimension, which could be necessary to reveal subtle lung texture details, whereas prominent elements in the coarse texture of the brain tumour case (e.g. cell nuclei) can be segmented and used for tumour subtypes differentiation. As for the tissue stochastic texture where it does not usually have a repetitive pattern but homogeneous statistical properties, the directionality and density of the discontinuities in the texture's surface help define the tissue (e.g. normal or abnormal); moreover, tissue with a large amount of edges is considered rich with features which will make the feature extraction algorithm more capable of delivering a better characterisation.

1.2 Our perception of texture

Understanding how humans perceive texture was a point of interest for much research in the fields of neuroscience, psychophysics and computer science. Being able to detect, classify and segregate scene objects in a human vision manner requires identifying how the brain processes visual information, that is, how related neural processes respond to various stimuli of different texture patterns. The latter is the main

concern in neuroscience and psychophysics studies, while computer science, or more precisely biologically inspired computer science, tends to quantify these visual processes by mathematical modelling or capturing the texture properties for automated recognition.

One of the earliest texture perception studies of human vision was proposed by Julesz, who laid out the fundamentals of preattentive vision [5-9]. The concept of texture being “effortlessly or preattentively discriminable”, i.e. the spontaneous perception of texture variations without focused attention, is illustrated in Fig. 1.3, where the left side area is considered preattentively discriminable while the right side is not. Julesz attributed this to the order of image statistics of texture patterns, where textures having equal second order statistics (i.e. identical joint distribution of grey level pairs) tend to be *not* preattentively discriminable, as the case between the L-shape background and the T-shape right region of Fig. 1.3. This is known as *Julesz conjecture* which he and his colleagues refuted afterwards using carefully constructed textures having equal second order and different third and higher order statistics [6]. Nevertheless, this conjecture gave a better understanding of texture perception which led to the proposal of the *texton theory*. The theory states that texture discrimination is achieved by its primitive or fundamental elements, named *textons* [7, 8] or sometimes called texels (stands for texture elements) [10], which have conspicuous local features. These textons can be in the form of terminations or endpoints of line segments (e.g. closure, connectivity, corners, etc.), elongated blobs (e.g. granularity), or colours. If we examine Fig. 1.3 again, preattentive texture perception can be interpreted based upon Julesz’s texton theory using first order density, as the difference in the number of texton terminations in each region. That is, the number of terminations of the background L-shape and the left region X-shape figures are not equal (3 terminations for L against 4 for X); thus we can say that the two textures are preattentively discriminable. In contrast there is no difference between the terminations of the T- shapes of the right region and the background (i.e. the two regions are indiscriminable).

While the psychophysiological work of Julesz et al focused on early or low level human visual system (HVS) through investigating local texture feature statistics at various orders [9], other researchers showed that the HVS has a spatial frequency and orientation sensitivity, performing a multichannel spatial frequency filtering on images projected on the retina [11]. Biologically inspired computer vision studies made use of the multichannel theory in an endeavour for a more effective approach in analysing and segmenting texture in a human-like perception. Implementing computational models via filter banks, as the Gabor filter, is one of the well known techniques used in HVS simulation. Kulikowski et al showed that the spatial response profile of the simple cells in the visual cortex can be mathematically described by a Gabor filter bank [12]. An early example of filter bank application in texture segregation is Turner’s use of the Gabor filter for preattentive texture discrimination, showing it can act as a detector for textons, such as collinear or elongated segments [13]. Bovik et al used the power spectrum characteristics of individual textures for segmentation. Upon empirical information, differences between channel amplitude responses were used for detecting boundaries between texture regions. Filter locations were selected

using the most significant spectral peak along direction of orientation for strongly oriented textures, while the lowest fundamental frequency was used in periodic textures. For non-oriented textures, the centre frequency of the two largest maxima was chosen [14].

The main motivation of all visual texture perception techniques, whether it relies on characterising texture to its statistics or modelling the HVS response using filter banks, aims to learn from how we interestingly discern texture to eventually develop more “clever” computer systems. With the various mathematical algorithms developed for the purpose of visual automation, a new discipline called texture analysis emerged, becoming an essential component in the computer vision problem.

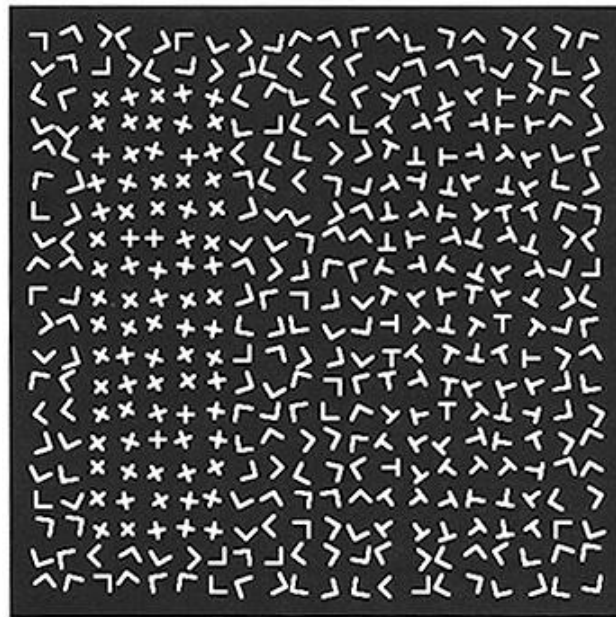


Fig. 1.3 An example of preattentive discrimination [15]. In the background which is composed of L-shape figures, the region to the right having X-shape figures is easily distinguishable compared to the region to the right which is composed of T-shape figures.

1.3 Texture analysis and its applications

Texture analysis is the process of extracting meaningful information from the surface of an object(s) appearing in an image, where this object could occupy a small region or the whole image. In a typical computer vision problem illustrated in Fig. 1.4, texture analysis can be involved in any of the stages following the acquisition stage. Image regions having certain textural properties can be delineated as for the pre-processing stage, while the feature extraction stage quantitatively captures texture patterns for classification, and the cost of prediction errors can be considered in the post-processing stage. The efficiency of any texture analysis system is assessed by the accuracy of its quantitative representation to classify patterns or identify objects. Accuracy can be improved either by developing an effective feature extraction algorithm which can provide high quality features or by designing a powerful classifier that can

deal with nonlinear and high dimensional features, while this thesis is more concerned with the former problem. There are four different methods for extracting texture features [16], which differ in the way the spatial relationship between the image pixels are observed. Statistical-based methods describe the grey level relationship between the image pixels through either first order (single) pixels statistics of histograms that do not take into consideration neighbourhood pixel interactions, or second order grey level statistics, that define the relationship between the pixels through displacement distance and orientation. Model-based methods rely upon capturing the fundamental qualities of the studied texture through constructing an image model having certain parameters; wavelet-based methods give a multiresolution interpretation to image texture in analogy similar to the HVS; geometrical-based characterises texture in terms of the geometrical properties of its elementary elements (e.g. Voronoi tessellation).

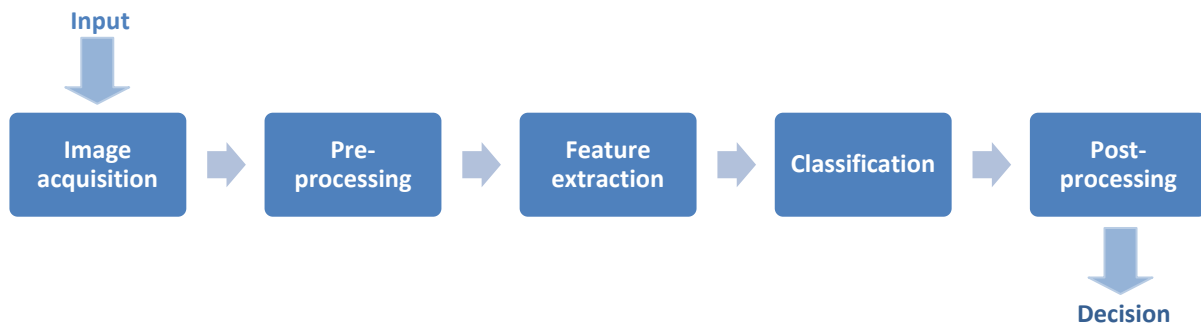


Fig. 1.4 Stages of a typical computer vision system

The extracted texture features can be deployed in many useful applications in computer vision. Major applications of texture analysis, such as classification, segmentation, texture synthesis and shape from texture [16, 17] are briefly discussed below.

1.3.1 Classification

Assessing the performance criteria of the applied feature extraction process requires selecting an appropriate classification algorithm or metric (dis)similarity measures. The differentiation between one classification method and another resides in their ability to overcome feature nonlinearity in order to distinguish the differences between compared texture regions; however, no matter how good the applied feature extraction process is if a poor classification design was implemented.

Classification can be generally implemented in two ways [18]: quantitative performance analysis and automated class assignments. The former operates by analysing and then finding differences between the feature values of the various texture or cluster regions (e.g. placing a threshold), while in the latter each distinctive region is assigned a class and then error estimation (i.e. classification accuracy) is indicated from the testing set.

Removing a portion of the data set for testing and keeping the remaining for training the classifier is known as *cross validation*. The main objective is to ensure fidelity and replication (i.e. non-randomness) of reported classification results when a different sample is investigated. There are several approaches for cross validating the classification results, the *hold-out* method is simply splitting the data set into two disjoint training and testing sets; *K-fold* cross validation method splits the data set into K subsets, for which one of the subsets or folds is used for testing and the remaining $K-1$ are used for training, it can be viewed as running the hold-out method K different times; *leave-one-out* method is the extreme case of the K -fold method, in which for a data set of length N , the number of folds K is equal to N ; *bootstrap* method randomly generates sample sets of size N by sampling with replacement, unlike the previous methods which used sampling without replacement, that is, once a sample is selected the data set for training or testing cannot be drawn again. Advantages and disadvantages of each method can be found in [19].

1.3.2 Segmentation

Texture segmentation is similar to the classification problem in the sense of identifying texture from its feature values, yet segmentation can be more complex, for which multiple texture regions are present in an image (see Fig. 1.5). The task is to search for regions with uniform texture and then correctly label them with their relevant classes, taking into account texture boundaries where window samples may contain more than one type of texture. Texture segmentation can be divided to supervised and unsupervised, as the names state, the number of classes (i.e. prior knowledge of number of textures) in the former is assumed beforehand unlike the latter.

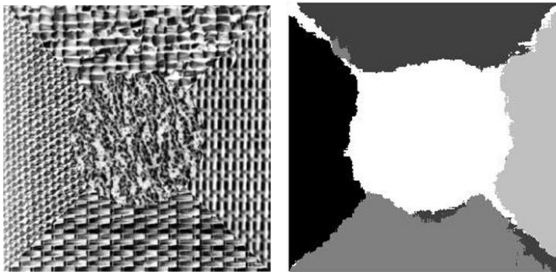


Fig. 1.5 Example of segmenting a Nat-5 Brodatz image composed of five types of textures using co-occurrence features.

1.3.3 Texture synthesis

Texture synthesis is a way to generate large textures from a model of a small texture sample, so that the synthesised texture would perceptually appear as having the same stochastic characteristics of the initial sample but not identical to it. Mainly model-based feature extraction methods such as fractals and Markov-Gibbs random fields [17] are used for model generation. Texture synthesis has many applications especially in computer graphics, where texture mapping is used to wrap up surfaces and for interactive scene rendering.

1.3.4 Shape from texture

Analysing the various cues appearing in a 2-D image can allow one to infer the 3-D shape of a surface. Cues such as the variation of shading on an object surface or viewing the surface from a slant, can give inference of the surface shape from the perspective texture gradient. This gradient can be used to compute depth information so the surface orientation can be estimated [16]. Shape from texture has many applications in automated object recognition as autonomous navigation.

1.4 Summary

Image texture remains a challenging field with many efforts exerted to conceptualise this term. The various properties that define a certain surface vary from image to image and from one application to another, calling for robust approaches to overcome such disparities in object surface display, i.e. that can achieve efficient characterisation, and which would make the job of automated object identification easier and more effective. Moreover, the heterogeneous nature of medical images – the focus of this thesis – is another challenging aspect and would contribute in further increasing the complexity of the examined texture. We take this challenge and attempt to provide solutions to some of the problems associated with tumour texture classification.

In this thesis, chapter 2 defines the type of textures encountered in medical images and how to characterise it, followed by an overview of the functionalities of the main biomedical imaging modalities used in the medical arena, and then background on lung and brain tumours. A survey of the various approaches developed for the purpose of identifying and classifying these tumours concludes the chapter. Chapter 3 explains how we can increase lung cancer staging accuracy from conventional computed tomography images using the fractal dimension, which is followed in chapter 4 by investigating the effect of noise on these images when applying seven different texture measures. Chapters 5 and 6 investigate a different texture (acquired via microscopy modality) for a different tumour (brain meningioma) from a mono and a multiresolution perspective; respectively. Finally, the thesis ends with a concluding discussion in chapter 7.

Chapter 2

OVERVIEW OF CT LUNG AND DM BRAIN TUMOUR IMAGING TECHNIQUES

The various biomedical imaging techniques have a main objective which is to make the patient's diagnosis and treatment faster, easier and more efficient. Operation of these imaging modalities is based on incorporating both hardware and software techniques for image acquisition and analysis to address the questions of pathology and diagnosis. The hardware part has the responsibility of the invasive or non-invasive non-destructive interaction with patient's body and then detecting and measuring the response. This happens while patient safety remains the fundamental principle concerning diagnostic procedures, and the functions of body organs should remain unaffected or are able to recover while its image is being acquired. After the details required for image formation has been captured, the software role emerges to arrange this raw information in an understandable format for display. Exploiting the computer's processing power, various mathematical algorithms are applied in this process depending on the function of the modality in use. The displayed image can then be further processed using enhancement, segmentation and analysis techniques to facilitate decision taking or for automated classification under clinician supervision.

The appearance of body organs in addition to other medical tests, such as biopsy specimens, body fluid analysis and measurement of body functions, can be significant for physicians to reach to a decision on the medical situation of the patient. The healthiness state in most cases is reflected on the surface, which is in analogy to facial expressions where a person can be identified as happy or angry without the need to communicate verbally to ask about how he or she feels; similarly, physicians can have an initial idea on the (ab)normality of the observed organ from its general appearance via an image captured using a non-invasive or minimally invasive procedure. Image texture is one of the important cues that could give physicians such indication, which would trigger certain treatment procedures, if texture is found abnormal, depending on the nature of the disease.

To avoid diagnosing disease at an advanced stage when it has already progressed and hence patient's prognosis (i.e. prediction of disease course or outcome) becomes poor, early detection of disease can be improved by using effective clinical diagnosis systems. While there are numerous studies on lung and brain disease detection and evaluation, work in this thesis will focus on tumour disease as it serves as one of the primary threats to life. This chapter begins by defining types of texture in the medical environment and then describing the various biomedical imaging modalities used for acquisition. Brief medical background on the type of tumours dealt with in this work will be given. Finally we conclude with coverage of major work done throughout the last decade on lung and brain tumour imaging acquired via computed tomography and digital microscopy modalities.

2.1 Texture characterisation

Image texture in biomedical imaging may be characterised at two levels, cellular and tissue, each of which represent the biological properties of an organ of interest in a zoomed-in or out fashion. Tissue level images, which are basically acquired noninvasively, concentrate on the appearance of the blood vessels and other connective tissues resulting in images known to have a *micro-scale* structure due to the fine overall appearance of the texture. In contrast, cellular images are acquired from minimally invasive biopsies or blood samples, for which the internal structure of these small specimens is magnified multiple times until their molecular properties are revealed. At this zoomed-in level, the cell nuclei become the main descriptors of the texture beside other extracellular fluids, and the morphology of the scattered cell nuclei, i.e. shape, colour, structure and pattern, and with their relatively large size adds the grainy appearance for this type of texture to be defined as having a *macro-scale* structure.

2.2 Biomedical imaging modalities

Different approaches were introduced for the purpose of revealing the hidden structure of the body organs with minimal invasiveness. However, patient safety receives priority consideration when designing biomedical imaging devices, with the main challenge residing in being able to capture the clearest and most descriptive image of an organ with limited side effects. The study of the organ tissue ranges from using minimally invasive mechanical techniques as extracting a small biopsy from the organ tissue to be studied *ex vivo* via a digital microscope (DM), or even using an electron microscope which can magnify the structure a thousand times more than that of an ordinary light microscope. Another related method is inserting an endoscope into the patient's body where real-time images are transmitted by a fibre optic system, and can be used also for tissue specimen extraction. Alternatively, non-invasive techniques can be used for *in vivo* diagnosis which relies on the interaction of an external signal or internally injected substance with the tissue of the organ of interest, and then measuring the power of response emerging from that region. This interaction should be within acceptable ranges specified by certain limits of doses that a patient should be exposed to. For instance, modalities that employ ionising electromagnetic radiation such as radiography or computed tomography record how much attenuation occurs to a focused X-ray beam after it has penetrated the scanned region, and the higher the dosage the more the damage caused for the tissue, making its recovery very difficult. Also, in nuclear medicine the emitted electromagnetic gamma-rays from the nucleus of a radioactive isotope administered intravenously are detected by a gamma camera after interaction with the tissue. Other much safer modalities (i.e. which do not use ionising radiation) are ultrasound and magnetic resonance imaging, where in the former high frequency waves are transmitted and their energy is measured after reflection from different tissue densities as they travel inside the body to the designated region, while in the latter the radio frequency response of the hydrogen protons in water to the perturbation created by an external applied magnetic field is detected.

Virtually all non-invasive modalities can be used for comprehensive imaging as they rely on the principle of wave energy attenuation as it passes through the body tissue of different densities, yet their performance varies due to reasons related either to the properties of the type of focused energy or depending on the location and density of the scanned organ. Modalities that use ionising radiation tend to have very high energies enabling both X-rays and gamma-rays to penetrate deeply in the human body passing through soft or low density tissues, such as lung, kidney...etc., and hard or high density tissues, such as bones. For instance, bones appear lighter on the gamma or X-ray projected images since it is very dense and absorbs most of the electromagnetic waves compared to the surrounding cartilage and other soft tissue. Yet health risks are usually associated with such ionising radiation, constraining their use to certain dosage limits and thus cannot be used extensively. On the other hand “safer modalities” such as ultrasound are good at soft tissue imaging and can be used with small children and pregnant women, yet it suffers from high signal attenuation in air and high density regions, therefore not suitable for imaging tissue located behind bones such as brain or lungs. Patients with cardioverter defibrillators and pacemaker implants may not be safe for them to undergo a magnetic resonance imaging scan due to the effect of the strong magnetic field and radiofrequency pulses generated during the scan. Given the advantage of ease and comfort that non-invasive modalities might deliver to the patient during the diagnosis session compared to the invasive counterparts; however, high diagnosis accuracies can be achieved with invasive techniques and are mainly used for verifying non-invasive results which may be prone to noise and other distortions as patient movement. The main imaging modalities used for diagnosis and some for treatment as well are listed in Table 2.1 with a brief description of functionality.

2.3 Tumours

According to the World Health Organisation malignant tumours or cancer has become the leading cause of death worldwide [20], with many efforts being directed towards a better understanding of this disease with a hope to make it a completely curable disease.

Several steps can be followed to tackle this disease; one is the early detection before it starts to spread, that can be achieved by improving the efficiency of the biomedical imaging modalities used and increasing health awareness among people to recognise early disease signs. Another is suppressing the disease itself, as part of preventive medicine, through avoiding factors which can evoke this disease leading to a rise in cell changes, and eventually causing tumour growth. Examples of such risk factors are consumption of tobaccos and alcohols [21]; exposure to carcinogenic substances physically such as ultraviolet radiation in sunlight and other natural and artificial ionising radiations, or chemically as urban air pollution, chemical dyes, asbestos, coal tar, etc.; and we should not forget some of the bad habits delivered with modern civilisation as not following a healthy life style – need to eat less meat, more fruit and vegetables – and low physical activity, all may contribute in increasing the chance for a tumour to develop.

Table 2.1 Main biomedical imaging modalities used for disease detection and diagnosis

Invasiveness	Modality type	Description
Invasive	Microscopy	<p><i>Light or optical microscopy:</i> The simplest type of microscope based on visible light which uses a system of lenses for magnifying biopsy or autopsy samples. This type of microscope can be modified to capture sample images in a digital format using a charged-coupled device (CCD) camera; to be known as <i>digital microscopy</i>.</p> <p><i>Electron microscopy:</i> A type of microscope that uses electron beams instead of visible light which is used in ordinary optical microscopes. The electrons' shorter wavelength as compared to visible light rays assists in achieving a higher linear magnification and resolving power (i.e. ability to distinguish fine details) exceeding one million, which is several hundred times the resolving power of an ordinary optical microscope [22]. This possibility of observing objects at a molecular level made electronic microscopes play an important role in paving the path for new research possibilities in biology, chemistry and other related nanotechnology sciences.</p>
	Endoscopy	<p>A technique used for viewing the internal surface of an organ through the insertion of a rigid or flexible tube – containing a light source and lens system to visualise and transmit back images via a fibre optic system – into the body. Some are also equipped with surgical medical instruments to enable the removal of biopsies for external examination.</p> <p>Recently a new endoscopic technique, called wireless capsule endoscopy (WCE), has been developed which can make the procedure of viewing in-vivo structures more pleasant and easier for patients [23]. The WCE comprises a tiny coloured digital video camera, wireless radiofrequency transmitter, light source and a battery which all are implanted inside a small pill made of a safe biomaterial and resistant to stomach acids and digestive enzymes. This camera can provide a digital movie of the patient's entire intestine so the physician can later examine on his/her computer and diagnose.</p>
Non-invasive	Radiography	<p>Can be defined as the use of an ionising electromagnetic radiation, such as X-ray, for imaging internal body structures. Types of radiographic imaging [24]:</p> <p><i>Projection X-ray:</i> is the conventional type of X-ray imaging technique where static images are captured by projecting the generated X-ray energy from the X-ray tube on the body. Nowadays, the analog film is replaced by a digital sensor in order for images to be acquired and sent to a computer for viewing. Mainly used for examination of bone fractures.</p> <p><i>Mammography:</i> a type of projection X-ray where a specially designed X-ray machine projects X-ray beams on very high contrast and high resolution digital film for acquiring detailed images of breasts for diagnosis.</p> <p><i>Fluoroscopy:</i> an X-ray imaging technique that employs a continuous or a pulsing X-ray beam at a lower dose rate of radiation for producing real-time dynamic images of internal structures. It is used in gastrointestinal studies and catheterisation, where a contrast agent (e.g. barium or iodine) is administered allowing the physician to see the internal structures of the image organ while the contrast agent passes through.</p>
	Computed Tomography	<p>Computed tomography or computerised axial tomography (CT/CAT) is a cross-sectional improved X-ray technique that produces images of any part of the body. A fan of thin X-ray beams are directed over the patient's</p>

	body from an X-ray tube mounted on one side of the circular-shape CT scanner and received by detectors on the opposite side. As the rotating CT scanner frame spins around the patient's body, multiple profiles are recorded and then processed by a computer to construct a series of cross-sectional images or slices both horizontally and vertically. CT scans provide more detailed images compared to conventional X-ray, making it suitable to examine many body organs as brain, lungs, liver and kidney.
Magnetic Resonance	In MRI, unlike CT, a non-ionising radiation is applied for generating cross-sectional images of body soft tissues. Since hydrogen is the most abundant atom in the body – nearly two-thirds of the human body consists of water – the nuclear magnetic resonance of protons (i.e. nuclei of hydrogen atoms) are used to produce proton density images. First a magnetic field is focused from the MRI magnet on the body to align the protons in a parallel formation, which are then exposed to a strong but harmless pulse of radio waves that will scatter back this alignment to the initial random pointing position. While the protons spin or align themselves back again, they produce a radio signal which will be detected by a receiver in the MRI scanner. Finally, based on the strength of the received signal – which shows how much hydrogen is present in the scanned organ – images are generated by the computer so that the stronger the signal the brighter the image, and vice versa.
Ultrasound	Ultrasound (US) – also called sonography – is a noninvasive diagnostic medical procedure that uses high frequency sound waves above the human hearing range (i.e. greater than 20 kHz) to produce dynamic visual images of organs, tissues or blood flow inside the body [25]. The ultrasound transducer receives the returning or bouncing back high frequency sound waves when transmitted to an area of interest. The transmitted sound wave will incur losses to its energy when penetrating the examined organ depending on the properties of the medium (e.g. bones have little water as compared to tissue). Thus, the variation in attenuation between the organs and the surrounding fluid and due to different tissue densities would contribute to the pixel intensity levels in the acquired real-time image. US can be used to examine many parts of the body, such as the abdomen, breasts, prostate, heart and blood vessels and other soft tissue organs. Also it is considered safe, inexpensive and portable as compared with other imaging modalities [26].
Nuclear medicine	Nuclear medicine (NM) operates in an opposite manner to that of other X-ray modalities, for which the electromagnetic waves are emitted from within the tissue (i.e. internally) and not from an external source. The process starts by the patient ingesting or being injected with a nuclear material (radiopharmaceutical agent) into the blood stream for creation of radioactive tracers to localise in specific body organ systems. These tracers accumulate eventually in the organ of interest and give off energy in the form of gamma-rays emitted from the nucleus of the unstable radioactive atoms. Then a special camera detects these emitted energies and digitises them into images by a computer. Applications of NM include detection of cancer spread and bone fractures, and evaluation of functions of heart, kidneys, lungs, stomach and thyroid. Examples of NM are gamma cameras, positron emission tomography (PET) and single photon emission tomography (SPECT), where the last two operate similarly to the gamma camera but have the advantages of tomography (i.e. slicing) in providing 3-D images.

Next we define what exactly is a tumour, how does it occur and what are its different types, then emphasis is given to lung and meningioma brain tumours which are the focus in this thesis.

2.3.1 Defining and identifying tumours

A tumour is recognised as the existence of an abnormal mass of tissue with a capacity for progressive growth. It is a term used to describe body cell chaotic growth and divisions occurring in an uncontrollable fashion, usually due to cell DNA change or damage [27]. These disorders would affect the life span of the cells in when they need to die and when to form new cells (i.e. divide), as a result, these mutated extra cells – which consume oxygen, nutrients and occupy space from the healthy cells – would contribute to the formation of the tumour tissue.

Tumours can be classified into two main classes of benign or malignant [28]:

- *Malignant (cancerous) tumours*: Cells in these tumours can invade nearby tissues by breaking away from a malignant tumor and travelling through the bloodstream or lymphatic system to form new tumours in other parts of the body. The spread of cancerous cells from one part of the body to another is called metastasis which is a major cause of death from cancer. The site that the cells initially spread from is called the primary tumour and the nearby affected site is called the secondary or metastatic tumour. Malignant tumours are dealt with surgically followed by radiation and chemotherapy to kill any non-spotted remaining malignant cells, or by chemotherapy alone if it is difficult to surgically remove the tumours; especially for late stages.
- *Benign (non-cancerous) tumours*: Cells in benign tumours would not grow in an unlimited manner and do not invade surrounding tissue or spread to other parts of the body (i.e. metastasise). Often these can be reduced in size or completely removed without reoccurring again and there is usually little threat to life if not removed.

Essentially, there are as many different types of tumours as there are different types of human cells, just over 200 types, with some being very common, while others are extremely rare [29]. Nearly all tumours are named after the organ or type of cell that they originate from. For example, the tumours start in lungs are called lung tumours, and those that start in skin cells – known as melanocytes – are called melanoma. However, tumour types can be grouped into broader categories. The main categories of tumour as specified by the U.S. National Cancer Institute [28] are:

- Carcinoma - begins in the skin or in tissues that line or cover internal organs.
- Sarcoma - begins in bone, cartilage, fat, muscle, blood vessels, or other connective or supportive tissue.

- Leukaemia - starts in blood-forming tissue such as the bone marrow and causes large numbers of abnormal blood cells to be produced and enter the blood.
- Lymphoma and myeloma - begin in the cells of the immune system.
- Central nervous system cancers - begin in the tissues of the brain and spinal cord.

To prevent diagnosing the disease at advanced stages when the prognosis is poor, it is in the patient and physician's best interest to locate early and specify the type of tumour – benign or malignant – and the amount of metastasis which determines the selection of the appropriate treatment procedure.

2.3.2 Lung tumours

Lung tumours are the leading cause of death from cancer in both men and women throughout the world [30]. They are formed in cells lining air passages, and most lung tumours are found to be malignant [31] (i.e. can metastasise to other places). Lung tumours generally do not cause symptoms, especially for early stages, and it is usually as a result of the tumour growing – reaching an advanced stage – and causing pressure or pain. Also lungs are also considered a common place to metastasise from tumours affecting other body organs[32].

According to the cell size of the tumour from a histopathological specimen viewed with a microscope, lung tumours can be divided into two main groups which account for about 95% of all cases [31]:

- Non-small cell lung cancer (NSCLC): makes up about 75% of all cases and it includes several subtypes of tumours, which are: adenocarcinoma, the most common type of lung cancer, making up 30% to 40% of all cases; squamous cell carcinoma is the second most common type of lung cancer, making up about 30% of all lung cancers; while large cell cancer makes up 10% of all cases. Treatment is done by surgery – especially for early stages – or radio/chemical therapy or a combination of both.
- Small cell lung cancer (SCLC): are less common – makes up about 20% of all cases – but they grow more quickly and are more likely to metastasise than NSCLC. Often SCLCs have already spread to other parts of the body when the cancer is diagnosed, and mainly treated by radiation or chemotherapy rather than surgery.
- About 5% of lung cancers are of rare cell types, such as carcinoid tumour and lymphoma.

Once the lung tumour is recognised there is a need for the diagnosis to be represented in a comprehensible form to all physicians. Staging of lung cancer disease would reduce the variation in the reported diagnosis, assist in selecting the appropriate treatment procedure whether it was invasive (e.g. surgical) or non-invasive (e.g. radiation or chemotherapy) or a combination of both, and also in estimating long-term survivability (i.e. prognosis). The American Joint Committee on Cancer proposed a

scheme for NSCLC lung cancer based on the TMN system (see Table 2.2), where the staging scheme was revised in 1986 and again in 1997 [33].

In brief, the T stands for tumor size and invasiveness and is staged from T1 to T4. Tumours with size less than 3 cm are staged as T1, while for greater sizes and if the tumour is grown to the main bronchus it is T2. T3 means the tumour has reached the chest wall but it is still operable. T4 tumours have invaded the mediastinum – the area and organs between the lungs – which involve the heart, great vessels, trachea or esophagus, or because it involves the pleura (i.e. lining of the lung) with accumulation of fluid in the surroundings. The N letter stands for the degree of lymph node involvement and is represented from N1 to N3, and M represents the presence or absence of metastases which is staged as 1 for presence and 0 for otherwise. For example, if there was a stage two diagnosed tumor represented as T2N1M0, then it can be interpreted as a lung tumour having a size greater than 3 cm, with first degree lymph node involvement and no metastasis.

Table 2.2 Lung tumour staging based on the TNM system

Stage	Size	Lymph	Metastasis
Stage IA	T1	N0	M0
Stage IB	T2	N0	M0
Stage IIA	T1	N1	M0
Stage IIB	T2	N1	M0
	T3	N0	M0
Stage IIIA	T1	N2	M0
	T2	N2	M0
	T3	N1	M0
	T3	N2	M0
Stage IIIB	Any T	N3	M0
	T4	Any N	M0
Stage IV	Any T	Any N	M1

The SCLC is represented by two stages: limited stage where the cancer is found in one lung and adjacent tissue, and extensive stage where tumour has spread outside the lung to the chest or has metastasised to distant organs.

In this work we will focus on NSCLCs which make up two-thirds of reported cases with an objective of investigating tumour aggressiveness which will assist in differentiating between early and late stage tumours.

2.3.3 Brain tumours

Although brain tumours are not as common as lung tumours and most of the cases are benign and very few are found to be malignant [34], their occurrence is in a very sensitive organ, rendering them very serious and maybe life threatening. Moreover, some of the benign tumours may exhibit malignant properties (i.e. aggressiveness) if this happen to be located in a sensitive or vital area in the brain. Brain tumours can be categorised in two groups [34]:

- Primary brain tumours: are benign or malignant tumours which were originally developed in the brain tissue. Primary brain tumours can be further subdivided to gliomas, which begin in the glial (supportive) tissue, and non-gliomas. The different types of gliomas are astrocytomas, brain stem gliomas, ependymomas and oligodendrogliomas. The other types of brain tumours that do not begin in the glial tissue are meningiomas, medulloblastomas, schwannomas, craniopharyngiomas and germ cell tumours or pineal region tumours.
- Secondary (Metastatic) brain tumours: cancer cells are originally developed outside the brain, where it metastasises to the brain via the blood from distant affected organ such as a lung, breast, kidney, colon or skin. The incidence of this tumour category is usually higher than that of primary brain tumours.

The grade of a brain tumour refers to its cells' shape when observed under a microscope. Classification is done by grades – from low grade (grade I) to high grade (grade IV). Cells from higher grade tumours are more abnormal looking and generally grow faster than cells from lower grade tumours; higher grade tumours are more aggressive than lower grade tumours [35]. Treatment of malignant brain tumours is often done by radio/chemotherapy, while for some cases, depending on the tumour type and stage, surgical removal of the tumour would be a better option [36].

Meningioma tumours – the type of tumour dealt with in this thesis – usually occur in adults, with a marked female bias represented by a one to three man to women ratio [37]. It also accounts for 27% of all primary brain tumours, making it the most common tumour of that type [38]. Meningiomas can have three grades, benign, atypical and anaplastic which are numbered from I to III, respectively. Here, we are more concerned with classifying different subtypes of meningioma tumours referred to as Grade I, which is considered a more difficult task compared to grade differentiation where differences become more obvious. An automated meningioma grading system is essential in improving reproducibility by overcoming subjective diagnosis due to variability associated with expert's evaluation. That is, when differences become minor between tumour subtypes of the same grade this might trigger for an increase in intra-observer variability, i.e. pathologist not being able to give the same reading of the same image at more than one occasion, and inter-observer variability, i.e. increase in classification variation between different pathologists; and thereby reducing uncertainty that may impact patient outcome.

A survey of the variety of approaches applied in lung and brain tumour detection and diagnosis acquired via CT and DM modalities, respectively, are discussed in the following section. The survey covers major work done in this field over the last decade, especially after the increase in computer processing power and storage capacity, which facilitated the advent of new mathematical algorithms for developing clinical diagnostic systems with better image feature extraction qualities and discrimination capabilities.

2.4 CT lung tumour imaging

Physicians use lung screening for verifying causes of suspected lung disorder symptoms, such as coughing, shortness of breath, wheezing, chest pain, swelling in legs and arms, or other signs indicating lack of oxygen in the blood (e.g. bluish or purplish discolouration of lips or nail beds) and/or body respiratory system failure. Deficiencies in lung functions could be due to several reasons which can take several forms, such as [39]:

- Chronic obstructive pulmonary disease: e.g. emphysema,
- Interstitial lung disease: e.g. pulmonary fibrosis,
- Pneumonia: inflammation of lungs caused by bacteria,
- Pulmonary embolism: blockage of pulmonary artery by foreign matter or blood clot,
- Cystic fibrosis: inherited disease in secretory glands,
- Primary pulmonary hypertension: an increase in blood pressure in the pulmonary artery, vein or capillaries,
- Tuberculosis
- Lung cancer

Different approaches and numerous methods were developed by researchers for the purpose of computer aided diagnosis of lung problems. Depending on the type of lung disorder, each of the lung pathologies may require a specific approach to follow in order to characterise the disease. Since the focus of this thesis is on lung cancer classification, one way is to look for lung nodules – which are round masses of tissue in the lungs and can be early signs of cancer – and try to investigate whether they are benign or malignant. Also by means of measuring the characteristics of these tumour masses, one can predict their aggressive behaviour (i.e. how high is their metabolic activity). Major approaches in lung nodule detection and classification are discussed next.

Neural networks and genetic algorithms machine learning techniques were applied in some studies for automated detection of pulmonary nodules. Suzuki et al developed a computer aided diagnostic (CAD) scheme that uses a massive training artificial neural network (MTANN) – which is a trainable nonlinear filter based on an artificial neural network (ANN) – for distinction between benign and malignant lung nodules in low-dose helical CT scans [40]. Six parallel arranged expert MTANNs were used to differentiate between malignant nodules and six different types of benign nodules. The MTANNs were trained with ten typical malignant and ten benign nodules for each of the six types. Training was done independently using input CT images and teaching images containing the estimate of the distribution for the “likelihood of malignancy”, that is, the teaching image contains a 2-D Gaussian distribution of a malignant nodule whereas its peak is located at its centre, and that of the benign has a zero value. Then the six MTANNs outputs were combined using an integration ANN in order to provide a value for

malignancy assessment, with high values relating to malignant nodules and vice versa to the benign nodules. Zhang et al applied a 3-D cellular neural network (CNN) to detect small pulmonary nodules in high resolution helical CT scans [41]. Relying on the local shape properties for the purpose of voxel classification, local shape differences between nodules and blood vessels were captured using a shape index feature. While classification by voxels would allow for coverage of neighbouring information, the 3-D CNN was trained using genetic algorithm (GA) to deal with the shape index variation pattern of nodules. Lee et al combined two template matching methods based on a GA and conventional template matching techniques for detection of lung nodules in helical pulmonary CT images [42]. Nodules were detected within the lung area by the GA after specifying the target position and selecting the appropriate template image from several reference patterns, while the conventional matching template method was used to determine lung nodules along the lung wall by rotating semicircular models – serving as reference patterns – according to the orientation of the target point on the contour of the lung wall. Then 13 texture features were extracted and employed for false-positive (FP) findings elimination. Li et al evaluated psychophysical measures' capability in distinction between benign and malignant lung cancers in low dose CT scans [43]. Subjective similarity ratings for benign and malignant nodules were recorded by 10 radiologists. Then after feature extraction, the performance of four different techniques for determination of similarity measures, namely, feature-based pixel value difference-base, cross correlation-based and neural network-based techniques were evaluated by correlation with subjective similarity ratings.

Others focused on the geometric and/or morphological shape of the pulmonary nodules. Brown et al used a generic CAD system model where baseline scans were employed for detection of candidate lung nodules for previously unseen patients [44]. Nodule features such as position, shape and volume would serve as baseline results, to be used then for comparison in follow-up scans. Farag et al used four different types of deformable templates to describe typical geometry and grey level distribution of lung nodules [45]. The four types are: solid spherical models of large size classified and non-classified nodules; hollow spherical model of large lung cavity nodules; circular model of small nodules; and semicircular model of lung wall nodules. Then the normalised cross correlation template matching by genetic optimisation and Bayesian post-classification are combined for nodule detection. Ge et al developed a CAD system that detects nodules and reduces FP through extracting 3-D shape information features from VOIs [46]. 3-D gradient field features and ellipsoid fitting were designed to distinguish nodules – which have a spherical shape – from the elongated shape of blood vessels. Classification was performed using linear discriminant analysis with stepwise feature selection, and a receiver operating characteristic (ROC) analysis was used to evaluate the FP reduction performance. Paik et al developed a CAD technique using a surface normal overlap method for detection of lesions [47]. This technique assumes that lesions such as lung nodules and colonic polyps tend to have some convex regions on their surface, and thus an intersection might occur between the inward pointing surface normal vectors of these features and the tissue. However, the type of nodule (benign or malignant) was not investigated. Armato et al applied a ROC analysis to

evaluate the performance of a linear discriminant classifier to distinguish between benign and malignant nodules in low dose helical CT images [48]. Morphological and grey level features were computed from each lung nodule candidate after specifying their locations using grey level thresholding and then fed to the classifier. Some focused on nodule volumetric measurements as a mark of malignancy, such as Kostis et al who measured the volumetric growth of small pulmonary nodule over time using 3-D methods applied to HRCT images for the purpose of distinguishing malignant from benign nodules [49]. 3-D intensity and morphology-based segmentation algorithms were developed for four different morphologic classes of pulmonary nodules. They showed that 3-D methods for nodule growth estimation rate are more accurate than those based on 2-D measurements. In an extension to Kostis et al work, Reeves et al determined the likelihood of malignancy of pulmonary nodules from CT images via measuring the growth rate (i.e. change in nodule size) from two successive CT image scans recorded at close but different times [50]. Benign nodules have usually a slow growing rate compared to malignant nodules, and quantitative volumetric measurements can serve as a predictor of nodule's possible malignancy. The growth rate measurement accuracy was improved by using methods that match two images according to density (adaptive thresholding), location (registration), and vessel removal consistency (rule-based segmentation).

Clustering techniques were used by Tanino et al using principal component (PC) analysis clustering for classification of ground glass opacities – a radiological term to describe hazy opacities within the lungs [51]. Suspicious shadows are first classified according to size into two sub-clusters, and then further classified into two new sub-clusters according to PC scores, where the last step is iterated recursively. Finally the abnormality of suspicious shadows is determined via Mahalanobis discriminant functions. Kanazawa et al detected candidates of lung cancer from helical CT images through delineating lung and blood vessels regions using fuzzy clustering algorithm [52]. Then features related to shape, grey value and position is extracted from each region and certain diagnostic rules were applied for detecting lung cancer nodule candidates.

Examples of model-based techniques include the employment of the fractal dimension by Al-Kadi et al for improving lung cancer staging prediction accuracy from conventional CT modality [1]. Tumour region of interests (ROIs) were extracted from contrast enhanced CT images and quantitative performance analysis was used for discriminating between early and late stage tumours. Also strong correlation was shown between extracted tumour ROIs FD values and corresponding tumour staging as determined by positron emission tomography scan. Takizawa et al used a 3-D Markov random field model (MRF) for lung nodule recognition from X-ray CT images [53]. A mathematical morphology filter was used for locating suspicious shadow candidates, then volume of interests (VOIs) containing the shadows were extracted. A 3-D MRF model is used to evaluate the relationship between the geometrical object models (i.e. nodules and blood vessels) after calculating the probabilities of the hypothesis that a

certain VOI relates to a nodule or a blood vessel. Moreover, filtering techniques were applied by Arimura et al, a difference-image technique for lung nodule enhancement and suppression of normal background structure [54]. Using low dose lung cancer CT images, a ring average filter and a matched filter were applied to generate a nodule-suppressed image and a nodule-enhanced image, respectively. The difference-image would then represent the subtraction of the nodule-suppressed and enhanced images. FPs were reduced using rule-based schemes and MTANNs. Li et al developed a selective lung nodule enhancement filter for improvement of nodule detection and reduction of FP rate [55]. The aim was to simultaneously enhance nodules and suppress other normal anatomic structures such as blood vessels and airway walls. Classification was done via an automated rule-based classifier and a case-based four-fold cross validation for performance evaluation.

2.5 DM brain tumour imaging

For an accurate examination of disease, histopathological biopsies or surgical specimens are examined by a pathologist mainly using a light microscope. Although invasive, studies that deal with brain tissue images captured via DM modalities can provide a closer view of neuropathologies which otherwise may be difficult to discern. Histopathological features might appear generally similar in a sense that all consist of cell nuclei immersed in cytoplasm; nevertheless, various discriminating morphological characteristics may exist between normal tissues and in between different disease types as well. To capture tissue deformations led by disease, the denseness and morphology of the cell nuclei can be an important cue in determining the global manifestation of the diseased tissue. Studies that deal with exclusively neuropathologies acquired via DM modality will be covered next.

2.5.1 Meningioma-related work

Lessmann et al employed a self organising map (SOM) – a type of ANN trained using unsupervised learning – in order to link the morphological histopathological image characteristics to the space spanned by features derived from HSV (hue, saturation and brightness) colour model and wavelet packet (WP) transform [56]. For four different subtypes of meningiomas, an average of 79% for the entire data set was classified correctly. In another similar study which utilised SOMs for classification of histopathological images [57], human observer defined features were used for clustering certain histological characteristics on a scale from one to four. Also Wirjadi et al applied a supervised learning method for classification of meningioma cells [58], using a decision tree, the most relevant features were selected from a base of grey and coloured image features.

Qureshi et al extracted features from four meningioma subtypes using adaptive WP transform and local binary patterns (LBP) methods [59]. In the applied WP technique, the most separable or best set of subbands are selected by simply measuring the discriminating power between all decomposed subbands at a certain level using Hellinger distance. While for the LBP method, the neighbouring pixels for each

pixel were thresholded by the value of the central pixel and a binary number was produced, for which first order statistics can be derived from its histogram. After comparing the performance using both methods individually and combined, the WP method gave the best results when the extracted features were classified via a support vector machine classifier after applying a principal component analysis for dimensionality reduction. Also in a similar study the performance of the WP was assessed after deriving co-occurrence matrix features from the decomposed subbands, and an improvement in meningioma discrimination was claimed in comparison if a WP was not used [60]. Both studies reported a classification accuracy of 82.1%; however, 92.5% was achieved using the same histopathological data set as shown by [61]. Therein, a combined statistical and model-based approach relying on Gaussian Markov random field and run-length matrix was used to capture the textural characteristics, and classification was done using a Bayesian classifier after eliminating highly correlated features by a correlation thresholding method.

2.5.2 Other types of brain histopathologies

Demir et al followed a graph-based method – called a cell-graph – for classification of histopathological glioma images through probabilistically assigning a link between cell clusters [62]. Cell-graphs are generated by calculating the probability of the link between pair of nodes, which correspond to a cell or a cell cluster, using the Euclidean distance between node pairs. Edges of the cell-graphs represented by the pairwise relation or links between the cells would then be used as topological features for investigation. The performance of this method in characterising gliomas gave a better accuracy in comparison with the cell-distribution and co-occurrence matrix approaches. The multilayer perception-based neural network and with a 30-fold cross validation recorded the highest classification results, with a 92% in differentiating malignant glioma from benign (non-neoplastic reactive) tissue. Sertel et al extracted co-occurrence and LBP features from neuroblastoma images for discrimination into two cases –stroma-rich and stroma-poor [63]. A sequential floating forward feature selection method was employed, and the k -nearest neighbour classifier with a leave-one-out for cross validation was used for performance evaluation; reporting an overall accuracy of 88.4%.

Others extracted morphological (e.g. area, roundness and concavity), and first and second order (e.g. histogram, and co-occurrence and run-length matrices, respectively) features to quantify astrocytoma brain tumours [64]. The degree of malignancy was determined after feeding the extracted features to a support vector machine classifier, and when cross validated by a leave-one-out method it gave an accuracy of 83.8% and 87.5% for distinguishing low for high grade tumours and grade III from grade IV tumours, respectively. In a more recent study, they improved their results by applying a least squares mapping technique for reducing the extracted features dimensionality prior to classification, achieving an overall performance of 95.2% [65]. However, their research was mainly concerned in differentiating

between different astrocytoma tumour grades, while this thesis focuses on discriminating meningioma subtypes – a more challenging problem given the minor differences between some subtypes as compared to the differences between different grades.

2.6 Summary

The main purpose of a CAD system is to provide decision support for physicians in the diagnostic process for a better patient prognosis. Thus, various feature extraction and machine learning techniques were developed by researchers for characterising diseased tissue relying on its textural appearance, each of which focused on how to delineate abnormality with the aim of improving efficiency, ease and speed of patient's diagnosis. Previous work on lung tumour CT images was mainly concerned with nodule detection and also in investigating their clinical state, i.e. whether they are benign or malignant. Chapter 3 in this thesis will take this work a step further by discriminating between malignant tumour stages in order to provide a tumour aggression index, which is considered a harder task given the minor differences between malignant tumours compared to the differences between malignant vs benign and malignant vs normal tissue. Also the study of the effect of noise encountered in CT images on texture measures will be discussed in chapter 4. Regarding histopathological meningioma images, most past work on focused on tumour grade differentiation, and a few concentrated on subtype differentiation. In chapter 5 and 6 we will show that previously reported results on meningioma grade I subtype differentiate can be further optimised to higher accuracies by two different novel methods.

Chapter 3

FRACTAL DIMENSION AS A LUNG TUMOUR QUANTITATIVE CLASSIFIER

Preview

This chapter presents the potential for fractal analysis of time sequence contrast enhanced (CE) computed tomography (CT) images to differentiate between aggressive and non-aggressive malignant lung tumours (i.e. high and low metabolic tumours). The aim is to enhance CT tumour staging prediction accuracy through identifying malignant aggressiveness of lung tumours. As branching of blood vessels can be considered a fractal process, the research examines vascularised tumour regions which exhibit strong fractal characteristics. The analysis is performed after injecting 15 patients with a contrast agent and transforming at least 11 time sequence CE CT images from each patient to the fractal dimension and determining corresponding lacunarity. The fractal texture features were averaged over the tumour region and quantitative classification showed up to 83.3% accuracy in distinction between advanced (aggressive) and early stage (non-aggressive) malignant tumours. Also it showed strong correlation with corresponding lung tumour stage and standardised tumour uptake value of fluorodeoxyglucose as determined by positron emission tomography. These results indicate that fractal analysis of time sequence CE CT images of malignant lung tumours could provide additional information about likely tumour aggression that could potentially impact on clinical management decisions in choosing the appropriate treatment procedure.

3.1 Introduction

Computed tomography (CT) is one of the best imaging techniques for soft tissue imaging behind bone structures [66]. A modern multislice CT machine enables the rapid acquisition of precise sets of successive images with very high resolution supporting a more confident diagnosis. Multislice CT images having millimetre slice thickness and high spatial resolution, with fast acquisition times, minimises artefacts due to abdominal movement and enables the clear visualisation of anatomical features and structures for the purpose of anatomical texture analysis. Yet, conventional anatomical imaging of lung cancers gives little indication as to tumour aggression apart from size (i.e. big is bad) and ground glass (i.e. favourable) opacification, while the status of the tumour vasculature is related to tumour aggression and survival [67]. Assessment of lesion heterogeneity and/or surface irregularity on CT and chest radiographs, including fractal analysis, can distinguish between normal tissue and tumours [68-75]. Nevertheless, commercial systems for computer assisted diagnosis of lung nodules are available for lesion detection and not for characterisation and identification of aggressiveness through examining image texture.

Texture analysis is concerned with the study of the variation in intensity of image elements (pixel) values

acquired under certain conditions. From a medical imaging perspective, physical quantities at scales smaller than the scales of interest can be analysed for proper classification [76]. In this research, the image intensities are transformed to the fractal dimension (FD) domain for the purpose of texture analysis of the fractal features (i.e. fractal analysis). The process of fractal analysis has many applications including image compression and segmentation as well as in image processing. Being able to extract useful but otherwise hidden information through digitally processing medical images is an important tool for physicians to support the accurate diagnosis without the need for biopsies — a process that can be unpleasant for patients and requires time, effort and incurs additional costs. The ability to predict the type of tumour with good accuracy from the image could be very advantageous.

Many studies have applied fractal analysis for different imaging modalities using different approaches for the calculation of FD in cases where expert radiologists may have difficulty identifying features. A number of studies reported successful results making use of fractals in texture analysis which are summarised in Table 3.1. Most studies were primarily concerned with distinguishing between normal and abnormal cases. This research is more concerned with lung tumour classification by determining FD feature vectors for regions of interest (ROIs), and using these vectors as predictors for tumour aggression. So far, investigation of abnormal cases only (i.e. aggressiveness of malignancies) and classifying them according to their aggressiveness and determining how FD relates to real medical key indicators has not been investigated before. The aim is to improve tumour stage prediction accuracy and not simply differentiating between normal and abnormal tissue. Amongst malignant lesions, the propensity for spread of tumour to other organs is variable. More aggressive lesions are associated with earlier and more extensive tumour spread. The extent of spread is described by the tumour stage, with higher stages reflecting more extensive disease. The ability of conventional CT to accurately determine the stage of lung cancer is limited in comparison to functional imaging techniques such as fluorodeoxyglucose positron emission tomography (FDG-PET) [77]. Furthermore, FDG-PET can assess tumour metabolic activity which also tends to be greater in aggressive tumours. Therefore, it would be very promising if tumour aggression could be determined with good accuracy through examining its texture from CE CT images only.

The FD of a structure provides a measure of its texture complexity. For example, if the pixel intensities in a CT image are regarded as the height above a plane, then the intensity surface can be perceived as a rugged surface. Fractals deal with structures that are not exactly Euclidean (i.e. “in-between dimensions”) giving the potential for a richer description of the examined surface; resembling in analogy the relation of fuzzy logic to digital logic. Although the FD alone cannot provide sufficient information to indicate the aggression of the tumours, this work extracts vector basis of FDs for tumour ROIs and correlates them with other clinical factors, investigating whether the texture complexity could be linked to other factors that have already been shown to be capable of predicting the aggression of the examined tumour in its early stages.

This chapter describes the research as follows. Section 3.2 provides an overview of the notion of fractal dimension. Section 3.3 describes the procedures and methodology, followed by experimental results and a discussion in sections 3.4 and 3.5, respectively. The chapter ends in section 3.6 with an assessment of the findings.

Table 3.1 Some studies which used FD for texture analysis and classification

Examined organ	Researchers	Modality	Method used
Lung	Kido et al & [70]	CT	Fractal feature extraction based on DBC
	Uppaluri et al [78]	CT	Using multiple statistics with FD
Liver	Wu et al [79]	US	Extracting multi-threshold FD vector
	Lee et al [80]	US	Fractal feature vector based on M-Band wavelet transform
Breast lesions	Chen et al [81]	US	Fractal feature extraction based on fBm
	Penn et al [82]	MR	Fractal-Interpolation Function (FIF)
	Mavroforakis et al [83]	X-ray	Quantitative approach based on advanced classifier architectures supported by fractal analysis
Blood perfusion in tumour tissue of canine subject	Craciunescu et al [84]	MR	FIF for 3-D tumour perfusion reconstruction

3.2 Theoretical concepts of fractal dimension

Mathematically, fractals can be defined as a geometrical set whose Hausdorff-Besicovitch dimension strictly exceeds the topological dimension [85]. The term fractal was first introduced by Benoit Mandelbrot to describe non-Euclidean structures that show self-similarity at different scales. Given that most biological and natural features show discontinuities and fragmentation, they tend to have a FD. Also most of these natural structures are complex and rarely have an exact Euclidean (smooth) shape so that they can be precisely measured.

In Euclidean n -space, a bounded set S can be considered statistically self-similar if S is the union of N_d non-overlapping subsets with respect to a scaling factor r , each of which is of the form $r(S_n)$ where the N_d and S_n sets are congruent in distribution to S . Thus, the Hausdorff-Besicovitch dimension – which is the fractal dimension – of a bounded set S in \mathbb{R}^n is a real number used to characterise the geometric complexity of S in the same way as length is used as a measurement tool in the Euclidean (discrete) space. Hence the FD can be computed as follows [85]:

$$\text{Fractal Dimension}(FD) = \frac{\log(N_r)}{\log(1/r)} \quad (3.1)$$

where N_r is the number of self-similar (invariant) shapes and r is the corresponding scaling factor.

A mathematical fractal, as the Sierpinski triangle shown in Fig. 3.1, can be self-similar on infinite scales; thus, its FD can be easily estimated using (3.1) as:

$$FD = \frac{\log(3)}{\log(2)} = \frac{\log(9)}{\log(4)} = \frac{\log(3^k)}{\log(2^k)} \approx 1.585$$

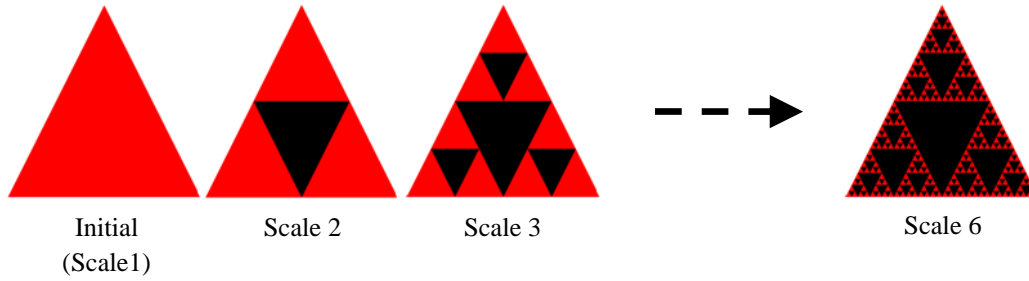


Fig. 3.1 Sierpinski triangle fragmented up to six scales.

Similarly, the FD for each of the lung tumour ROIs in the time sequence CE CT images can be estimated by first computing a multidimensional matrix of N_r defined as $N_d(x, y, d)$, where the first dimension d represents the original image after it has been filtered by kernel of scale 2, and the second dimension represents the image filtered by kernel of scale 3, and so on until reaching the highest scale j .

$$N_d(x, y, d) = \begin{pmatrix} p_{11d} & p_{12d} & \cdots & \cdots & p_{1Nd} \\ p_{21d} & p_{22d} & \cdots & \cdots & p_{2Nd} \\ \vdots & \vdots & \ddots & & \vdots \\ \vdots & \vdots & & \ddots & \vdots \\ p_{M1d} & p_{M2d} & \cdots & \cdots & p_{MNd} \end{pmatrix} \quad (3.2)$$

where M, N are the size of the processed image and $d = 1, 2, 3, \dots, j-1$ is the dimension of matrix $N_d(x, y, d)$.

Given $N_d(x, y, d)$ which represents the number of boxes necessary to cover the whole image, we perform the log operation on all elements of $N_d(x, y, d)$ and the corresponding scaling factor r . One of the advantages of the logarithm operation is that it expands the values of the dark pixels in the image while

compressing the higher-brighter-level values; also it compresses the dynamic range of images with large variations in pixel values [86].

After applying the logarithmic operations, each element from each array in $N_d(x, y, d)$ will be saved in a new row vector v . That is, the first element in all arrays of $N_d(x, y, d)$ will compose vector v_1 , and all second elements will compose vector v_2 , and so on as shown in (3.3). This process is depicted in Fig. 3.2.

$$\begin{pmatrix} v_1 \\ v_2 \\ v_3 \\ \vdots \\ v_{M \times N} \end{pmatrix} = \begin{pmatrix} p_{111} & p_{112} & \cdots & \cdots & p_{11j} \\ p_{121} & p_{122} & \cdots & \cdots & p_{12j} \\ \vdots & \vdots & \ddots & & \vdots \\ \vdots & \vdots & & \ddots & \vdots \\ p_{MN1} & p_{MN2} & \cdots & \cdots & p_{MNj} \end{pmatrix} \quad (3.3)$$

Finally, having the number of boxes required to cover the entire image area $N_d(x, y, d)$ with the scaling factor r we can then determine the slope b of the least square linear regression line by computing the sums of squares:

$$S_{rr} = \sum_{i=1}^{j-1} r_i^2 - \frac{\left(\sum_{i=1}^{j-1} r_i \right)^2}{j-1} \quad (3.4)$$

$$S_{rv} = \sum_{i=1}^{j-1} \sum_{k=1}^{j-1} r_i v_k - \frac{\left(\sum_{i=1}^{j-1} r_i \right) \left(\sum_{k=1}^{j-1} v_k \right)}{j-1} \quad (3.5)$$

The slope of the linear regression line gives the FD:

$$b = \frac{S_{rv}}{S_{rr}} = \begin{pmatrix} b_{11} & b_{12} & \cdots & \cdots & b_{1N} \\ b_{21} & b_{22} & \cdots & \cdots & b_{2N} \\ \vdots & \vdots & \ddots & & \vdots \\ \vdots & \vdots & & \ddots & \vdots \\ b_{M1} & b_{M2} & \cdots & \cdots & b_{MN} \end{pmatrix} \quad (3.6)$$

Actually, most natural and some mathematical self-similar fractals are random, meaning that they scale in a statistical fashion. The resemblance between shapes seen at different scales in natural fractals – and blood vessels branching in lungs are an example – is usually approximate and are considered to be random rather than self-similar. In theory, an examined fractal structure should have invariant self-similar fragmented and irregular shapes at all scales of measurement reaching to infinity. Yet, in biological structures this could only be true for a finite number of scales, depending on the resolution and depth of

the acquired image. Therefore, for each examined natural fractal there is a finite scaling range, such that below and above it, the structure becomes smooth (i.e. Euclidean) or completely rough and non self-similar (i.e. random).

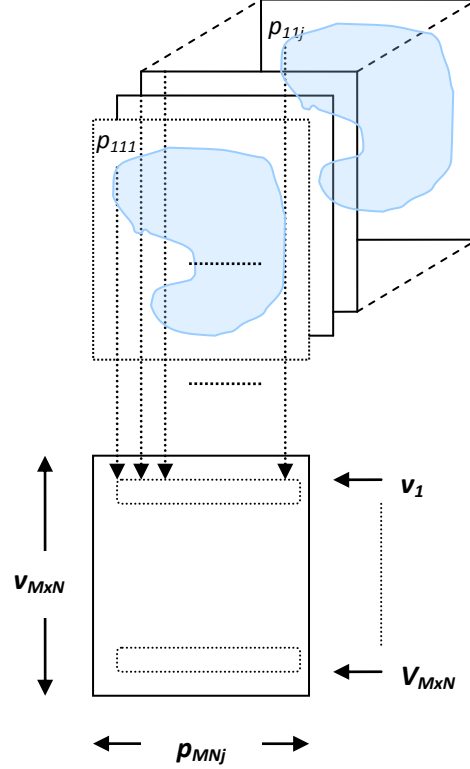


Fig. 3.2 Obtaining an array of row vectors from a multidimensional array $N_d(x, y, d)$.

In order to differentiate between two textures if their FD value was to be identical even though the two textures might not be similar, we need to compute the lacunarity (L) of the FD texture. Lacunarity measures the “lumpiness” of the fractal data, providing meta-information about the computed FD values in the image. The higher the lacunarity, the more heterogeneous the examined fractal area; and vice versa. It is defined in terms of the ratio of the variance over the mean value of the function as in (3.7), where M and N are the size of the FD processed image $I_{FD}(x, y)$ [76].

$$L = \frac{\frac{1}{MN} \sum_{x=0}^{M-1} \sum_{y=0}^{N-1} I_{FD}(x, y)^2}{\left(\frac{1}{MN} \sum_{x=0}^{M-1} \sum_{y=0}^{N-1} I_{FD}(x, y) \right)^2} - 1 \quad (3.7)$$

To practically represent how L can further differentiate between two or more texture patterns that may exhibit similar FD values, 25 different texture images representing natural patterns were selected from the Brodatz album for this purpose (see Fig. 3.3). After transforming each of the patterns in Fig.3.3 to the FD,

many of the patterns, although different, had their FD values similar as shown in Table 3.2; therefore, computing corresponding L can add another dimension for discrimination between *FD-alike* textures. For example, an FD value of 1.65 was recorded for textures D25, D19, D16, D86, D52, D23 and D47; and 1.69 for textures D112, D48, D95, D72, D30, D44 and D68; while D12, D62, D92 and D85 textures had a FD value of 1.80, thus all can be distinguished from their corresponding L values.

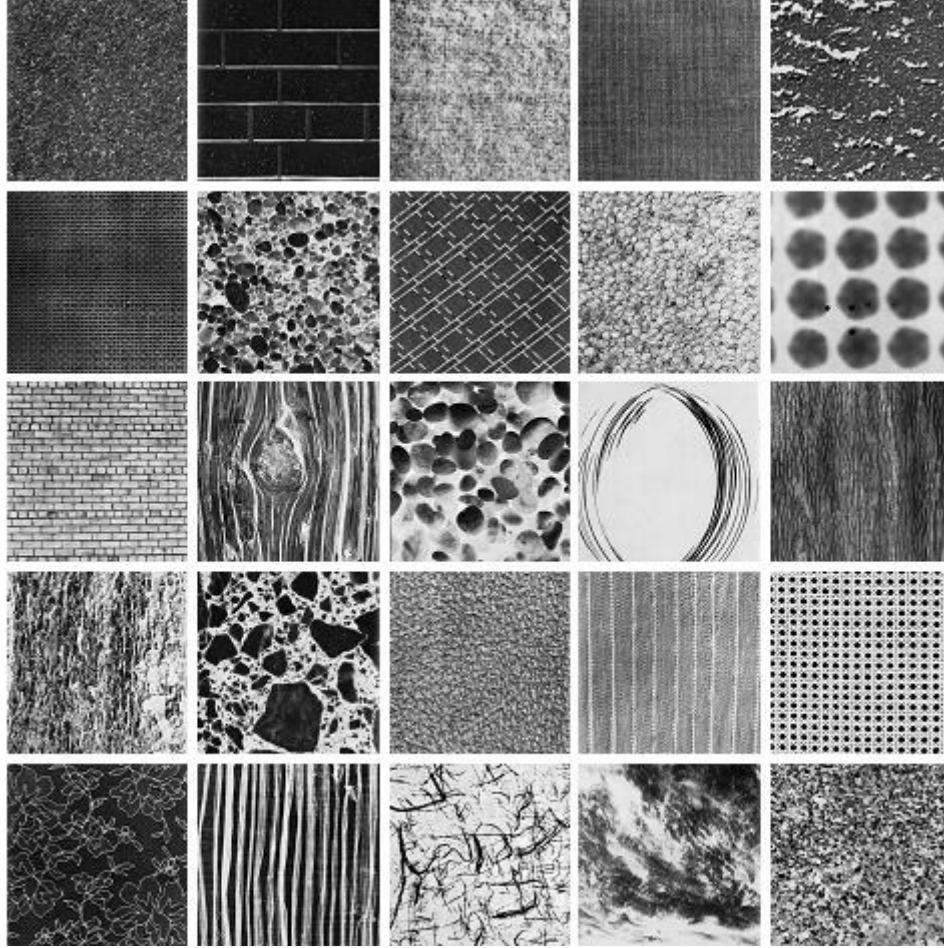


Fig. 3.3 Different texture patterns selected from the Brodatz album (reading from left to right, top to bottom), which are, D29, D25, D19, D16, D86, D52, D23, D47, D112, D48, D95, D72, D30, D44, D68, D12, D62, D92, D85, D103, D41, D51, D108, D90, D54; respectively.

Table 3.2 Fractal dimension (FD) and its corresponding lacunarity (L) for each of the patterns P shown in Fig.3.3

P	FD	L	P	FD	L	P	FD	L
D12	1.80	0.031	D48	1.69	0.145	D92	1.80	0.025
D16	1.65	0.107	D51	1.88	0.041	D95	1.69	0.082
D19	1.65	0.053	D52	1.66	0.123	D103	1.14	0.558
D23	1.66	0.045	D54	1.59	0.068	D108	1.48	0.223
D25	1.65	0.088	D62	1.80	0.055	D112	1.69	0.077
D29	1.64	0.083	D68	1.69	0.075			
D30	1.69	0.058	D72	1.69	0.080			
D41	1.71	0.131	D85	1.80	0.050			
D44	1.69	0.174	D86	1.65	0.079			
D47	1.66	0.069	D90	1.76	0.050			

3.3 Methodology

The work described in this section is divided into the following phases. The first is the processing phase where all sets of sequences of CE CT images — in Digital Imaging and Communication in Medicine (DICOM) format — are acquired for each case and then transformed to FD values for each pixel. The FD transformation resulted in images that were considerably enhanced compared to the original images, making it easier to extract the tumour ROIs. The edges separating different tissue structures and the branching structures of the larger blood vessels become more distinguishable. Then comes the fractal analysis phase where the maximum FD average (FD_{avg}) is computed — an average FD value for the tumour area is calculated for each image in the time series and the maximum was selected — with its corresponding lacunarity (i.e. the degree of non-homogeneity). The baseline FD_{avg} is also calculated as the FD of the tumour in the first image in the sequence of DICOM images once the contrast agent starts to diffuse, directly after injection. These values are then correlated with two markers of survival: tumour stage and standardised tumour uptake value of FDG as determined by positron emission tomography (PET). In a further study, the impact of CT acquisition parameters on FD_{avg} and lacunarity is investigated using a phantom structure.

3.3.1 Image Acquisition

In the first part, quantitative CE CT^a was undertaken on 15 patients' (10 males and 5 females with age 63 ± 8 years, and having lung cancers greater than 10mm^2) incorporated into a conventional CT examination performed for clinical tumour-staging. A dynamic sequence of 12 bit/pixel DICOM images of the thorax was acquired at the anatomical level containing the largest transverse dimension of the lung tumour. 50mL of conventional contrast material (Iopamidol, Bracco, Milan) with an iodine concentration of 370 mg/mL were administered intravenously at 7 mL/sec. Patients were instructed to hold their breath during the examination period. Data acquisition started at the time of contrast material injection, and from 1 to 14 one-second images with a slice-thickness of 10mm (120 kV, 300 mAs) were obtained using a cycle time of 3 seconds. The second part of the acquisition process involved that all patients undergo a PET-FDG scan for acquiring two markers of survival — tumour stage and standardised tumour uptake value of FDG — which gives a better prediction of the tumour state.

Using this approach, we managed to record the change in intensity that the contrast agent contributes as it diffuses in the blood vessels, reaching its peak and eventually when it starts to diffuse away. As the blood vessels become more apparent, the chaotic nature of the blood vessels in the lungs can be examined more easily. Hence, the FD, as it changes during the time when the contrast agent concentration is rising and then falling in the tumour, can be compared with different tumour stages. Moreover, the PET-FDG markers of survival would justify the accuracy of the applied texture analysis method.

^a Images were provided by the University of Sussex Clinical Imaging Science Centre.

3.3.2 FD transformation

The acquired CE CT images are transformed to FD images using the differential box-counting (DBC) algorithm [87-91] at various different scales, then displayed for tumour ROI identification, followed by texture analysis. The DBC approach is commonly used when dealing with thousands of data values per sample (the images here are all 512×512 pixels in size) [92]. In this study, both the DBC and fractional Brownian motion (fBm) algorithms (described in chapter 5 in 5.2.4.1 model-based features methods) were in fact initially applied to the images, the DBC algorithm was adopted for subsequent analysis as it performed faster in the FD calculations of the 512×512 CE CT images.

The original DICOM image $I(x, y)$ of size $M \times N$ is transformed to a FD image by applying a varying size non-linear kernel $w(x, y)$ of size $m \times n$ as in (3.8) that operates by block processing on the neighboring pixels and finds the difference between the highest (p_{max}) and lowest (p_{min}) intensity pixels at positions x and y (see Fig. 3.4). The two variables a and b are nonnegative integers which are computed in order to centre the kernel $w(s, t)$ on pixel p_{xy} in the original image, where the m and n are nonnegative integers which depend on the scaling factor r . The kernel is calculated as in (3.8) and applied as in (3.9).

$$w(x, y) = \text{floor} \left[\frac{p_{max} - p_{min}}{r} \right] + 1 \quad (3.8)$$

where $r = 2, 3, 4, \dots, j$

$$a = \text{ceil} \left(\frac{m-1}{2} \right) \quad \text{and} \quad b = \text{ceil} \left(\frac{n-1}{2} \right)$$

$$N_d(x, y, d) = \sum_{s=-at=-b}^a \sum_{t=-b}^b w(s, t) I(x+s, y+t) (j/r)^2 \quad (3.9)$$

Herein, $d = 1, 2, 3 \dots j-1$ is the dimension of matrix $N_d(x, y, d)$ which represents the necessary number of boxes to overlay the image. Empirically, the scaling factor r was chosen to be in the range between 2 and 9. Theoretically, r should represent how much a specific structure of pixels are self similar to its surrounding. For the $512 \text{ mm} \times 512 \text{ mm}$ CE CT images having a resolution of 12 bits/pixel, Fig. 3.5 shows that the best scaling is achieved in this range (i.e. correlation between N_d and r is greater than 0.94). The FD image starts to become blurry due to non-linearity and resolution constraints and if we extend the range much further this would certainly change the accuracy of the calculated FD value. Similarly choosing a smaller range would result in an insufficient number of surrounding pixels to correctly estimate the FD value. Finally, the slope of the linear regression line of $N_d(x, y, d)$ and r would represent the FD of that pixel. To further investigate the fractal homogeneity of the lung tumour texture, FD lacunarity was also computed.

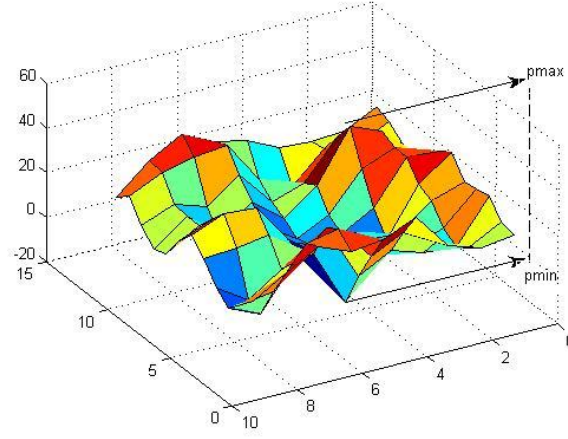


Fig. 3.4 Surface of the selected ROI shown in Fig 3.7 displaying the max and min peaks.

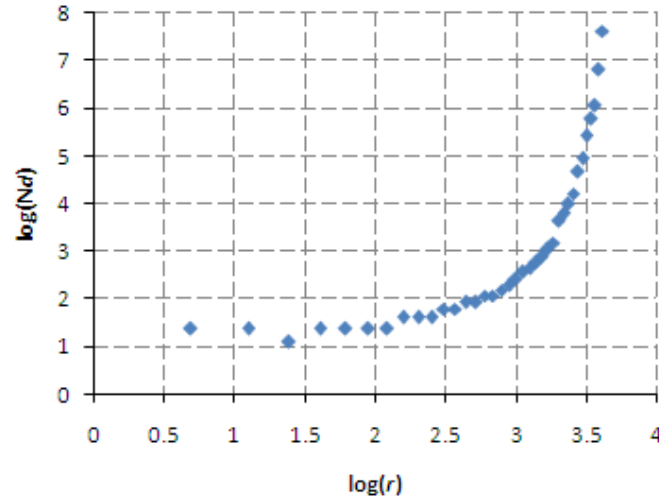


Fig. 3.5 Scaling factor (r) vs required number of boxes to overlay each image pixel (N_d) in log-log scale.

3.3.3 Region of Interest & Feature extraction

Having the FD transformed images and under the supervision of a clinical expert, it was comparatively easy to select a ROI that lies within the tumour area for all images in the sequence for each patient. The ROIs were selected manually as using an automated segmentation procedure could not guarantee the texture of the tumour area not to include accidentally some surrounding tissue. Fig. 3.6(a), (b) and (c) shows the baseline CT image (slice 1) once the contrast agent starts to diffuse, before and after FD transformation. In the upper right side of the left lung in Fig. 3.7(a) it can be seen that the blood vessel became very bright as compared to Fig. 3.6(a). This corresponds to the point at which the effect of the contrast agent appears to be at its maximum, which varies from one case to another. In this case it reached its maximum in the fifth slice. The vascularisation of the tumour – indicated by the lower white arrow – can be easily distinguished from the surrounding structure as shown in Fig. 3.7(c). Fig. 3.6(b) and 3.7(b)

are the windowed versions (i.e. post-processing by nondestructively changing the CT image contrast and brightness) of the original DICOM images with the window width (WW) – which determines the contrast of the image – and window grey level (WL) – the image pixel value at the centre of the window – set in Hounsfield units for tumours, which are 300 HU and 20 HU, respectively. Then the ROIs are extracted for each set (see Fig. 3.8) by first displaying the first image in the set of images and bounding the examined area by a polygon. We have to ensure that no surrounding tissue is included in this polygon in any of the sequence of images, since respiratory motion may affect the image registration. Subsequently, identical ROIs are extracted from all successive slices. Again all ROIs are visually checked for no inclusion of nearby boundaries due to patient's possible respiratory motion (see Fig. 3.9). Finally, the average FD is computed for each ROI for each time sequence image for a specific patient and then selecting the maximum FD_{avg} which will be correlated with the already-known tumour stage and FDG value and the baseline FD_{avg} value representing the first image in the sequence. It should be noted that all procedures in this study have received ethical approval.

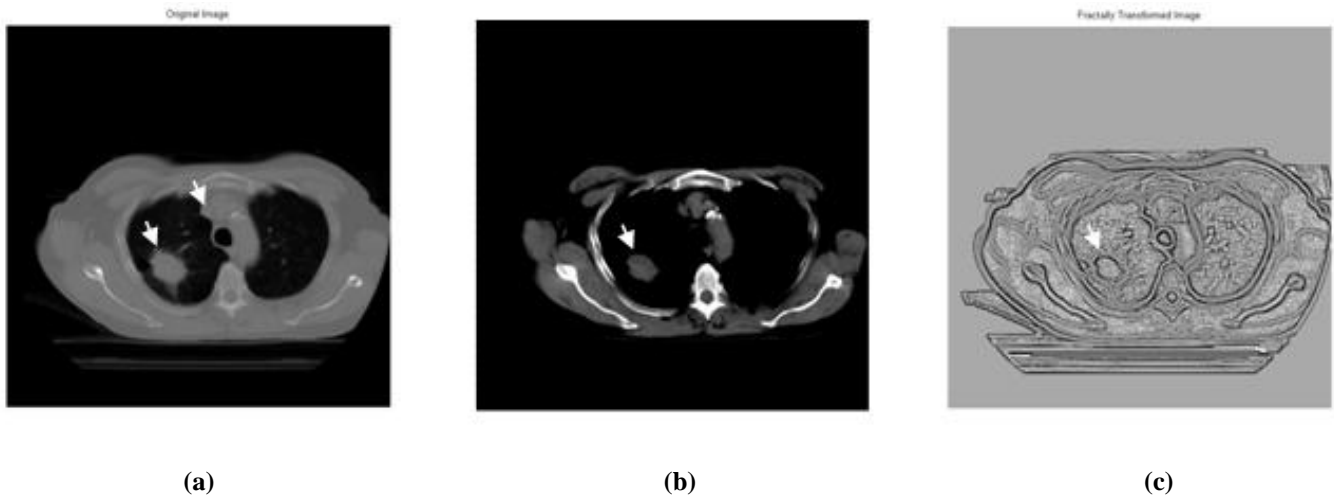


Fig. 3.6 (a) Original baseline image (slice 1) lower and upper arrows indicating tumour and blood vessel location, respectively, (b) windowed DICOM image (slice 1), and (c) fractally transformed baseline image (slice 1).

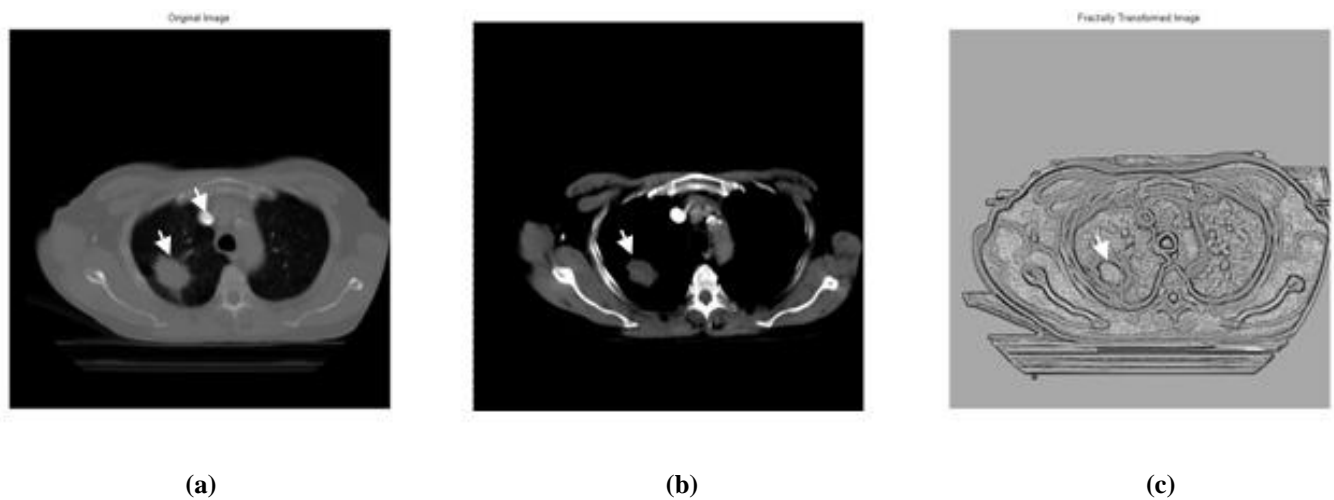


Fig. 3.7 (a) Original maximum contrast image (slice 5), (b) windowed DICOM image (slice 5), and (c) fractally transformed maximum contrast image (slice 5).

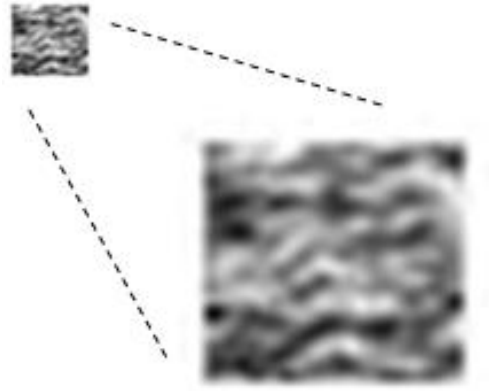


Fig. 3.8 Selected FD tumour ROI enlarged to show texture.

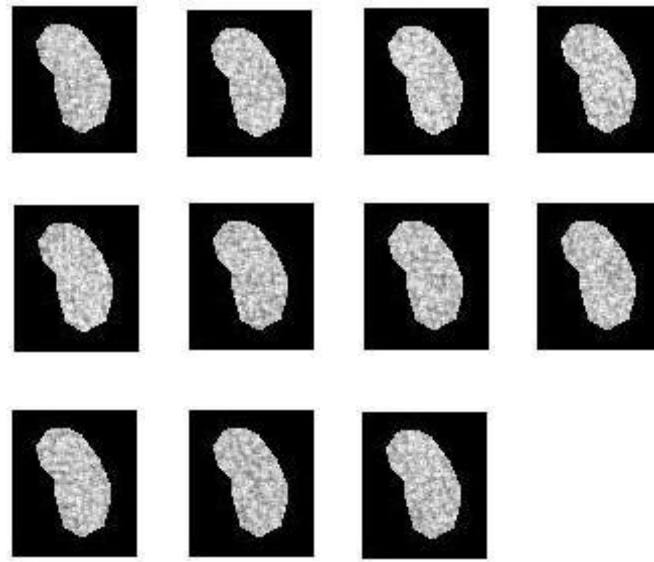


Fig. 3.9 From left to right – 11 ROIs extracted from 11 successive CT images with slice No. 3 giving the highest FD_{avg} .

3.3.4 Impact of CT tube voltage and current on FD_{avg} and Lacunarity

We need to further investigate what impact the X-ray voltage and tube current parameter might have on the calculated FD texture measures from CE CT images. Using a phantom structure, 4 different data sets with 10 slices in each and having a fixed 5mm thickness were acquired by varying the voltage and tube current for each slice. All 40 slices were processed to get the FD_{avg} and lacunarity features, as shown in Table 3.3 for one of the sets. Then each corresponding slice from each set is placed in a separate group, each group represents a specific slice number giving us a total of 10 groups with four slices in each. The standard deviation for each group was computed to see which group (i.e., slice number acquired according to a specific voltage and current value) would represent the least error in calculation of FD texture measures.

3.4 Experimental results and evaluation

3.4.1 Fractal Analysis

Most cases which were diagnosed as aggressive tumours (stage 3 & 4) gave a higher FD_{avg} value as compared to the non-aggressive cases (stage 1). For example, results gave a FD_{avg} value of 2.046 for lung tumour ROI classified as aggressive (i.e. high metabolic) in Fig. 3.10(a), while Fig. 3.10(b), classified as non-aggressive (i.e. low metabolic), gave a much lower FD_{avg} value of 1.534.

As the median is not strongly affected by skewed data as much as the mean, where FD values as low as 1.5344 can be encountered, the median would be a better option to act as a threshold for the quantitative analysis. Hence, the value of 1.913 which is the median of all maximum FD_{avg} values referring to all 15 cases we analysed would act as a threshold differentiating between aggressive and non-aggressive tumours, Table 3.4 shows most aggressive tumours (stages 3 & 4) which are all highly metabolic lie above this threshold, with 83.30% of stage four cases above the threshold. This threshold could be used in CT scan software systems which would assist the physician in distinguishing between aggressive and non-aggressive cases.

Table 3.3 Slices for phantom group 3 showing corresponding CT acquisition parameters (X-ray tube voltage (V) & current (C)) for fractal features (FD_{avg} & lacunarity)

Phantom set 3				
Slice	FD_{avg}	Lacunarity	V (kV)	C (mAs)
1	2.1898	0.0214	80	100
2	2.1947	0.0199	80	150
3	2.2090	0.0178	80	200
4	2.2052	0.0176	80	250
5	2.2183	0.0161	100	150
6	2.2182	0.0161	120	100
7	2.2209	0.0139	120	150
8	2.2026	0.0134	120	200
9	2.1883	0.0130	120	250
10	2.2032	0.0135	140	150

Table 3.4 Number of cases greater than threshold 1.913

Tumour stage	$FD_{avg} > 1.913$
1	0.00%
2	25.00%
3	66.67%
4	83.30%

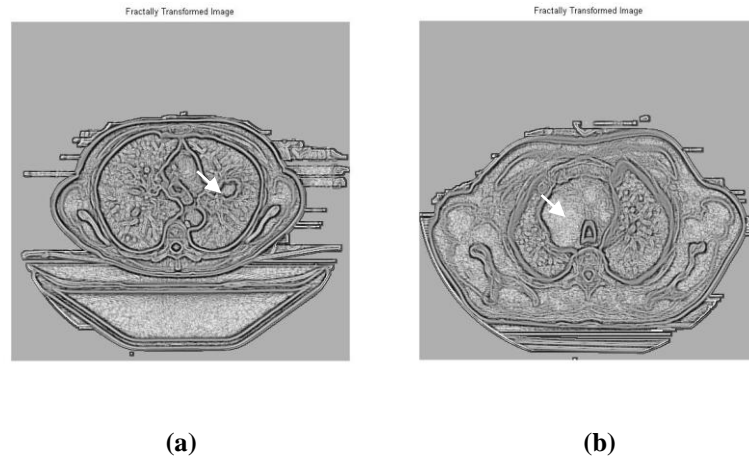


Fig. 3.10 (a) Fractally transformed image of early stage non-aggressive lung tumour, (b) fractally transformed image of advanced stage aggressive lung tumour.

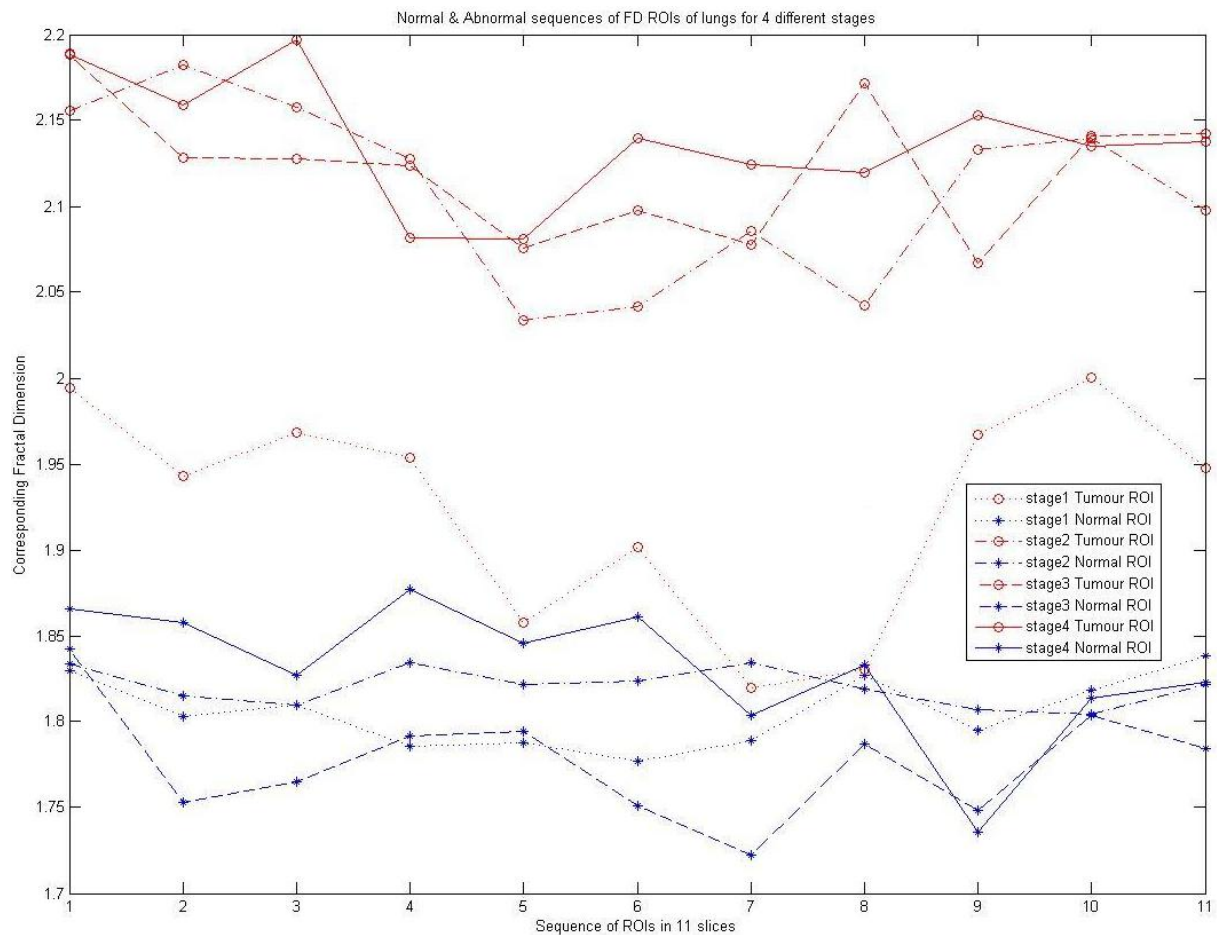


Fig. 3.11 Different sequence of FD ROIs, representing four different stage tumours and four normal, upper four sequences are the lung tumour FD ROIs which represents four different stages while the lower 4 sequences are corresponding normal FD ROIs.

Also as shown in Table 3.5 for every tumour stage, the higher the FD, the lower the corresponding lacunarity value. This gives some indication that aggressive tumours tend to be more homogeneous. Moreover, the average lacunarity over the whole set of image sequence referring to each case correlates strongly with FDG ($\rho = -0.6273$, $p = 0.0123$). Moreover, Fig. 3.11 shows an 11 sequence of eight different FD ROIs with the starting slice 1 acting as the baseline image and slice 11 is when the contrast agent has completely diffused. These FD ROIs are classified as four normal and four vascularised (i.e. tumour) which refer to the four different stages of lung tumours. For each tumour FD ROI a corresponding normal region is selected from the normal part of the lung, by this, we have two ROIs from each case.

It can be seen that non-aggressive tumours (e.g. stage 1) such as the fifth dotted line from down in Fig. 3.11 tend to have a different range than other tumours — upper three lines in Fig. 3.11 — where their FD_{avg} values are all above 2, with stage 4 — first solid line from up — achieving the highest FD value. Also, normal ROIs were included in the graph for clarification purposes to make sure that their FD_{avg} ranges values are completely different to those of the tumour, especially if the baseline or maximum FD_{avg} was used for classification.

3.4.2 Statistical tests

Using the Spearman rank order correlation test, the tumour baseline FD_{avg} and the maximum FD_{avg} were correlated with the corresponding lung tumour stages, giving correlation coefficients of 0.537 and 0.52 with a significance level of 0.0387 and 0.0468 for 2-tailed p -value; respectively. Also, using linear regression the tumour maximum FD_{avg} and baseline FD_{avg} correlated with tumour uptake of FDG as determined by PET, giving $\rho = 0.63$, $p = 0.012$ and $\rho = 0.634$, $p = 0.011$, respectively (see Fig. 3.12).

A summary of the complete results for all sets of sequences of images corresponding to 15 patients is given in Table 3.5. The table shows for each patient the number of slices acquired, tumour stage, area of tumour, computed FDG value, the maximum FD_{avg} and its corresponding lacunarity, as well as the baseline FD_{avg} and the behavioral direction ΔFD . ΔFD simply represents the difference between the minimum and the maximum FD_{avg} rate of change with respect to time. It shows that only two cases from all 15 had a positive trend and these cases were classified as early stage. This needs to be further investigated through applying this procedure to more cases to see whether ΔFD for early stage tumours in time series CE CT images tend to change in a different way. The rates of change with respect to time for the FD and its corresponding lacunarity and for all 15 cases are shown in the appendix.

3.4.3 Phantom tests

Group 2 for FD_{avg} and group 6 for lacunarity gave the least standard error of the mean as shown in Fig. 3.13. From Table 3.3, the corresponding voltage and current parameters for FD_{avg} and lacunarity are 80 kV and 150 mAs and 120 kV and 100 mAs; respectively.

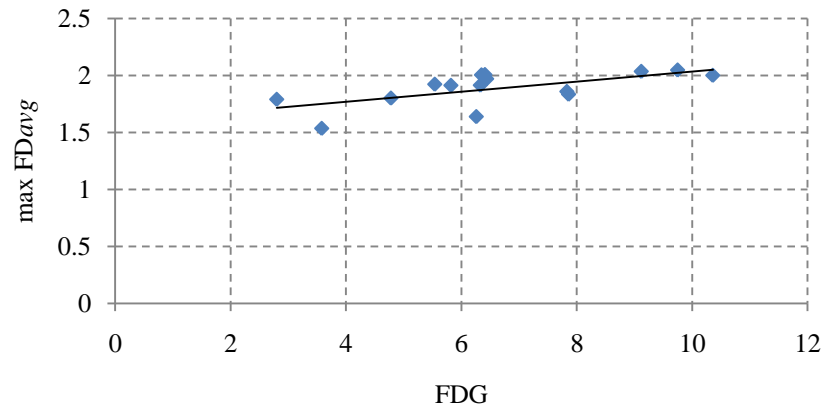
3.5 Discussion

This chapter aims to specify a lung tumour aggression index to assist in better classifying and staging lung tumours from CT images without the need for a PET scan. Results show that selecting tumour ROIs from slices that have the maximum and baseline FD_{avg} can improve stage prediction.

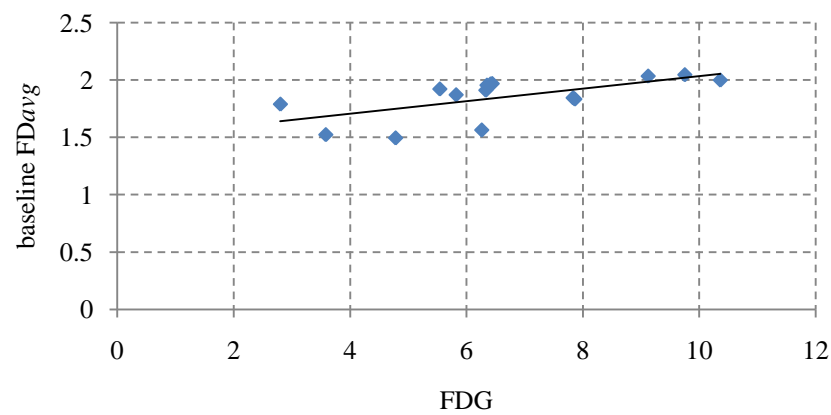
The presumed reason behind the observation that non-aggressive cancers have a lower maximum FD_{avg} value as compared to the aggressive cancers is that given that blood vessels in the lungs appear as fractals, the action of administering a contrast agent will enhance the intensity of the blood vessels in the image, as we are viewing the image from a FD perspective. We would expect that the FD_{avg} would increase with time reaching a maximum at some point near the middle image of the sequence, after the tumour has been infused by the contrast agent and before it has started diffusing away. Although this is true for ROIs from non-aggressive cancers, as the blood vessels in that region still maintain some of its fractal characteristics, in the aggressive tumours, the general shape of the blood vessels has been altered and deformed in such a way, becoming very rough, resulting in some increase in the original blood vessels' fractal characteristics. This increase in roughness contributed to the observed maximum FD_{avg} value in these cases as compared to the non-aggressive cases.

Regarding the selection of the DBC algorithm, Penn & Loew [93] studied the effectiveness of the DBC algorithm and the power spectrum which is based on a fBm algorithm, in performing texture analysis to separate classes of blood cell images. They suggest that these approaches may be inaccurate if applied to data-limited, low resolution images. We overcame this problem by using high resolution CE CT scans for image acquisition. The images that we applied the DBC algorithm to had a resolution of 12 bits per pixel – a total of 4096 shades of gray – with no obvious distorting noise, thus reducing possibility of miscalculations in the FD computations due to poor resolution.

The DBC algorithm transformed the image to the FD approximately 2.5 times faster than the fBm approach, making it more practical for clinical use in order to reduce diagnostic time required by physicians for analysing multiple sequences of CT images; therefore it was adopted for subsequent analysis. In order to reduce processing time still further, we could have transformed just the ROIs to the FD values, and perform the subsequent fractal analysis on this data. However, as the FD transformation is a very effective edge enhancer technique [94], we decided to enhance the acquired image first in order to help identify the tumour region precisely, ruling out any possible inclusion of any adjacent tissue boundaries into the FD tumour calculations. This is especially important as we are working with multiple CE CT images acquired over time where the tumour area can change in size and position due to the patient's respiratory movements. Hence, we needed to balance the trade-off between choosing the smallest possible area size for the whole sequence of CE CT images not including any nearby normal tissue, and making sure that the ROI is sufficiently large to obtain an accurate fractal dimension estimate of the examined tumour region.



(a)



(b)

Fig. 3.12 Significant correlation between standard tumour uptake of fluorodeoxyglucose with (a) maximum FD_{avg} and (b) baseline FD_{avg} .

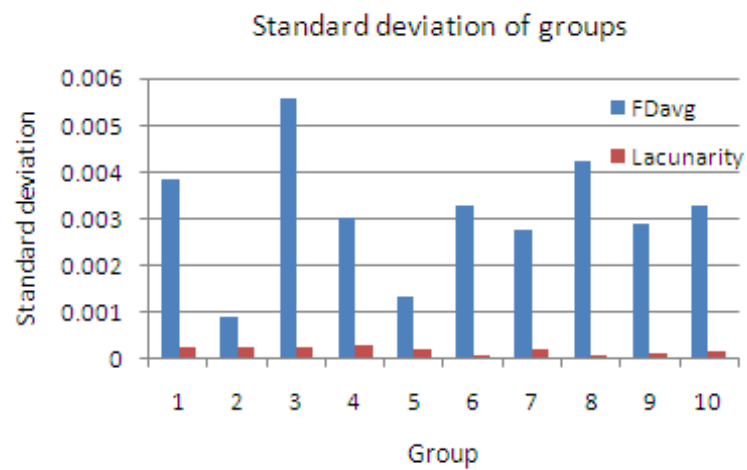


Fig. 3.13: Standard deviation of fractal features for groups of similar phantom slices acquired under specific voltage (kV) and tube current (mAs) CT parameters.

Table 3.5 FD texture analysis data for all 15 cases

Patient	Tumour stage	No. of slices	Area (cm ²)	FDG	maxFD _{avg}	Lacunarity	Baseline FD _{avg}	ΔFD
Case 1	2 ^b	11	1.439	4.78	1.7997 (5) ^c	0.0457	1.4937	0.306
Case 2	4	11	1.072	5.54	1.9214 (1)	0.0275	1.9214	-0.367
Case 3	4	12	7.533	7.86	1.8330 (1)	0.0450	1.8330	-0.162
Case 4	3	13	32.982	9.12	2.0341 (1)	0.0201	2.0341	-0.069
Case 5	4	11	42.123	6.41	2.0061 (2)	0.0268	1.9649	-0.055
Case 6	1	14	3.555	3.58	1.5344 (6)	0.1333	1.5223	0.012
Case 7	2	11	11.850	6.33	1.9131 (2)	0.0430	1.9106	-0.181
Case 8	4	11	19.298	10.36	1.9992 (1)	0.0235	1.9992	-0.216
Case 9	1	11	3.300	2.8	1.7890 (1)	0.0415	1.7890	-0.254
Case 10	3	13	12.160	6.44	1.9687 (1)	0.0348	1.9687	-0.178
Case 11	4	11	28.044	9.75	2.0461 (1)	0.0171	2.0461	-0.152
Case 12	4	13	5.050	5.82	1.9114 (3)	0.0553	1.8708	-0.311
Case 13	3	11	3.611	6.26	1.6374 (2)	0.1411	1.5630	-0.122
Case 14	2	13	26.154	6.35	2.0034 (2)	0.0256	1.9550	-0.087
Case 15	2	11	6.546	7.83	1.8575 (2)	0.0273	1.8444	-0.222

Additionally, Lee et al [80] used a kernel that calculates the standard deviation multiplied by two inside the operating box instead of the difference between the maximum and minimum intensities divided by the scaling factor in order to reduce the effect of noise in the acquired images. Although the FD tends to not enhance noise since it is a roughness representation of the surface [94], the CE CT images that we processed had a high spatial resolution, comparatively free from visible noise. So using the standard deviation method on high quality images could result in loss of some relevant information from the processed image; it was therefore more appropriate to use the differential method for our case.

Others used the same modality for texture analysis. Kido et al [70, 71] and Uppaluri et al [95] showed that FD for lung CT images could be useful in differentiating between normal and abnormal lung tissues for non-tumour cases. In contrast, our focus was specific to only abnormality trying to differentiate between lung tumours upon their aggression. Also, we used time sequence CE CT images to more reliably estimate the FD while the previously mentioned two studies operated on ordinary CT images. This assisted us in identify to what extent we can extend the range of the scaling factor confidently in the DBC algorithm so the computed FD for each pixel would have more fidelity. Furthermore, to assess the accuracy of the computed texture measures, we correlated the FD_{avg} values for ROIs with the medical key factors, FDG and staging, which were measured using PET. Hence we can better estimate the stage and aggression state of the examined tumour from CT images.

Lacunarity of the FD transformed ROI was measured to further differentiate between ROIs which showed similar FD values. Moreover, it was shown that calibrating the CT voltage and tube current parameters with the values presented in the experimental results section would assist in calculating the FD texture measure more accurately, yet it needs to be verified on real CE CT lung images to check consistency.

^b 1 for early stage while 4 for advanced stage

^c indicates the occurrence in slice number (*n*)

Nevertheless, analysis of tumours of less than 10 mm^2 in size in this study would have been possible, but due to inherent noise resolution of CT would make such analysis unreliable. The results would have been improved if CT slice thickness was thinner and the data acquired with a higher resolution (e.g. 16 bits/pixel). This could have made possible the investigation of tumours having a size smaller than 10 mm^2 . However, the likelihood of increased noise when acquired images are higher resolution reduces the accuracy of the texture estimates.

3.6 Conclusion

A fractal analysis of aggressive and non-aggressive lung tumours based on correlation with other related key medical factors was proposed in this study. Previous work done was mainly concerned with distinguishing normal and abnormal tissue, while this technique assesses the potential for tumour FD measurements through CE CT images to provide an indication of tumour aggression. After specifying a threshold, most late stage cases resulted in a higher FD_{avg} as compared to the early cases. Moreover, there was a significant correlation between tumour stage severity and FDG acquired by PET scan with the baseline and maximum value of FD_{avg} occurring in one of the time sequence CE CT images. This implies that the FD_{avg} value computed from the tumour ROI could serve as a prognostic marker assisting in deciding whether the tumour should be further investigated by a PET scan.

Usually aggressive cancers are dealt with by non-surgical procedures such as chemotherapy, since surgical intervention can provoke the tumour to spread and grow faster. These preliminary results could assist physicians in non-invasively investigating the behaviour of the examined lung tumour from time sequence CE CT images with no need of biopsy to be taken. It was also shown that through selecting the appropriate CT acquisition parameters can play a significant role in improving the computation accuracy of the FD. Future work would be studying the effect of CT image reconstruction algorithms on FD_{avg} and the possible application of this technique to other imaging modalities (MRI and US) and for other types of tumours.

Chapter 4

NOISE IMPACT ON LUNG TUMOUR TEXTURE MEASURES

Preview

Seven different texture measurement methods (two wavelet, two model and three statistical-based) were applied to investigate their susceptibility to subtle noise caused by acquisition and reconstruction deficiencies in medical images. Features of lung tumours were extracted from two different conventional and contrast enhanced computed tomography (CT) image data sets under filtered and noisy conditions. Noise of Gaussian and Rayleigh distributions with varying mean and variance was encountered in the analysed CT images. The Fisher distance was used to differentiate between an original extracted lung tumour region of interest (ROI) with the filtered and noisy reconstructed versions. Through examining the texture characteristics of the lung tumour areas by the seven different texture measures, it was determined that the wavelet packet (WP) and fractal dimension measures were the least affected by noise, while the Gaussian Markov random field, run-length and co-occurrence matrices were the most affected. Depending on the selected ROI size, it was concluded that texture measures with fewer extracted features can decrease susceptibility to noise, with the WP and the Gabor filter having a stable performance in both clean and noisy CT versions and for both data sets. The knowledge of the robustness of each texture measure under noise presence can assist physicians using an automated lung texture classification system in choosing an appropriate feature extraction algorithm for a more accurate diagnosis.

4.1 Introduction

Texture in medical images can offer an important source of information on the state of the health of an examined organ. Diseased tissue usually has a more rough or chaotic structure than the healthy counterparts, and this can be characterised quantitatively for an automated diagnostic support system. The quality of the extracted texture measures is of significant importance for a correct diagnosis, especially when the difference between two different tissues becomes minor.

Often computed tomography (CT) medical images are degraded by different types and levels of noise, which might arise for example, but is not limited to, fluctuations in X-ray photons, low radiation doses, instability or deficiencies in the detectors' electronics receiver system and/or quantisation errors [96]. These distortions affecting the fine structure of the examined tissue texture may obscure some prominent characteristics that could distinguish one tumour subtype from another, or could decrease the tumour staging accuracy, and hence have a negative impact on the overall patient's prognosis. Therefore, having clear and relatively noise-free images plays a significant role in medical image analysis. A number of

studies applied various techniques in an endeavour to deal with noise issues in CT images, by reducing direct noise and streak artefacts [97-99], or by removing statistical random noise [100-102]. Although all denoising techniques report a reduction in measured noise levels and a better visual appearance, a complete removal of noise cannot be guaranteed and noise removal might be accompanied with a slight deformation or edge blurring of the tissue structure, reducing the differences between the various examined tissues. Usually tumour regions occupy a small portion of the acquired CT image, and the analysis is constrained to this small region of the diseased tissue for deriving discriminative features; whereas additive noise would further complicate the diagnostic process. Hence comes the importance of the applied texture measures to effectively characterise the tumour texture and the robustness of their performance under noisy conditions (i.e. unfiltered images) or even in cleaned (filtered) images with remaining noise residues.

Physicians tend to use computed texture measures from regions of interest (ROIs) for diagnosis purposes and for eventually choosing the appropriate treatment procedure. Many techniques have been applied for the purpose of lung texture analysis: such as using the fractal dimension to exploit the fractal nature of the lung tissue structure [1, 70, 78], overcomplete wavelet filters — also called wavelet frames — to investigate the tissue at multiple resolutions [103, 104], combining Gabor filter response with histogram features [105], and using the co-occurrence matrix [106]. A review of the various methods used in computer analysis of lung CT scans can be found in [107]. However, we need to take into consideration when examining the texture of a small ROI in a medical image, that noise could adversely affect the accuracy of the measured texture parameters and cause errors in the reported diagnosis [108]. Although many studies concerned with noise reduction and CT image enhancement have been undertaken [97-102, 109], there is still a need to evaluate the texture measures' feature extraction performance under actual noisy conditions. The impact of additive white noise on Gabor filters and co-occurrence matrices, and on local power and phase spectra feature extraction ability from ordinary texture images of the Brodatz album was studied in [110, 111]; nevertheless, there is limited research in the literature regarding evaluating texture measures' performance under noisy conditions for medical CT images. This chapter aims to provide a comparison study between seven different well-known texture measures to investigate their susceptibility to noise occurring in CT images, giving an indication of their reliability and fidelity in analysing medical images. Main emphasis was given to subtle statistical random noise rather than artefact noise which might appear as obvious streaks in the image. Moreover, our intention was to assess the performance of the texture features and not the classifier, as it is well-known that the choice of classifier influences the classification accuracy for given features. Some features may perform better than others only because their distribution is a better fit for the assumptions underlying the classifier model.

4.2 Material and methods

The type of noise needs first to be identified, then two images are generated from each original CT image, one with a reduced noise and another with an enhanced noise. These versions are CT reconstructed and two new ROIs — one from each of the two reconstructed versions — are extracted from the tumour area (see arrow 1 in Fig. 4.1(a) and (b)) and compared with the original ROI according to seven different texture measures. The reason for image reconstruction was to simulate the process of acquiring the CT images under noisy conditions, where noise would influence the CT acquisition parameters in the process of the CT image generation differently than simply adding it afterwards. The process is summarised in Fig. 4.2, and the used procedure is described in detail as follows:

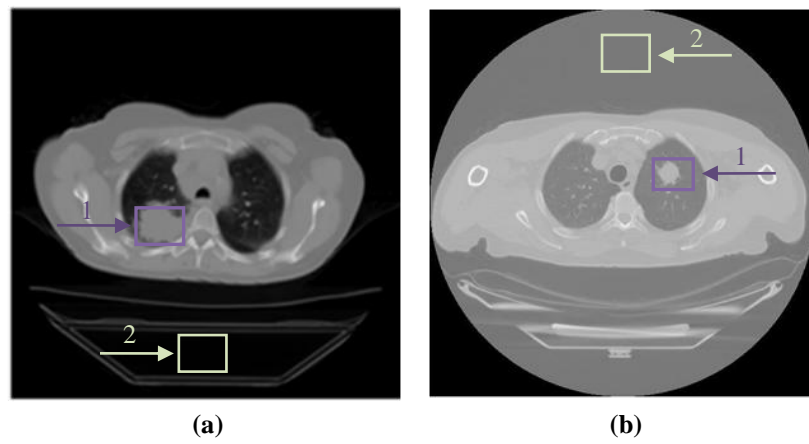


Fig. 4.1 Two images selected from a CE CT (case 1) and a NCE CT (case 5) data sets are shown in (a) and (b), respectively. Arrow 1 shows the selected lung tumour area, and arrow 2 the selected open air region below the patient for (a) and above the patient for (b) which is used for noise estimation.

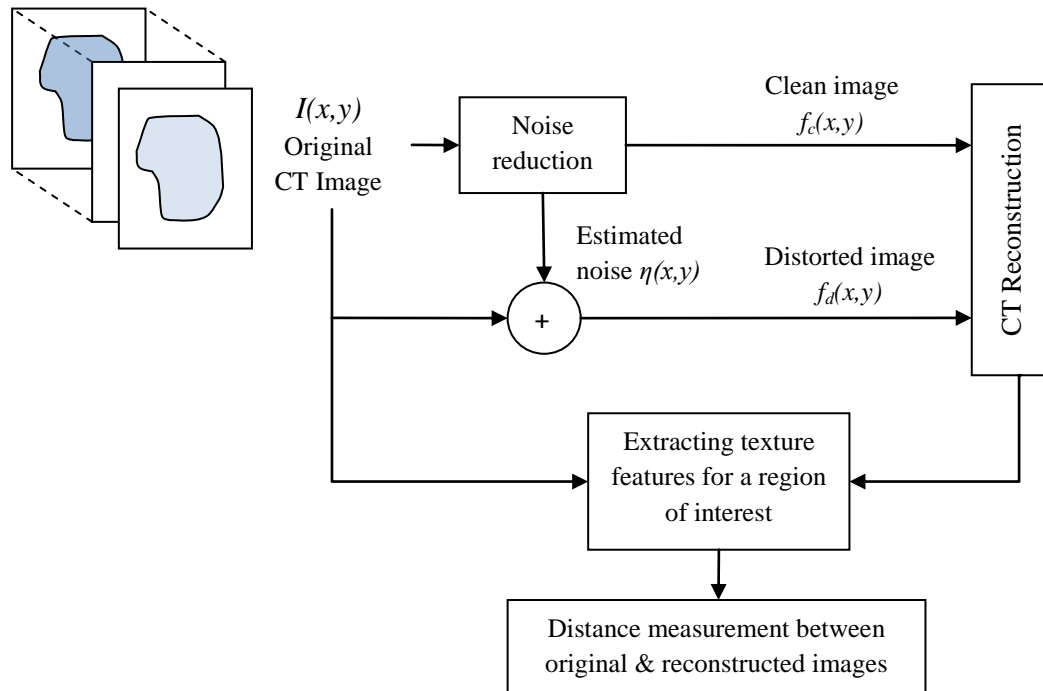


Fig. 4.2 Methodology used to assess texture measures' susceptibility to noise for lung tumour CT images.

4.2.1 Image acquisition

Two different data sets of lungs affected with tumours of varying stages – provided by clinical imaging science centre at the University of Sussex – were available for analysis. The first data set which was used earlier in our preliminary research [2] and also in chapter 3, was a set of contrast enhanced (CE) CT angiography DICOM (Digital Imaging and Communication in Medicine) images referring to 11 patients with lung cancers greater than 10 mm² and having a resolution of 12 bits per pixel (bpp). The CE images were acquired — after injecting a dose of a contrast agent into one of the large veins of each patient — with an X-ray tube voltage and current of 140 kV and 200 mAs, a 10 mm slice thickness with matrix size 512 x 512 and B reconstruction filter.

The second data set consists of conventional or non-contrast enhanced (NCE) CT images of 56 different cases of patients also diagnosed with lung cancer. The acquisition parameters of the NCE images were similar to the CE data set with the only difference in the resolution and slice thickness, where the NEC CT had an improved resolution of 16 bpp and a thinner slice thickness of 2mm. It should be stated that all acquisitions were ethically approved, and our work did not influence the diagnostic process or the patient's treatment.

4.2.2 Noise evaluation

The original image is first inspected for presence of noise, and the type of noise is appropriately identified for removal without destroying the fine structure of the image texture. Two new images are produced from this phase, a clean (i.e. filtered original image) and distorted (i.e. the detected noise in the original image is doubled) versions.

4.2.2.1 Noise estimation

A reasonably constant grey level area in the CT image was selected and checked for uniformity. The transverse section of the scanning table in the CT images of the CE data set and the region above the scanning gantry for the NCE data set was chosen for analysis (see arrow 2 in Fig. 4.1(a) and (b)), and the histogram was plotted for each. Then the mean (μ) and variance (σ^2) which were estimated from the plotted histogram were used to determine the parameters of three other types of noise probability density functions (PDFs) for their histograms to be plotted as well (see Table 4.1). The selected noise types for this study were Gaussian, Rayleigh and Erlang [86], which are the most commonly encountered in CT images. Then the estimated histogram from the CT image will be matched against the generated noise PDFs to see to which one it best corresponds. This process was carried out for all 67 images (11 for the CE and 56 for the NCE data sets).

Table 4.1 PDFs for three different types of noise and their corresponding mean and variance

Noise	Gaussian	Rayleigh	Erlang
PDF	$P_z(z) = \frac{1}{\sqrt{2\pi}b} \exp\left(-\frac{(z-a)^2}{2b^2}\right)$ <p>where $-\infty < z < \infty$</p>	$P_z(z) = \begin{cases} \frac{2}{b}(z-a) \exp\left(-\frac{(z-a)^2}{b}\right) & z \geq a \\ 0 & z < a \end{cases}$	$P_z(z) = \frac{a^b z^{b-1}}{(b-1)!} \exp(-az)$ <p>where $z \geq 0$</p>
Mean & Variance	$\mu = a, \quad \sigma^2 = b^2$	$\mu = a, \quad \sigma^2 = b^2$	$\mu = a, \quad \sigma^2 = \frac{b}{a^2}$

The intensity histograms obtained from the CE CT uniform areas had a shape resembling additive Gaussian and multiplicative Rayleigh noise PDFs with μ and σ^2 varying between 13.2 to 17.4 and 24.7 to 65.9; respectively. While the most dominant noise in the NCE CT data set was the Gaussian, with μ and σ varying between 7.2 to 25.1 and 7.5 to 86.8; respectively. Matusita distance — also known as first order Hellinger distance — which is invariant to scale in between two probability density distributions was used to compare between the original noise (P_O) and the three generated noise (P_N) distributions to see to which the measured noise is least deviated as shown in (4.1).

$$M(P_O, P_N) = \sqrt{\sum_i (\sqrt{P_O(i)} - \sqrt{P_N(i)})^2} \quad (4.1)$$

Fig. 4.3 shows a histogram of noise obtained from one of the CT images compared to three different types of generated noise (Gaussian, Rayleigh and Erlang) using the estimated μ and σ^2 . We can see for this case that the shape of the Rayleigh noise appears to resemble the CT noise histogram, and the distance measure supports this conclusion (see case 3 in Table 4.2). Also in Table 4.2, six of the examined cases showed a Rayleigh noise distribution while the rest appeared to have a Gaussian distribution. It has been shown that if the standard deviation of the estimated noise is far less than the mean intensity, the noise will approach a Gaussian distribution, while if it is far greater than the mean intensity it will have a Rayleigh distribution [112]. Additionally, the NCE data set in Table 4.3 shows that the noise in 51 of the 56 cases was Gaussian, while 2 was Rayleigh and 3 of Erlang type. Nevertheless, the reason not having a single noise type in the analysed CT images even though the same CT scanner was used needs to be further investigated.

4.2.2.2 Adaptive filtering

Having identified the type of noise, we need to clean each of the CT images given the corresponding noise variance. As the tumour area is relatively small as compared to the total image size, an adaptive filter is needed which can reduce local noise and preserve the edges and fine structures in the CT image for subsequent accurate analysis. Since the main focus of this chapter is to compare the extracted texture features robustness before and after noise reduction, a simple noise filter was used. An adaptive filter (S_{xy})

of size 5 x 5 which covers nearly 1% of the image in each step is applied for local noise reduction. Its behaviour changes adaptively depending on the statistical characteristics of the region inside the filter as defined in the following formula [86]:

$$f_c(x, y) = I(x, y) - \frac{\sigma_\eta^2}{\sigma_L^2} [I(x, y) - \mu_L] \quad (4.2)$$

Here $I(x, y)$ is the value of the original image suspected to have subtle noise at (x, y) ; σ_η^2 the variance of the noise corrupting $f_c(x, y)$ to form $I(x, y)$; μ_L is the local mean of the pixels in S_{xy} ; and σ_L^2 , the local variance of the pixels in S_{xy} . In case of noise absence (i.e. $\sigma_\eta^2 = 0$) the filter will return the original image. Also it preserves the edges in case the local variance is high. If noise and local variances are equal the filter returns the arithmetic mean value of the pixels in S_{xy} .

In order to study the impact of increased noise on texture analysis measures used in CT images, a distorted image $f_d(x, y)$ is generated by simply adding the estimated noise $\eta(x, y)$ — which is a by-product of the adaptive filtering process — to the original image $I(x, y)$, as in (4.3).

$$f_d(x, y) = I(x, y) + \eta(x, y) \quad (4.3)$$

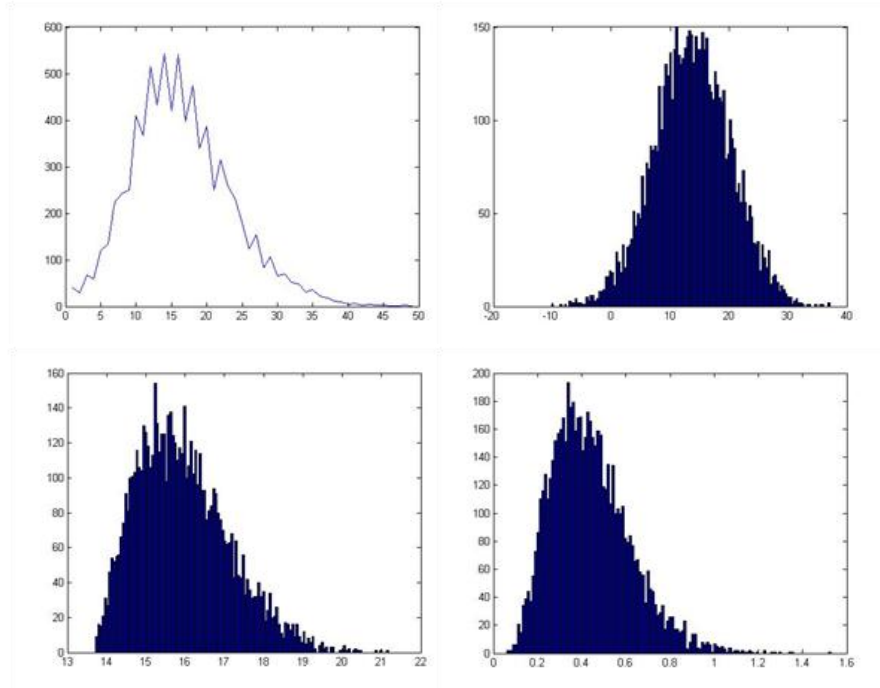


Fig. 4.3 From left to right and from top to bottom, histograms with $\mu_n = 13.6977$, $\sigma_n^2 = 41.1472$ of transverse section of scanning table in CT images followed by corresponding generated Gaussian, Rayleigh and Erlang noises; respectively.

Table 4.2 Matusita distance between original extracted uniform lung tumour ROIs from data set 1 and three types of noise distributions

CT Image ROI	Generated noise		
	Gaussian	Rayleigh	Erlang
Case1	0.3091	0.5578	0.6001
Case2	0.1611	0.5681	0.7889
Case3	0.5181	0.2855	0.6115
Case4	0.1646	0.4927	0.9515
Case5	0.3359	0.5238	0.4315
Case6	0.3616	0.6888	0.5170
Case7	0.6601	0.1967	0.5712
Case8	0.4542	0.3016	0.7447
Case9	0.6217	0.2311	0.6211
Case10	0.4069	0.3255	0.7019
Case11	0.3971	0.3219	0.6046

Table 4.3 Matusita distance between the original extracted uniform lung tumour ROIs from the NCE data set and three types of noise distributions

CT Image ROI	Generated noise			CT Image ROI	Generated noise		
	Gaussian	Rayleigh	Erlang		Gaussian	Rayleigh	Erlang
Case1	0.1310	0.5829	0.3295	Case29	0.1260	0.7726	0.2252
Case2	0.1196	0.6920	0.2587	Case30	0.2261	0.8018	0.1799
Case3	0.1641	0.6144	0.2413	Case31	0.1856	0.7318	0.2465
Case4	0.1054	0.8062	0.1808	Case32	0.1049	0.7425	0.1489
Case5	0.2917	0.6421	0.4261	Case33	0.0744	0.8057	0.0960
Case6	0.4858	0.3308	0.5651	Case34	0.0828	0.8229	0.1802
Case7	0.2667	0.5617	0.5434	Case35	0.1617	0.6089	0.5036
Case8	0.1128	0.8820	0.2720	Case36	0.1876	0.6488	0.4768
Case9	0.1166	0.5163	0.2639	Case37	0.1104	0.7509	0.2891
Case10	0.1278	0.6762	0.3564	Case38	0.1008	0.7061	0.3670
Case11	0.2089	0.6434	0.3290	Case39	0.2363	0.5937	0.3633
Case12	0.2577	0.5556	0.3190	Case40	0.2145	0.6355	0.2766
Case13	0.2285	0.6953	0.3640	Case41	0.0808	0.7709	0.1156
Case14	0.3079	0.5587	0.3944	Case42	0.2288	0.5809	0.4149
Case15	0.0696	0.8070	0.1083	Case43	0.2441	0.7554	0.4109
Case16	0.3398	0.6876	0.1480	Case44	0.1232	0.7209	0.1167
Case17	0.2639	0.4937	0.4038	Case45	0.0884	0.7855	0.1445
Case18	0.2287	0.6462	0.4406	Case46	0.1011	0.8567	0.1542
Case19	0.1987	0.8667	0.2099	Case47	0.1563	0.7811	0.1954
Case20	0.1197	0.6638	0.3013	Case48	0.2287	0.6227	0.2321
Case21	0.0499	0.6971	0.2296	Case49	0.4678	0.2707	0.5274
Case22	0.0913	0.7483	0.2115	Case50	0.1490	0.6771	0.2428
Case23	0.1533	0.6834	0.1810	Case51	0.3142	0.4813	0.4954
Case24	0.1004	0.6499	0.2211	Case52	0.1054	0.6101	0.2631
Case25	0.1057	0.6649	0.2388	Case53	0.1584	0.6709	0.2234
Case26	0.1390	0.9036	0.1781	Case54	0.1703	0.7428	0.2012
Case27	0.0732	0.7123	0.1113	Case55	0.3024	0.5964	0.3350
Case28	0.2416	0.6581	0.3072	Case56	0.1104	0.6800	0.2731

4.2.3 CT image reconstruction

Instead of using the filtered versions, we intended to simulate the process of acquiring the CT images calibrated to the same parameters that were initially used for the original images. As known, the selection

of the CT acquisition slice thickness, tube voltage and tube current parameters would influence the final appearance of the image; hence simulating the acquisition process under noisy and reduced noise conditions would be closer to reality.

An open-source software package called CTSim [113] was used in the simulation process to reconstruct the CT images under noisy and reduced noise conditions. The software simulates the process of collecting X-ray data of phantom objects. The intensity of each pixel in the original DICOM CT image was considered as a rectangular object of unit distance representing the X-ray attenuation coefficient referring to that position. By the end of this stage, three different CT images represent each case, which are the original and two versions acquired under different conditions. The amount of estimated subtle noise represented by the difference between the clean and original NCE CT image of Fig. 4.1(b) is shown in Fig. 4.4(b). Also a horizontal profile along the middle of the 32 x 32 pixels open air ROI indicated by arrow 2 in Fig. 4.1(a) illustrates the difference between the original, clean and noisy CT image versions is shown in Fig. 4.5. Texture analysis is then performed first on the 33 CE CT images in the CE data set and then on the 168 NCE CT data set as described in the next section.

4.2.4 Texture feature extraction

As different lung tumours have different sizes, dependent on the stage of development and aggression, a size that ensures capturing of the texture variation in each ROI is needed. Smaller areas would not have sufficient pixels to reliably compute the texture parameters, while larger areas would exclude relatively small size tumours from the calculations. Therefore, we have empirically chosen an ROI of size 32 x 32 pixels to be extracted from each tumour region of the 201 CT images representing both data sets (33 CE and 168 NCE), as this chosen size would balance the trade-off between tumour size and texture area.

Seven different texture analysis methods were applied to analyse the texture characteristics of the ROIs. These methods are represented by Gaussian Markov random field (GMRF) and fractal dimension (FD) which are model based, and autocovariance function (ACF), runlength matrix (RLM) and grey level co-occurrence matrix (CM) which are statistically based, and discrete wavelet packet transform (WP) and Gabor filters (GF) being wavelet-based.

The applied statistical and model-based texture measures are as described in chapter 5, and the multiresolution chapter explains the wavelet-based measures. The only difference is in how the WP features are extracted, for which, each tumour ROI is decomposed down to two levels of resolution and the strongest energy subband for the leaves of each of the first level nodes (i.e. LL_{11} , LH_{12} , HL_{13} and HH_{14}) are solely included in the ROI feature vector. An example is illustrated in Fig. 4.6, where a tumour ROI of the 56th case in the NCE CT data set is extracted and decomposed into WPs down to the second level, with the corresponding subbands energy values shown in Fig. 4.7.

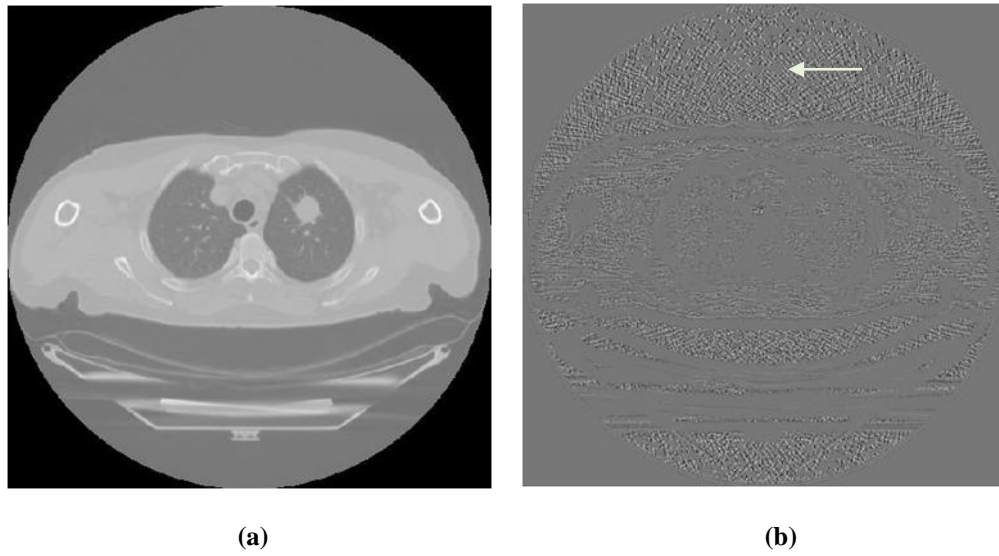


Fig. 4.4 Noise suppression after adaptive filtering (a) is the clean reconstructed CT image, and (b) is the difference image between the clean and original image. The amount of reduced subtle noise becomes obvious in the open-air background above the patient which is indicated by an arrow.

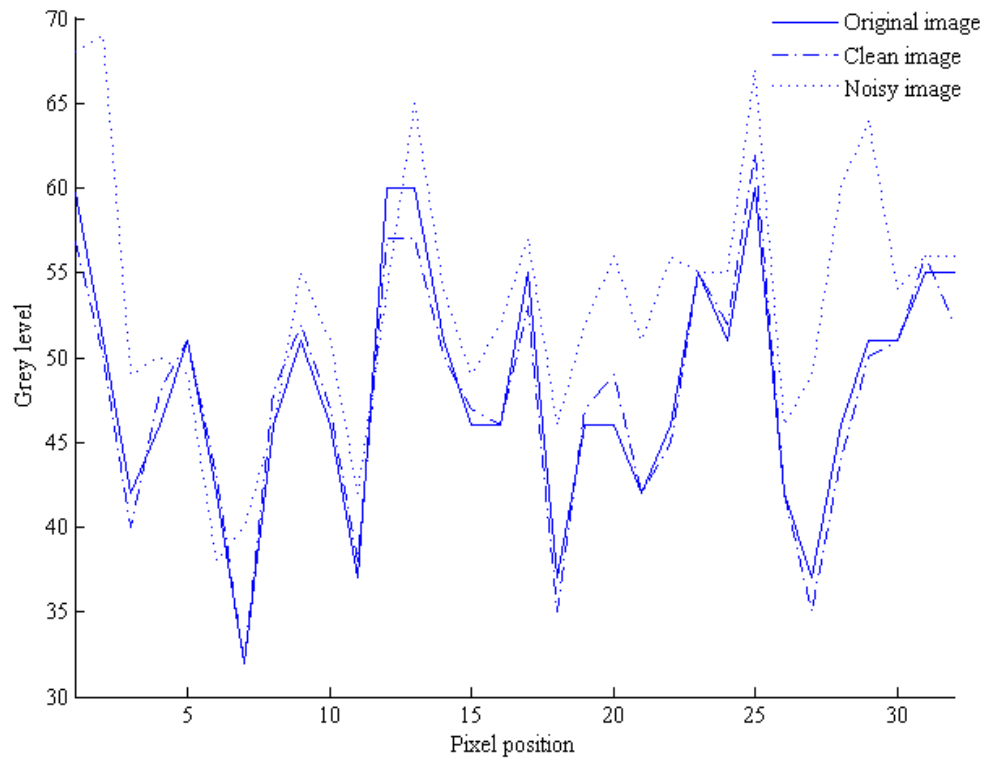


Fig. 4.5 One dimensional horizontal grey-level profile along the middle of an extracted ROI from the background (open air) uniform area in the CT image of Fig. 4.1(a) and its corresponding reconstructed clean and noisy versions.

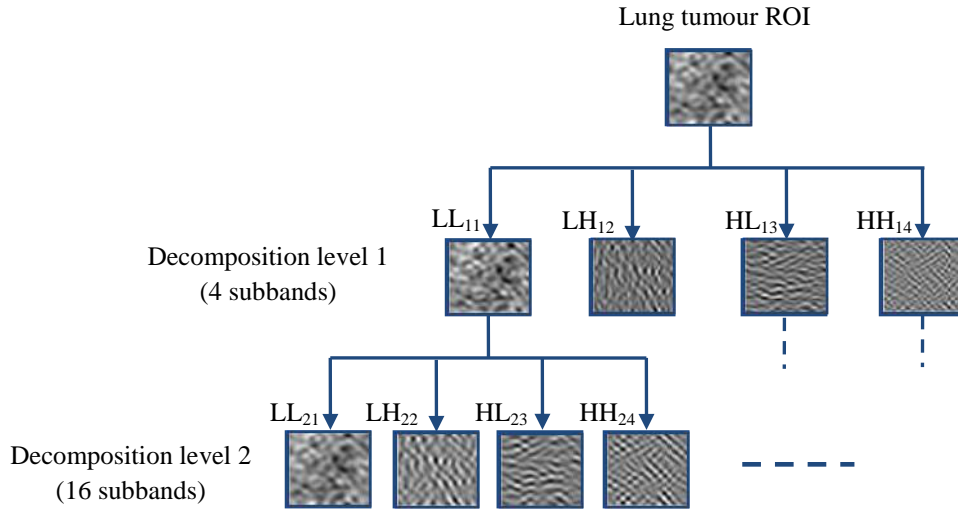


Fig. 4.6 A two level wavelet packet transform decomposition for an extracted lung tumor ROI of case 56 in the NCE CT data set. The subscripts for each subband (e.g. HL_{23}) indicate the level and the subband number; respectively.

	2.84×10^5			
	LL_1	LH_1	HL_1	HH_1
	2.36×10^5	2.70×10^4	1.80×10^4	4.42×10^3
LL_2	2.21×10^5	6.56×10^3	6.86×10^3	3.80×10^2
LH_2	6.56×10^3	1.90×10^4	3.80×10^2	1.04×10^3
HL_2	6.86×10^3	3.80×10^2	1.01×10^4	6.30×10^2
HH_2	3.80×10^2	1.04×10^3	6.30×10^2	2.36×10^3

Fig. 4.7 Subband energy values for the tumour ROI decomposition in Fig. 4.6. The highlighted subbands represent the highest energies in the second level of decomposition.

4.2.5 Measuring separability quality

The final phase in this chapter is the comparison process where the reconstructed images are compared to the original CT images in terms of how much deviation is incurred in the reconstructed images due to noise (removal/addition) after normalising all extracted texture measures. The Fisher's criterion which is a nonparametric statistical distance measure was used for comparison by assessing the quality of separability of two classes. It represents the ratio of the between-class variance relative to the within-class

variance. Considering a c -class problem and for N images, the between-class scatter matrix (S_B) and within-class scatter matrix (S_W) can be defined as

$$S_B = \sum_{i=1}^c N_i (\mu_i - \mu)(\mu_i - \mu)^T \quad (4.4)$$

$$S_W = \sum_{i=1}^c \sum_{x_k \in X_i} (x_k - \mu_i)(x_k - \mu_i)^T = \sum_{i=1}^c S_{W_i} \quad (4.5)$$

where μ is the mean of all images, μ_i is the mean of class X_i , S_{W_i} is the covariance of class X_i , and N_i is the number of images in X_i . In case of a multi-feature vector, the distance can be measured by the formula [114]:

$$J(W_j) = \frac{W_j^T S_B W_j}{W_j^T S_W W_j} \quad (4.6)$$

where $W_j, j = 1, 2, \dots, k$, are the set of discriminant eigenvectors of S_B and S_W , corresponding to the k largest eigenvalues λ_j . Although distance measures are often used in determining accuracy of clusters separability, it is used here to indicate how non-separable (i.e. close) the reconstructed images are to the original. Our aim is to find the best non-separable texture measure between the original and reconstructed images which is least susceptible to noise. For our case smaller values show better performance since the larger the Fisher criterion values the more significant the difference between the two assessed classes.

4.3 Results and discussion

For both CE and NCE CT data sets, the class separability between the original CT image and its reconstructed clean and distorted versions measured by Fisher's distance is listed in Table 4.4 by J_{oc} and J_{on} ; respectively. In order to make the analysis of Table 4.4 easier, the texture features are sorted in ascending order in Table 4.5, placing the least separable at the top and vice versa. From the first glance, it can be seen that the WP was the least affected by noise in both data sets and for the cleaned and distorted versions as well. Regarding the CE CT data set, there was no difference in the order between the used texture methods for characterising the clean and distorted versions CT images. This shows that CE CT images can assist in highlighting the lung texture variations, and hence reducing the effect of distortion on the extracted tissue characteristics.

As the noise found in the both data sets was subtle, the distorted CT image versions contributed in giving some emphasis to this noise. However, we assume that the noise encountered in the CT images is within acceptable ranges and not quite visible to the extent that would deform the structure of the observed ROI — which is in fact the case in most captured CT images. Additionally, the FD, ACF and GF, which came next to the WP, scored nearly a similar score in terms of separability, with the FD being the least affected by noise among them. The RLM, CM and GMRF which derive texture features in four different

directions did not perform as efficiently as the rest of the previously mentioned texture methods, with the GMRF scoring as being the most susceptible to noisy conditions. On the other hand, the NCE CT data set witnessed some change in the order of the tested texture methods, and in-between the clean and distorted CT versions. Although CE CT images would improve the reliability of the used texture methods for analysis, these images are not easy to acquire in comparison to the conventional NCE CT images, where patients need to be injected with a special contrast agent into a large blood vessel prior to image capturing, rendering it unpleasant for patients. The administered contrast agent needs also to be eventually eliminated in the body by the kidneys; therefore, patients might need to undergo blood tests to evaluate their kidney dialysis performance before injection. Moreover, some patients might also have an allergic reaction to the contrast agent used [115], and having an allergy to iodine would contribute towards increasing this risk, making this technique not suitable for all patients. It can also be seen from Table 4.5 that the noisy versions of the NCE CT images preserved the same noise susceptibility order as in its CE counterpart except for the last two methods, where the CM was the most affected in comparison to the GMRF. Furthermore, the FD had nearly no difference between the clean and distorted versions, yet its order has improved in case of distortion — second in the fourth column in Table 4.5 — similar for the GMRF and RLM which showed a one step improvement compared to the clean case, while WP and GF had the same position in both clean and distorted versions.

It should be noted that this work does not intend to compare the performance of these texture measures in terms of discrimination capability or which provides a better characterisation of the lung tissue, but to assess their immunity when used under the presence and absence of the same noise detected in the investigated CT images. However, it is no coincidence for WP and FD texture measures which showed the least susceptibility to noise to offer good performance in lung tissue analysis [1, 103]. Thus, a relation between the immunity of a texture measure to noise and how effectively it can characterise a texture under investigation exists; especially when analysing non-stationary medical texture, which creates another challenge in addition to noise. The improved capability of the WP and FD in analysing lung tissue could be interpreted as their ability to exclude noise with minimum effect on the analysed texture. That is, by decomposing the ROI into several subbands for the WP case, high subbands can be easily eliminated from further decomposition where random noise is usually present in the high subbands. Herein, the subbands with the strongest energy were only selected from the leaves of each decomposed subband for the feature vector. Also the FD can mitigate the effect of noise as it gives a quantitative assessment of the roughness of the surface by examining the texture ROI at different scales; thus the noise would not have a similar effect at all scales. Another point is that the ACF came second for the J_{oc} NCE CT images and third in the rest of Table 4.5; nevertheless, it has a poor performance in image classification [3]. This means that the ACF is less susceptible to noise, yet this is due to its initial poor characterisation of texture resulting in the little difference between the original and the clean and distorted image versions.

Observing the number of features generated from each texture measure, it seems that the number of extracted features plays an important role in susceptibility to noise. CM or RLM which extracts 16 different features was more prone to noise as compared to the WP which had only 4 features. This might be due to the fact that texture measures with large number of features tend to capture more variations of the intensity, and as a result the probability of noise contribution would be amplified. Furthermore, not all extracted features relevant to a specific texture method have the same discriminating power, and thus optimisation might result in a fewer number of features which can still efficiently characterise the selected ROI and be less susceptible to noise distortion. On the other hand, although some studies reported signal dependent Gaussian noise distributions in low-dose CT images [116], and the Gaussian was the dominant type of noise in the NCE CT data set, this work showed that types of noise other than Gaussian can be encountered even when using the same CT scanner, which might be due to insufficient isolation of some of the CT scanner electronics when some of the images were acquired.

This indicates that noise can have some impact on the variability of diagnosis reports depending on the texture measure used for analysis and classification. Some texture measures are more reliable in terms of classification [3, 117], yet their accuracy might start to give misleading results in case of noise presence, causing an increase in inaccuracy as noise becomes more obvious. Therefore, accuracy and noise susceptibility must be taken into consideration by the physician depending on the type of analysis and the area of texture. Given the variation in size, shape and stage between the different extracted lung tumours in this study, the texture measures were applied to a 32 x 32 size ROI which ensures the inclusion of all tumours (i.e. the small size ones as well). So based on the results and whenever it becomes difficult to extract a sufficiently large ROI for analysis, physicians can use texture measures which exhibited the least susceptibility to noise such as WP or FD for small areas (e.g. size $\leq 32 \times 32$) of texture where the probability of noise deforming the structure of the texture is higher, and use the texture measures known for their good capability in texture discrimination. But their performance was more prone to noise, as the CM or GMRF for example, for larger ROIs. Also, the Fisher's distance showed that the five of the seven clean CE CT reconstructions are much nearer to the original from the distorted ones, therefore adaptive filtering can assist in improving some of the texture measures' efficiency.

Possible improvement in order to enhance the reliability of the reported results in this work is that noise susceptibility comparison can be made after applying an optimum feature selection technique for each of texture methods. By that, features with weak discriminating capability are eliminated and the total number of features for each method is reduced to a minimum. Also the difference in the acquired images slice thickness between the CE and the NCE data sets might affect the accuracies of the measured Fisher's distances; yet this needs to be further investigated. A future trend would be assessing the quality of the extracted features under reduced radiation dose (RRD) CT images. For patient's safety and to avoid the relatively high dose of radiation in CT modalities, RRD CT images are acquired in case of children as their tissue is more sensitive to the radiation effect [118], or for adults depending on the kind of organ

under investigation. Lowering the radiation dose can be achieved by decreasing the tube current (mAs) or beam energy (kV) with high pitches or table-speed, and using thicker slices [119]. The effect of RRD CT images, which usually yield noisier and lower contrast images, on extracted texture measures can assist in performance comparison under noisy and lower quality image conditions. Also investigating the texture measures susceptibility in other modalities when other types of noise might be present would be advantageous.

Table 4.4 Fisher's distance between original and reconstructed clean and noisy CT images, with the number of extracted features for each texture measure shown between brackets

Texture measure	Normalised Fisher's distance			
	CE		NCE	
	J_{oc}	J_{on}	J_{oc}	J_{on}
RLM (16)	1.16×10^{-27}	2.17×10^{-27}	2.07×10^{-26}	9.60×10^{-27}
CM (16)	1.90×10^{-26}	2.84×10^{-26}	6.91×10^{-27}	1.29×10^{-26}
ACF (8)	3.92×10^{-28}	1.68×10^{-28}	7.00×10^{-30}	3.16×10^{-29}
FD (5)	1.00×10^{-28}	1.29×10^{-28}	2.93×10^{-29}	2.90×10^{-29}
GMRF (13)	1.12×10^{-24}	1.07×10^{-24}	6.24×10^{-26}	1.16×10^{-26}
GF (12)	9.61×10^{-28}	1.48×10^{-27}	1.85×10^{-28}	3.18×10^{-28}
WP (4)	3.66×10^{-31}	8.61×10^{-31}	1.25×10^{-31}	8.70×10^{-32}

Table 4.5 Sorted (from lowest to highest) texture measures in Table 4.4 according to class separability

CE		NCE	
J_{oc}	J_{on}	J_{oc}	J_{on}
WP	WP	WP	WP
FD	FD	ACF	FD
ACF	ACF	FD	ACF
GF	GF	GF	GF
RLM	RLM	CM	RLM
CM	CM	RLM	GMRF
GMRF	GMRF	GMRF	CM

4.4 Conclusion

The robustness or how well a specific texture measure can tolerate noise in a CT image of lung tumour texture was investigated. Susceptibility of seven different texture analysis measures to noise was investigated by using Fisher's distance to compare the original CT images with their corresponding reconstructed clean and noisy versions. Two different data sets were used; Rayleigh and Gaussian noise was encountered in the CE data set, while the Gaussian noise was the dominant in the NCE data set. It was shown that CE CT images yield more stable results in comparison to their conventional or NCE counterparts, while the WT and GF wavelet-based texture methods were stable in both data sets. The WP and FD which could characterise the lung tissue better than the other texture measures were the least affected by noise. Moreover, WP and FD had the least number of extracted features in comparison to RLM and CM which had the highest number of features, and the last two with the GMRF were most sensitive to noise. As well, adaptively filtered images can assist in reducing subtle noise, and hence offer better texture classification accuracy.

Chapter 5

MULTI-FEATURE CLASS ASSIGNMENT FOR HISTOPATHOLOGICAL MENINGIOMA TUMOUR IMAGES

Preview

Providing an improved technique which can assist pathologists in correctly classifying meningioma tumours with significant accuracy is our main objective. The proposed technique, which is based on optimum texture measure combination, inspects the separability of the RGB colour channels and selects the channel which best segments the cell nuclei of the histopathological images. The morphological gradient is applied to extract the region of interest for each subtype and for elimination of possible noise (e.g. cracks) which might occur during biopsy preparation. Meningioma texture features are extracted by four different texture measures (two model-based and two statistical-based) and then corresponding features are fused together in different combinations after excluding highly correlated features, and a Bayesian classifier was used for meningioma subtype discrimination. The combined Gaussian Markov random field and run-length matrix texture measures outperformed all other combinations in terms of quantitatively characterising the meningioma tissue, achieved an overall classification accuracy of 92.50%, improving from 83.75% which is the best accuracy achieved if the texture measures are used individually.

5.1 Introduction

Meningiomas are one of the most recurring tumours which affect the central nervous system [120-122]. These types of tumours, which have a variable growth potential, develop from the meninges — hence the naming — which are the membranes that cover the brain and spinal cord, and usually do not metastasise (i.e. spread) beyond the location where it originates [38]. It is one of the only brain tumours more common in women than in men, and in general, in 94% of the cases the tumour is benign, and the remaining 2% and 4% it is considered malignant and aggressive; respectively [37].

A means of inspecting histopathological characteristics at a molecular or cellular level is the motivation for the use of microscopic imaging. This modality has the advantage of providing coloured high resolution images exposing the richness or denseness of the examined underlying texture as compared to other non-invasive imaging modalities, assisting in giving a better interpretation to histopathological images, through studying the effect of disease on the cellular characteristics of the body tissue. This is done by previously staining the extracted tissue biopsies with dyes for visual contrast improvement, which will then facilitate the delineation of cell nuclei, giving a better tissue characterisation. Despite this modality being invasive, which is unpleasant for patients, physicians usually require a biopsy for a definite answer if they are suspicious about a certain abnormality in an image acquired by a non-invasive

imaging modality, and a closer view of the histopathological specimens can assist in verifying the tumour type.

Pathologists have been using microscopic images to study tissue biopsies for a long time, relying on their personal experience on giving decisions on the healthiness state of the examined biopsy. This includes distinguishing normal from abnormal (i.e. cancerous) tissue, benign versus malignant tumours and identifying the level of tumour malignancy. Nevertheless, variability in the reported diagnosis may still occur [123-125], which could be due to the non-homogeneous nature of the diseases (i.e. not all samples referring to a certain tumour subtype look identical, raising the issue of misclassification), noise arising from the staining process of the tissue samples,...etc. Therefore, through the past three decades, quantitative techniques have been developed for computer-aided diagnosis, which aim to assist pathologists in the process of cancer diagnosis [126]. Currently, the challenge remains in developing a better technique that not just automates the diagnostic procedure, but also applies the optimum texture feature extraction that better captures and understands the underlying physiology to improve cancer recognition accuracy.

A number of research studies have been applied to histopathological images for different tumours in an attempt to automate the diagnosis procedure. Some of them relied upon one texture measure (i.e. method) for feature extraction, such as extraction of wavelet-based features [56, 127, 128], or using other measures individually like fractal dimension (FD) or gray-level co-occurrence matrix (CM) for classification [129, 130]. Using more than one measure for classification was applied as well, such as using spatial and frequency texture features for classification by regression trees analysis [131]. Some used morphological characteristics for feature extraction [132, 133] and others focused more on classifier improvement [134, 135]. Regarding meningiomas, some used unsupervised learning techniques for training artificial neural networks, e.g. a self organizing map, for classifying meningioma features derived by wavelet packet (WP) transform [56]. An average accuracy of 79% was reported for classifying four different meningioma subtypes. Others applied a supervised learning method for classification of meningioma cells [58], using a decision tree after selecting the most relevant features from a base of grey and coloured image features. Also in another two studies the performance of features extracted from four meningioma subtypes using adaptive WP transform was compared to local binary patterns (LBP) [59] and to co-occurrence methods [60]. The WP method gave the highest classification accuracy of 82.1% when features were classified via a support vector machine classifier after applying a principal component analysis for dimensionality reduction.

As there is very limited research in the literature on fully-automating meningioma classification with significant accuracy, this research sets out to provide a novel method that combines model and statistical-based texture measures in an endeavour to provide a better understanding on how they relate to the underlying physiology. The aim is to improve the classification accuracy by integrating the RGB colour

channels that better assists the morphological process in segmenting the tumour structure with the best combination of texture features that best captures the characteristics of the examined case.

We intend to seek possible answers to several questions on histopathological image classification: a) will selecting the appropriate colour channel contribute to improving texture classification? b) which texture combinations –after removal of highly correlated features– perform better than the best of the individual measures and why (i.e. how do they relate to underlying physiology)? c) will using multiple texture extraction methods (e.g. more than two methods) guarantee a higher classification accuracy? d) and what is the effect of noise on histopathological images?

This chapter is arranged as follows. Section 5.2 explains the applied technique, and section 5.3 will show the experimental results. Then an analysis of the applied texture measures behaviour followed by a discussion is presented in sections 5.4 and 5.5; respectively. Finally, section 5.6 summarises the major outcomes.

5.2 Methodology

Two main stages are involved in the histopathological discrimination technique. In the pre-feature extraction stage, the best colour channel that maximises cell nuclei structure separation from the background is selected, then this colour channel will be used to morphologically process all histopathological specimens (i.e. training and testing images). In the next stage, the texture features are extracted and fused in all possible combinations, and the optimum features are selected for classification. The complete process is depicted in Fig. 5.1.

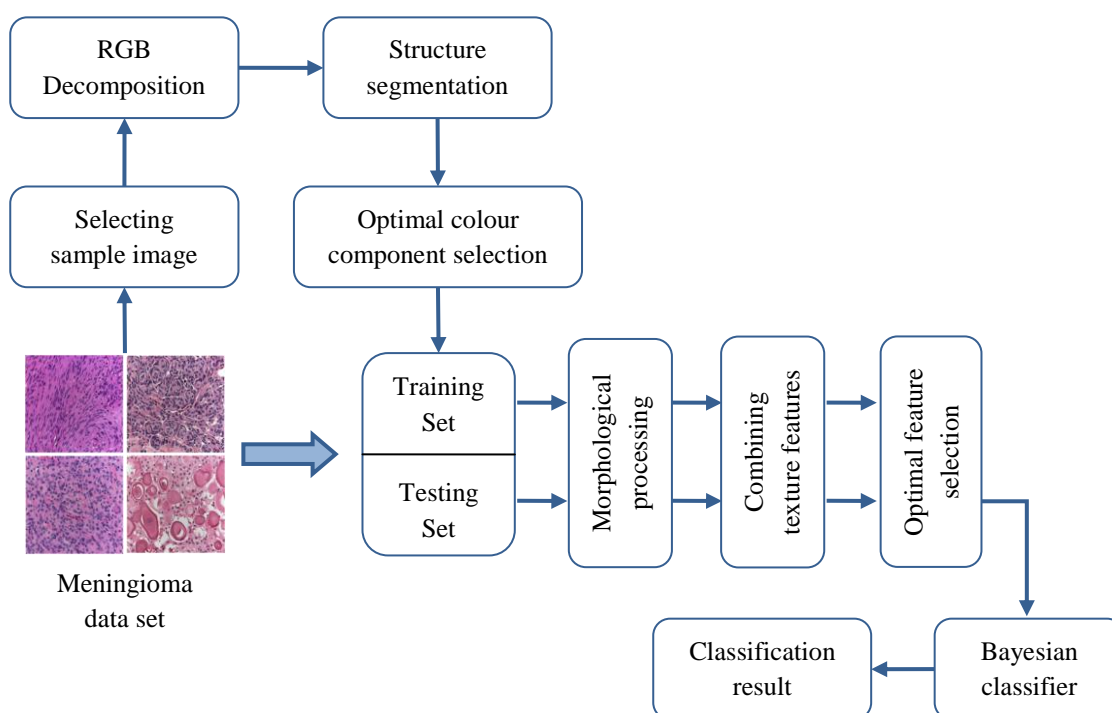


Fig. 5.1 Diagram explaining the process followed in classification of the histopathological meningioma images.

5.2.1 Image acquisition and preparation

Four subtypes of grade I meningioma tissue biopsies (see Fig. 5.2) distinguished according to the World Health Organisation (WHO) grading system [136] are used in this study. Each subtype has its own features (Table 5.1) which pathologists look for in the processes of tumour classification. The diagnostic tumour samples were derived from neurosurgical resections at the Bethel Department of Neurosurgery, Bielefeld, Germany for therapeutic purposes, routinely processed for formalin fixation and embedded into paraffin. Four micrometer thick microtome sections were dewaxed on glass slides, stained with Mayer's haemalaun and eosin (H&E), dehydrated and cover-slipped with mounting medium (Eukitt®, O. Kindler GmbH, Freiburg, Germany). Archive material of cases from the years 2004 and 2005 were selected to represent typical features of each meningioma subtype. Slides were analysed on a Zeiss Axioskop 2 plus microscope with a Zeiss Achroplan 40×/0.65 lens. After manual focusing and automated background correction, 1300 × 1030 pixels, 24 bit, true colour RGB pictures were taken at standardised 3200 K light temperature in TIF format using Zeiss AxioVision 3.1 software and a Zeiss AxioCam HRc digital colour camera (Carl Zeiss AG, Oberkochen, Germany). Five typical cases were selected for each diagnostic group and four different photomicrographs were taken of each case, resulting in a set of 80 pictures. Each original picture was truncated to 1024 × 1024 pixels and then subdivided in a 2 × 2 subset of 512 × 512 pixel pictures. This resulted in a database of 320 sub-images for further analysis. All acquired images were fully anonymised and our work did not influence the diagnostic process or the patient's treatment.

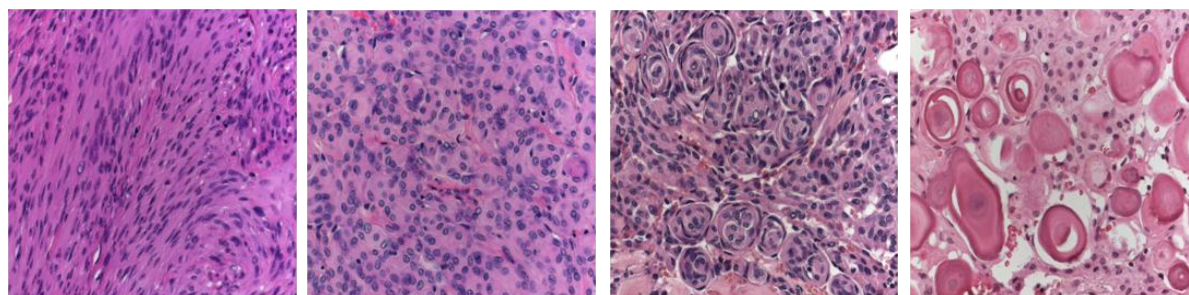


Fig. 5.2 Four types of grade I meningioma, from left to right (fibroblastic, meningothelial, transitional and psammomatous).

Table 5.1 Main histological features for the four meningioma subtypes in Fig. 5.2

Subtype	Characteristics
Fibroblastic	Spindle-shaped cells resembling fibroblasts in appearance, with abundant amounts of pericellular collagen.
Meningothelial	Broad sheets or lobules of fairly uniform cells with round or oval nuclei.
Transitional	Contains whorls, few psammoma bodies and cells having some fibroblastic features (i.e. spindle-shaped cells)
Psammomatous	A variant of transitional meningiomas with abundant psammoma bodies and many cystic spaces.

5.2.2 RGB space colour segmentation

Although the RGB colour model is not as intuitive as the HSV (hue, saturation and brightness) model for human perception, coloured image segmentation generally achieves better results using the former colour model [86]. Therefore the coloured histopathological images were decomposed to the red, green and blue colour channels to investigate which colour would better distinguish the cell nuclei from the background, hence assisting in improving the classification accuracy in the subsequent morphological and texture feature extraction stages.

One image $I(x, y, z)$, where z is the RGB colour component, is randomly selected from each of the four meningioma subtypes. Then a simple segmentation procedure is applied by first determining the mean RGB vector $a_z = [a_R, a_G, a_B]$ of a sample cell nucleus (see Fig. 5.3), where each component of the vector represents the corresponding colour channel mean. This vector will be used in segmenting each of the colour channel images on a pixel-by-pixel basis. As recommended by [86], the size of the operation box used in the segmentation process was chosen to be 1.25 times the standard deviation σ_z of the corresponding colour component of the selected cell nucleus sample values. Shown in (5.1), each of the pixels were then classified as either 1 or 0 by comparison with a_z giving the segmentation mask which when multiplied with the corresponding colour channel will give the segmented image I_{seg} . Also a reference image I_{ref} is generated for each of the randomly selected subtype images after manually segmenting the cell nuclei. Fig. 5.4 shows I_{seg} and I_{ref} for the blue colour channel of the transitional meningioma subtype.

$$I_{seg}(x, y, z) = \begin{cases} 1 & \text{if } I(x, y, z) \in (a_z \pm 1.25\sigma_z) \\ 0 & \text{Otherwise} \end{cases} \quad (5.1)$$

The Bhattacharyya distance was used to assess the quality of segmentation. For classes with a Gaussian distribution, the Bhattacharyya distance $B_{I_1 I_2}$ is used to estimate the upper bound of classification error P_ϵ between feature image pairs as in (5.2) [114]. A smaller error value indicates improved separability between the reference and the segmented image. Finally, the colour component with the best segmentation output would be selected for morphological processing.

$$B_{I_1 I_2} = \frac{1}{8} (\mu_1 - \mu_2)^T \left(\frac{\Sigma_1 \Sigma_2}{2} \right)^{-1} (\mu_1 - \mu_2) + \frac{1}{2} \ln \left(\frac{|\Sigma_1 + \Sigma_2|}{2\sqrt{|\Sigma_1||\Sigma_2|}} \right)$$

$$P_\epsilon = \sqrt{P(I_1)P(I_2)} \exp(-B_{I_1 I_2}) \quad (5.2)$$

Here $|\Sigma_i|$ is the determinant of Σ_i , and μ_i and Σ_i are the mean vector and covariance matrix of class I_i (which refers to I_{ref} and I_{seg}), and $P(I_i)$ is the probability of I_i .

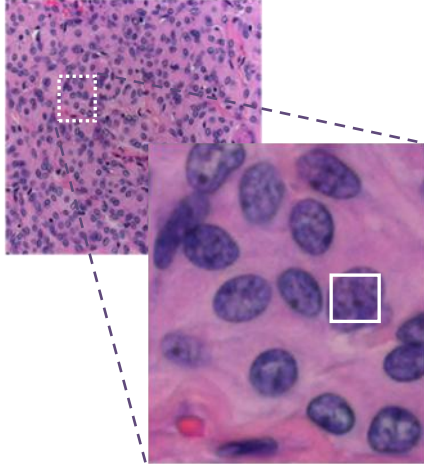


Fig. 5.3 The solid white rectangle in the magnified region indicates the selected sample cell nucleus used for segmenting all relevant meningothelial subtypes.

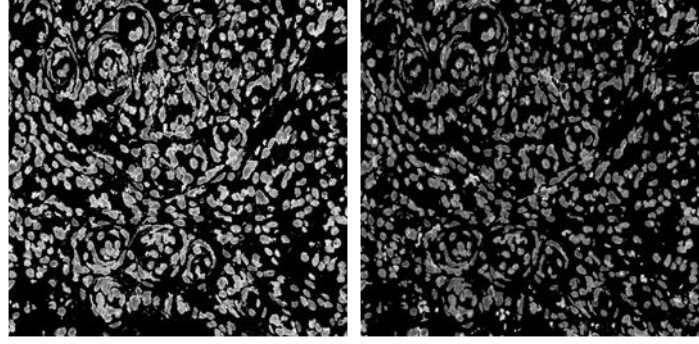


Fig. 5.4 Left to right, segmented and reference image for transitional meningioma subtype.

We will see afterwards that the selection of the colour component of texture plays a significant role in classification accuracy depending on the colour of the examined structure.

5.2.3 Morphological processing

Having selected the appropriate colour channel, morphological processing is required to make the cell nuclei more distinguishable from the background, which has also another advantage which is the elimination of possible noise occurrence [137]. All sets of images are pre-processed by computing the morphological gradient (M_g), which is simply the difference between the dilation and erosion of each processed image. It assists in highlighting the edges of the general structure of the texture, which is shown in Fig. 5.5. To simplify indexing, the image $I(x, y)$ is translated instead of the structuring element k [86].

The gray-scale dilation of image $I(x, y)$ by structuring element $k(x, y)$ can be regarded as the function of all displacements (s, t) , such that $I(x, y)$ and $k(x, y)$ overlap by at least one element, this is emphasised in the (5.3) as $(s - x)$ and $(t - y)$, and x and y have to be in domain I and k ; respectively.

$$(I(x, y) \oplus k(x, y))(s, t) = \max\{I(s - x, t - y) + k(x, y) \mid (s - x), (t - y) \in D_I; (x, y) \in D_k\} \quad (5.3)$$

D_I and D_k are the domains of I and k , respectively. The structuring element $k(x, y)$ operates in analogy to a convolution kernel applied to an image. We empirically chose the size of the structure element to be a square 5 x 5 pixels of ones.

Similarly, gray-scale erosion of $k(x, y)$ by image $I(x, y)$ is the function of all displacements (s, t) such that $I(x, y)$, translated by (s, t) , is contained in $k(x, y)$.

$$(I(x, y) \ominus k(x, y))(s, t) = \min\{I(s + x, t + y) - k(x, y) \mid (s + x), (t + y) \in D_I; (x, y) \in D_k\} \quad (5.4)$$

Hence M_g can be represented as,

$$M_g = (I(x, y) \oplus k(x, y)) - (I(x, y) \ominus k(x, y)) \quad (5.5)$$

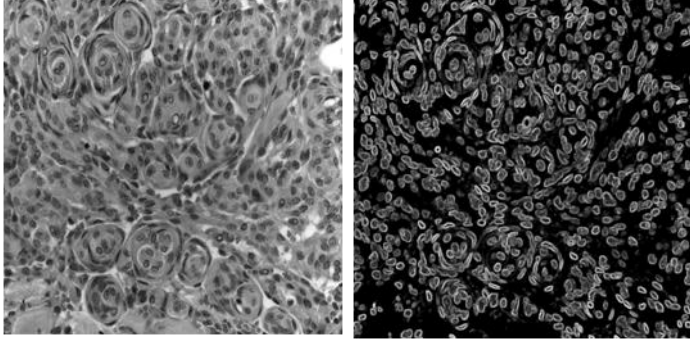


Fig. 5.5 Blue colour channel image and its corresponding morphological gradient.

5.2.4 Feature extraction approaches

Five different methods – two model and three statistical based – were used to extract different texture features from 320 image samples referring to four meningioma subtypes, as follows:-

5.2.4.1 Model-based features methods

a) Random fields

Based upon the Markovian property, which is simply the dependence of each pixel in the image on its neighbours only, a Gaussian Markov random field model (GMRF) for third order Markov neighbours was used [76] (see Fig. 5.6). Seven GMRF parameters were estimated using the least square error estimation method.

The GMRF model is defined by the following formula:

$$p(I_{xy} | I_{kl}, (k, l) \in N_{xy}) = \frac{1}{\sqrt{2\pi\sigma^2}} \exp \left\{ -\frac{1}{2\sigma^2} \left(I_{xy} - \sum_{l=1}^n \alpha_l s_{xy;i} \right)^2 \right\} \quad (5.6)$$

The right hand side of (5.6) represents the probability of a pixel (x, y) having a specific grey value I_{xy} given the values of its neighbours, n is the total number of pixels in the neighbourhood N_{xy} of pixel I_{xy} , which influence its value, α_l is the parameter with which a neighbor influences the value of (x, y) , and $s_{xy;i}$ is the sum of the values of the two pixels which are in symmetric position about (x, y) and which influence the value of (x, y) with identical parameters (see Fig. 5.6) where,

$$\begin{aligned}
s_{xy;1} &= I_{x-1,y} + I_{x+1,y} & s_{xy;3} &= I_{x-2,y} + I_{x+2,y} & s_{xy;5} &= I_{x-1,y-1} + I_{x+1,y+1} \\
s_{xy;2} &= I_{x,y-1} + I_{x,y+1} & s_{xy;4} &= I_{x,y-2} + I_{x,y+2} & s_{xy;6} &= I_{x,y-2} + I_{x+1,y-1}
\end{aligned}$$

For an image of size M and N the GMRF parameters α and σ are estimated using a least square error estimation method, as follows:

$$\begin{pmatrix} \alpha_1 \\ \vdots \\ \alpha_n \end{pmatrix} = \left\{ \sum_{xy} \begin{bmatrix} s_{xy;1} s_{xy;1} & \cdots & s_{xy;1} s_{xy;n} \\ \vdots & \ddots & \vdots \\ s_{xy;n} s_{xy;1} & \cdots & s_{xy;n} s_{xy;n} \end{bmatrix} \right\}^{-1} \sum_{xy} I_{xy} \begin{pmatrix} s_{xy;1} \\ \vdots \\ s_{xy;n} \end{pmatrix} \quad (5.7)$$

$$\sigma^2 = \frac{1}{(M-2)(N-2)} \sum_{xy} \left[I_{xy} - \sum_{l=1}^n \alpha_l s_{xy;l} \right]^2 \quad (5.8)$$

The values shown in Table 5.1 represent the GMRF parameters for the four different meningioma subtypes in Fig. 5.2. The difference between some of the subtypes GMRF parameters could be minor; therefore, having a larger model order that can be more sensitive to the neighbourhood of each pixel is important. Nonetheless, we need to manage the tradeoff between having a large order model which would be sufficient to capture the characteristics of each subtype texture, where small order models might overlook some complimentary information; on the other hand, not too large to include redundant information which would increase the processing time and dimensionality of the estimations. Empirically, a third order GMRF model was the most suitable given the nature of the texture under investigation. Using the same classifier discussed in the pattern classification technique section, the 3rd order model had a 25% and 11.25% classification improvement over the 2nd (having 5 parameters) and 4th (having 13 parameters) models respectively.

$I_{x+2,y-2}$	$I_{x+2,y-1}$	$I_{x+2,y}$	$I_{x+2,y+1}$	$I_{x+2,y+2}$
$I_{x+1,y-2}$	$I_{x+1,y-1}$	$I_{x+1,y}$	$I_{x+1,y+1}$	$I_{x+1,y+2}$
$I_{x,y-2}$	$I_{x,y-1}$	I_{xy}	$I_{x,y+1}$	$I_{x,y+2}$
$I_{x-1,y-2}$	$I_{x-1,y-1}$	$I_{x-1,y}$	$I_{x-1,y+1}$	$I_{x-1,y+2}$
$I_{x-2,y-2}$	$I_{x-2,y-1}$	$I_{x-2,y}$	$I_{x-2,y+1}$	$I_{x-2,y+2}$

Fig. 5.6 Third order Markov neighbourhood (in dark) for a sample image pixel I_{xy} , compared to second and fourth order Markov neighbourhood represented by the 3×3 inner box and the 5×5 outer box, respectively.

Table 5.2 Estimated GMRF parameters using a 3rd order Markov neighbours for the subtypes shown in Fig. 5.2

Meningioma type	α_1	α_2	α_3	α_4	α_5	α_6	σ
Fibroblastic	0.5049	0.5376	-0.2577	-0.2466	-0.0078	-0.0311	1.0046
Meningothelial	0.5157	0.5285	-0.2519	-0.2523	-0.0147	-0.0259	1.0445
Psammomatous	0.5177	0.5239	-0.2558	-0.2527	-0.0126	-0.0213	0.9077
Transitional	0.5157	0.5275	-0.2536	-0.2535	-0.0129	-0.0238	1.3348

b) Fractals

As discussed in the previous chapter, fractals are used to describe non-Euclidean structures that show self-similarity at different scales [85]. There are several fractal models used to estimate the fractal dimension; the fractal Brownian motion (fBm) which is the mean absolute difference of pixel pairs as a function of scale as shown in (5.9) was adopted [94].

$$E(\Delta I) = K\Delta r^H \quad (5.9)$$

$\Delta I = |I(x_2, y_2) - I(x_1, y_1)|$ is the mean absolute difference of pixel pairs; $\Delta r = \sqrt{(x_2 - x_1)^2 + (y_2 - y_1)^2}$ is the pixel pair distances; H is called the Hurst coefficient; and K is a constant.

The fractal dimension (FD) can be then estimated by plotting both sides of (5.9) on a log-log scale and H will represent the slope of the curve that is used to estimate the FD as: $FD = 3 - H$.

By operating pixel by pixel, an FD image was generated for each meningioma subtype where each pixel has its own FD value, see Fig. 5.7. Then first order statistical features shown in Table 5.3 were derived from each processed image, which are: mean, variance, kurtosis, lacunarity, and skewness. Also for comparison, the same features were estimated using the DBC algorithm used in the previous chapter.

If we examine the images in Fig. 5.7, we can see that the fBm generated FD images had more visible discontinuities compared to the DBC ones. More discontinuities in the absence of visible noise would mean a texture with richer information, and hence a more reliable estimation of the roughness of the image surface. Thus, we can say that the fBm is better suited to represent textures with macro structures (i.e histopathological images) compared to the fine texture in the case of lung tumour CT images; thus fBm was adopted for the meningiomas.

Table 5.3 First order statistics derived from a fractal dimension generated image using fractal Brownian motion (without brackets) and differential box counting (inside brackets) algorithms

Fractal dimension derived statistics	Meningioma subtype			
	Fibroblastic	Meningothelial	Psammomatous	Transitional
Mean	2.8013 (1.7070)	2.8009 (1.7142)	2.8447 (1.7887)	2.7534 (1.6851)
Variance	0.0313 (0.1352)	0.0349 (0.1396)	0.0247 (0.1259)	0.0416 (0.1393)
Kurtosis	3.1335 (4.5085)	3.4256 (4.5756)	4.7077 (7.0275)	2.5989 (4.2659)
Lacunarity	0.0112 (0.0792)	0.0124 (0.0814)	0.0087 (0.0704)	0.0151 (0.0827)
Skewness	-0.9488 (-0.7799)	-1.0671 (-0.8490)	-1.3915 (-1.2258)	-0.7109 (-0.6962)

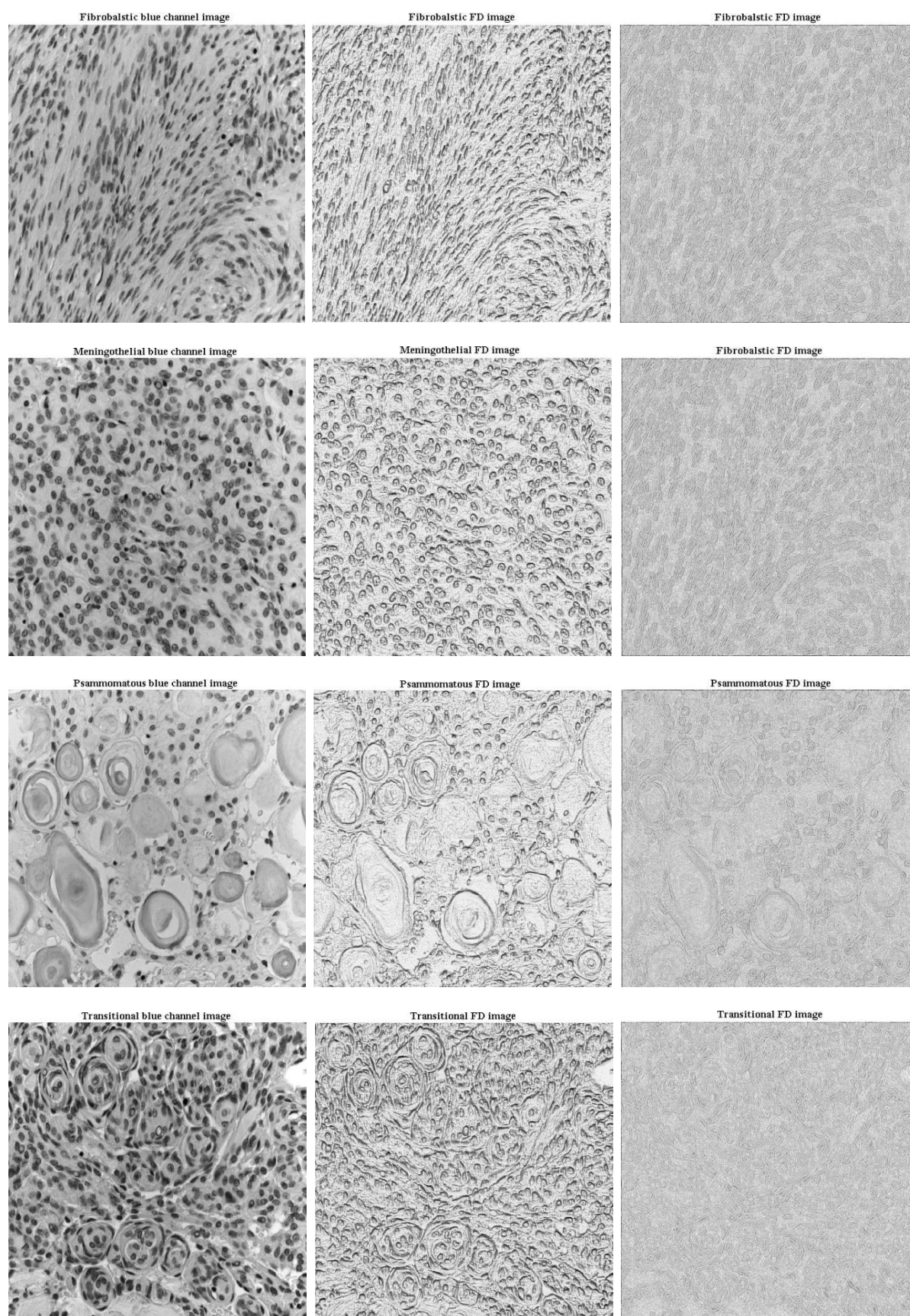


Fig. 5.7 First column represents the blue channel image for meningioma fibroblastic, meningothelial, psammomatous and transitional subtypes, whereas the second and third columns are their corresponding fractal dimension images computed using the fractal Brownian motion and the differential box counting algorithm; respectively.

5.2.4.2 Statistical-based features methods

a) Co-occurrence matrices

The grey level co-occurrence matrix (CM) $P_{CM}(i, j | \delta, \theta)$ represents the joint probability of certain sets of pixels having certain grey-level values. It calculates how many times a pixel with grey-level i occurs jointly with another pixel having a grey value j . For an $M \times M$ image and by varying the displacement vector δ between each pair of pixels, up to $M-1$ CMs with different directions θ can be generated. The CM can be formally defined as [76]:

$$P_{CM}(i, j | \delta, \theta) = \sum_m \sum_n \Delta(i - I(m, n)) \Delta(j - I(m + \delta \cos \theta, n + \delta \sin \theta)) \quad (5.10)$$

where $I(m, n)$ is the image grey value of pixel (m, n) ; $I(m + \delta \cos \theta, n + \delta \sin \theta)$ is the grey value of another pixel at distance δ and direction θ ; $P_{CM}(i, j | \delta, \theta)$ is the total number of paired pixels identified in the image with grey values i and j . For the above expression

$$\Delta(x - y) = \begin{cases} 1 & \text{if } x = y \\ 0 & \text{if } x \neq y \end{cases}$$

A simple graphical illustration for a 5 grey level image with four directions and the displacement vector set to one is illustrated in Fig. 5.8.

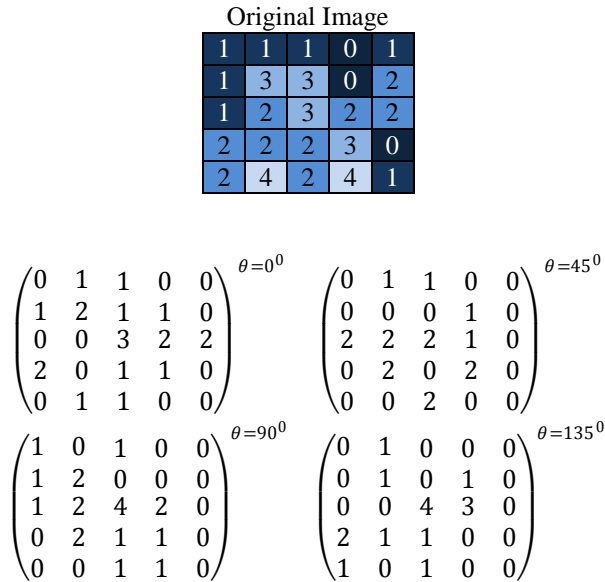


Fig. 5.8 A 5×5 pixel image and its corresponding co-occurrence matrix with $\delta = 1$ and $\theta = 0^\circ, 45^\circ, 90^\circ$ and 135° .

It should be noted that the above example does not show the co-occurrence for the last column and row of the given image (i.e. the CMs was computed without padding). Regarding the medical images used in this work and in order not to ignore the information at the end of each image, circular padding was applied — presuming that texture is continually extended in both directions. This step is recommended to highlight subtle differences between textures, and since different tumour subtypes usually have specific patterns, it is more meaningful having circular padding rather than padding with constant values or replicates of the last pixels.

As mentioned before, $A \times (M - 1)$ CMs can be generated for a specific texture, where M is the size of the image with A number of used angles. The extraction of features from all these CMs would be deemed unpractical as this will result in increasing the dimensionality of the feature vector used for classification, and not all extracted features would have good discrimination capabilities. Thus, a careful selection of the δ and θ parameters will assist in better characterizing the regions of interest in each texture. The smaller the δ the more sensitive the CM becomes to small changes, and θ assists in showing which orientation would result in more co-occurrences, hence identifying the textures' pattern direction. Since there is not an agreed upon rigorous method for selection of CM parameters and the cell nuclei —which are the principal textons that differentiate between the texture of the meningioma subtypes — had a relative small size in three out of the four subtypes, and a large δ would overlook the small texture variations, thus a small value would be more appropriate. Additionally, some subtypes (e.g. fibroblastic) had their cell nuclei distributed in a specific direction which calls for computing the CMs with multiple orientations θ . Therefore for each histopathological image, the δ was set to one and four CMs having directions (0° , 45° , 90° & 135°) were generated, see Fig. 5.9.

Also, the CMs have been quantised to 32-grey levels (6-bits) to reduce computational time while still having clear and discriminable features, and which could also assist in increasing the number of neighbouring structures (i.e. edges) for each pixel in the image [76]. An image can be mapped to G grey levels by

$$P_{CM}(i, j)_Q = \text{round} \left[\frac{P_{CM}(i, j)_N}{(G_{old} - 1)} \times (G_{new} - 1) \right] \quad (5.11)$$

where subscripts Q and N indicated quantised and normalised versions of the CM, and G_{old} and G_{new} are the maximum grey level before and after quantisation.

Having the CM normalised to be represented as a joint probability density function, we can then derive eight second order statistical features, which are also known as Haralick features [138], for each image. Haralick initially proposed a set of 14 features, each of which defines certain properties to be derived from the CMs. We have selected eight features, which are the most commonly used in the literature, which are:

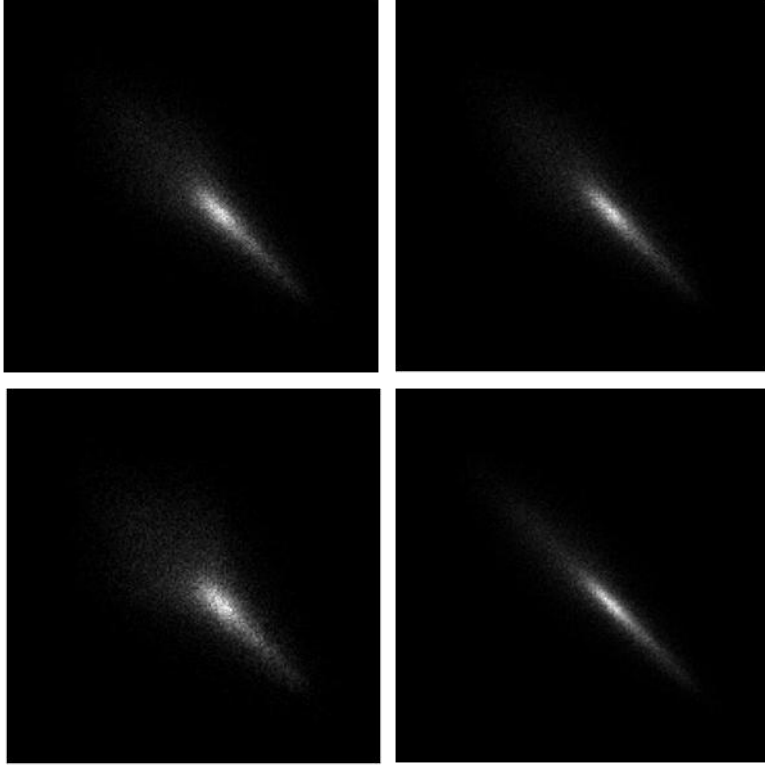


Fig. 5.9 Co-occurrence matrices of the blue colour channel for fibroblastic subtype in Fig. 5.2 with 256 grey levels, having $\delta = 1$ for $\theta = 0^\circ, 45^\circ, 90^\circ$ and 135° , shown clockwise.

i) Energy (ENG) also referred to as angular second momentum or uniformity: is a way to measure disorders in an image through summing the square of all pixels, with lower values indicating a more uniform image.

$$ENG = \sum_{i=0}^{G-1} \sum_{j=0}^{G-1} P(i,j)^2 \quad (5.12)$$

ii) Entropy (ENT): is a measurement of randomness in the image, with higher entropy values indicating complex or random texture.

$$ENT = \sum_{i=0}^{G-1} \sum_{j=0}^{G-1} P(i,j) \log_2(P(i,j)) \quad (5.13)$$

iii) Contrast (CON) also known as inertia: is the measurement of intensity contrast or local variations between the image pixels, giving lower values for uniform texture.

$$CON = \frac{1}{(G-1)^2} \sum_{i=0}^{G-1} \sum_{j=0}^{G-1} (i-j)^2 P(i,j) \quad (5.14)$$

iv) Correlation (COR): estimates the correlation between each pixel and its neighbours throughout the image.

$$COR = \frac{1}{\sigma_x \sigma_y} \sum_{i=0}^{G-1} \sum_{j=0}^{G-1} ij P(i, j) - \mu_x \mu_y \quad (5.15)$$

where

$$\begin{aligned} \mu_x &= \sum_{i=0}^{G-1} i \sum_{j=0}^{G-1} P(i, j) & \mu_y &= \sum_{j=0}^{G-1} j \sum_{i=0}^{G-1} P(i, j) \\ \sigma_x &= \sum_{i=0}^{G-1} (i - \mu_x)^2 \sum_{j=0}^{G-1} P(i, j) & \sigma_y &= \sum_{j=0}^{G-1} (j - \mu_y)^2 \sum_{i=0}^{G-1} P(i, j) \end{aligned}$$

v) Dissimilarity (DIS): gives a measure how each pixel differs (i.e. how far) from its neighbours in the image.

$$DIS = \sum_{i=0}^{G-1} \sum_{j=0}^{G-1} |i - j| P(i, j) \quad (5.16)$$

vi) Homogeneity (HOM): is the measurement of how close is the distribution of pixels in the image

$$HOM = \sum_{i=0}^{G-1} \sum_{j=0}^{G-1} \frac{P(i, j)}{1 + |i - j|} \quad (5.17)$$

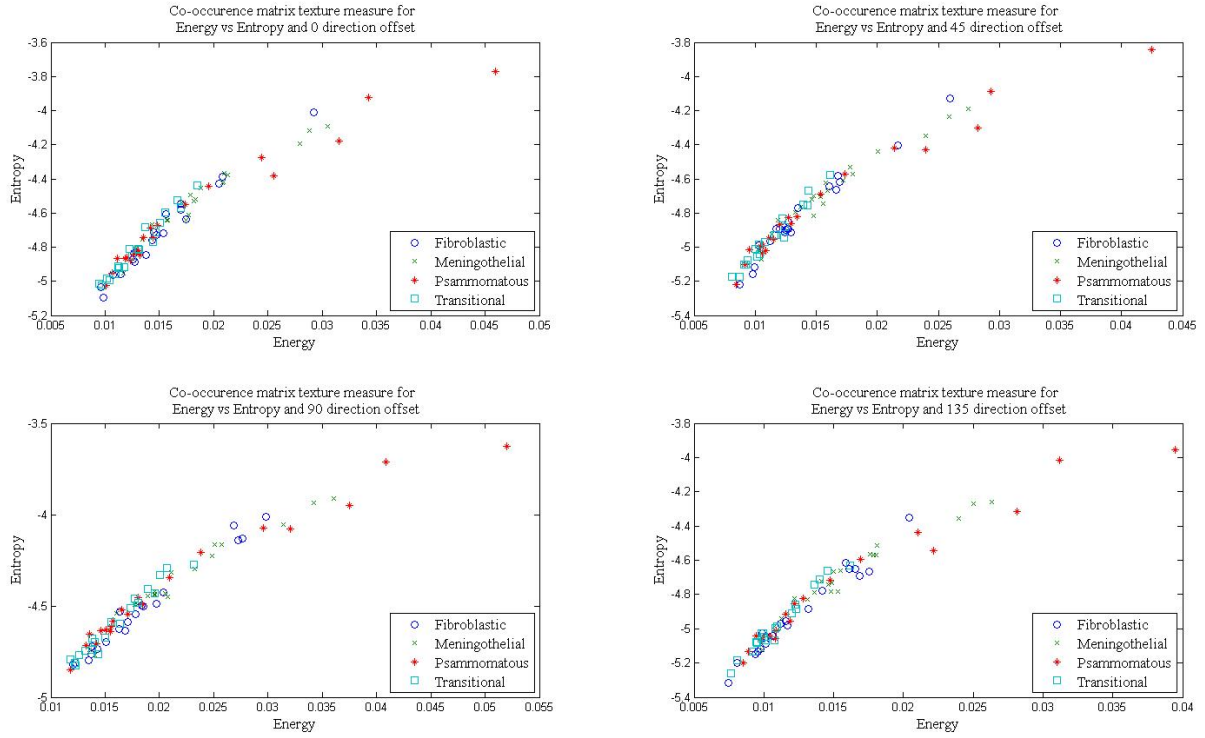
vii) Inverse Difference Momentum (IDM): similar to homogeneity, but with giving more emphasis — the square in the denominator — to the difference between pixels.

$$IDM = \sum_{i=0}^{G-1} \sum_{j=0}^{G-1} \frac{P(i, j)}{1 + (i - j)^2} \quad (5.18)$$

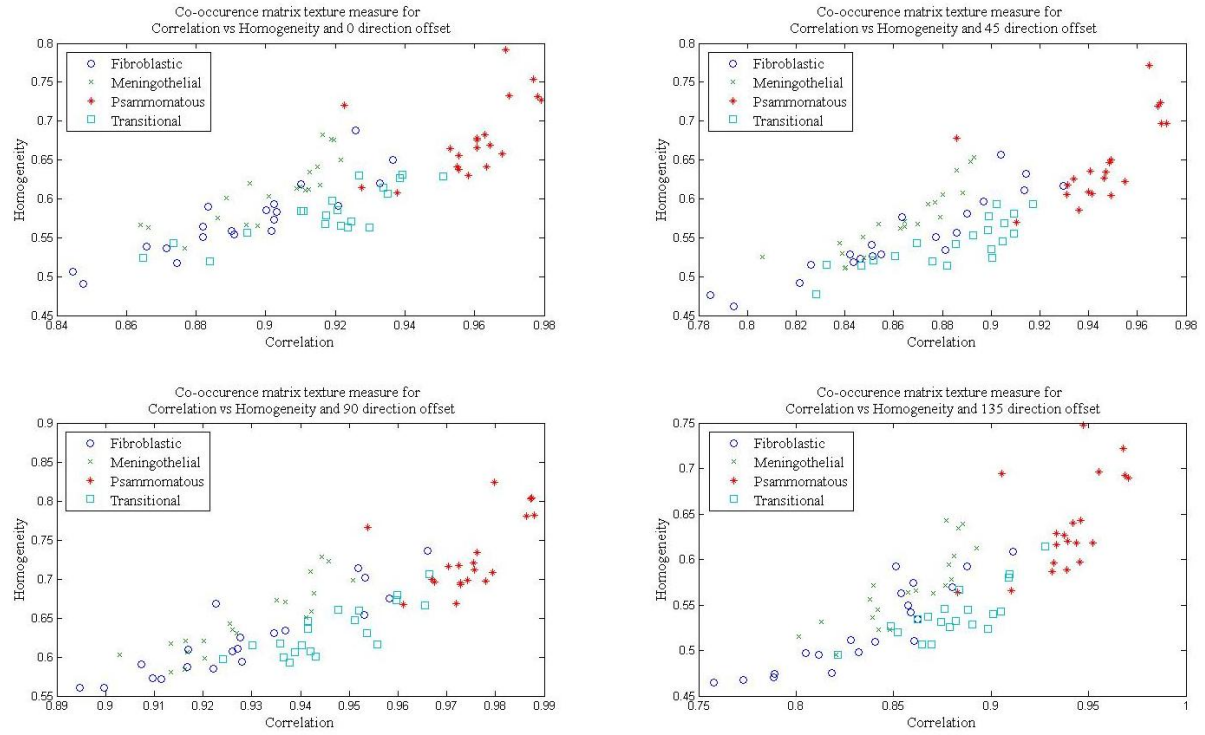
viii) Maximum probability (MP): obtains the value of the most occurring paired combination of pixels in the image.

$$MP = \max_{ij} (P(i, j)) \quad (5.19)$$

All the eight extracted features from the CM may not have equal discriminatory power, and some features when fused together may perform much better than with others. The high correlation between some features would also affect its feasibility for texture discrimination; thus, a selection procedure that excludes highly correlated features would be required. This is evident in Fig. 5.10, where combining the homogeneity and correlation features together can give a better separability between the meningioma subtypes as compared to the combination of the entropy and energy features, where different subtypes do not cluster away from each other.



(a)



(b)

Fig. 5.10 Co-occurrence matrix derived features in four directions for 80 different meningioma images equally divided to four subtypes plotted against each other in pairs (a) entropy vs energy, and (b) homogeneity vs correlation.

b) Run-length matrices

Another way for extracting higher order statistical texture features is the use of grey level run-length matrix (RLM) $P_{RLM}(i, j | \theta)$, defined as the number of occurrence of runs with pixels of gray level i and run length j co-linear in a given direction θ [139]. The example in Fig. 5.11 illustrates this process for four directions ($\theta = 0^\circ, 45^\circ, 90^\circ$ & 135°) using a five grey level random 5×5 pixels image. It can be observed that the first column in the RLMs contains most of the texture information; this is also reflected in Fig. 5.12 where the four different direction RLMs of the fibroblastic subtype in Fig. 5.2 are concatenated with each other and shown as a surface plot. Considering the number of run-lengths as well, it can be seen that the RLM with 45° has a stronger response, and hence a better representation for this image.

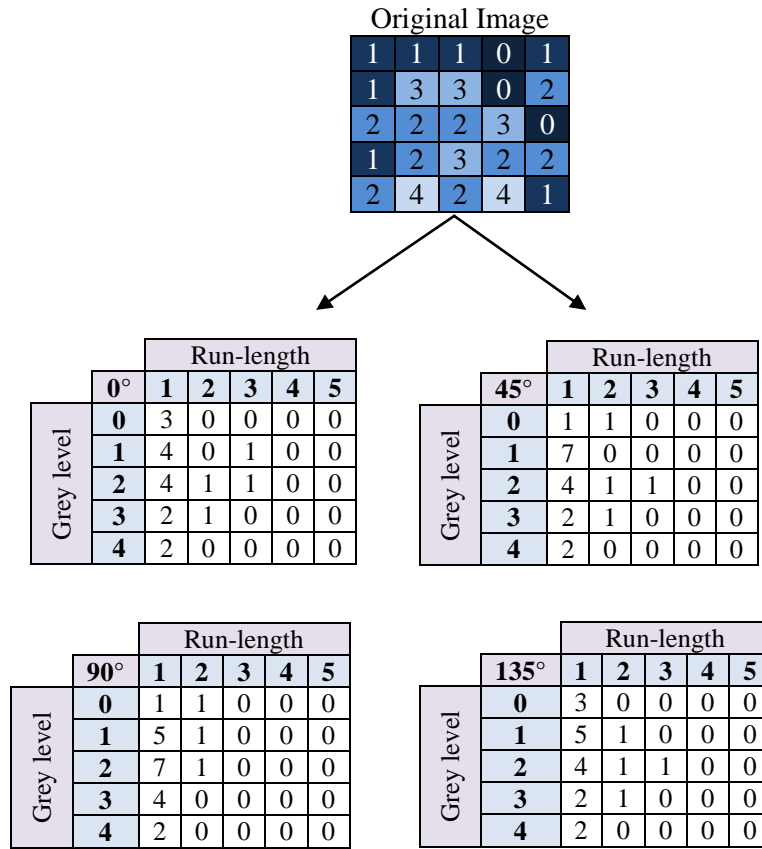


Fig. 5.11 An example of run-length matrices for five grey levels and four different directions.

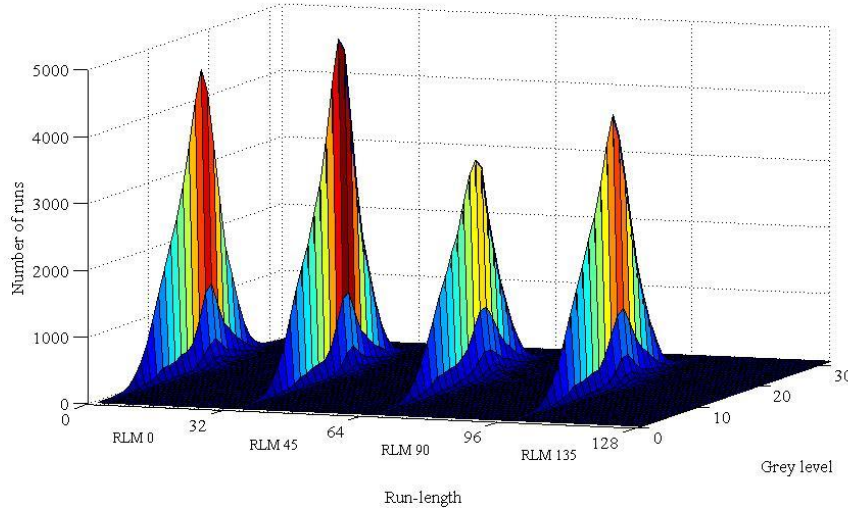


Fig. 5.12 Run-length matrices in four directions (0° , 45° , 90° & 135°) of fibroblastic subtype image in Fig. 5.2 after quantisation to 32 grey levels. Most information is condensed in the first (left-most) column, this information starts to fade as we move to higher run-lengths (to the right side).

For a number of grey levels G and maximum run-length R , several texture features can be derived, the initial five features proposed by Galloway [139] are as follows.

i) Short Run Emphasis (SRE):

$$SRE = \frac{1}{n_R} \sum_{i=1}^G \sum_{j=1}^R \frac{P(i, j | \theta)}{j^2} = \frac{1}{n_R} \sum_{j=1}^R \frac{P_R(j | \theta)}{j^2} \quad (5.20)$$

ii) Long Run Emphasis (LRE):

$$LRE = \frac{1}{n_R} \sum_{i=1}^G \sum_{j=1}^R P(i, j | \theta) \cdot j^2 = \frac{1}{n_R} \sum_{j=1}^R P_R(j | \theta) \cdot j^2 \quad (5.21)$$

iii) Grey level Non-uniformity (GLN):

$$GLN = \frac{1}{n_R} \sum_{i=1}^G \left(\sum_{j=1}^R P(i, j | \theta) \right)^2 = \frac{1}{n_R} \sum_{i=1}^G P_G(i | \theta)^2 \quad (5.22)$$

iv) Run Length Non-uniformity (RLN):

$$RLN = \frac{1}{n_R} \sum_{j=1}^R \left(\sum_{i=1}^G P(i, j | \theta) \right)^2 = \frac{1}{n_R} \sum_{j=1}^R P_R(j | \theta)^2 \quad (5.23)$$

v) Run Percentage (RP):

$$RP = \frac{n_r}{n_p} \quad (5.24)$$

where P_R and P_G are the run length and grey level run number vectors; $n_r = \sum_{i=1}^G \sum_{j=1}^R p(i, j|\theta)$ is the total number of runs, and n_p is the number of pixels in the image. In order to distinguish between textures for which its SRE and LRE are equal, Chu et al [140] added two new features giving this time the emphasis to the grey level.

i) Low Grey level Runs Emphasis (LGLRE):

$$LGRE = \frac{1}{n_R} \sum_{i=1}^G \sum_{j=1}^R \frac{P(i, j|\theta)}{i^2} = \frac{1}{n_R} \sum_{i=1}^G \frac{P_G(i|\theta)}{i^2} \quad (5.25)$$

ii) High Grey level Runs Emphasis (HGLRE):

$$HGRE = \frac{1}{n_R} \sum_{i=1}^G \sum_{j=1}^R P(i, j|\theta) \cdot i^2 = \frac{1}{n_R} \sum_{i=1}^G P_G(i|\theta) \cdot i^2 \quad (5.26)$$

Also Dasarathy and Holder [141] further introduced four new measures based on the joint statistics of grey level and run-length, as follows,

i) Short Run Low Grey level Emphasis (SRLGLE):

$$SRLGE = \frac{1}{n_R} \sum_{i=1}^G \sum_{j=1}^R \frac{P(i, j|\theta)}{i^2 \cdot j^2} \quad (5.27)$$

ii) Short Run High Grey level Emphasis (SRHGLE):

$$SRHGE = \frac{1}{n_R} \sum_{i=1}^G \sum_{j=1}^R \frac{P(i, j|\theta) \cdot i^2}{j^2} \quad (5.28)$$

iii) Long Run Low Grey level Emphasis (LRLGLE):

$$LRLGE = \frac{1}{n_R} \sum_{i=1}^G \sum_{j=1}^R \frac{P(i, j|\theta) \cdot j^2}{i^2} \quad (5.29)$$

iv) Long Run High Grey level Emphasis (LRHGLE):

$$LRLGE = \frac{1}{n_R} \sum_{i=1}^G \sum_{j=1}^R P(i, j|\theta) \cdot i^2 \cdot j^2 \quad (5.30)$$

Since generating sparse matrices would degrade the quality of the derived features and hence produce more erroneous results, RLM, similar to CM, would be better estimated with coarser quantisation. Moreover, fewer grey levels would also reduce noise-induced effects; e.g. making the image more independent of the effect of non-uniform illumination (day light or artificial) conditions during image acquisition. Thus for the histopathological images used in this work, and to enrich the feature space, the RLMs were quantised to 32 grey levels prior to feature extraction; this also saves memory and reduces computational time. RLMs were generated for each sample image segment having directions ($\theta = 0^\circ, 45^\circ, 90^\circ \& 135^\circ$), then the previous eleven statistical features were derived.

c) Autocovariance function

The autocovariance function (ACF) is the autocorrelation function after subtracting the mean. It is a way to investigate non-randomness by looking for replication of certain patterns in an image, i.e. measuring dependency between pattern pixels. The ACF is defined as:

$$\rho(x, y) = \frac{1}{(M-x)(N-y)} \sum_{i=1}^{M-x} \sum_{j=1}^{N-y} (I(i, j) - \mu)(I(i+x, j+y) - \mu) \quad (5.31)$$

where $I(i, j)$ is the grey value of a $M \times N$ image, μ is the mean of the image before processing and x, y are the amount of shifts. After calculating the ACF for each image, the peaks K of the horizontal x and vertical y margins were fitted using least squares by an exponential and parabola functions; see Fig. 5.13. The exponential function can be defined as

$$\rho_d(d) = K_d \exp(-S_d d) \quad (5.32)$$

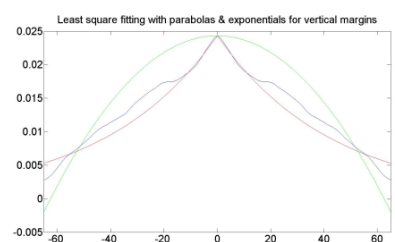
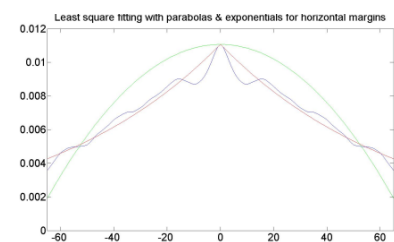
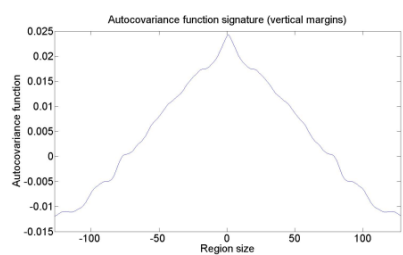
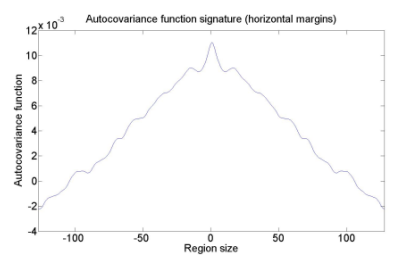
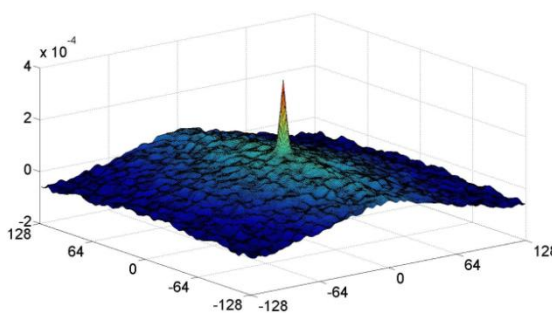
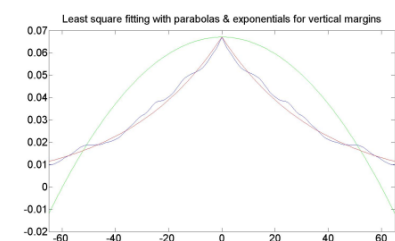
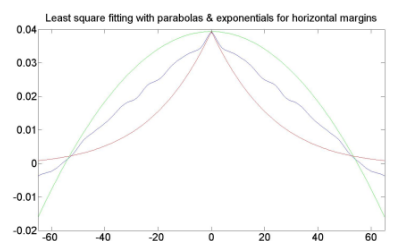
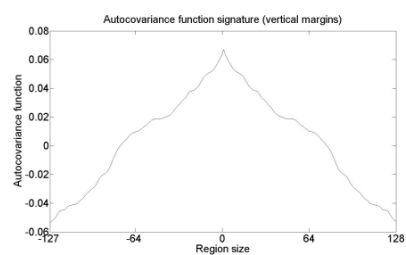
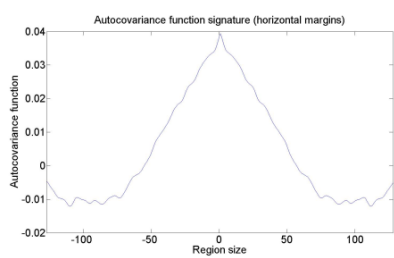
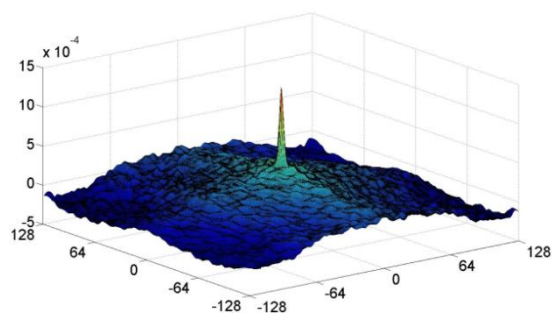
where d is the ACF projection along the x or y direction, and the total error to be minimised is

$$E = \sum_i (\ln K_x - S_x x_i - \ln \rho_{xi})^2 \quad (5.33)$$

had a better fit to the shape of the ACF margins, its signatures were selected as the texture features and the parabola features were excluded. Therefore, each sample is represented by four different parameters, which are the horizontal margin ACF peak (K_x) and its corresponding exponential fitting (S_x), and the vertical margin ACF peak (K_y) and its corresponding exponential fitting (S_y). Table 5.4 shows the ACF corresponding parameters for each of the sample meningioma subtypes in Fig. 5.2.

Table 5.4 Autocovariance function least squares exponential fittings, here K_x and K_y , S_x and S_y represent the ACF peak (K) and exponential parameters (S) for the horizontal (x) and vertical (y) margins.

ACF parameters	Meningioma subtype			
	Fibroblastic	Meningothelial	Psammomatous	Transitional
K_x	0.0045	0.2106	0.0070	0.0212
K_y	0.0077	0.2787	0.0041	0.0131
S_x	0.0119	0.0235	0.0152	0.0282
S_y	0.0123	0.0284	0.0151	0.0198



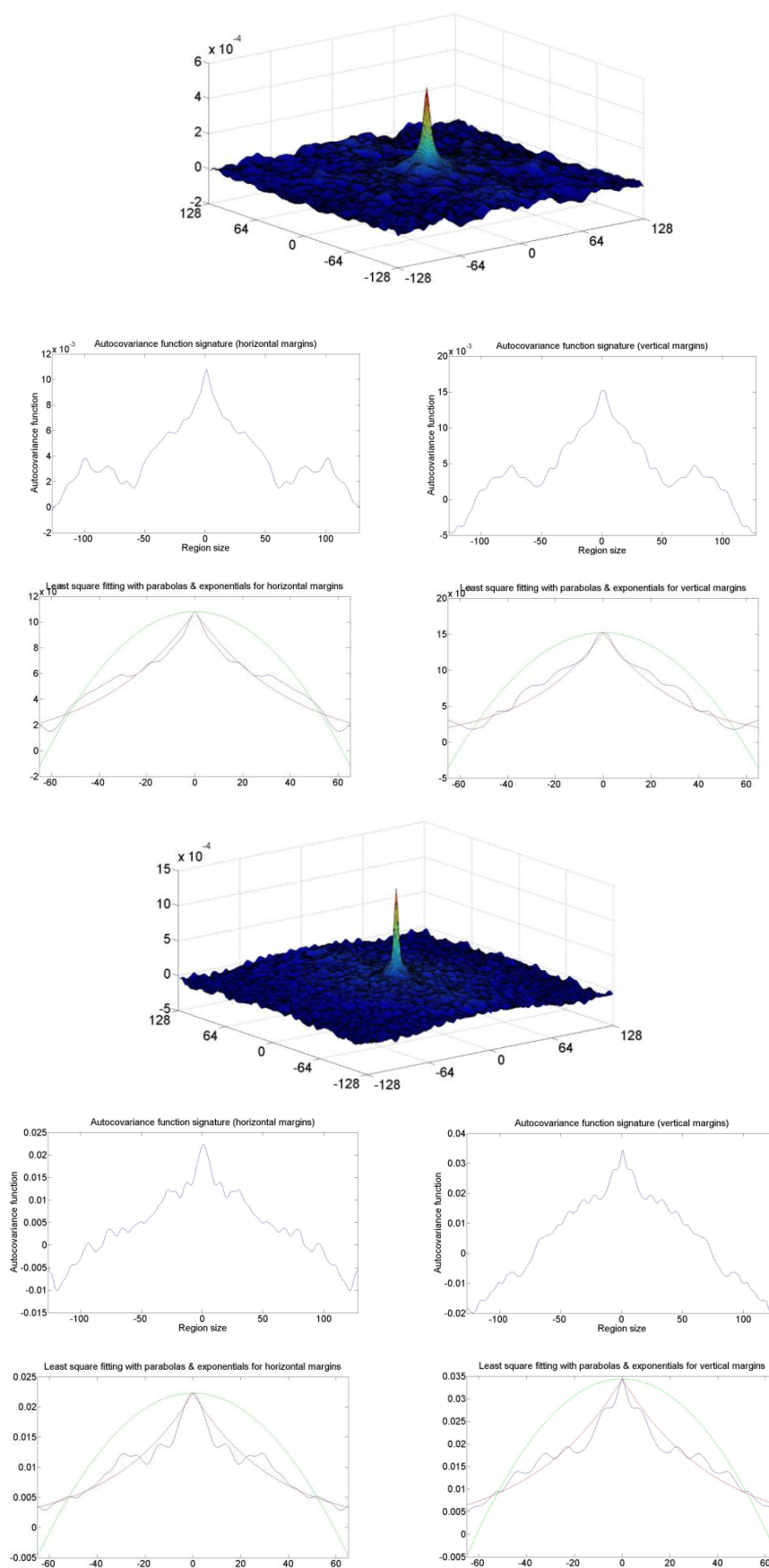


Fig. 5.13 Surface plot of normalised autocovariance functions (ACFs) referring to meningioma fibroblastic, meningothelial, psammomatous and transitional subtypes; respectively. The ACF horizontal and vertical signatures are shown in the first row beneath each ACF, whereas the second row illustrates their corresponding exponential (in red) and parabola (in green) least square fitting.

5.2.5 Features selection by correlation thresholding

All extracted features in the combined texture measures were checked for possibly highly correlated features. This process assists in removing any bias towards certain features which might afterwards affect the classification procedure. Although each texture measure tends to characterise the examined texture from a different perspective, some extracted features arise to behave similar. Another advantage is the alleviation of the curse of dimensionality of texture features [19], which will decrease the computational time and memory required.

An approach which is based on the summation of the divergence measure D_i for each feature f_i between the four different meningioma subtypes was adopted [142]. An advantage of using the divergence function for inspecting feature separability is that it places no prior assumption on class-conditional densities, and has a direct relation with Bayes error [143]. The divergence function can be defined by the following formula:

$$D_i(f_i) = \sum_{k=1}^{n_c} \sum_{l>k}^{n_c} \frac{(\sigma_{k,f_i} - \sigma_{l,f_i})^2 (1 + \sigma_{k,f_i} + \sigma_{l,f_i})}{2\sigma_{k,f_i} \sigma_{l,f_i}} \quad (5.34)$$

where n_c is the number of subtypes — four for this work — and σ_{k,f_i} and σ_{l,f_i} are the standard deviation of feature f_i for class k and l ; respectively.

Next the features are ranked in a descending order according to their corresponding divergence values and then the correlation between each pair of features is calculated. A threshold of 0.8 is set for the correlation values, considering correlation values above 0.8 to be highly correlated; therefore, if the absolute value of a certain correlation was found to be greater than the specified threshold, the feature with the lower divergence was excluded while the order of the remaining features is preserved. Moreover, independent features (i.e. correlation equal 0) are excluded as well, as they could represent simply noise. Hence, only the features that maximise the separability (i.e. with highest divergence) between the different subtypes are kept. For instance, fusing texture features extracted via CM and FD methods from the meningioma subtypes in Fig. 5.2 — listed in Table 5.5 — resulted in up to 37 different features, where each feature vector was labelled with a different index (e.g. index 1 refers to CM contrast feature acquired with 0° angle, index 2 for CM contrast 45° ... and so on). All CM features had their δ set to one, and the FD features are derived after generating an FD image for each subtype as discussed in the fractals section. These features are then ranked according to their divergence values as shown in Table 5.6. Finally a 37×37 correlation matrix is generated and the optimum features are selected by discarding highly correlated (or redundant) features that exceed the set threshold, see Table 5.7. The redundant features have very limited contribution towards adding information and are merely considered as added noise to the classifier. The features in bold in Table 5.6 are the optimised ones, which are CM MP135°, CM IDM45°, FD Lacunarity and CM ENG45°.

This procedure achieved an 89% reduction in the dimensionality of the CM & FD combined feature vector. Additionally, examining the optimised features, it also shows that extracting CM features with different directions — 45° and 135° the best for this case — rather than with a specific direction; or deriving statistics from a generated FD image, such as lacunarity, rather than simply using the mean FD value alone, creates a larger bank of features which broadens the options for selecting the best features that would give a more effective tissue representation (i.e. assisting the classifier by providing high quality features).

At the end of this stage, we will have five texture measures indicated by X_k with their selected optimum features f_{ki} , X_C is the fusion of X_k in different combinations.

$$X_C = [X_1(f_{11}, f_{12} \dots f_{1N}) | X_2(f_{21}, f_{22} \dots f_{2M}) | \dots X_k(f_{k1}, f_{k2} \dots f_{kI})] \quad (5.35)$$

Table 5.5 Labeled grey level co-occurrence matrix and fractal dimension texture features

Index	Texture features
1-4	CM contrast (0°,45°,90°&135°)
5-8	CM correlation (0°,45°,90°&135°)
9-12	CM energy (0°,45°,90°&135°)
13-16	CM entropy (0°,45°,90°&135°)
17-20	CM homogeneity (0°,45°,90°&135°)
21-24	CM dissimilarity (0°,45°,90°&135°)
25-28	CM inverse difference moment (0°,45°,90°&135°)
29-32	CM max probability (0°,45°,90°&135°)
33-37	FD (mean, variance, skewness, kurtosis & lacunarity)

Table 5.6 Sorted texture features of Table 5.5 in descending order according to corresponding divergence

Sorted texture features divergence			
Index	value	Index	value
32	4.8247	4	0.7932
16	4.6746	36	0.3330
27	4.0484	29	0.2445
11	3.9767	13	0.2268
8	3.8932	5	0.1803
3	3.5729	21	0.1627
24	3.3887	26	0.0819
19	3.3404	37	0.0797
30	2.1359	34	0.0607
14	1.9339	10	0.0446
22	1.7574	2	0.0187
6	1.5981	35	0.0131
17	1.4529	18	0.0103
25	1.3185	33	0.0099
9	1.2477	31	0.0001
1	1.0658	15	0
20	0.8399	7	0
28	0.8384	23	0
12	0.8299		

Table 5.7 Correlation matrix for the 37 different texture features listed in Table 5.6, where the optimised features are highlighted

Index	32	16	27	11	8	3	24	19	30	14	22	6	17	25	9	1	36	29	13	5	21	26	37	34	10	2	18	33	31	15	7	23	35	4	12	28	20
32	1.00	1.00	0.99	0.98	1.00	0.99	1.00	0.98	-0.99	-0.92	-0.95	-1.00	-0.91	-0.97	-0.83	-0.99	0.92	1.00	0.97	1.00	0.98	0.67	-0.16	-0.17	0.57	0.65	0.74	0.14	0.97	0.84	0.99	0.91	-0.95	0.98	0.95	0.98	0.96
16	1.00	1.00	0.99	0.98	1.00	0.99	1.00	0.99	-0.98	-0.94	-0.97	-1.00	-0.93	-0.96	-0.86	-0.99	0.92	0.99	0.98	1.00	0.98	0.63	-0.18	-0.19	0.59	0.62	0.75	0.16	0.96	0.86	0.99	0.93	-0.94	0.98	0.96	0.99	0.97
27	0.99	0.99	1.00	1.00	0.98	1.00	0.98	1.00	-0.98	-0.94	-0.97	-0.99	-0.94	-0.96	-0.88	-0.99	0.95	0.98	0.98	0.99	0.98	0.55	-0.32	-0.33	0.49	0.51	0.65	0.31	0.96	0.88	0.99	0.94	-0.97	1.00	0.98	1.00	0.98
11	0.98	0.98	1.00	1.00	0.98	1.00	0.98	1.00	-0.96	-0.96	-0.98	-0.98	-0.96	-0.95	-0.90	-0.99	0.94	0.97	0.99	0.98	0.98	0.51	-0.35	-0.36	0.51	0.48	0.66	0.33	0.95	0.91	0.99	0.96	-0.95	1.00	0.99	1.00	0.99
8	1.00	1.00	0.98	0.98	1.00	0.98	1.00	0.98	-0.99	-0.92	-0.96	-1.00	-0.91	-0.97	-0.83	-0.99	0.92	1.00	0.97	1.00	0.98	0.67	-0.14	-0.15	0.58	0.66	0.76	0.13	0.97	0.84	0.99	0.91	-0.95	0.97	0.95	0.98	0.95
3	0.99	0.99	1.00	1.00	0.98	1.00	0.98	1.00	-0.97	-0.95	-0.97	-0.99	-0.94	-0.96	-0.88	-0.99	0.95	0.98	0.98	0.99	0.98	0.54	-0.32	-0.33	0.50	0.51	0.66	0.30	0.96	0.89	0.99	0.94	-0.96	1.00	0.98	1.00	0.99
24	1.00	1.00	0.98	0.98	1.00	0.98	1.00	0.98	-0.98	-0.94	-0.97	-0.99	-0.93	-0.95	-0.86	-0.98	0.90	0.99	0.98	1.00	0.99	0.64	-0.15	-0.16	0.62	0.64	0.78	0.13	0.95	0.86	0.98	0.93	-0.93	0.98	0.96	0.98	0.96
19	0.98	0.99	1.00	1.00	0.98	1.00	0.98	1.00	-0.96	-0.96	-0.98	-0.98	-0.96	-0.94	-0.90	-0.99	0.94	0.98	0.99	0.98	0.99	0.51	-0.34	-0.35	0.52	0.48	0.67	0.31	0.95	0.91	0.99	0.96	-0.95	1.00	0.99	1.00	0.99
30	-0.99	-0.98	-0.98	-0.96	-0.99	-0.97	-0.98	-0.96	1.00	0.86	0.91	1.00	0.85	1.00	0.76	0.99	-0.96	-1.00	-0.93	-0.99	-0.94	-0.71	0.17	0.17	-0.46	-0.67	-0.66	-0.17	-1.00	-0.77	-0.99	-0.86	0.98	-0.96	-0.92	-0.97	-0.93
14	-0.92	-0.94	-0.94	-0.96	-0.92	-0.95	-0.94	-0.96	0.86	1.00	1.00	0.91	1.00	0.83	0.98	0.91	-0.81	-0.90	-0.99	-0.91	-0.98	-0.36	0.34	0.36	-0.67	-0.38	-0.75	-0.28	-0.83	-0.98	-0.91	-1.00	0.83	-0.96	-0.99	-0.95	-0.98
22	-0.95	-0.97	-0.97	-0.98	-0.96	-0.97	-0.97	-0.98	0.91	1.00	1.00	0.94	0.99	0.87	0.96	0.94	-0.85	-0.93	-1.00	-0.95	-1.00	-0.44	0.29	0.30	-0.67	-0.46	-0.77	-0.23	-0.87	-0.96	-0.94	-0.99	0.86	-0.98	-0.99	-0.97	-0.99
6	-1.00	-1.00	-0.99	-0.98	-1.00	-0.99	-0.99	-0.98	1.00	0.91	0.94	1.00	0.90	0.98	0.82	1.00	-0.95	-1.00	-0.96	-1.00	-0.97	-0.66	0.19	0.20	-0.52	-0.63	-0.70	-0.19	-0.98	-0.82	-1.00	-0.90	0.97	-0.98	-0.95	-0.98	-0.95
17	-0.91	-0.93	-0.94	-0.96	-0.91	-0.94	-0.93	-0.96	0.85	1.00	0.99	0.90	1.00	0.81	0.99	0.90	-0.81	-0.89	-0.98	-0.90	-0.98	-0.32	0.38	0.39	-0.65	-0.34	-0.72	-0.31	-0.82	-0.99	-0.90	-1.00	0.82	-0.96	-0.99	-0.95	-0.98
25	-0.97	-0.96	-0.96	-0.95	-0.97	-0.96	-0.95	-0.94	1.00	0.83	0.87	0.98	0.81	1.00	0.72	0.99	-0.97	-0.99	-0.90	-0.98	-0.90	-0.71	0.20	0.20	-0.37	-0.65	-0.59	-0.22	-1.00	-0.72	-0.99	-0.82	0.99	-0.95	-0.89	-0.95	-0.90
9	-0.83	-0.86	-0.88	-0.90	-0.83	-0.88	-0.86	-0.90	0.76	0.98	0.96	0.82	0.99	0.72	1.00	0.82	-0.73	-0.80	-0.94	-0.82	-0.93	-0.18	0.44	0.46	-0.66	-0.21	-0.69	-0.36	-0.72	-1.00	-0.82	-0.99	0.73	-0.90	-0.95	-0.89	-0.95
1	-0.99	-0.99	-0.99	-0.99	-0.99	-0.99	-0.98	-0.99	0.99	0.91	0.94	1.00	0.90	0.99	0.82	1.00	-0.97	-0.99	-0.96	-0.99	-0.96	-0.61	0.28	0.28	-0.45	-0.57	-0.63	-0.28	-0.99	-0.83	-1.00	-0.90	0.98	-0.99	-0.96	-0.99	-0.96
36	0.92	0.92	0.95	0.94	0.92	0.95	0.90	0.94	-0.96	-0.81	-0.85	-0.95	-0.81	-0.97	-0.73	-0.97	1.00	0.94	0.87	0.93	0.87	0.55	-0.41	-0.41	0.22	0.46	0.43	0.44	0.97	0.73	0.97	0.81	-0.99	0.94	0.90	0.95	0.90
29	1.00	0.99	0.98	0.97	1.00	0.98	0.99	0.98	-1.00	-0.90	-0.93	-1.00	-0.89	-0.99	-0.80	-0.99	0.94	1.00	0.95	1.00	0.96	0.69	-0.17	-0.17	0.51	0.65	0.70	0.16	0.99	0.81	0.99	0.89	-0.97	0.97	0.94	0.98	0.95
13	0.97	0.98	0.98	0.99	0.97	0.98	0.98	0.99	-0.93	-0.99	-1.00	-0.96	-0.98	-0.90	-0.94	-0.96	0.87	0.95	1.00	0.96	1.00	0.48	-0.28	-0.29	0.64	0.49	0.76	0.23	0.90	0.95	0.96	0.98	-0.89	0.98	0.99	0.98	0.99
5	1.00	1.00	0.99	0.98	1.00	0.99	1.00	0.98	-0.99	-0.91	-0.95	-1.00	-0.90	-0.98	-0.82	-0.99	0.93	1.00	0.96	1.00	0.97	0.67	-0.16	-0.17	0.55	0.65	0.73	0.15	0.98	0.83	0.99	0.90	-0.96	0.98	0.95	0.98	0.95
21	0.98	0.98	0.98	0.98	0.98	0.98	0.99	0.99	-0.94	-0.98	-1.00	-0.97	-0.98	-0.90	-0.93	-0.96	0.87	0.96	1.00	0.97	1.00	0.52	-0.24	-0.25	0.66	0.52	0.78	0.19	0.91	0.94	0.96	0.98	-0.89	0.98	0.98	0.98	0.99
26	0.67	0.63	0.55	0.51	0.67	0.54	0.64	0.51	-0.71	-0.36	-0.44	-0.66	-0.32	-0.71	-0.18	-0.61	0.55	0.69	0.48	0.67	0.52	1.00	0.52	0.52	0.38	0.98	0.61	-0.47	0.71	0.19	0.62	0.33	-0.63	0.50	0.40	0.52	0.42
37	-0.16	-0.18	-0.32	-0.35	-0.14	-0.32	-0.15	-0.34	0.17	0.34	0.29	0.19	0.38	0.20	0.44	0.28	-0.41	-0.17	-0.28	-0.16	-0.24	0.52	1.00	1.00	0.33	0.62	0.35	-0.99	-0.20	-0.44	-0.27	-0.38	0.32	-0.36	-0.41	-0.35	-0.39
34	-0.17	-0.19	-0.33	-0.36	-0.15	-0.33	-0.16	-0.35	0.17	0.36	0.30	0.20	0.39	0.20	0.46	0.28	-0.41	-0.17	-0.29	-0.17	-0.25	0.52	1.00	1.00	0.31	0.62	0.33	-0.98	-0.20	-0.45	-0.28	-0.39	0.32	-0.37	-0.42	-0.35	-0.40
10	0.57	0.59	0.49	0.51	0.58	0.50	0.62	0.52	-0.46	-0.67	-0.67	-0.52	-0.65	-0.37	-0.66	-0.45	0.22	0.51	0.64	0.55	0.66	0.38	0.33	0.31	1.00	0.53	0.96	-0.44	0.38	0.66	0.45	0.66	-0.29	0.50	0.55	0.50	0.56
2	0.65	0.62	0.51	0.48	0.66	0.51	0.64	0.48	-0.67	-0.38	-0.46	-0.63	-0.34	-0.65	-0.21	-0.57	0.46	0.65	0.49	0.65	0.52	0.98	0.62	0.62	0.53	1.00	0.72	-0.59	0.65	0.22	0.57	0.35	-0.55	0.47	0.39	0.49	0.41
18	0.74	0.75	0.65	0.66	0.76	0.66	0.78	0.67	-0.66	-0.75	-0.77	-0.70	-0.72	-0.59	-0.69	-0.63	0.43	0.70	0.76	0.73	0.78	0.61	0.35	0.33	0.96	0.72	1.00	-0.43	0.59	0.69	0.64	0.73	-0.51	0.65	0.67	0.65	0.67
33	0.14	0.16	0.31	0.33	0.13	0.30	0.13	0.31	-0.17	-0.28	-0.23	-0.19	-0.31	-0.22	-0.36	-0.28	0.44	0.16	0.23	0.15	0.19	-0.47	-0.99	-0.98	-0.44	-0.59	-0.43	1.00	0.21	0.35	0.27	0.31	-0.34	0.33	0.36	0.32	0.35
31	0.97	0.96	0.96	0.95	0.97	0.96	0.95	0.95	-1.00	-0.83	-0.87	-0.98	-0.82	-1.00	-0.72	-0.99	0.97	0.99	0.90	0.98	0.91	0.71	-0.20	-0.20	0.38	0.65	0.59	0.21	1.00	0.73	0.99	0.82	-0.99	0.95	0.89	0.96	0.90
15	0.84	0.86	0.88	0.91	0.84	0.89	0.86	0.91	-0.77	-0.98	-0.96	-0.82	-0.99	-0.72	-1.00	-0.83	0.73	0.81	0.95	0.83	0.94	0.19	-0.44	-0.45	0.66	0.22	0.69	0.35	0.73	1.00	0.83	0.99	-0.73	0.91	0.96	0.89	0.95
7	0.99	0.99	0.99	0.99	0.99	0.99	0.98	0.99	-0.99	-0.91	-0.94	-1.00	-0.90	-0.99	-0.82	-1.00	0.97	0.99	0.96	0.99	0.96	0.62	-0.27	-0.28	0.45	0.57	0.64	0.27	0.99	0.83	1.00	0.90	-0.98	0.99	0.96	0.99	0.96
23	0.91	0.93	0.94	0.96	0.91	0.94	0.93	0.96	-0.86	-1.00	-0.99	-0.90	-1.00	-0.82	-0.99	-0.90	0.81	0.89	0.98	0.90	0.98	0.33	-0.38	-0.39	0.66	0.35	0.73	0.31	0.82	0.99	0.90	1.00	-0.82	0.96	0.99	0.95	0.98
35	-0.95	-0.94	-0.97	-0.95	-0.95	-0.96	-0.93	-0.95	0.98	0.83	0.86	0.97	0.82	0.99	0.73	0.98	-0.99	-0.97	-0.89	-0.96	-0.89	-0.63	0.32	0.32	-0.29	-0.55	-0.51	-0.34	-0.99	-0.73	-0.98	-0.82	1.00	-0.95	-0.90	-0.96	-0.91
4	0.98	0.98	1.00	1.00	0.97	1.00	0.98	1.00	-0.96	-0.96	-0.98	-0.98	-0.96	-0.95	-0.90	-0.99	0.94	0.97	0.98	0.98	0.98	0.50	-0.36	-0.37	0.50	0.47	0.65	0.33	0.95	0.91	0.99	0.96	-0.95	1.00	0.99	1.00	0.99
12	0.95	0.96	0.98	0.99	0.95	0.98	0.96	0.99	-0.92	-0.99	-0.99	-0.95	-0.99	-0.89	-0.95	-0.96	0.90	0.94	0.99	0.95	0.98	0.40	-0.41	-0.42	0.55	0.39	0.67	0.36	0.89	0.96							

5.2.6 Pattern classification technique

A simple —also called naïve — Bayesian classifier (NBC) was applied for measuring the performance. A NBC in supervised learning is considered optimal if all attributes are independent given the class. Despite the fact that this condition might not be frequent in practice, this fast and simple classifier was reported to perform well even with the presence of strong attribute dependence [144].

The Bayesian decision rule classifies an observation to the class having the highest probability, for which the NBC can be represented in a set of discriminant functions as:

$$d_i(X) = P_i(C_i|X) = \frac{P(X|C_i)P(C_i)}{P(X)} \quad i = 1, 2, \dots, K \quad (5.36)$$

where $P(C_i|X)$ is the *a posteriori* probability of assigning class i given feature vector X , $P(X|C_i)$ is the probability density function (PDF) of X within the i^{th} class C_i for a total number of K classes, $P(C_i)$ and $P(X)$ are the *a priori* probability of class C_i and feature vector X ; respectively. Since $P(X)$ does not depend on C_i therefore it can be ignored, and the discriminant functions can be defined as:

$$d_i(X) = \log P(X|C_i) + \log P(C_i) \quad (5.37)$$

The classifier assigns a feature vector X to class C_i if $d_i(X) > d_j(X)$ for all $j \neq i$ after assuming an n -dimension (multivariate) normal PDF having the form

$$P(X|C_i) = \frac{1}{(2\pi)^{n/2} |\Sigma_i|^{1/2}} \exp \left[-\frac{1}{2} (X - \mu_i)^T \Sigma_i^{-1} (X - \mu_i) \right] \quad (5.38)$$

where Σ_i and μ_i are the covariance matrix and mean vector of feature vector X of class C_i ; $|\Sigma_i|$ and Σ_i^{-1} are the determinant and inverse of the covariance matrix; and $(X - \mu_i)^T$ is the transpose of $(X - \mu_i)$. Substituting the Gaussian PDF in eqn. (5.37), it is easy to show that the discriminant functions yields

$$d_i(X) = \log P(C_i) - \frac{1}{2} \left(\log |\Sigma_i| + (X - \mu_i)^T \Sigma_i^{-1} (X - \mu_i) \right) \quad (5.39)$$

The 320 samples which refer to 20 patients were equally divided into four diagnostic groups (i.e. the four meningioma subtypes), each group consists of 80 samples extracted from five different patients (16 each) diagnosed with the same meningioma tumour subtype. Since the number of image subsets is not small, a holdout validation approach was used for validation of classification, by randomly selecting four patients from each group for training and the remaining for testing.

5.3 Experimental results

5.3.1 Colour channel selection

The results of the Bhattacharya distance which specifies the segmentation quality for the three colour channels of the four meningioma subtypes are shown in Table 5.8, with the smallest (i.e. most separable) values in bold. All of the meningioma subtypes except the fibroblastic had a better segmentation quality using the blue colour channel.

Table 5.8 Assessing classification quality for each colour channel

Meningioma type	Red	Green	Blue
Fibroblastic	0.0010	0.0082	0.0161
Meningothelial	0.0066	0.0032	0.0020
Psammomatous	0.1261	0.2045	0.1250
Transitional	0.0016	0.0081	0.0011

Colour channel selection was reflected in the classification accuracies for the texture measures. Table 5.9 shows the RLM RGB colour channel classification accuracy for the four meningioma subtypes, with the blue channel achieving the highest overall. Similar results were obtained for the rest of the used texture measures, for succinctness they are not presented here.

Table 5.9 The RGB colour channels classification accuracies for the RLM texture measure

Meningioma type	Red	Green	Blue
Fibroblastic	80.00%	95.00%	90.00%
Meningothelial	95.00%	80.00%	75.00%
Psammomatous	80.00%	90.00%	85.00%
Transitional	70.00%	50.00%	85.00%
Overall accuracy	81.25%	78.75%	83.75%

5.3.2 Individual and combined classification accuracies

Testing classification accuracies for each of the individual textures and in different combinations are as shown in Table 5.10 and 5.11; respectively. These results represent the morphological gradient images of the blue colour component meningioma images for all four subtypes. The ACF method was excluded from all subsequent analysis as it recorded a very low discrimination of 27.81%.

When selectively combining certain texture features, the classification accuracy would increase above the highest achieved if an individual texture features method was used alone. For example, Table 5.10 shows the overall classification accuracies if the extracted texture features would be used individually (i.e. without combining them with each other). The RLM texture feature achieved the highest overall accuracy by 83.75%. Yet, when fusing the texture features with each other, and in all possible combinations, some combination improved the overall accuracy up to 92.50% as in the GMRF & RLM paired features (as shown in Table 5.11). By taking the RLM classification accuracy from Table

Table 5.10 Individual texture features testing classification accuracy of the blue colour component of meningioma images

Meningioma type	FD	RLM	CM	GMRF
Fibroblastic	35.00%	90.00%	75.00%	70.00%
Meningothelial	50.00%	75.00%	75.00%	90.00%
Psammomatous	75.00%	85.00%	90.00%	70.00%
Transitional	65.00%	85.00%	80.00%	80.00%
Overall accuracy	56.25%	83.75%	80.00%	77.50%

Table 5.11 Classification accuracy of extracted texture features in different combinations ranked in descending order

Texture features	Fibroblastic	Meningothelial	Psammomatous	Transitional	Overall accuracy
GMRF&RLM	90.00%	95.00%	90.00%	95.00%	92.50%
GMRF&FD&RLM	80.00%	80.00%	90.00%	100.00%	87.50%
RLM&FD	80.00%	80.00%	90.00%	95.00%	86.25%
GMRF&FD&CM	90.00%	75.00%	90.00%	85.00%	85.00%
GMRF&CM	80.00%	75.00%	85.00%	85.00%	81.25%
GMRF&RLM&CM	70.00%	90.00%	85.00%	80.00%	81.25%
RLM&CM	60.00%	95.00%	85.00%	80.00%	80.00%
RLM&FD&CM	80.00%	90.00%	80.00%	80.00%	80.00%
GMRF&RLM&FD&CM	80.00%	70.00%	90.00%	80.00%	80.00%
FD&CM	80.00%	75.00%	90.00%	70.00%	78.75%
GMRF&FD	70.00%	70.00%	90.00%	70.00%	75.50%

Table 5.12 Optimum features for the top four texture combination features in Table 5.11 which improved the classification accuracy beyond the set threshold

Texture features	Index	Divergence	Optimum features
GMRF&RLM (51) ^d	5	1.8543	RLM LRE0°
	49	0.0011	GMRF s_{xy} ;5
	51	0.0008	GMRF σ
	36	0.0001	RLM SRHGLE135°
GMRF&FD&RLM (56)	5	1.8543	RLM LRE0°
	49	0.0011	GMRF s_{xy} ;5
	51	0.0008	GMRF σ
	36	0.0001	RLM SRHGLE135°
	52	0.0000	FD mean
RLM&FD (49)	5	1.8543	RLM LRE0°
	26	0.0001	RLM HGLRE45°
	36	0.0001	RLM SRHGLE135°
	45	0.0000	FD mean
	29	0.0000	RLM SRGLE0°
GMRF&FD&CM (44)	32	1.7274	CM MP135°
	37	1.0535	GMRF s_{xy} ;5
	39	0.8265	GMRF σ
	43	0.4548	FD kurtosis
	26	0.0722	CM IDM45°

5.10 and setting it as a threshold – as it achieved the highest in case if each texture feature was used individually – then we can see that the first four rows in Table 5.11 for the combined texture feature improved the accuracy. To investigate the significance of the results, a Wilcoxon signed-rank test – a

^d Number between brackets indicates the total number of combined texture features before optimum feature selection

nonparametric alternative to the paired t-test – was applied to determine the significance between the texture measure combinations that improved the overall accuracy and the individual approaches. The test shows there is a statistical significant difference on a significance level of 0.05 (i.e. $p < 0.05$).

The optimum texture features for each of the texture features combinations that improved the classification accuracy are ranked according to their divergence power and listed in Table 5.12. For completeness, the confusion matrix for the best combination (RLM & GMRF) is given in Table 5.13.

Table 5.13 Four class meningioma classification confusion matrix for the combined GMRF and RLM texture measures

Meningioma type		Classification			
		Fibroblastic	Meningothelial	Psammomatous	Transitional
True class	Fibroblastic	90%	5%	0%	0%
	Meningothelial	0%	95%	0%	5%
	Psammomatous	0%	0%	90%	0%
	Transitional	10%	0%	10%	95%

5.3.3 Morphological processing

A comparison between morphological and non-morphological processing effect on the image classification accuracy is shown in Fig. 5.14. All MP texture measures except FD witnessed an increase in the overall classification accuracy. We chose to go forward with the morphological gradient option as the FD gave the least classification accuracy as compared to the rest of the texture measures.

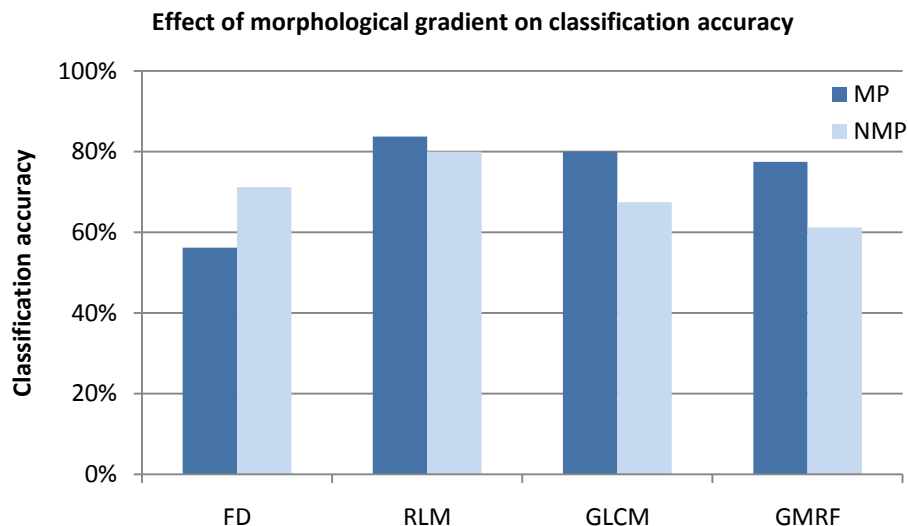


Fig. 5.14 Individual texture measures' classification accuracy for morphologically processed (MP) and non-morphologically processed (NMP) of the four class meningioma images

5.4 Texture measures behaviour analysis

5.4.1 Relevance to histopathological texture

To explain why certain combinations of texture features used in this work tend to work better, we applied the highest three texture features that improved the overall accuracy to a set of 15 different generated images having jelly-bean shapes resembling in analogy the shape of the cell nuclei in the meningioma images (see Fig. 5.15). These pseudo-cell nuclei images start with a specific number of similar shapes in the first image, and then increase gradually by an amount equivalent to the number of shapes in the first image, until reaching the last image in the set. By this, we intend to see how the performance of each texture measure is affected as the frequency of the examined structure changes. Then the morphological gradient is computed for each of these images as was done with the real meningioma images.

In reality, the different images of a certain type of meningioma do not necessarily have an identical structure or the same number of cell nuclei. Thus, it is interesting to know how the applied texture measures cope with this situation and how their performance is affected. Hence one can better understand why certain combinations might work better.

The variation is assessed by measuring the mean (μ) and standard deviation (σ) of the extracted texture features and then representing them by the ratio σ/μ which would reflect the susceptibility of the examined texture measure to the increase and decrease of the frequency (i.e. denseness) of the examined structure. Clausi et al studied the effect of Gaussian additive noise on Gabor filters and CM texture features together, they showed that CM is less susceptible to noise as compared to Gabor filter [110]. Yet we use this ratio first to investigate the structure denseness impact on the used texture measures, and then in the next subsection the noise effect is presented.

As explained in the feature extraction section, the RLM was represented by 11 features, GMRF by 7 and the FD by 5, so the ratio σ/μ would represent the joint effect of all extracted features relevant to each texture measure after excluding highly correlated features. That is, the optimum features that improved the overall accuracy in Table 5.12 for GMRF, RLM and FD when combined were normalised and then plotted. Fig. 5.16 represents the value of the ratio σ/μ for each of the 15 generated images, which is interpreted as the lower the ratio the less susceptible the texture measure. It is noticed that the GMRF extracted features are nearly uniform throughout the image set, with a very slight increase in the variation as frequency increases. On the contrary, the RLM and FD show more susceptibility in low frequencies and are less susceptible in the high frequency as compared to GMRF. It is also shown that the RLM performs better in the low and high frequencies as compared to FD, while the FD is more stable in the mid range frequencies. Although the RLM and GMRF had two optimum features (RLM LRE0° & RLM SRHGLE135° and GMRF sxy;5 & GMRF σ), there was no

difference when either of the optimum features used for variability assessment; in other words, all gave the same results as in Fig. 5.16.

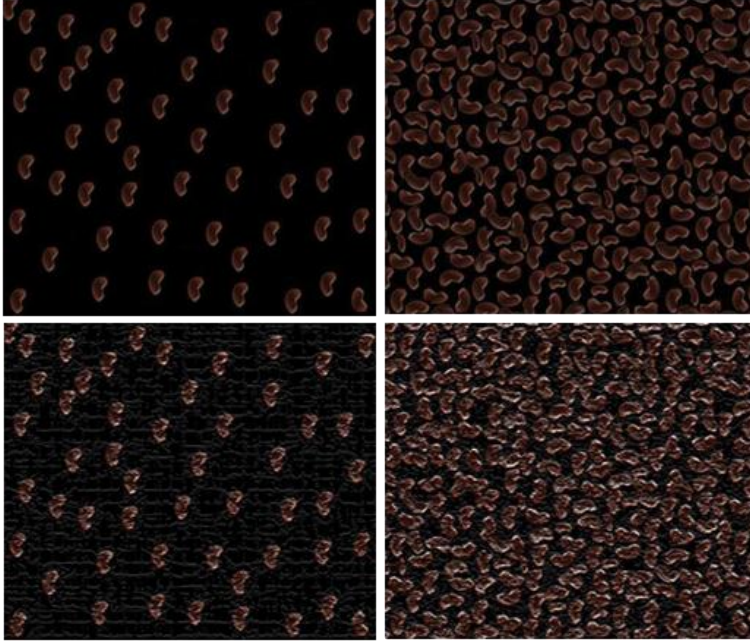


Fig. 5.15 The first row is the initial and final images in the 15 generated pseudo-cell nuclei images to test texture measures susceptibility to variation in shape frequency, the second row is the corresponding distorted images.

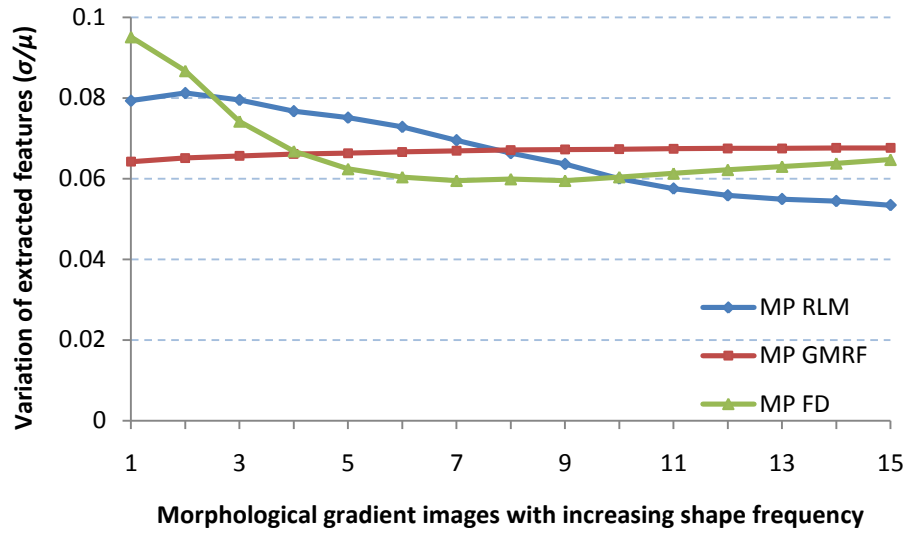


Fig. 5.16 Susceptibility of RLM, GMRF and FD texture measures to 15 morphologically processed pseudo-cell nuclei images with increasing shape frequency.

5.4.2 Simulation of noise impact on extracted features

To study the impact of noise on the meningioma images, distortion having an effect resembling fine cracks or craquelures which appear on old paintings was applied to 15 pseudo-cell nuclei images (see

Fig. 5.15). As the most probable noise to affect the histopathological images in the process of preparation is the cracks in the biopsy sample which is most obvious as the white regions in the psammomatous meningioma images in Fig. 5.2. A 1-D horizontal cross section in a pseudo-cell nuclei image before and after noise distortion is shown in Fig. 5.17.

Although the applied morphological gradient eliminates the background – including the white cracks in the image sample (see upper right corner of Fig. 5.5) – to extract the general cell nuclei structure, these cracks can still alter the general shape that a certain type of meningioma cell nuclei should take.

Analysing the susceptibility of the texture measures as shown in Fig. 5.18, the GMRF was the least affected by the added noise as it gave nearly a uniform response throughout all images. The RLM and FD behaved oppositely to each other in response to noise in a monotonically decreasing/increasing fashion, respectively. In a way, RLM is less susceptible to noise in high shape frequency of occurrence; vice versa for FD. Therefore the response of each texture measure somehow depends on the structure that the noise affects. For example if the noise occurs in dense image structures, the RLM measure could produce a more reliable estimate as compared to the other measures. We can also see that roughly similar noise susceptance is produced in between image 7 and 8 for all three texture measures.

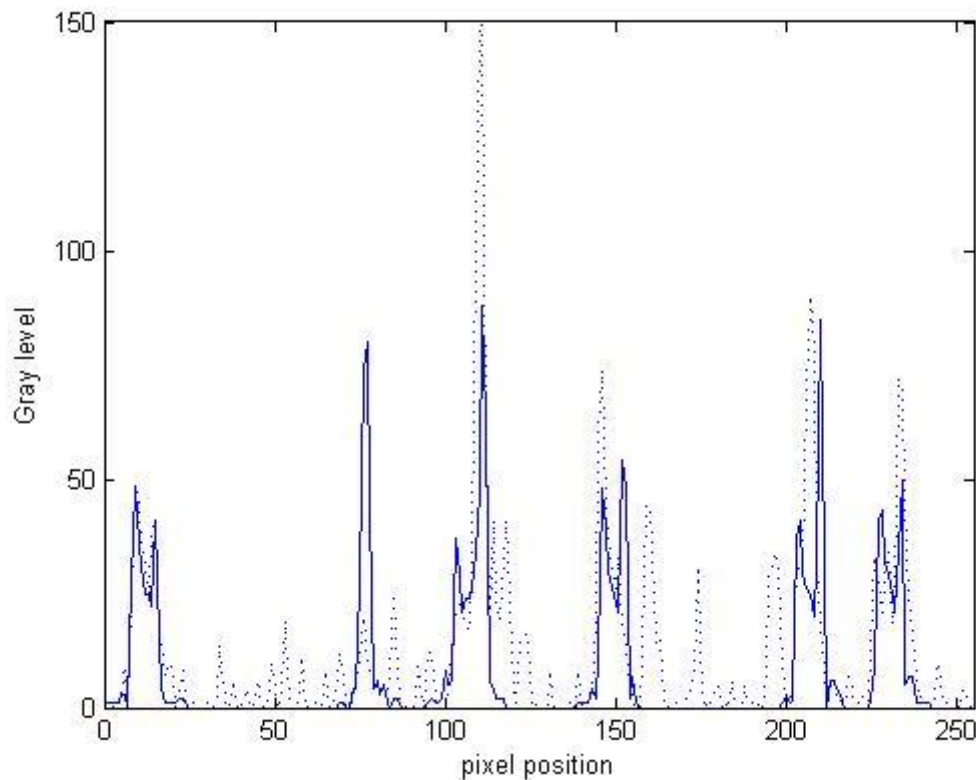


Fig. 5.17 One dimensional horizontal gray-level profile along the first pseudo-cell nuclei image, the dotted line indicates the profile of the effect of added craquelures distortion.

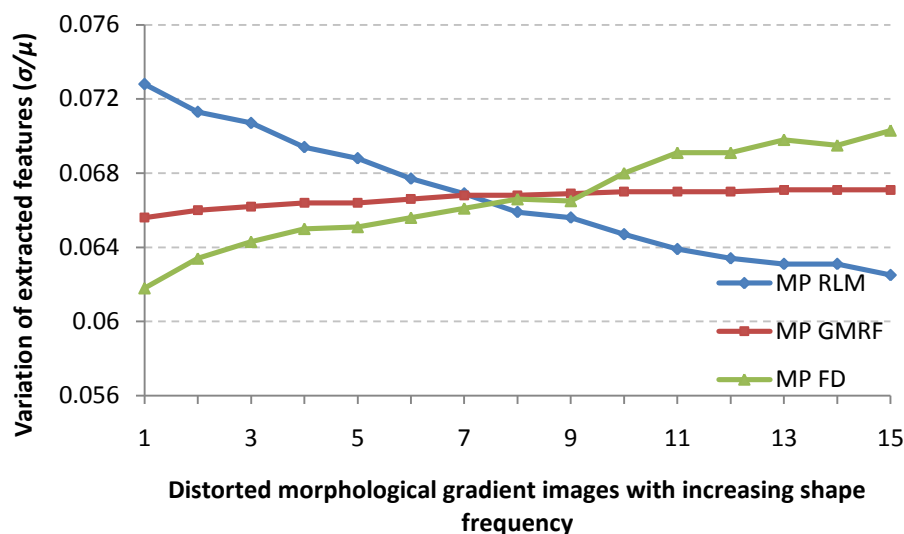


Fig. 5.18 Effect of noise distortion on texture measures applied to images in Fig. 5.2.

5.5 Discussion

The main objective was to improve meningioma histopathological image classification accuracy to overcome inter-and- intra-observer variations in human reported diagnosis. The technique exploits the physiological structure of the cell nuclei with five different texture measures, and tries to find the best combination that maximises the difference in-between the meningioma subtypes.

It was shown that the choice of colour channel can increase or decrease the classification accuracy, in terms of which better defines the borders of the region of interest – the cell nuclei in our case – from the background. The quality of segmentation performed on a sample image from each subtype favoured the blue colour channel for three of the four subtypes. This is due to the dyes used in staining the meningioma biopsies which gave the cell nuclei a purple colour and the background (i.e. cytoplasm) a pink colour, where the better segmentation performance can be interpreted as the dominance of blue component in the purple colour which consists mainly of mixtures of blue and red. Usually the fibroblastic subtype is harder to differentiate from other subtypes [145]; furthermore, the relatively small size and the faint colour of some of the fibroblastic cell-nuclei as compared to the other subtypes contributed towards giving the red colour channel a better separability. Yet, the subtypes overall classification results showed that the blue colour channel was the best for all subtypes.

Also it was shown that combining more than one texture measure instead of using just one might improve the overall accuracy. Different texture measure tends to extract different features each capturing alternative characteristics of the examined structure. The two model and statistical-based

texture measures (GMRF and RLM) improved the overall accuracy up to 92.50% with none of the classified meningioma subtypes achieving below 90.00%. As indicated in the confusion matrix, we see that all misclassified subtypes are related only to a single other subtype (e.g. fibroblastic and psammomatous subtypes were always misclassified as transitional). The misclassification occurs mainly due to non-homogeneity of the cell nuclei structure for the prepared biopsies. Another reason is in the subdivision of each of the 1024x1024 pixel images to four quadrants (i.e. subsets), the shape of the structure in some of the four 512x512 pixel quadrants and with the possible presence of some biopsy preparation cracks in that quadrant, might not be sufficient to capture the original subtype cell-nuclei shape, and hence be more probable to be misclassified. In addition, the reduction in the dimensionality of the feature vector was essential in improving the classification accuracies as well. Only four out of the 51 features which resulted from the GMRF & RLM combination was required, and five features from the each of the GMRF&FD&RLM, RLM&FD and GMRF&FD&CM combinations which initially had 56, 49, and 44 features; respectively.

Nevertheless, using a combination of multiple texture measure does not necessarily guarantee a better accuracy, even with the removal of highly correlated features. All four texture measures combined – appearing in the ninth row of Table 5.11 – gave an 80%, degrading the overall classification accuracy below the 83.75% set threshold. Meaning fewer (paired) texture measures could best characterises the examined texture and produce far better classification results in a shorter CPU processing time.

Moreover, classification results suggest that taking the morphological gradient for the histopathological images would serve most texture measures' capability to capture tissue characteristics, yet the stability of the texture measures' response varies depending on the examined structure shape denseness. By studying the variation of the texture measure features as the number of cell-nuclei increases, the GMRF was nearly uniform, while the RLM and FD performed better in the high frequencies. That is, in the GMRF and RLM combined, the RLM is less affected (i.e. the variation of the normalised features is less as compared to GMRF features) if the number of cell-nuclei increase suddenly in on of the examined samples above the expected average, which will assist in classifying it correctly. In a way, they compensate for each others weaknesses.

Varying amounts and types of noise is inevitable in medical imaging which will have some effect on used texture measures [2]. Fine cracks in the tissue biopsies are a major source of noise that can affect histopathological images. The texture measures' response to additive texture distortion noise while varying cell-nuclei shape densities was studied. The GMRF was the least affected, yet the RLM and FD performed better in high and low shape frequency; respectively.

A limitation of the proposed meningioma classification technique is that segmentation separability assessment is required in order to select the optimum colour channel, yet we need this process only once (i.e. before training).

5.6 Conclusion

A technique for histopathological meningioma tumour classification based on texture measures combination has been proposed in this chapter. The morphological gradient of the RGB colour channel that best discriminates the cell-nuclei from the cytoplasm background is selected, and then feature extraction is performed by four statistical and model-based texture measures for discrimination using a Bayesian classifier. The pre-processing phase represented by the appropriate colour channel selection and morphological processing proved it was necessary for increasing texture feature separability, and hence can improve classification accuracy.

It can be concluded that certain selected texture measures play a complementary role to each other in the process of quantitative texture characterisation. In other words, a certain texture measure can represent a pattern better than another depending on the region of interest frequency of occurrence and noise in the examined structure. This also applies to certain combinations which might outperform other texture measure fusions. However, combining more than two texture measure would not necessarily give a better accuracy even with the removal of highly correlated features. This will increase feature complexity, hence having a negative effect on the classifiers performance. It was found that the combination of the GMRF and RLM texture measures are the best for characterizing meningioma subtypes of grade I, these two measures outperformed other measures in the study individually and combined. Furthermore, it would be interesting to test the compatibility of the suggested meningioma classification approach to discern in-between subtypes and/or grades of other similar histopathological diseases.

Chapter 6

MULTIRESOLUTION VIA WAVELET TRANSFORM AND GABOR FILTERS

Preview

With the heterogeneous or non-stationary nature of medical texture, using a single resolution approach for optimum classification might not suffice. In contrast a multiresolution wavelet packet analysis approach can decompose the input signal into a set of frequency subbands giving the opportunity to characterise the texture structure at the appropriate frequency channel. We propose an adaptive best bases algorithm for optimal bases selection for meningioma histopathological images, applying the fractal dimension (FD) as the bases selection criterion in a tree-structured manner. Thereby, the most significant subband that better identifies texture discontinuities will only be chosen for further decomposition, and its fractal signature would represent the extracted feature vector for classification. The best basis selection using the FD outperformed the energy based selection approach, achieving an overall classification accuracy of 91.25% as compared to 83.44% and 73.75% for the co-occurrence matrix and energy texture signatures; respectively. Another multiresolution approach was used as well, applying this time Gabor filters for feature extraction. The Gabor filter energy output of each magnitude response was combined with four other mono-resolution texture signatures — half model based and the other half statistical based — with and without cell nuclei segmentation. The highest classification accuracy of 95.00% was reached when combining the Gabor filters' energy and the meningioma subimage fractal signature as a feature vector without performing any prior segmentation. This shows that the use of the FD with wavelet packet transform and Gabor filters assists in achieving an optimum classification.

6.1 Introduction

The main concern in texture analysis is how to capture distinctive characteristics that will maximise the difference in-between the analysed images and subsequently facilitate the pattern classifier's mission. Each feature extraction method has its own unique trend for detecting discontinuities in image texture, yet its efficiency is determined by how they formulate the relationship between primary image elements.

Feature extraction can be categorised into single (or mono) and multiple resolution approaches. Despite the simplicity that mono-resolution texture analysis techniques (e.g. co-occurrences, run-length, autocorrelation...etc) provide, a limitation resides in their characterisation of texture from a single perspective — at a certain scale or fixed resolution level — discarding other possibilities which might have a better discriminative capability at a different scale. A multiresolution analysis

decomposes the input signal into a set of frequency bands to investigate a particular object at various spatial-frequency scales. This was initially inspired from how the human visual system (HVS) discerns objects, and multiresolution texture analysis techniques for pattern recognition applications are benchmarked according to their ability to mimic the HVS. The area of the brain responsible for processing visual stimuli is called the visual cortex which is located at the lower rear of the brain. Neurons in this area of the HVS respond to visual information through a set of mechanisms, each of which is tuned to a specific spatial frequency and orientation [146]. Psychophysiological research findings showed that the visual cortex of the human visual system can be modeled as a set of tuned independent channels with specific frequency and orientation [11]. There are a number of studies in the literature that used band-pass filter banks for mathematical modeling of visual cortex cells [12, 147-150]. The robustness and efficiency of the HVS in texture discrimination motivated many researchers in modeling human perception for improving computerised pattern recognition techniques; especially for texture discrimination and segmentation [13, 14, 151-153]. The feasibility of multiresolution models using wavelet transform coefficients and Gabor filters has then attracted considerable attention for many biomedical applications related to medical imaging. A review on applications of wavelets in biomedical image processing can be found in [154, 155], and a coverage of Gabor filter utilisation in various medical imaging modalities is presented in [156].

Medical texture is known to be heterogeneous, and a varying degree of texture heterogeneity exists whether the acquisition of the medical image was performed on a micro-scale (e.g. imaging by computed tomography (CT), magnetic resonance (MR), ultrasound, etc) having a tissue level view composed mainly from vessels and surrounding fluids, or on a macro-scale (e.g. microscopic images) where the texture is defined by the characteristics of the organ cells. Textures of the latter are considered less homogeneous due to the relative large size of the textons — the principal elements that form the texture— which is represented by the cells in this case. The non-stationary nature of medical image texture hinders the ability for an effective automated classification from a mono-resolution viewpoint, and image pre-processing prior to feature extraction might not be sufficient. On the other hand, viewing texture from a multiresolution perspective can filter out irrelevant features and distorting noise while simultaneously giving more emphasis on the features which contribute to better subtype distinction. Techniques such as wavelet transform coefficients and Gabor filters can also break down textures' statistical complexity to distinguish between different texture regions, and their high sensitivity to local features facilitates the processes of preattentive or subtle texture discrimination as well [13]. Furthermore, according to the uncertainty principle, the wavelet transform and Gabor function can achieve an optimal joint spatial-frequency localisation (i.e. simultaneously maintain a good boundary accuracy and frequency response) [157].

Wavelet packets (WPs) are a generalised framework of the multiresolution analysis and comprise all possible combination of subbands decomposition. However, it is unwieldy to use all frequency

subbands for texture characterisation as not all of them have the same discriminating power, and inclusion of weak subbands (i.e. subbands which do not effectively represent the texture structure) would have a negative impact on the classifier's performance. Whereas using an exhaustive search would be computationally expensive as the number of decomposition levels grows higher. Therefore an adaptive approach is required for selection of the basis with prominent discriminating power. The selection criteria can be done in two ways, either by selecting the best bases from a library of WPs or in a tree-structured approach. Coifman and Wickerhauser proposed to choose the best basis which gave the most compact representation after transforming the signal into different WP bases [158]. The entropy was used as the cost function for selection of the decomposition levels, where the subband that minimises the cost function, from a comparison between the nodes and its leaves in the WP decomposition tree, was considered the optimal choice. By extending the additive cost function in [158] to an arithmetic hence a geometric mean, Dansereau et al proposed a generalised Rényi entropy for best basis search [159], allowing for different moment orders and inclusion of possible incomplete probabilities in the search as well. Saito et al estimated the probability density of each class in each coordinate in the WP and local trigonometric bases, then applied the Kullback–Leibler divergence (relative entropy) as a distance measure among the densities for selection of the most M discriminating coordinates [160]. While Rajpoot compared the discrimination energy between the subbands by using four different distance metrics [161]. The Kullback-Leibler divergence, Jensen-Shannon divergence, Euclidean distance, and Hellinger distance were used to assess the dissimilarities in-between the WPs for selection of the most discriminant bases. Others excluded the set of frequency subbands whose energy signatures showed a degree of dependence identified by mutual information [162]. Another related work was based on best clustering bases, wherein clustering basis functions are selected according to their ability to separate the fMRI time series into activated and non-activated clusters [163]. The basis that concentrates the most discriminatory power on a small number of basis functions is selected. On the other hand, a tree-structured technique for best basis selection was proposed by Chang and Kuo, where only the subbands with the highest energy are selected for further decomposition [164]. An averaged l_1 – norm was used as the energy function for location of the dominant frequency channels, and decomposition is stopped if subbands' energy is less than a factor of the maximum energy at that resolution level. Acharyya and Kundu used M-band WP decomposition, giving M^{2^J} possible bases for each level J . This approach results in a large number of subbands, therefore they adopted the tree-structure approach by decomposing the subbands whose energy value are larger by a factor than the total energy of all subbands at the same resolution [165]. While the work in [166] maximised the Fisher's distance in-between the tree-structured decomposed subbands.

In this work a different approach for best basis selection for the processes of histopathological meningioma classification is proposed. The fractal dimension (FD) is used for guiding the subband

tree-structure decomposition instead of energy which is highly dependent on the subband intensity. The motivation to use such texture measure, besides its scale invariance or the capability to investigate self-similarity, is its surface roughness estimation that can be used to detect variance in cell nucleus structure orientation and size for differentiating between meningioma subtypes. Fractal analysis for the purpose of tumour discrimination at a micro-scale was proven to be successful in numerous studies related to various medical imaging modalities as in CT [1], X-ray [83], MR [167], and US [80]. This work takes advantage of FD in diagnosing medical texture, and applies it at a macro-scale for images acquired by the microscopy modality. Also with the large size of the meningioma images (512 x 512 pixels), the tree-structure was favoured to reduce computational time to explore the full texture characteristics at deeper levels, as an overcomplete dyadic wavelet transform was used holding the size of the transformed image to be the same as the original image without any down-sampling.

Features are derived from wavelet and Gabor coefficients as they cannot be used explicitly for texture analysis due to their high variability within the analysed texture. Texture signatures such as entropy or local energy [168, 169], histograms and second order statistic derived from co-occurrence matrix [170, 171] were mostly used to characterise the different spatial-frequency decompositions to provide a better localisation. Also model-based signatures such as fractals [80] and Markov random fields [172, 173] were used as well. In this work the FD is not only used as a subband feature vector (signature) but also as a criterion for best bases selection in the wavelet tree-structured decomposition. The feature vector will consist of FD's of all selected subbands according to their fractal discriminating power (i.e. surface roughness).

Finally the performance of another multiresolution technique is assessed in classifying the same data set through a set of Gabor filter banks. The co-occurrence and run-length matrices are used as statistical-based methods, and in addition to model-based Gaussian Markov random fields (GMRF) and FD, each are combined with the output energy of the Gabor filters.

6.2 Foundation of wavelet multiresolution representation

Multiresolution or multi-scale analysis is a fine to coarse analysis strategy for which the signal details are decomposed and examined at different levels of resolution. In terms of pattern recognition, large structures or high contrast are best localised at low resolution levels, while higher levels would be more appropriate for small size or low contrast objects [86]. Therefore multiresolution processing gives the advantage of analysing both small and large object characteristics in a single image at several resolutions. The decomposition of the image into multiple resolutions based on small basis functions of varying frequency and limited duration called wavelets was first introduced by Mallat [174], which is also discussed in detail in [175-177]. The wavelet analysis approach can be regarded

as the scale j and translation k of a basic function (called a mother wavelet) to cover the time-frequency domain.

A one-dimensional (1-D) decomposition of a function $f(x) \in L^2(\mathbb{R})$ relative to scaling $\varphi(x)$ and wavelet function $\psi(x)$, where $\varphi_{j,k}(x) = 2^{j/2}\varphi(2^j x - k)$ and $\psi_{j,k}(x) = 2^{j/2}\psi(2^j x - k)$ for all $j, k \in \mathbb{Z}$ and $\varphi(x)$ and $\psi(x) \in L^2(\mathbb{R})$, can be written in the following expansion

$$f(x) = \sum_k c_{j_0}(k) \varphi_{j_0,k}(x) + \sum_{j=j_0}^{\infty} \sum_k d_j(k) \psi_{j,k}(x) \quad (6.1)$$

where j_0 is an arbitrary starting scale and the expansion coefficients $c_{j_0}(k)$ and $d_j(k)$ are determined by

$$c_{j_0}(k) = \langle f(x), \varphi_{j_0,k}(x) \rangle = \int f(x) \varphi_{j_0,k}(x) dx \quad (6.2)$$

$$d_j(k) = \langle f(x), \psi_{j,k}(x) \rangle = \int f(x) \psi_{j,k}(x) dx \quad (6.3)$$

$\{\varphi(x), \psi(x)\}$ are mutually orthogonal functions and \langle, \rangle is the inner product operator. $\varphi(t)$ satisfies the dilation equation $\varphi(x) = \sqrt{2} \sum_k h_0(k) \varphi(2x - k)$ with $h_0(k)$ denoting scaling filter, while $\psi(x)$ satisfies the wavelet equation $\psi(x) = \sqrt{2} \sum_k h_1(k) \psi(2x - k)$ with $h_1(k)$ denoting wavelet filter. These two filters need to satisfy certain conditions for the set of basis wavelet functions to be unique and orthonormal [174, 176, 178].

For image processing, the 1-D wavelet basis functions can be easily expanded to 2-D by the product of two 1-D wavelet basis functions (scaling function and corresponding wavelet) along the horizontal and vertical directions; producing one separable scaling function and three separable directionally sensitive wavelets.

$$\varphi(x, y) = \varphi(x)\varphi(y) \quad (6.4)$$

$$\psi^H(x, y) = \psi(x)\varphi(y) \quad (6.5)$$

$$\psi^V(x, y) = \varphi(x)\psi(y) \quad (6.6)$$

$$\psi^D(x, y) = \psi(x)\psi(y) \quad (6.7)$$

Then the discrete wavelet transform for a function $f(x, y)$ of size $M \times N$ can be represented as follows [86]

$$W_\varphi(j_0, m, n) = \frac{1}{\sqrt{MN}} \sum_{x=0}^{M-1} \sum_{y=0}^{N-1} f(x, y) \varphi_{j_0,m,n}(x, y) \quad (6.8)$$

$$W_\psi^i(j, m, n) = \frac{1}{\sqrt{MN}} \sum_{x=0}^{M-1} \sum_{y=0}^{N-1} f(x, y) \psi_{j,m,n}^i(x, y) \quad i = \{H, V, D\} \quad (6.9)$$

where $W_\varphi(j_0, m, n)$ defines an approximation of $f(x, y)$ at scale j_0 , and $W_\psi^i(j, m, n)$ coefficients add horizontal, vertical and diagonal details for scales $j \geq j_0$. A 2-D decomposition filter bank of a two band (dyadic) wavelet system is shown in Fig. 6.1.

As dyadic wavelet transform depends mainly on the scaling $h_0(k)$ and wavelet $h_1(k)$ filters for image decomposition, one does not need to express the $\varphi(x)$ and $\psi(y)$ in their explicit form. The decomposition process can be viewed as passing the signal through a pair of lowpass L and highpass H filters, also known as *quadrature mirror* filters, having impulse responses $\tilde{h}_0(k)$ and $\tilde{h}_1(k)$, and then downsampling by dropping every other sample. The impulse responses of L and H are defined as

$$\tilde{h}_0(k) = h_1(-k), \tilde{h}_1(k) = h_1(-k) \quad (6.10)$$

For signal reconstruction the operation is reversed, through upsampling the decomposed signals (i.e. subbands) by inserting zeros between neighbouring samples before filtering by $h_0(k)$ and $h_1(k)$ and finally adding the filtered signals together. The decomposition is performed recursively to the output of the lowpass filter \tilde{h}_0 , which leads to a pyramid-structure decomposition or known as conventional wavelet transform. Hence, given the scaling and translation parameters, j and k , the corresponding 2-D filter coefficients can be expressed as in (6.11) with subscripts indicating the low and high pass filtering characteristics in the x and y directions.

$$\begin{aligned} h_{LL}(j, k) &= h_0(j)h_0(k) & h_{HL}(j, k) &= h_1(j)h_1(k) \\ h_{LH}(j, k) &= h_0(j)h_1(k) & h_{HH}(j, k) &= h_1(j)h_1(k) \end{aligned} \quad (6.11)$$

By decomposing the signal's approximation coefficients as well, the wavelet transform can be extended in the middle and high frequency channels (LH, HL and HH bands) and not only in the low frequency channels (LL-band), providing a better partitioning of the spatial-frequency domain, which is known as the wavelet packet (WP) transform [158]. As features of some textures would be more prevalent in the higher frequency channels, WPs would give the high frequency structures in an image an equal opportunity for investigation of possible interesting information.

We are concerned more with a better representation of the texture characteristics at each decomposition; therefore, this work presents an overcomplete tree-structured wavelet representation by omitting image down-sampling operation at each decomposition step, holding the size of the transformed image the same as the original image.

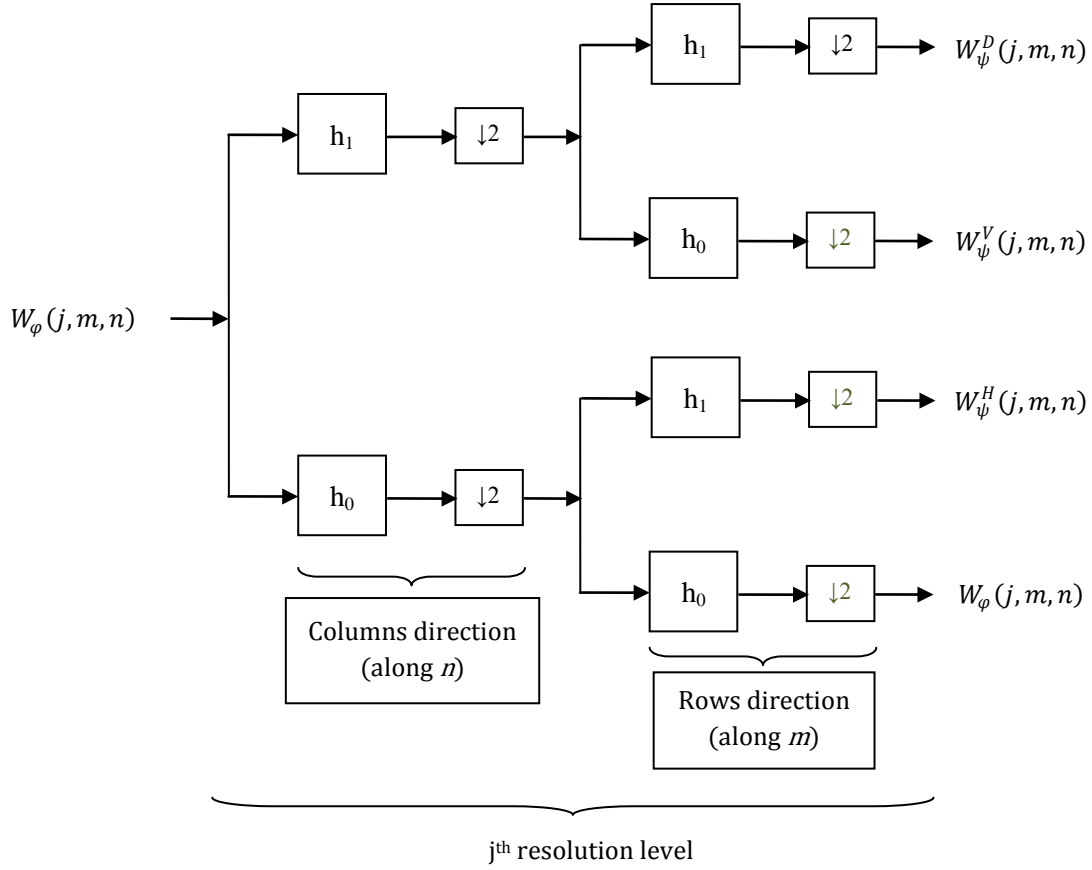


Fig. 6.1 Decomposition filter bank for a 2-D wavelet transform.

On the other hand, signal transform methods such as wavelet and Fourier transforms, are in a sense similar in the localisation of their basis functions in the frequency domain, yet the simultaneous localisation in the time domain gives an advantage for the former. A joint spatial-frequency localisation will give a sparse representation of the image which is useful in feature detection, compression and noise removal [179, 180]. This is related to the way the basis functions of the two transforms cover the spatial-frequency domain. In order to achieve a joint localisation for the Fourier transform case, a constant size translating window is used as an envelope for a range of frequencies. In windowed Fourier transform, the sine and cosine functions are truncated to fit into a square wave (i.e. the fixed-size window), causing for a constant resolution analysis for all frequencies, which will result in poor spatial localisation as the temporal information has been approximated in the transformation process. In contrast wavelet transform — under the assumption of orthogonal or biorthogonal scaling functions— uses a limited duration family of functions (i.e. wavelets), where the size of the window can be varied to accommodate for the condition of the analysed frequency; hence a better localisation can be achieved in the spatial-frequency domain.

Achieving a good spatial-frequency localisation depends on understanding the relation between the two domains. It is known that the time and frequency are inversely related according to the Heisenberg uncertainty principle. This means that more time domain precision in analysing a certain

function will be at the expense of frequency precision, and vice versa. Thus having a varying size and constant area window which adapts to the range of the analysed frequencies could manage the trade-off. This is illustrated graphically in Fig. 6.2 using tiles, also called Heisenberg boxes, which show the concentration of the basis functions' energy [86]. Orthonormal basis functions are assumed, therefore time-frequency tiling is characterised by non-overlapping tiles. Time-frequency tiling using a delta function basis as in Fig. 6.2(a) identifies the time of sampling occurrence but provides no frequency information. Inversely, the Fourier transform in Fig. 6.2(b) provides the frequency information but lacks the time resolution. The windowed Fourier transform decomposes the signal into a set of equal size frequency intervals resulting in constant frequency and time resolution, as shown in Fig. 6.2(c). Finally, the wavelet transform has varying size frequency intervals that can pack all oscillations of the basis wavelet into a narrow interval for high frequencies and into wide intervals for low frequencies, shown in Fig. 6.2(d). This way non-periodic and/or non-stationary functions whose frequencies vary in time can be more appropriately analysed. As short or narrow basis functions are required for detection of signal discontinuities, detailed frequency analysis requires long or wide basis functions. The wavelet transform using a Daubechies wavelet basis functions for example can represent both situations by having narrow high and wide low frequencies simultaneously, see Fig. 6.3(b).

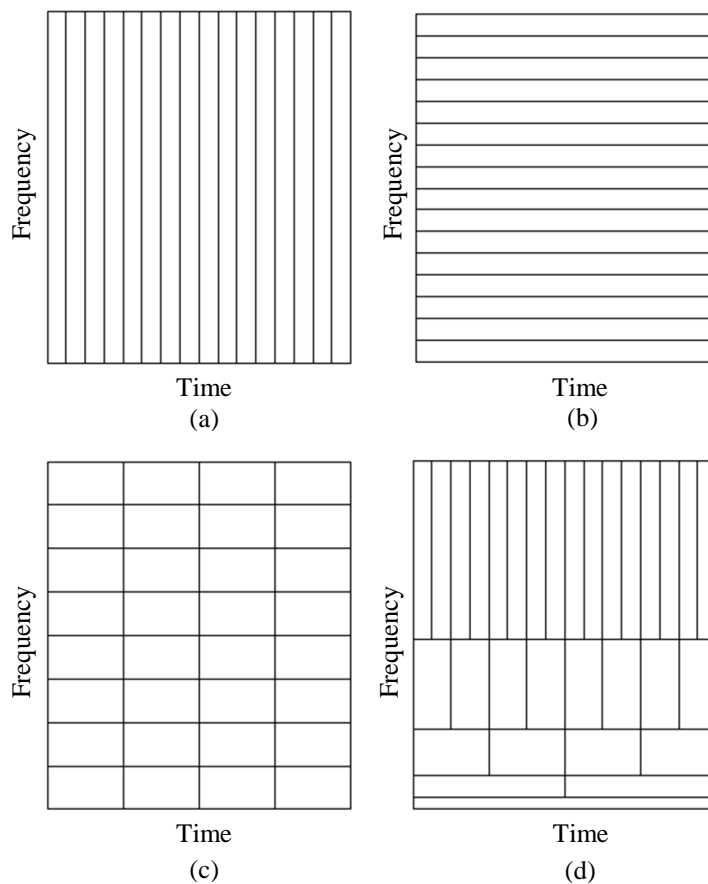


Fig. 6.2 Time-frequency tiling for (a) sampled data, (b) Fourier transform, (c) windowed Fourier transform, and (d) wavelet transform.

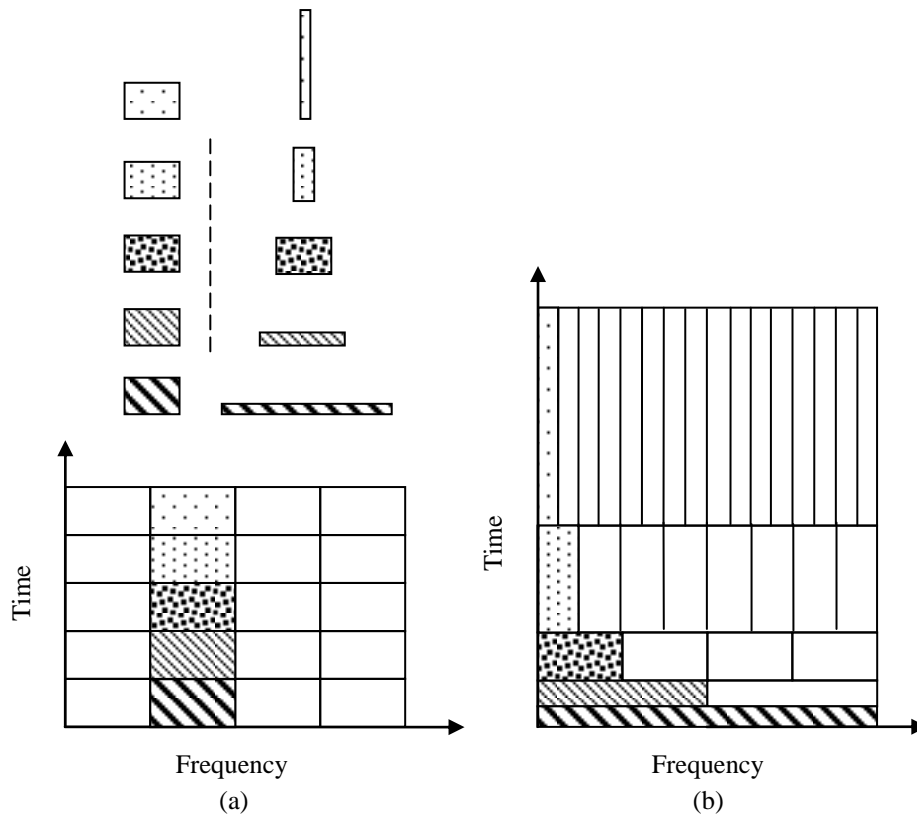


Fig. 6.3 Comparing tiling covering of the time-frequency domain using (a) sinusoidal basis function for windowed Fourier transform, and (b) Daubechies wavelet basis functions for wavelet transform.

6.3 Image pre-processing

All four meningioma images were first segmented prior to feature extraction by applying the technique used in the previous chapter (see Fig. 6.4 and its corresponding first level decomposition in Fig. 6.5). This is done by investigating the separability of the RGB colour channels before selecting the appropriate colour channel for cell nuclei segmentation, followed by applying the morphological gradient to extract the general structure and elimination of any possible tissue cracks that may occurred during biopsy preparation procedure. This assists in highlighting the size and orientation of the cell nuclei structure, which would reflect on the quality of the texture signatures to be extracted from each subband.

6.4 Subband selection optimisation

A 8-tap Daubechies filter [181] (see Table 6.1) was used in obtaining the WPs where the decomposition was implemented in a tree structure approach [164], expanding only the basis having the most significant signature (i.e. having relatively more information). This approach was adopted to investigate the possibility of higher frequency channels to provide significant information as compared to the classical low-frequency decomposition approach for the segmented histopathological images. Fig. 6.6 supports this trend, in which the middle and high wavelets subbands for the first level of decomposition have stronger Fourier spectrum as compared to the low frequency channel, especially for the first level of resolution.

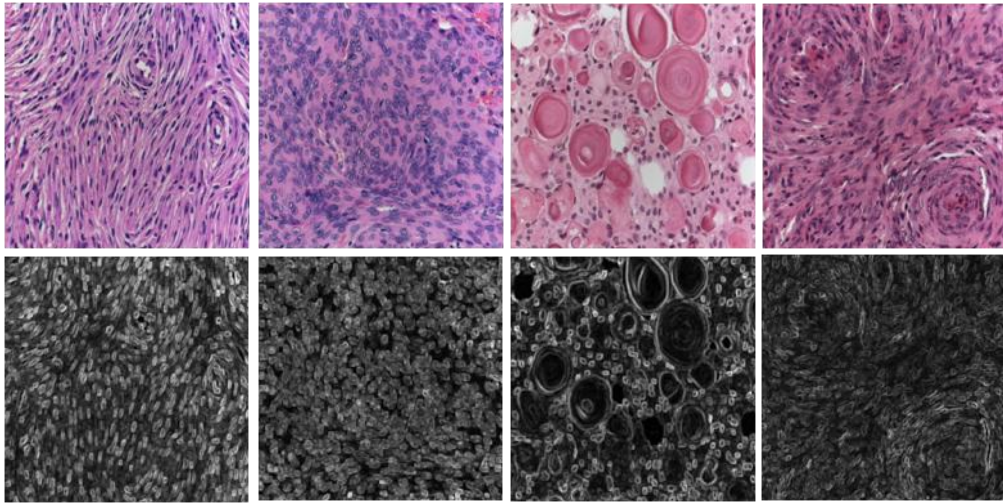


Fig. 6.4 Upper row (left-right) is the meningioma fibroblastic, meningothelial, psammomatous and transitional subtypes. Second row is the corresponding grey-level segmented cell nuclei general structure.

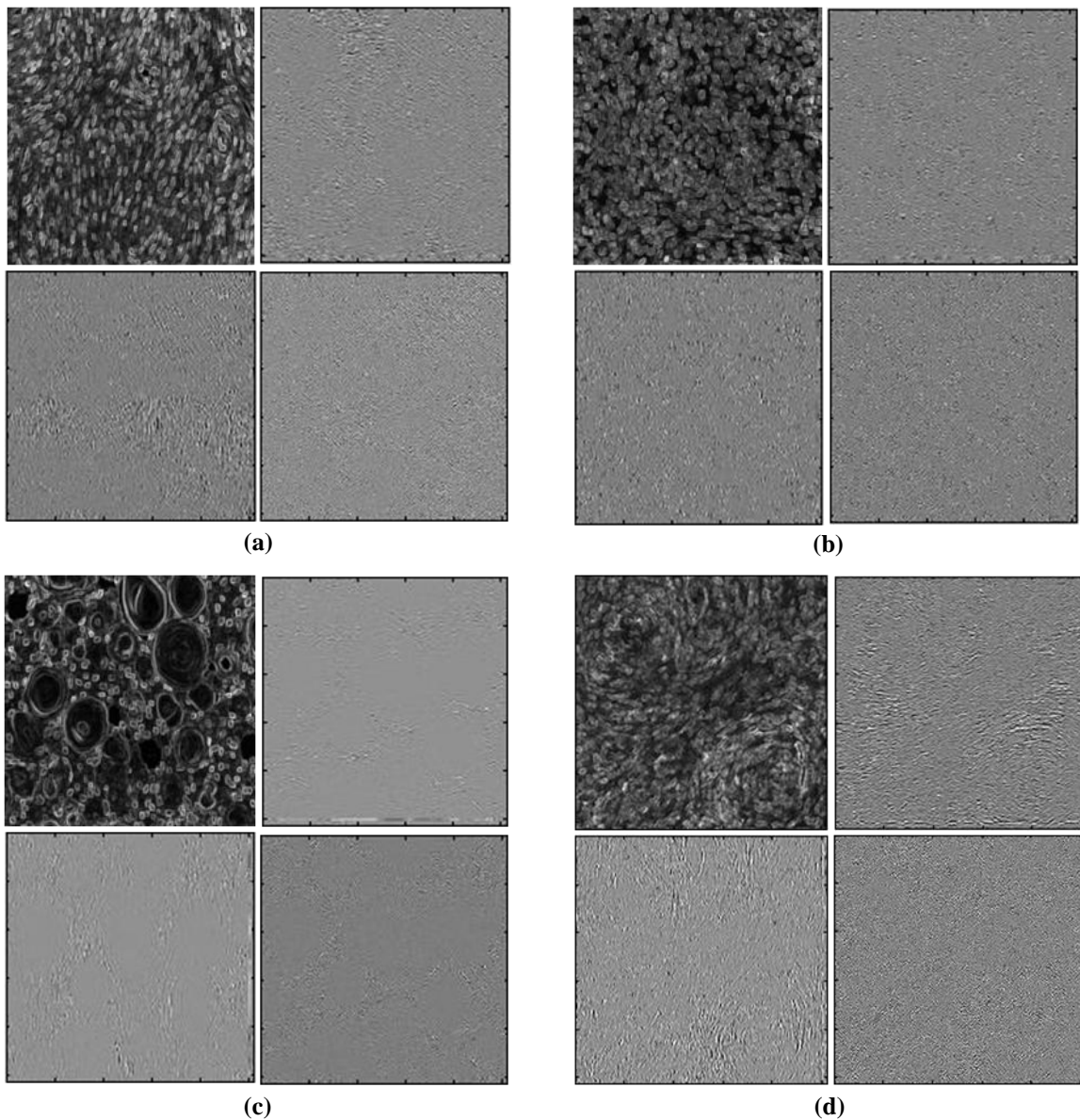


Fig. 6.5 First level of decomposition showing the LL, LH, HL and HH bands for (a) fibroblastic, (b) meningothelial, (c) psammomatous and (d) transitional subtypes; respectively.

Table 6.1 Wavelet transform 8-tap Daubechies filter coefficients

Coefficient	Value
$h(0)$	-0.01059740
$h(1)$	0.03288301
$h(2)$	0.03084138
$h(3)$	-0.18703481
$h(4)$	-0.02798376
$h(5)$	0.63088076
$h(6)$	0.71484657
$h(7)$	0.23037781

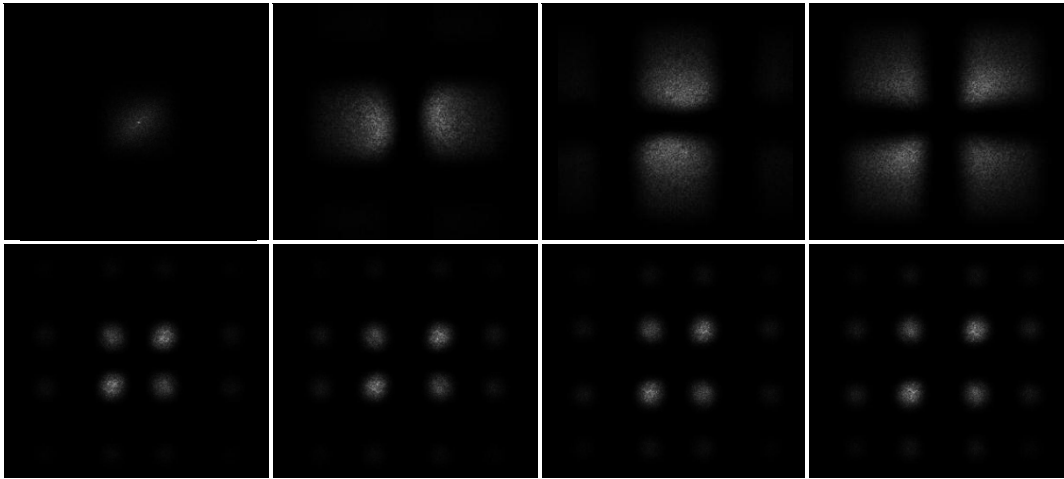


Fig. 6.6 Fibroblastic meningioma power spectrum of LL, LH, HL and HH wavelet bands for the 1st (upper row) and 3rd (lower row) level of resolution.

6.4.1 Fractal signature approach

The wavelet subband selection process was based upon exploiting possible fractal characteristics that images of meningioma cell nuclei may possess. Depending on the size and orientation of the cell nuclei, each subtype has a distinct structure which can be approximately self-similar for a number of scales — see the twirls in the bottom right of Fig. 6.5. As the case for most biological structures which exhibit fractal characteristics, they are constraint to a limited number of self-similar scales and not to infinity, and the zoomed-in scales are not identical to the mother structure but a random approximation.

The FD signatures are estimated for all subbands at each level of WP decomposition, where the FD is computed on a pixel by pixel basis to producing a FD image where each pixel has its own FD value. Features at image boundaries are computed after assuming the image is mirror-like continually extended in both directions. Then the mean would represent the FD of the subband, which would give a more reliable estimation as compared if the FD was directly estimated from the whole subband; e.g. a relatively large crack in a biopsy might have a negative effect on the accuracy of the estimated FD, while generating an FD image and then averaging all FD pixels would mitigate this effect. Finally the

subband with the highest FD is selected for further decomposition. For example, Table 6.2 lists the estimated FD values for each subband at each decomposition level, where the W_{HH} subband which had the highest FD value for first resolution level was the chosen basis for the second decomposition level, and so on. The *fractal map* representing the FD signature of the tree-structured wavelet decomposition defined in the spatial-frequency domain and its corresponding quad-tree structure for the first three decomposition level is shown in Fig. 6.7. Although the applied multiresolution technique is similar to the one used by Chang and Kuo [164], the FD instead of the energy is used to guide the direction of tree expansion, and the classification results will show the feasibility of this approach.

At the end of the feature extraction stage, a feature vector $W_{FD} = (f_1^i, f_2^i, \dots, f_j^i)$ consisting of all selected subbands FD signatures f to a certain decomposition level j will be produced for each of the meningioma subimages i . In order to save processing time and when the difference in-between the FD signatures become less significant, a designated threshold λ would reduce the dimensionality of the extracted feature vector. By that, unnecessary decompositions are avoided which could have a negative effect on the classifier's performance. This can be expressed as if the condition $(\forall f_j^i \in W_{FD}) \leq \lambda$ is satisfied, then the decomposition should terminate. Therefore, the FD signatures' absolute difference $D_f = |f_1^j - f_2^j|$ between all four wavelets subbands (W_{LL} , W_{LH} , W_{HL} and W_{HH}) for a certain resolution level needs to be less than or equal to λ (empirically choosing $\lambda = 0.05$ for psammomatous and 0.012 for the other subtypes) before decomposition terminates. The best basis selection processes can be summarised in the following pseudo code:

```

FOR each meningioma subtype
  FOR each filtered subband W {
    compute the FD signature for each subband;
    find the absolute difference between all FD signatures;
    IF all subbands FD signatures  $\leq$  set threshold THEN
      terminate;
    ELSE choose the band with the highest FD signature;
    ENDIF
  }
ENDFOR
ENDFOR

```

Table 6.2 Fractal dimensions for each corresponding fibroblastic wavelet subband

Resolution	W_{LL}	W_{LH}	W_{HL}	W_{HH}
level 1	2.5038	2.6797	2.7105	2.7897
level 2	2.9346	2.8918	2.8994	2.8239
level 3	2.9585	2.9655	2.9669	2.9722
level 4	2.9877	2.9857	2.9860	2.9838
level 5	2.9930	2.9937	2.9939	2.9945
level 6	2.9975	2.9972	2.9973	2.9970
level 7	2.9986	2.9987	2.9987	2.9988
level 8	2.9994	2.9994	2.9994	2.9994

Resolution	W_{LL}	W_{LH}	W_{HL}	W_{HH}
level 1	2.6897	2.8352	2.8734	2.9163
level 2	2.9767	2.9592	2.9648	2.9315
level 3	2.9853	2.9878	2.9887	2.9907
level 4	2.9958	2.9952	2.9954	2.9947
level 5	2.9976	2.9979	2.9979	2.9982
level 6	2.9991	2.9991	2.9991	2.9990
level 7	2.9995	2.9996	2.9996	2.9996
level 8	2.9998	2.9998	2.9998	2.9998

Resolution	W_{LL}	W_{LH}	W_{HL}	W_{HH}
level 1	2.6217	2.7663	2.7896	2.8514
level 2	2.9578	2.9262	2.9311	2.8752
level 3	2.9737	2.9781	2.9784	2.9821
level 4	2.9922	2.9910	2.9910	2.9895
level 5	2.9956	2.9961	2.9961	2.9965
level 6	2.9984	2.9983	2.9982	2.9981
level 7	2.9991	2.9992	2.9992	2.9993
level 8	2.9997	2.9996	2.9996	2.9996

Resolution	W_{LL}	W_{LH}	W_{HL}	W_{HH}
level 1	2.5333	2.7041	2.7289	2.8068
level 2	2.9428	2.9032	2.9081	2.8375
level 3	2.9643	2.9701	2.9706	2.9756
level 4	2.9893	2.9876	2.9877	2.9857
level 5	2.9939	2.9946	2.9946	2.9952
level 6	2.9978	2.9976	2.9976	2.9974
level 7	2.9988	2.9989	2.9989	2.9990
level 8	2.9995	2.9995	2.9995	2.9995

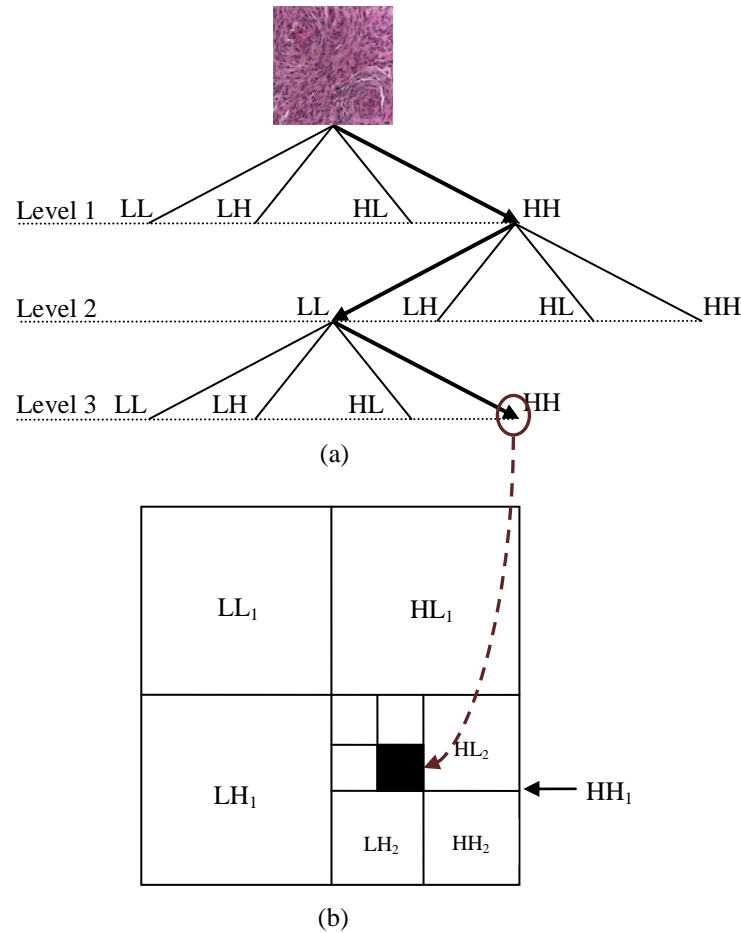


Fig. 6.7 (a) Wavelet quad-tree structure for first three decomposition levels of transitional subtype appearing in Fig. 6.5 and (b) its corresponding channel decomposition.

6.4.2 Other texture signatures

For the purpose of comparison, the performance of the FD would be benchmarked against other commonly used texture signatures for subband discriminant power assessment. These methods use the highest energy among the subbands for WPs expansion. Some of the most used methods for extraction of subbands texture signatures is the energy E_k , $k=1, 2$ in the form of l_1 -norm [164] and l_2 -norm [182] as in (6.12).

$$E_k = \frac{1}{MN} \sum_{y=0}^{M-1} \sum_{x=0}^{N-1} |I_f(x, y)|^k \quad (6.12)$$

Here M and N are the size of the subband intensity $I_f(x, y)$. Also the co-occurrence matrix (CM) [170] $C_{\theta, \delta}(i, j)$ representing the joint probability of grey-level pixel i and j , within a certain distance δ and orientation θ . Then the unnormalised entry $C_{\theta, \delta}$ can also be expressed in an alternative way to the CM definition in chapter 5 as

$$C_{\theta, \delta}(i, j) = \#\{(x_1, y_1), (x_2, y_2) \in (M \times N) \times (M \times N) : I_f(x_1, y_1) = i, I_f(x_2, y_2) = j, \text{ where } x_1 - x_2 = \delta \cos \theta \text{ and } y_1 - y_2 = \delta \sin \theta \text{ or } x_1 - x_2 = -\delta \cos \theta \text{ and } y_1 - y_2 = -\delta \sin \theta\} \quad (6.13)$$

The $\#$ denotes the number of elements in the set, and M and N are the horizontal and vertical dimensions of $I_f(x, y)$. Hence, by varying θ and δ multiple co-occurrence matrices can be generated for each wavelet subband. Then different second order statistic features can be derived from the generated co-occurrence matrix.

6.5 Texture signature classification

The same Bayesian classifier applied in the previous chapter was used here for discrimination between the texture signatures. A leave-one-out approach [19] was applied to validate the classification results, which is done by designing the classifier using $(n-1)$ samples and then evaluated on the remaining set-aside sample. This process is repeated n times covering all possible unique sets of other samples. Thereby an unbiased estimation is achieved although the performance is sometimes overestimated.

6.6 Wavelet packet results

The FD values of each corresponding subband for the optimum level of resolution are shown in Table 6.3. The psammomatous subtype needed only two levels of decomposition to reach its optimum performance (i.e. before the absolute difference between the decomposed subbands becomes less or equal than the set threshold). The decomposition terminated at the third level for meningothelial and transitional and at the fourth for fibroblastic subtypes.

The classification performance with up to eight levels of resolution using the FD signature for best basis selection (BBS_{FD}) is shown in Table 6.4, where a threshold value for the FD signature was not used to stop the WP decomposition. The best classification accuracy of 90.31% was achieved at the third level of decomposition. Alternatively, using the appropriate threshold as discussed in the subband optimisation section, the decomposition should terminate when there is no significant difference between the FD signatures — highlighted in bold — giving a slightly improved overall accuracy of 91.25%.

A comparison is also performed to evaluate the performance of the BBS_{FD} approach with two other first order statistics methods. The BBS_{FD} model based method suggested in this chapter used the FD signatures to guide the WP tree-structured expansion in order to construct a feature vector of the subbands having the highest FD signatures. On the other hand, the statistical approaches used the highest energy for best basis selection process, where the first method (abbreviated BBS_E) simply employed the computed highest energies of the subbands as signatures, and the second method (abbreviated BBS_{CM}) extracted the co-occurrence matrix correlation, entropy and energy (with $\delta = 1$ and $\theta = 0^\circ, 45^\circ, 90^\circ$ and 135°) as signatures for classification. The three subband decomposition approaches were also run at up to eight levels of resolution, and the corresponding classification accuracy is determined at each level. It is evident from Fig. 6.8 that the BBS_{FD} fractal approach outperformed the others, where the BBS_{CM} and BBS_E approaches achieved a maximum overall classification accuracy of 83.44% and 73.75%; respectively. Although the BBS_{FD} classification accuracies from level 2 to 4 remaining higher than the other two methods, it starts to degrade afterwards, scoring accuracies equal or lower to that of the energy approach BBS_E .

**Table 6.3 Optimum decomposition levels for meningioma subtypes’
FD signature absolute difference values**

Level	Subtype	W_{LL}	W_{LH}	W_{HL}	W_{HH}
2	Psammomatous	2.9767	2.9592	2.9648	2.9315
3	Meningothelial	2.9737	2.9781	2.9784	2.9821
	Transitional	2.9643	2.9701	2.9706	2.9756
4	Fibroblastic	2.9585	2.9655	2.9669	2.9722

**Table 6.4 Wavelet packet decomposition using maximum fractal dimension signature
for best basis selection**

Resolution	Meningioma subtype				Total Accuracy
	Fibroblastic	Meningothelial	Psammomatous	Transitional	
level 1	65.00	91.25	73.75	43.75	68.44%
level 2	82.50	91.25	95.00	86.25	88.75%
level 3	83.75	92.50	93.75	91.25	90.31%
level 4	86.25	86.25	93.75	88.75	88.75%
level 5	35.00	91.25	85.00	70.00	70.31%
level 6	75.00	82.50	91.25	27.50	69.06%
level 7	72.50	82.50	90.00	28.75	68.44%
level 8	47.50	75.00	87.5	40.00	62.50%

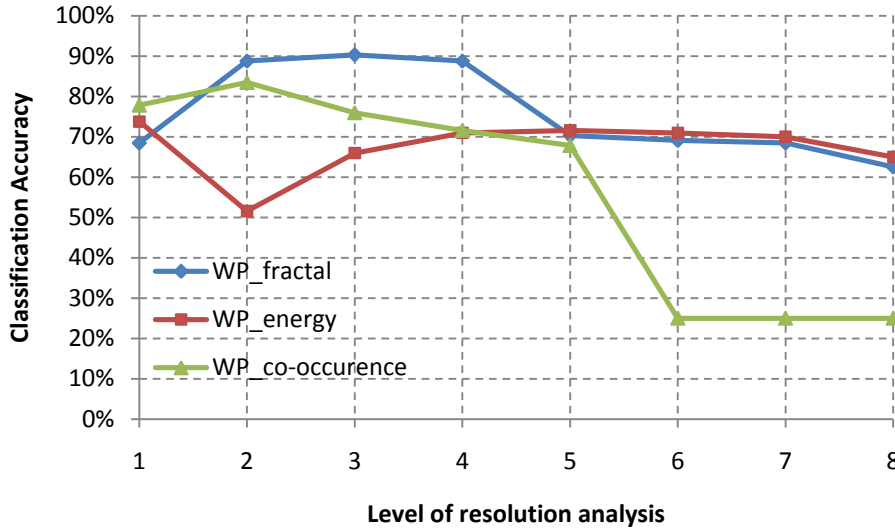


Fig. 6.8 Multiresolution level wavelet packet comparison of meningioma classification accuracy based on fractal dimension, energy and co-occurrence texture signatures.

6.7 Interpretation of wavelet packet results

Since wavelet decomposition in only low frequency channels might not provide sufficient distinguishable signatures [164], the feasibility of WPs based on fractal signature decomposition in classifying histopathological meningioma images was demonstrated in this work.

The fundamental motivation for multiresolution processing is to provide a different perspective for viewing texture, with the analogy of viewing a scene while varying the camera zoom lens. Varying the resolution can highlight objects which might appear clearer than if a single resolution approach was applied, as small size or low contrast objects are best examined at high resolution and vice versa for large objects [86]. This is actually what meningioma images need, as the cell nuclei shape, orientation and denseness differs from one subtype to another and sometimes within the same subtype, reflecting on the number of resolution levels required. Thus, multiresolution using wavelets gives the advantage of studying both cases (i.e. large and small cell nuclei structures) at the appropriate resolution level, through adopting the WP expansion to facilitate investigation of middle and high frequencies where the Fourier spectrum had apparent significant information.

It should be noted that down-sampling was not performed after each decomposition since selecting the subband with the most redundant values that could be represented in the minimum number of bits — leading to greater compression ratio — was not the focus of this work. The main emphasis was on choosing the best basis that can derive distinct texture characteristics to improve the classifier's accuracy.

In reality the general structure shape of the cell nuclei in one subtype are not exactly identical in all prepared tissue biopsies, and differences between two subtypes might be minor. Therefore, eliminating the cytoplasm background for cell nuclei segmentation was essential in providing a reliable estimate of the FD. It was shown in previous work that the segmentation process improves feature extraction, and hence classification performance [61]. A better classification performance for our case means enhancement of the differentiation capability to overcome the shape variability between and within the different meningioma subtypes.

A different approach in assessing the fractal characteristics instead of the energy of subbands was pursued for tree-structured wavelet extension. The best basis selection process relied upon selecting the subband with the roughest surface (i.e. highest FD) only for analyses and discarding other subbands from the same level, then the fractal signatures of the highest subbands would be used for meningioma subtypes discrimination. FD provides a complexity measure for the subband texture in a range between 2 and 3, by checking for self similarity at different scales within the same subband before further decomposition. We can think of this as virtually decomposing the already decomposed subbands into further different scales, in a way, exploring information richness embedded in each subband before deciding which to select.

Results showed that maximum classification accuracy was reached within two to four resolution decompositions — depending on the subtype — before starting to degrade. This was expected as the FD measures would give a reliable estimation to a certain level of resolution, whereas the more levels are decomposed the less details remains for the FD to measure; especially if the mid or high bands were selected for further analysis. Thus, determining the appropriate resolution level is not only important to save computational time but also to improve the quality of the extracted subband features. The decomposition insignificance was indicated according to the FD signature absolute difference between all subbands after empirically specifying a threshold, which specifies how deep the image resolution can be probed. This is equivalent to excluding FD signatures equal to or above 2.985, considering them as nearer to noise rather than a meaningful roughness estimation of the subimage surface. Moreover, comparing the suggested BBS_{FD} technique with the statistical BBS_{CM} and BBS_E techniques, a significant improvement in the classification accuracy was achieved by 7.81% and 17.50% if a threshold was used for determination of decomposition levels and a 6.87% and 16.56% improvement if a fixed level of decomposition was applied (three levels for this case); respectively.

The reason for meningioma subtypes not having their optimum classification performance at an equal level can be referred to the cell nuclei denseness variation between subtypes. Depending on the

subtype, denseness here means the size and number of cell nuclei existing in a biopsy and whether they overlap or not. Subtypes having many small size cell nuclei would expect to represent a rougher surface as compared to small overlapping or large size ones (i.e. fewer edges to detect). Therefore after the segmentation process the general structure of the cell nuclei distribution in each subtype is what remains, and the segmented images with more edges would be regarded as richer with texture information. For example, higher resolution levels would be more appropriate to analyse psammomatous subtypes which have less texture details (i.e. cell structure is less dense as compared to other subtypes, which required tweaking λ from 0.012 to 0.05 for decomposition to terminate earlier), while lower levels would be more appropriate for the remaining three other subtypes.

It would be more comprehensible to use the suggested BBS_{FD} technique with images that exhibit fractal-like characteristics, yet the FD measure can still be used with other type of images as it is simply an estimation of the examined surface roughness. A simple way to verify that would be to perform the same comparison done on the meningioma image but this time using clean non-medical images (e.g. images from the Brodatz album) where texture characteristics are more distinct throughout the image and virtually free of distorting noise.

Given that the opportunity to test the proposed technique on other histopathological tumour images was not available at this moment, the robustness of the decomposition insignificance threshold when applied to a different type of tumour needs to be investigated. Another issue would be the effect of noise and the quality of extracted features, and whether it would have a deteriorating effect on classification accuracy. The type and effect of noise vary depending on the used modality and the conditions the images are acquired in. For histopathological images, noise might arise due to cracks in the prepared biopsy, or dye/stain artefacts, which appear to be mechanical rather than electronic. Meaning it is less susceptible to Gaussian or speckle noise which affects other modalities like CT, MR or US, making the high frequency channels become less reliable in presence of noise. As a result, the effect on the segmented histopathological middle and/or high frequency channels — which possess a significant amount of the cell nuclei structure information — is minor as compared to the low frequency channel which is more prone to the mechanical deformations.

6.8 Gabor filter

Image texture can also be analysed in a similar wavelet-like multiresolution representation using Gabor filters. It can be defined as a Gaussian modulated sinusoid with a capability of multiresolution decomposition due to its localisation both in spatial and spatial-frequency domain. Making use of Denis Gabor's class of harmonic oscillating functions within Gaussian envelopes [183], Daugman showed that the orientation and spatial-frequency selective receptive field properties of neurons in the brain's primary visual cortex can be simply modeled by 2-D Gabor-like filters [184, 185]. Bovik et al

proposed a model for locating filters by exploiting individual texture power spectrum characteristics [14], while Jain and Farrokhnia further proposed a dyadic Gabor filter bank covering the spatial-frequency domain with multiple orientations [186]. Other studies proved Gabor filter to be very useful in detecting texture frequency and orientation as well [13, 153, 187] and references cited therein. The real impulse response of a 2-D sinusoidal plane wave with orientation θ and radial centre frequency f_0 modulated by a Gaussian envelope with standard deviations σ_x and σ_y respectively along the x and y axes is given by

$$h(x, y) = \frac{1}{2\pi\sigma_x\sigma_y} \exp\left\{-\frac{1}{2}\left[\frac{x^2}{\sigma_x^2} + \frac{y^2}{\sigma_y^2}\right]\right\} \cos(2\pi f_0 x) \quad (6.14)$$

$$\begin{aligned} \text{where } x &= x\cos\theta + y\sin\theta \\ y &= -x\sin\theta + y\cos\theta \end{aligned}$$

The Gabor filter in the corresponding spatial-frequency domain would be represented as two symmetrically spaced Gaussians as follows

$$H(u, v) = \exp\{-2\pi^2[(u - f_0)^2\sigma_x^2 + v^2\sigma_y^2]\} + \exp\{-2\pi^2[(u + f_0)^2\sigma_x^2 + v^2\sigma_y^2]\} \quad (6.15)$$

and spatial and corresponding spatial-frequency response are graphically shown bellow in Fig. 6.9.

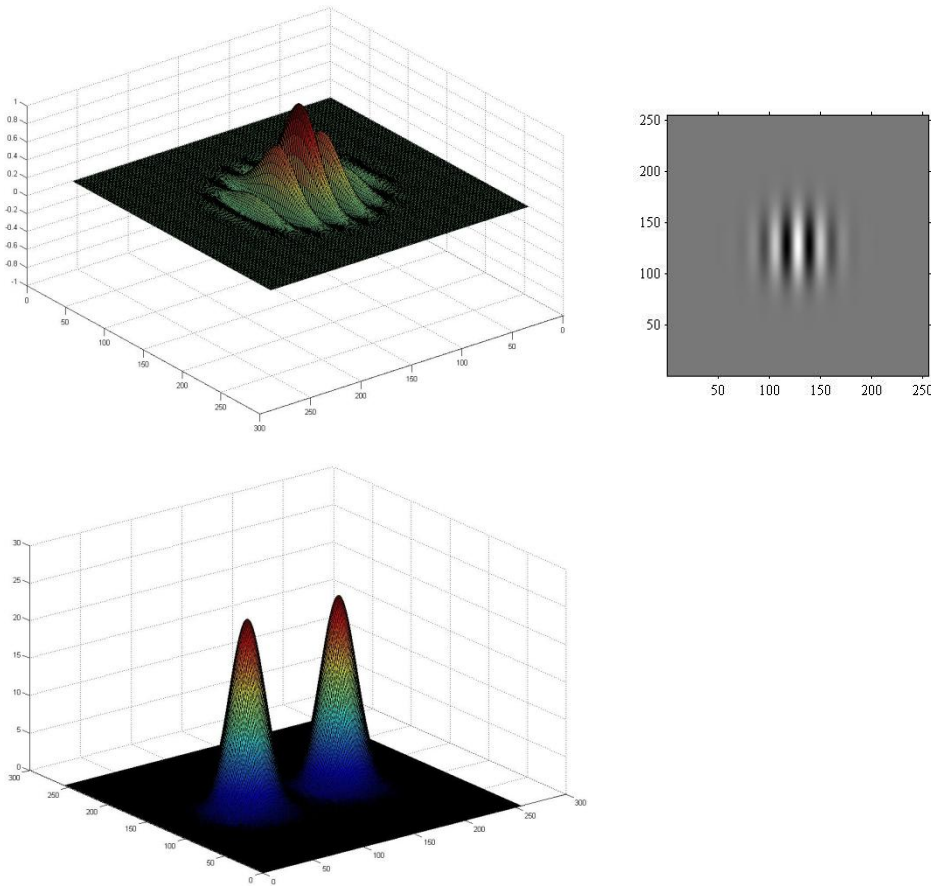


Fig. 6.9 Gabor filter having 0° orientation and 32 cycles / image width for a 256×256 size image.

Multiple filters covering the spatial-frequency domain can be generated by varying the filters' centre location through tuning the frequency f_0 with a specific angle θ . Fig. 6.10 shows the frequency response of the dyadic filter bank in the spatial-frequency domain. The Gaussian envelope unknowns σ_x and σ_y can be determined as in (6.16) after setting frequency cut-off to -6 db and the frequency and orientation bandwidths (B_f, B_θ) to constant values matching psychovisual data [188]. In particular an interval of one octave between the radial frequencies is recommended [186]. The frequency bandwidth specified by octaves (i.e. the interval between f_1 and its double f_2) increases in a logarithmic fashion given by $\log_2(f_2/f_1)$. This was inspired by experiments that showed the frequency bandwidth of simple cells in the visual cortex is roughly one octave [148]. For this work a circular Gaussian was chosen by setting $\sigma_x = \sigma_y$ to have an equal spatial coverage in all directions, and a 45° orientation bandwidth.

$$\sigma_x = \frac{\sqrt{\ln 2}(2^{B_f} + 1)}{\sqrt{2}\pi f_0(2^{B_f} - 1)} \quad \sigma_y = \frac{\sqrt{\ln 2}}{\sqrt{2}\pi f_0 \tan(B_\theta/2)} \quad (6.16)$$

Carefully setting the filter characteristics would result in proper capture of texture information and reduce the effect of aliasing. This is achieved by correctly selecting the filter position (f_0, θ) and bandwidth (σ_x, σ_y), and making sure the central frequencies of channel filters lie close to characteristic texture frequencies to prevent the filter response from falling off too rapidly [188]. From each of the images having size of 512 x 512 used in this work, the mean was first subtracted to reduce the filter's sensitivity to texture with constant variation, then six radial frequencies ($2^2\sqrt{2}, 2^3\sqrt{2}, 2^4\sqrt{2}, 2^5\sqrt{2}, 2^6\sqrt{2}$ and $2^7\sqrt{2}$ cycles/image-width) with four orientations ($0^\circ, 45^\circ, 90^\circ$ and 135°) was adopted according to [186], giving a total of 24 filters. In general, the number of dyadic Gabor filter banks required is given by $A * \log_2(N_c/2)$, where N_c is the image width and A is the number of orientation separations (e.g. $A = 4$ for a 45° orientation separation angle). Filters with radial frequencies $1\sqrt{2}$ and $2\sqrt{2}$ were excluded due to their insensitivity (i.e. the filters capture spatial variations that are too large to explain textural variation in an image). Also the highest frequency was selected to be $(N_c/4)\sqrt{2}$ in order to guarantee that the passband of the filter falls inside the image. Finally the extracted features would represent the energy of each magnitude response.

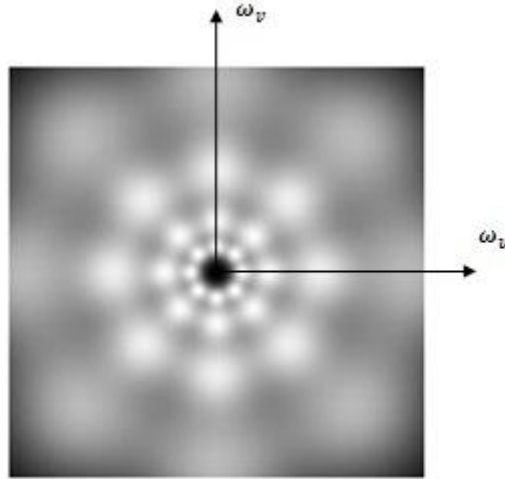


Fig. 6.10 Gabor filter defined in the spatial-frequency domain with radial frequencies 1 octave apart, bandwidth 1 octave each and 45° orientation separation (only filters' half-peak supports are displayed).

Applying a set of filter banks resembles the operation of wavelet transforming an image at selected spatial frequencies. In a way, the Gaussian function is modulated and translated for generation of the Gabor basis functions, in analogy to the scaling and translation of the mother wavelet and scaling function for wavelet basis generation. However, the Gabor function is considered an admissible wavelet [186], in other words, the basis produced by the Gabor function is non-orthogonal resulting in redundant decompositions. Also, depending on the size of the processed image, the number of required radial frequencies for positioning the centres of the Gabor filter banks needs to be specified prior to processing, which is similar to choosing the number of decomposition levels for the wavelet packets.

6.9 Gabor filter results

The Gabor filter was applied to the same histopathological images which were used in the wavelets section. The energy signature of each filter output was computed and used as a feature vector for classification. Additionally, the energy extracted features were also combined with four other texture measures of the processed image itself, and the fused signatures were used for classification. Model based signatures such as the fractal dimension (FD) and Gaussian Markov random fields (GMRF), and statistical signatures as the grey level co-occurrence matrix (CM) and the run length matrix (RLM) were used in the combinations. As a mean for comparison, this procedure was initially applied on the blue colour channel of each image — as it showed better performance in terms of classification accuracy due to the dyes used in staining the meningioma biopsies [61] — and then applied again on the same colour channel after having the cell nuclei general structure segmented.

Table 6.5 presents the results, where the subscript S and NS indicates whether the cell nuclei were segmented or not (see section 5.2.2 and 5.5.3 for segmentation process) before extraction of the Gabor

filter energy signature $G_f(E)$ alone or in combination with other texture measures. The highest classification accuracy of 95.00% was reached when combining the image filters' energy and the fractal characteristics $G_f(E \& FD)_{NS}$ as a feature vector without performing any prior segmentation.

Table 6.5 Classification accuracy comparison of Gabor filtered meningioma images after extraction of the energy and in combination with the fractal dimension, Gaussian Markov random fields, grey level co-occurrence and run-length matrices texture measures.

Filter texture signature	Meningioma subtype				Total Accuracy
	Fibroblastic	Meningothelial	Psammomatous	Transitional	
$G_f(E)_S$	93.75	82.50	96.25	85.00	89.38%
$G_f(E \& FD)_S$	91.25	82.50	95.00	83.75	88.12%
$G_f(E \& GMRF)_S$	95.00	81.25	95.00	90.00	90.31%
$G_f(E \& CM)_S$	93.75	78.75	95.00	87.50	88.75%
$G_f(E \& RLM)_S$	92.50	78.75	98.75	90.00	90.00%
$G_f(E)_{NS}$	83.75	86.25	90.00	73.75	83.44%
$G_f(E \& FD)_{NS}$	100	87.50	96.25	96.25	95.00%
$G_f(E \& GMRF)_{NS}$	97.50	77.50	97.50	92.50	91.25%
$G_f(E \& CM)_{NS}$	100	92.50	96.25	86.25	93.75%
$G_f(E \& RLM)_{NS}$	100	80.00	97.50	82.50	90.00%

6.10 Interpretation of Gabor filter results

An alternative multiresolution texture analysis approach based on Gabor filters was applied to the meningioma images. It was intended to investigate whether the meningioma subtype discrimination can be further improved, even when the Bayesian classifier used in the wavelet section remains the same. Unlike the WP section, it was more practical and less computationally intensive to combine the FD of each subimage with the corresponding energy of the filter outputs rather than having the FD computed for each of the 24 filters. This similarly applies for the rest of the mono-resolution measures used in the feature extraction process.

Using the energy of the Gabor filter outputs alone as a texture signature for discrimination between the meningioma subtypes proved to be more effective than single or mono-resolution texture measures discussed before. For instance, the highest accuracy achieved for four different mono-resolution methods used under the same conditions would not exceed 84% [61] as compared to 89.38% for the Gabor filter multiresolution case. Nevertheless, results showed that this is not the optimum extent that the classification accuracy can reach and there are still unexplored endeavours for improvement.

The coloured histopathological images were decomposed to the main RGB channels and the blue channel was chosen for operation as dyes used in the staining process of the meningioma tissue biopsies gave the cell nuclei — considered a major mark of distinction between the different subtypes — a colour near to blue. Then feature extraction was performed with and without having the meningioma cell nuclei segmented. The feature extraction involved the multiresolution Gabor filter

outputs applied individually for classification and in combination with other mono-resolution texture measures characterising the same image texture as well. The segmentation process worked well for the filter's output energy signature $G_f(E)_{NS}$ if no segmentation took place. While there was no difference between the segmented and non-segmented versions for the energy and RLM combination $G_f(E \& RLM)$, it was better to have the histopathological images not segmented when combining the energy of the filter outputs with the FD, GMRF or CM of the image.

All classification results gave an accuracy equal or above 90% when the mono and multiresolution methods were combined together and without segmentation. The remarkable combination is the $G_f(E \& FD)_{NS}$ which gave the highest classification accuracy — even higher than the 92.50% accuracy achieved by the BBS_{FD} WP technique — and the improvement was up by 6.88% when the subimages were not segmented. Although the classification performance degrades when the energy of the G_f was utilised alone without segmentation as indicated in Table 6.5, the loss is compensated and accuracy is further improved when the filter output is combined with the FD of the image. As it was previously shown that the use of the morphological gradient in the segmentation process would negatively affect the classification accuracy of the FD measure [61], it is expected that the fractal characteristics of the non-segmented images to have a better expression which was reflected in the 95.00% accuracy achieved.

It can be deduced that an optimum expression for the meningioma tissue requires both mono and multiresolution processing to maximise the difference in-between the subtypes. As the cell nuclei size varies between the different subtypes, the multiresolution approach can better identify these differences and represent them by a measurable quantity (e.g. Gabor filter banks energy signature for this case) exemplifying the amount of information at different scales. Yet relying on the on the energy of the filter outputs alone is deemed insufficient, thus analysing the texture at its highest resolution using a mono-resolution approach could contribute towards highlighting some of the aspects overlooked by the Gabor filter approach. An example was the FD signature which provides a mean to check for self-similarity or roughness of the surface, where smaller objects would result in a higher FD estimate and vice versa. It has also a considerable immunity to intra-variability of the number of cell nuclei in the same subtype. Similarly, the rest of the applied mono-resolution methods had also its own approach in texture characterisation, whether the emphasis was on the dependence of each pixel in the image only on its neighbours as the case in GMRF, or deriving first and second order statistics after computing the joint probability or the number of runs for a certain set of pixels with a certain grey-level value for CM and RLM; respectively.

Although finer quantisation was recommended by having an orientation angle of 30° for centring the location of the filters [188], a 45° orientation angle was used as its is less computationally expensive and finer orientation quantisation did not show significant improvement for the given histopathological texture samples. Also, experimenting by smoothing the subimages' texture with a Gaussian filter prior to extraction of the feature was applied as well. The approach suggested by Jain and Farrokhnia through setting the filter's window size relative to the radial frequencies of the corresponding tuned filter [186] resulted in an 1% decrease in the recorded accuracy. This can be referred to the blurring which negatively affected the accuracy of the FD signature.

An advantage of the mono-resolution approach is its simplicity in application and speed in processing. Yet unlike synthetic or artificial texture, the complexity and non-stationary nature of medical texture requires a multi-perspective analysis in order to spot subtle differences which might be crucial in subtype discrimination. This work takes a step further and demonstrates that a generated fused feature vector exploiting the strengths of both resolution approaches could provide an optimum characterisation for meningioma texture classification.

6.11 Conclusion

Enhancing the quality of the extracted features that can optimise meningioma texture classification was the main concern of this work. A novel approach that used the fractal dimension for wavelet tree-structured decomposition demonstrated its capability to distinguish grade I histopathological meningioma images with an improved accuracy as compared to energy based decomposition. The BBS_{FD} relies on revealing texture structure complexity which would better characterising the information situated in the middle and high frequency bands. Also, the appropriate decomposition level would be detected when no more significant difference in-between the subbands exist, saving unnecessary computational operations. Possible future developments would be using an M-band wavelet transform for subband decomposition.

On the other hand, the multiresolution approach based on Gabor filters proved to more effective in terms of classification accuracy as compared to four other mono-resolution approaches. Additionally, the generation of a feature vector mutually combining the energy signature of the Gabor filter outputs and either of the FD, GMRF, CM or RLM mono-resolution methods would improve subtype discrimination. The appropriate selection of the feature extraction method(s) according to the nature of the examined texture (tissue) is necessary for boosting the ability to distinguish subtle differences in-between the meningioma subtypes, which was optimised by the fusion of the fractal characteristics with the filter bank's energy signature. Furthermore, testing these techniques on other grades of meningioma or different types of brain tumours would assist in benchmarking their performance.

Chapter 7

CONCLUDING DISCUSSION

Various texture analysis methods were applied for the purpose of novel, and effective tumour discrimination. The applied techniques went beyond simply differentiating between normal and abnormal tissue to the process of tumour type and stage categorisation. The intention was to cover both kinds of textures that might be encountered in medical images: textures acquired at a molecular or *macro-scale* as in histopathological DM imaging; and at a tissue or *micro-scale* as in CT imaging. The proposed texture analysis techniques optimised the discrimination performance either by using one texture measure but with a special type of acquired CT images in order to enhance the feature extraction ability, or by optimising the performance of the texture measure itself by altering the way the features are extracted, or representing each texture with multiple feature extraction methods, using all possible combinations and then determining which pair(s) can improve the classification accuracy.

7.1 Challenges in medical texture characterisation

The first part of this thesis focused on analysing medical texture distinguished to have fine structure, and was an example of the kind of images we have to deal with when using a non-invasive modality. Then coarse texture acquired invasively was discussed in the second part, where another set of texture measures and a different classification approach was applied. Finally the noise impact on both types of texture was discussed as well.

7.1.1 Fine structure texture (CT Lung tumours)

Lung tumour texture acquired from CT images represents an example of extracting features from texture with relatively small size principal primitive elements (i.e. textons). Similar types of texture can be encountered in other non-invasive imaging modalities, such as MR and US, where the clinician decides the type of modality according to the organ to be diagnosed. Fractal feature extraction methods relate more to the underlying physiology for organ tissues which might exhibit fractal-like properties (e.g. lungs and brain), hence can be one of the most suitable texture measure to extract features for distinguishing between lung tumour stages. Besides the capability of capturing self-similarity, the FD scale and direction-invariance can give it an advantage in dealing with heterogeneous medical texture. The roughness of the lung tissue structure increases as the tumour stage progresses, thus deformation or chaoticity in the structure was coined quantitatively as an FD value and used in stage discrimination. Another point is the use of CE CT images in the fractal analysis for highlighting blood vessels in the tissue, since their shape is essential in characterising the tissue abnormality. Usually tumour cell growth is associated with formation of a network of blood

vessels – called angiogenesis – for supply of oxygen and other nutrients. In fact, this tumour angiogenesis is established in a chaotic manner, unlike vasculature in normal tissue, causing the roughness of the cancerous tissue. Additionally, sometimes leakage from the tumour vasculature to the surrounding tissue may occur, hence these deficiencies can be exploited to highlight tumour areas using the contrast agent for an efficient FD estimation of the surface. Aggressive tumours demand more oxygen and nutrients for its rapid and chaotic growth, and the more the aggressive the tumour the more the leakage of the injected contrast agent from its vasculature.

Selecting the appropriate X-ray voltage and tube current acquisition parameters can also assist in an accurate FD and corresponding lacunarity estimation of the examined tissue area. Yet there is a trend to acquire the CT images with the least amount of possible radiation dose – known as RRD CT images – to reduce the amount of radiation energy absorbed by the tissue. So the physicians may have to start to adapt themselves to deal with lower contrast quality images and with higher levels of associated noise; since higher quality images might not be the best option for diagnosis as far as patients' safety is concerned. This situation requires texture measures that can balance the trade-off of robustness under distortion, which interprets the suitability of using fractals for analysing texture in sub-optimal conditions. The FD was less susceptible to noise encountered in CT images (see chapter 4) in addition to its good capability for lung tissue discrimination (see chapter 3).

Advantages of fine structure texture reside in its non-invasiveness. CT, MR, US and other similar modalities aim to reveal as much information as possible regarding the organ of interest with minimal damage to patients' body. Also it is much faster compared to invasive DM modality, which requires biopsies to be taken for analysis. However, this comes at the expense of acquiring images with less contrast and resolution compared to DM images. Besides the ability to magnify the pathologies in the DM images, the dyes used to stain the biopsies and the associated biochemical reaction – giving certain region of interest distinguishable colours – can add to DM images another property which can enrich the quality of the extracted features. Nevertheless, both modalities are needed in the medical environment, usually the non-invasive for initial diagnosis, and if the physician is still unsure of the abnormality of the observed tissue, the invasive modality can be used for verification.

7.1.2 Coarse structure texture (DM brain tumours)

Histopathological or DM meningioma brain tumours images were an example of coarse structure texture encountered in medical image analyses. Larger texture primitives (e.g. cell nuclei for the meningiomas) in coarse texture facilitates the ability to discriminate between the different texture (tumour) types, as compared to the fine texture of lungs which consists of relatively small textons (blood vessels in this case). The blue colour channel which was found to be the best for characterising the meningioma cell nuclei from the cytoplasm background was selected for feature extraction. Then several texture measures were experimented on the histopathological images individually and

combined, and with and without cell nuclei segmentation. Carefully selecting more than one texture measure that suits the case under investigation can improve the classification accuracy, that is, the discriminating powers of both measures are combined, and each can compensate for each others weaknesses in texture characterisation. It was found that using multiple measures might not guarantee better classification accuracy, in fact, could have a negative effect even if the fused features vector dimensionality was reduced via an optimum feature selection approach (see Table 5.11). The RLM and GMRF combined together were the most suitable among the statistical and model-based texture measures to discern the different meningioma subtypes of grade I. The robustness of the RLM and GMRF for meningioma discrimination and under distortion affecting the DM images was investigated (see section 5.4). That was done by simulating the impact of crack or craquelure deformation on pseudo-cells resembling the shape of the meningioma cell nuclei; then features were extracted from multiple generated images having various cell densities. The segmentation process was used to eliminate possible cracks in the background and for leaving the cell nuclei only for processing.

A third feature extraction technique using multiresolution wavelet-based methods was also applied to the histopathological images. The high resolution and large size of the DM images enabled the decomposition into several scales, which facilitated the localisations of both small and large size object of interest (cell nuclei), depending on the meningioma subtype. The WP measure showed that it can record – without being combined with other measures – nearly a similar accuracy to that of the RLM and GMRF combined. That was achieved when the FD was employed for subband tree decomposition instead of the traditional energy-based decomposition. This takes advantage of the FD independence to image intensity linear transformations and to abrupt changes in texture (i.e. cracks in the prepared biopsy) in comparison to the traditional energy-based texture methods. Moreover, the other wavelet-based method, the Gabor filter, had a fairly good discrimination when the energy of each filter output was used. However, when the filter outputs were combined with the corresponding FDs of the same meningioma image samples, a highest classification accuracy, which outperformed all other previously mentioned texture measures, was achieved. This also demonstrates the significance of FD utilisation in CT and DM acquired images for detecting and analysing pathologies, whether it was used solely (chapter 3), or to guide the subband structured-tree decomposition, or combined with other texture measures (as the outputs of the Gabor filter).

Regarding distortion occurring in fine structure texture, as additive Gaussian and/or multiplicative Rayleigh noise which was found in the analysed CT images, might carry a more negative impact since its small textons can be easily obscured. Cracks in the histopathological coarse texture can alter the spatial relationship between texture textons, changing the way the texture pattern is organised. Nevertheless, the investigated CT and DM images were of good quality (i.e. the amount of distortion in both modalities was low), and distorted versions – through reconstructing noisy CT images or

generating pseudo-cell nuclei images with varying densities – were generated to assess the robustness of the applied texture measures in sub-optimal conditions.

7.2 Classification approach

As it was not easy to spot the difference between the lung tumour stages using texture only, especially for the early stages, a threshold representing the median of all estimated FD values was empirically placed to differentiate early from late stage tumours. Such classification technique, known as *quantitative performance analysis*, may be used when the differences between the various textures is minor, making it difficult to assign the feature values into separate classes. However, a disadvantage is that it is not a completely automated classification technique, and the threshold value might not be applicable to other tumours or cases acquired in a different manner (e.g. images are not contrast enhanced), thus the quantitative process might have to be performed again for selecting a suitable threshold. In the histopathological meningioma cases a Bayesian classifier, which is based on *class assignments classification*, was used to discern the variation between the subtypes, as the texture was coarse and the distinction between the various subtypes was more obvious.

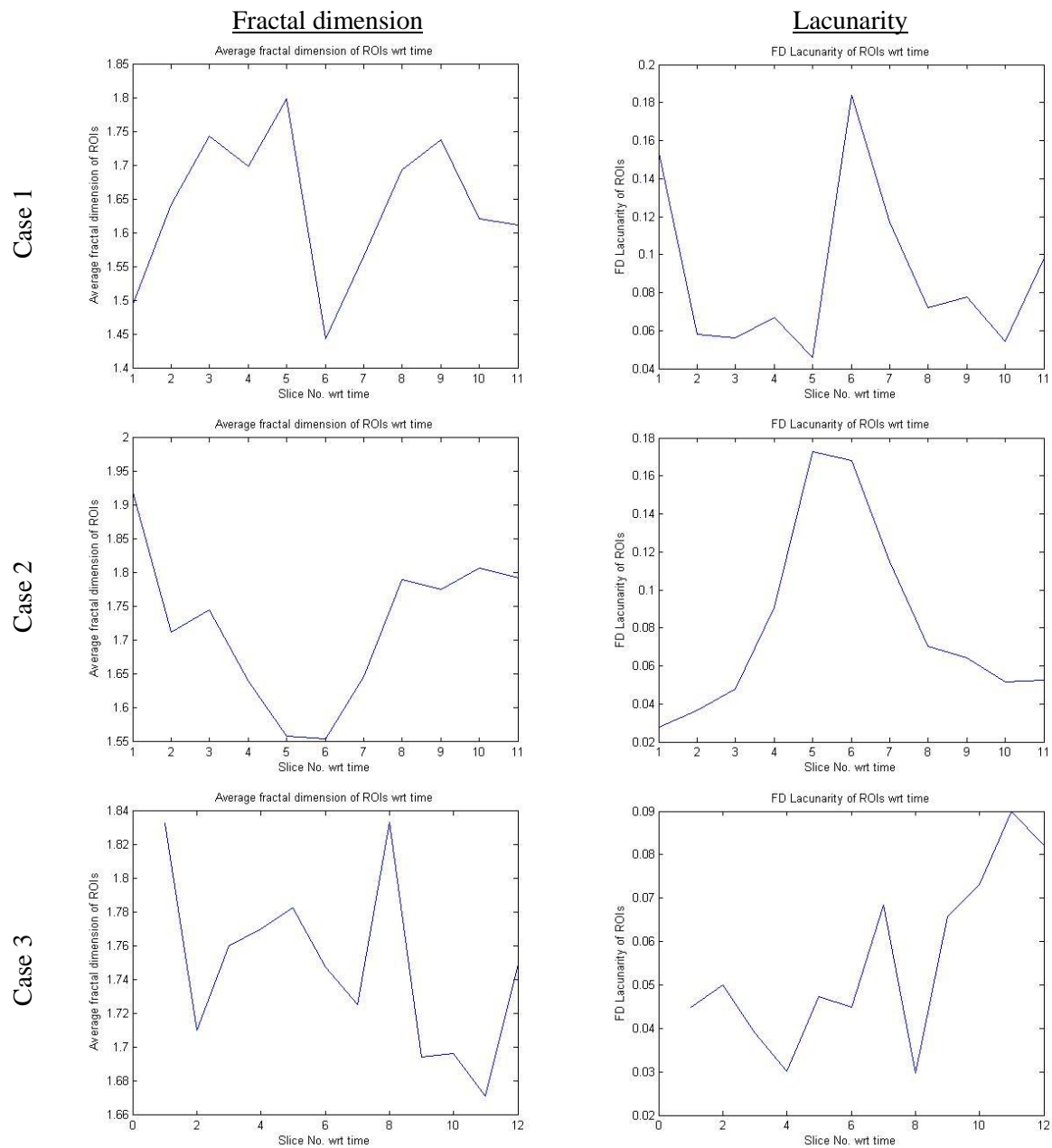
We believe that the presented work can improve the physician's ability to detect and analyse pathologies leading to a more reliable diagnosis. The proposed texture analysis techniques provide an automated tumour discrimination process through recommending the optimum features which best characterise CT lung and histopathological meningioma tumours. This can make the diagnostic process easier and faster, and can overcome the problem of variation in the reported diagnosis. Whether the concern was to improve lung stage prediction accuracy relying on CT images only without PET scans or for a highly accurate meningioma subtype discrimination technique, the early detection and the ability to efficiently characterise and reveal the degree of tumour type and severity can have a direct impact on the treatment procedure, and hence becoming crucial for saving patients' lives and promoting faster recovery.

Future work involves working with radiologists to study the effect of CT image reconstruction algorithms and imaging protocols of various scanners on the FD for lung tumour stage prediction, and for other texture measures as well. This will allow for standardising lung tissue texture analysis procedures which would maintain texture feature quality consistency. Also, maintaining clinicians' diagnostic accuracy is an important issue when reducing the radiation dose in CT images. Although RRD CT images are noisier and lower in image quality compared to the CT images used in this work, it is considered much safer for patients and is primarily used for paediatric and pregnant patient imaging. Thus, studying the texture analysis algorithm efficiency when applied to RRD CT images would assist in investigating robustness under sub-optimal image conditions; furthermore, expanding this study to include other types of soft-tissue organs, such as liver and kidney, would be interesting.

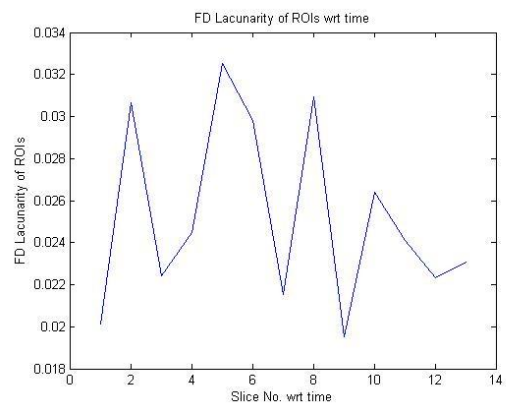
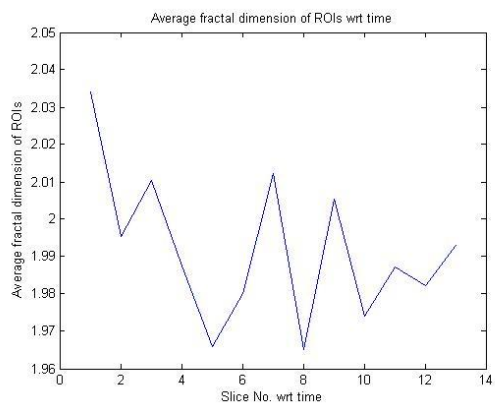
Finally, the developed BBS_{FD} technique for discriminating grade I histopathological meningiomas was based on the generalisation of the standard wavelet dyadic decomposition; however, we aim to expand the BBS_{FD} to a so-called M -band wavelet transform, where a particular type of filter bank architecture is used to subdivide each of the dyadic or octave bands into further M channels. This signal decomposition into M , instead of 2, channels could provide more flexible tiling of the time-frequency plane, and hence achieve a better multi-scale multi-directional image filtering.

APPENDIX

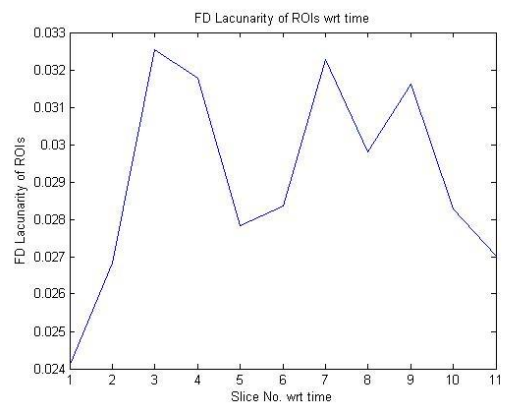
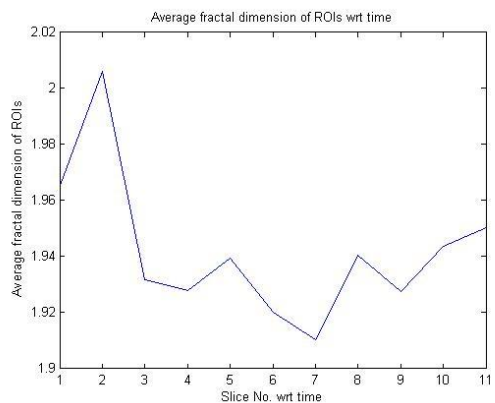
A.1 Fractal dimension and corresponding lacunarity for tumour ROIs extracted from 15 CE CT cases plotted with respect to slice number.



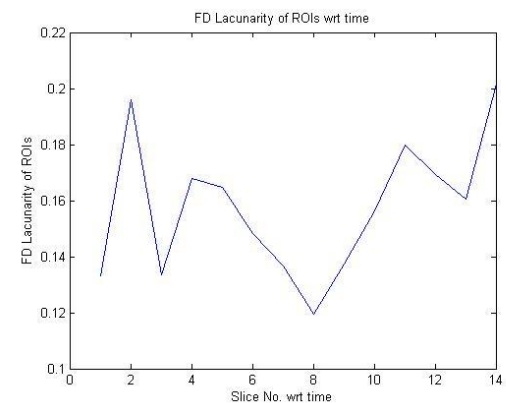
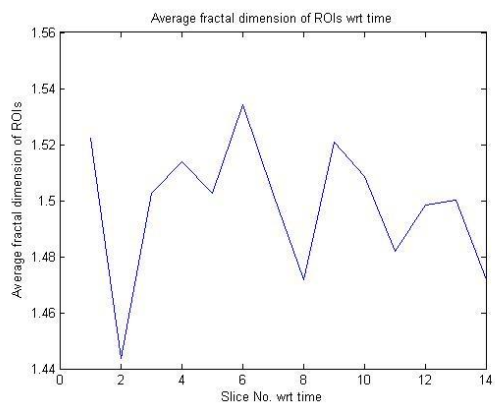
Case 4



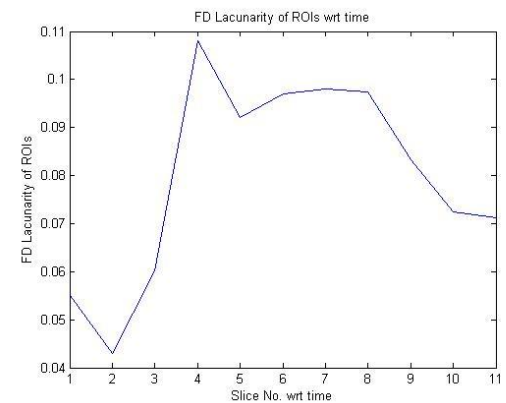
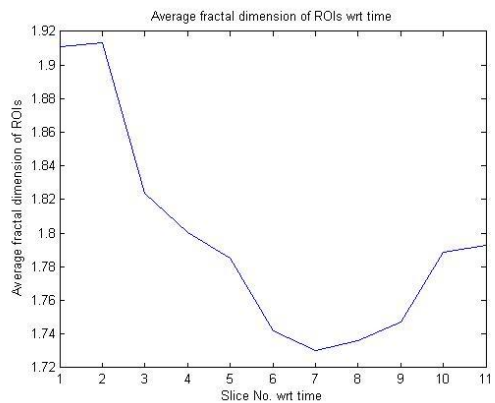
Case 5



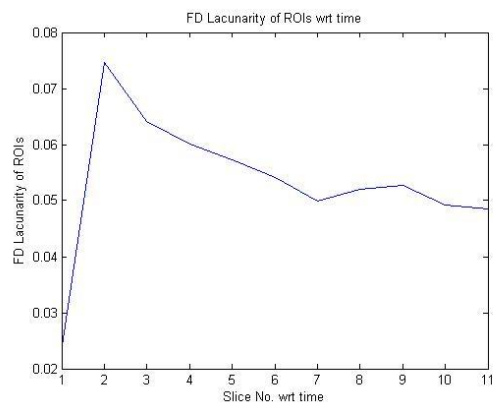
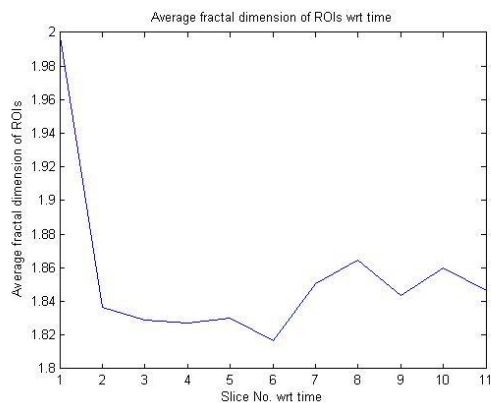
Case 6



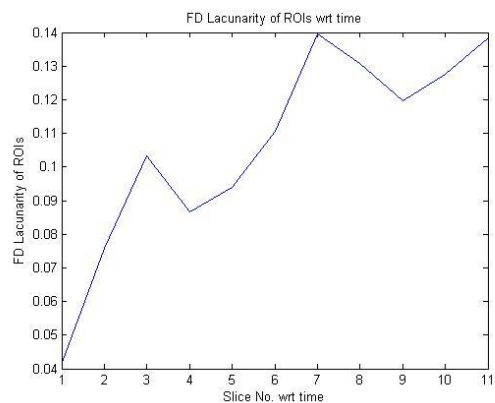
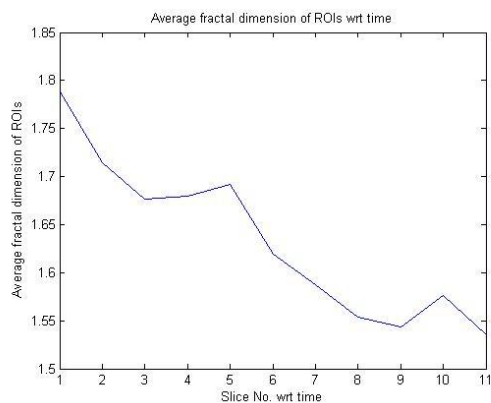
Case 7



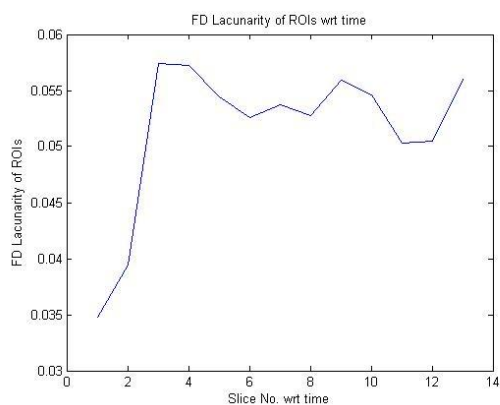
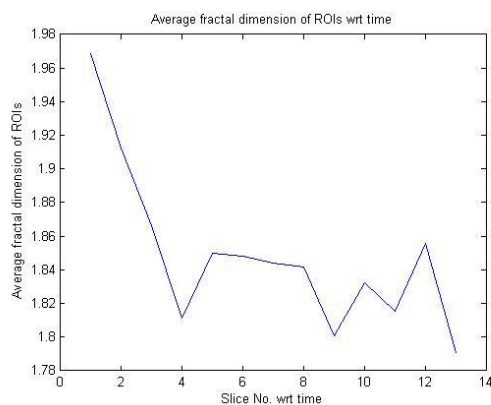
Case 8



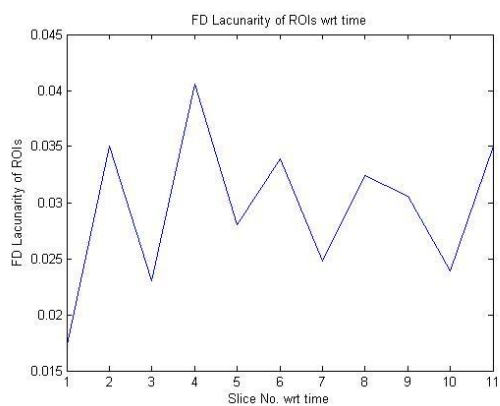
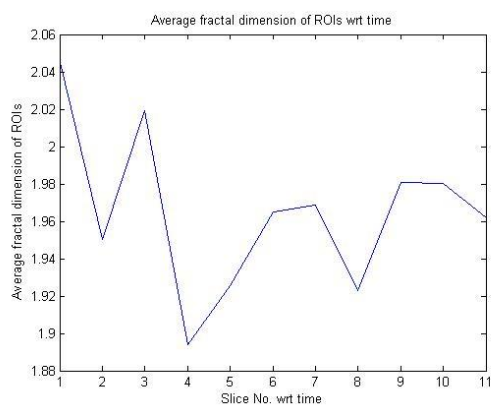
Case 9



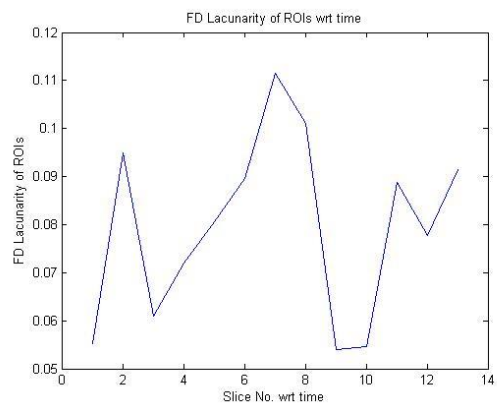
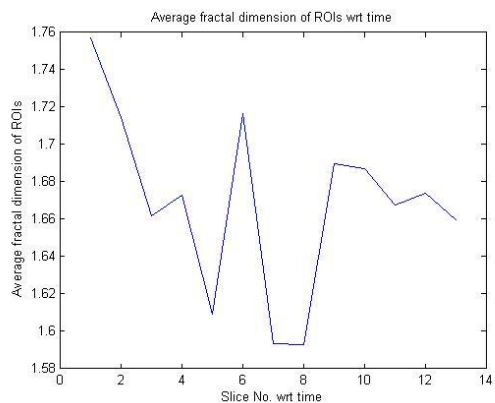
Case 10



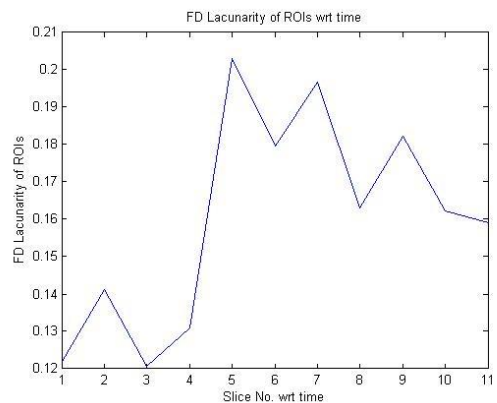
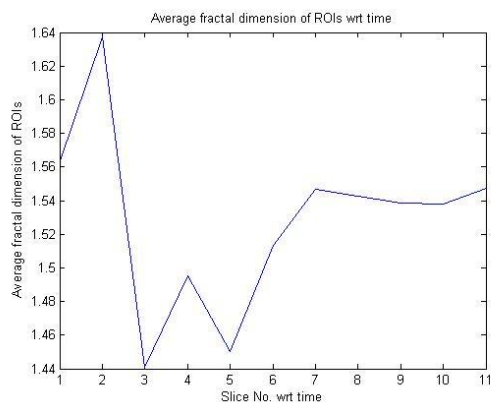
Case 11



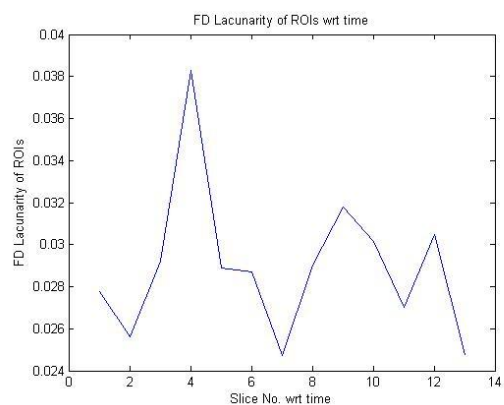
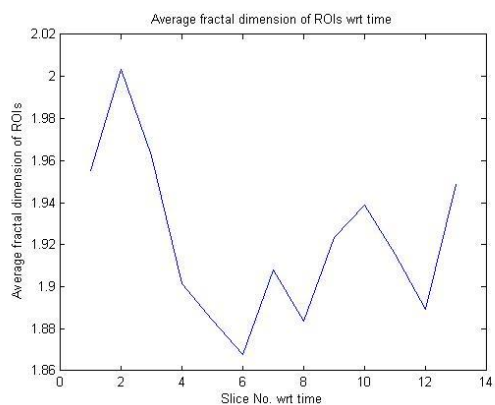
Case 12



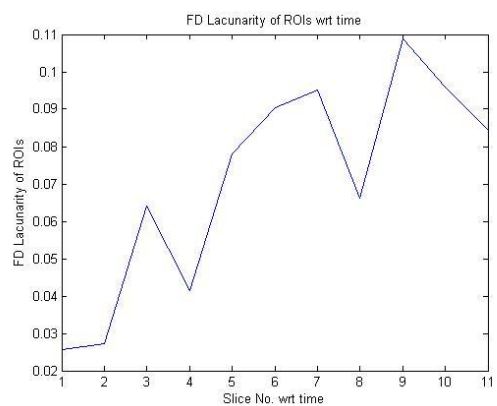
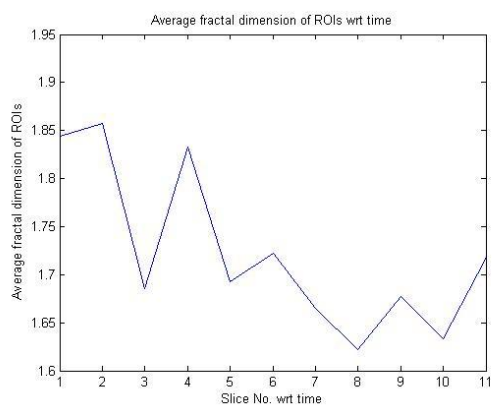
Case 13



Case 14

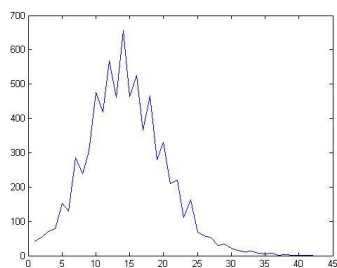


Case 15

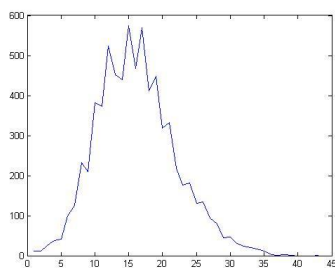


A.2 Histograms of noise detected in the uniform acquired regions of a cross section in the scanning table in Fig. 4.1(a) of 11 baseline CE CT lung tumour images.

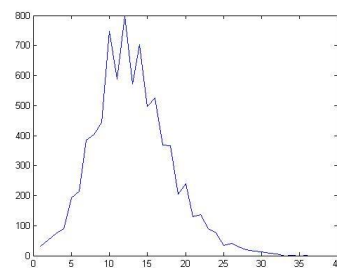
Case 1



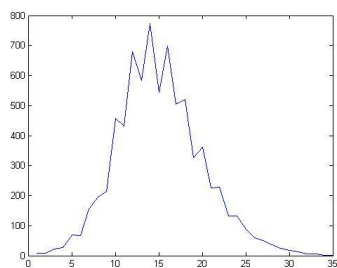
Case 2



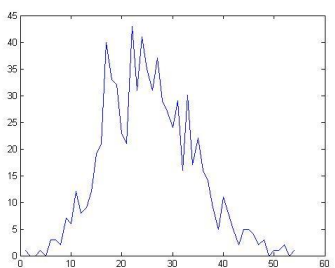
Case 3



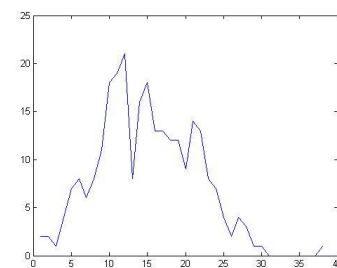
Case 4



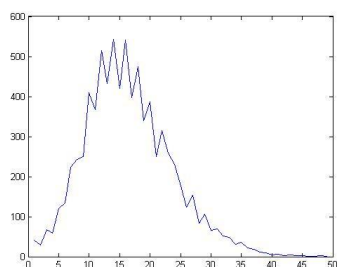
Case 5



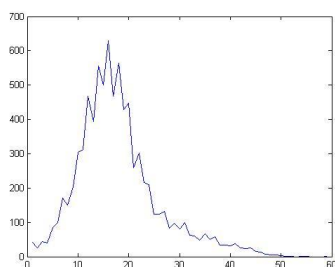
Case 6



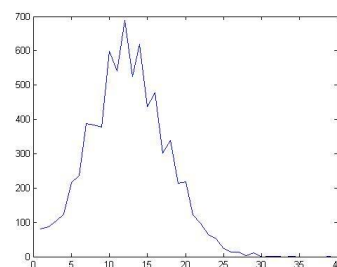
Case 7



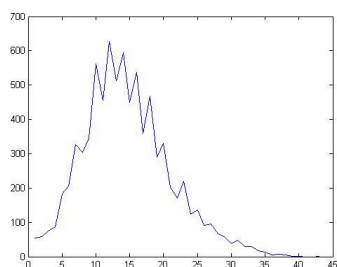
Case 8



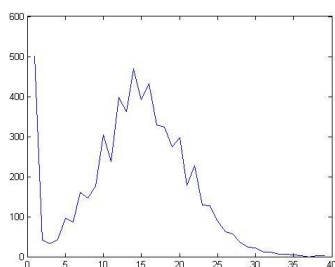
Case 9



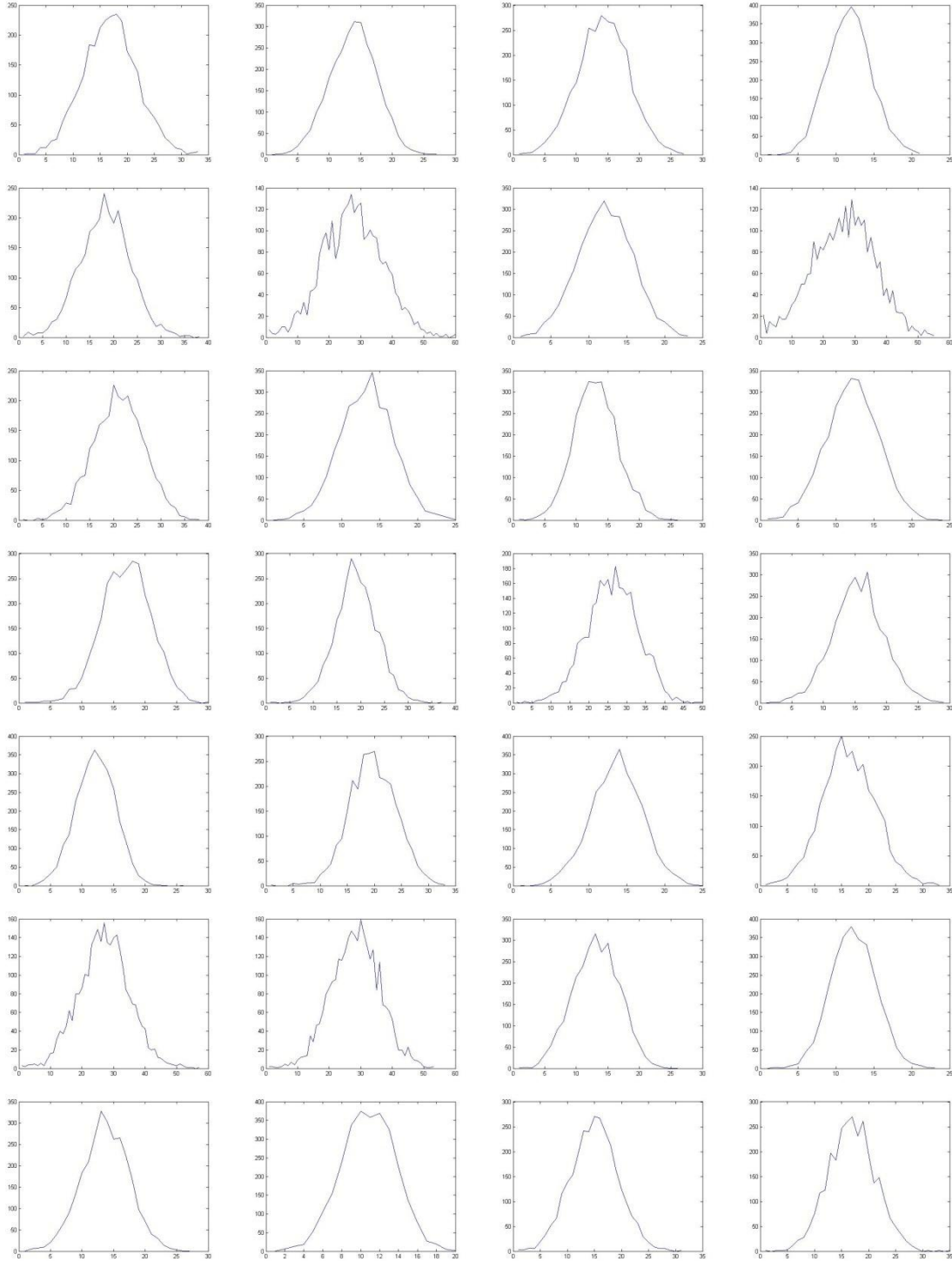
Case10

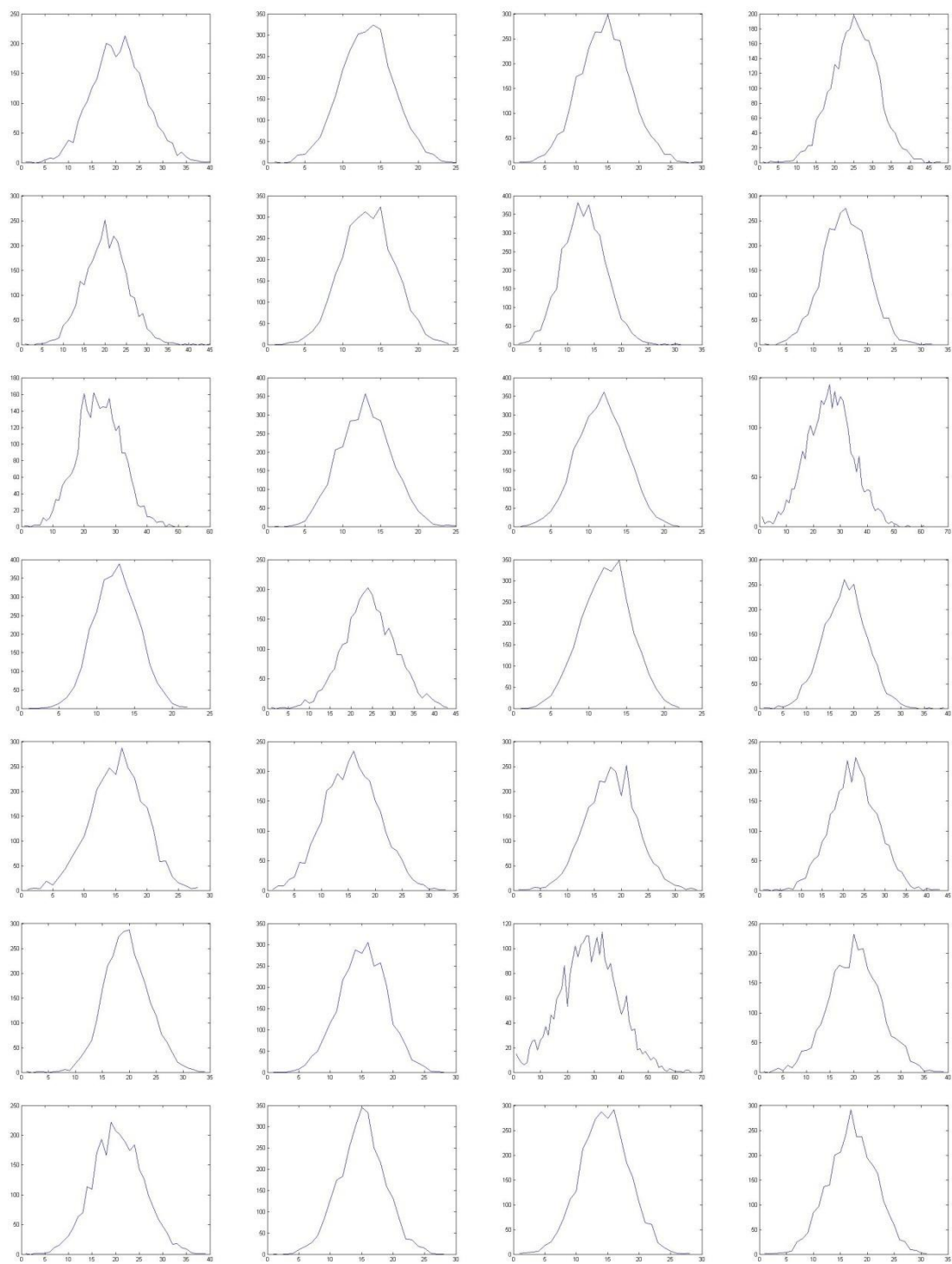


Case 11



A.3 Histograms of noise detected in the 56 NCE CT images having a 2mm slice thickness. Uniform grey level areas were selected from the dark background above the scanning gantry in Fig. 4.1(b). The shape of the histograms indicates that most noises have a Gaussian distribution (the cases are successively arranged in a raster-scan way).





BIBLIOGRAPHY

- [1] O. S. Al-Kadi and D. Watson, "Texture Analysis of Aggressive and non-Aggressive Lung Tumor CE CT Images," *IEEE Transactions on Biomedical Engineering*, vol. 55, pp. 1822-1830, 2008.
- [2] O. S. Al-Kadi and D. Watson, "Susceptibility of texture measures to noise: an application to lung tumor CT images," in *8th IEEE International Conference on BioInformatics and BioEngineering* Greece, 2008.
- [3] O. S. Al-Kadi, "Combined statistical and model based texture features for improved image classification," in *4th International Conference on Advances in Medical, Signal & Information Processing*, Italy, 2008, pp. 175-178.
- [4] A. S. Hornby, "Oxford Advanced Learner's Dictionary of Current English," 6 ed.: Oxford University Press, 2000.
- [5] B. Julesz, "Visual Pattern Discrimination," *IRE Transactions on Information Theory*, vol. 8, pp. 84-92, 1962.
- [6] B. Julesz, E. N. Gilbert, L. A. Shepp, and H. L. Frisch, "Inability of Humans to Discriminate between Visual Textures that Agree in Second-order Statistics- revisited," *Perception*, vol. 2, pp. 391-405, 1973.
- [7] B. Julesz, "A theory of preattentive texture discrimination based on first-order statistics of textons," *Biological Cybernetics*, vol. 41, pp. 131-138, 1981.
- [8] B. Julesz, "Textons, the Elements of Texture Perception, and their Interactions," *Nature*, vol. 290, pp. 91-97, 1981.
- [9] B. Julesz and R. A. Schumer, "Early visual perception," *Annual Review of Psychology*, vol. 32, pp. 575-627, 1981.
- [10] R. M. Haralick, "Statistical and Structural Approaches to Texture," in *Proceedings of the IEEE*, 1979, pp. 786- 804.
- [11] F. W. Campbell and J. J. Kulikowski, "Orientational selectivity of human visual system," *Journal of Physiology-London*, vol. 187, pp. 437-445, 1966.
- [12] J. J. Kulikowski, S. Marcelja, and P. O. Bishop, "Theory of spatial position and spatial-frequency relations in the receptive-fields of simple cells in the visual-cortex," *Biological Cybernetics*, vol. 43, pp. 187-198, 1982.
- [13] M. R. Turner, "Texture-discrimination by Gabor functions," *Biological Cybernetics*, vol. 55, pp. 71-82, 1986.
- [14] A. C. Bovik, M. Clark, and W. S. Geisler, "Multichannel texture analysis using localized spatial filters," *IEEE Transactions on Pattern Analysis and Machine Intelligence*, vol. 12, pp. 55-73, Jan 1990.
- [15] J. R. Bergen and M. S. Landy, "Computational Modeling of Visual Texture Segregation," MIT Press, 1991, pp. 253-271.
- [16] M. Tuceryan and A. Jain, *The Handbook of pattern Recognition and Computer Vision*, 2 ed.: World Scientific Publishing Co., 1998.

- [17] D. Zhou, "Texture Analysis and Synthesis using a Generic Markov-Gibbs Image Model," University of Auckland, Auckland, New Zealand, Ph.D. thesis 2006.
- [18] T. Ojala, M. Pietikainen, "Texture classification," in *CVonline*, Jan. 2004. [Online]. Available: http://homepages.inf.ed.ac.uk/rbf/CVonline/LOCAL_COPIES/OJALA1/texclas.htm. [Accessed: Apr. 29, 2009].
- [19] A. K. Jain, R. P. W. Duin, and J. C. Mao, "Statistical pattern recognition: A review," *IEEE Transactions on Pattern Analysis and Machine Intelligence*, vol. 22, pp. 4-37, 2000.
- [20] B. W. Stewart and P. Kleihues, *World Cancer Report*: IARCPress-WHO, 2003.
- [21] G. Danaei, S. Vander Hoorn, A. D. Lopez, C. J. L. Murray, M. Ezzati, and C. Comparative Risk Assessment, "Causes of cancer in the world: comparative risk assessment of nine behavioural and environmental risk factors," *Lancet*, vol. 366, pp. 1784-1793, Nov 2005.
- [22] S. Parker, "Mcgraw-Hill Concise Encyclopedia of Science and Technology ", 3 ed.: McGraw-Hill 1994.
- [23] R. Sidhu, D. S. Sanders, and M. E. McAlindon, "Gastrointestinal capsule endoscopy: from tertiary centres to primary care," *British Medical Journal*, vol. 332, pp. 528-531, Mar 2006.
- [24] J. T. Bushberg, J. A. Seibert, E. M. Leidholdt, and J. M. Boone, *The Essential Physics of Medical Imaging*, 2 ed.: Lippincott Williams & Wilkins, 2001.
- [25] "What is Ultrasound (Sonography)?" *The American Registry for Diagnostic Medical Sonography*. [Online]. Available: <http://www.ardms.org/default.asp?contentID=874>. [Accessed: Oct. 30, 2008].
- [26] S. Bushong *Diagnostic Ultrasound: Essentials of Medical Imaging Series* 1ed.: McGraw-Hill, 1999.
- [27] C. J. Louis, *Tumours: Basic principles and clinical aspects*: Longman Group Limited, 1978.
- [28] "Defining Cancer," *U.S. National Institute of Health - National Cancer Institute*, Aug. 2007. [Online]. Available: <http://www.cancer.gov/cancertopics/what-is-cancer>. [Accessed: Oct. 21, 2008].
- [29] "How many different types of cancer are there?" *Cancer Research UK*, Aug. 2007. [Online]. Available: <http://info.cancerresearchuk.org/cancerandresearch/cancers/?a=5441>. [Accessed: Oct. 21, 2008].
- [30] A. Jemal, R. Siegel, E. Ward, Y. P. Hao, J. Q. Xu, T. Murray, and M. J. Thun, "Cancer statistics, 2008," *Cancer Journal for Clinicians*, vol. 58, pp. 71-96, Mar-Apr 2008.
- [31] "What you need to know about lung cancer," *U.S. National Institute of Health - National Cancer Institute*, Jul. 2007. [Online]. Available: <http://www.cancer.gov/cancertopics/wyntk/lung/allpages>. [Accessed: Oct. 21, 2008].
- [32] "Lung cancer at a glance," *Cancer Research UK*, Aug. 2007. [Online]. Available: <http://info.cancerresearchuk.org/cancerandresearch/cancers/lung/#signsandsymptoms>. [Accessed: Oct. 21, 2008].
- [33] F. L. Greene, D. L. Page, I. D. Fleming, A. Fritz, C. M. Balch, D. G. Haller, and M. Morrow, *AJCC Cancer Staging Manual*, 6 ed.: Springer, 2002.

- [34] "What you need to know about brain tumors," *U.S. National Institute of Health-National Cancer Institute*, Mar.2003.[Online].Available: <http://www.cancer.gov/cancertopics/wyntk/brain/allpages>. [Accessed: Oct. 24, 2008].
- [35] A. Asher, P. Burger, D. Croteau, T. Mikkelsen, T. Omert, N. Paleologos, and J. Barnholtz-Sloan, *A primer of brain tumors: A patient's reference manual* 8ed.: American Brain Tumor Association, 1998.
- [36] "All About Brain Cancer," *Ohio State University Comprehensive Cancer Center*, Feb. 2006. [Online]. Available: <http://www.jamesline.com/cancertypes/brain/about/>. [Accessed: Oct. 27, 2008].
- [37] J. H. Lee, *Meningiomas: Diagnosis, Treatment, and Outcome* 1ed.: Springer, 2008.
- [38] F. E. Bloom, M. F. Beal, and D. J. Kupfer, *The Dana Guide to Brain Health* 1ed.: Free Press 2002.
- [39] "Respiratory Disease: Lung Disorders and Diseases," *University of Maryland medical center*, Jan. 2008. [Online]. Available: <http://www.umm.edu/respiratory/disease.htm>. [Accessed: May 14, 2009].
- [40] K. Suzuki, F. Li, S. Sone, and K. Doi, "Computer-aided diagnostic scheme for distinction between benign and malignant nodules in thoracic low-dose CT by use of massive training artificial neural network," *IEEE Transactions on Medical Imaging*, vol. 24, pp. 1138-1150, 2005.
- [41] X. W. Zhang, G. McLennan, E. A. Hoffman, and M. Sonka, "A complete CAD system for pulmonary nodule detection in high resolution CT images," in *Medical Imaging 2005 Conference*, San Diego, CA, 2005, pp. 85-96.
- [42] Y. Lee, T. Hara, H. Fujita, S. Itoh, and T. Ishigaki, "Automated detection of pulmonary nodules in helical CT images based on an improved template-matching technique," *IEEE Transactions on Medical Imaging*, vol. 20, pp. 595-604, 2001.
- [43] Q. Li, F. Li, J. Shiraishi, S. Katsuragawa, S. Sone, and K. Doi, "Investigation of new psychophysical measures for evaluation of similar images on thoracic computed tomography for distinction between benign and malignant nodules," *Medical Physics*, vol. 30, pp. 2584-2593, Oct 2003.
- [44] M. S. Brown, M. F. McNitt-Gray, J. G. Goldin, R. D. Suh, J. W. Sayre, and D. R. Aberle, "Patient-specific models for lung nodule detection and surveillance in CT images," *IEEE Transactions on Medical Imaging*, vol. 20, pp. 1242-1250, 2001.
- [45] A. Farag, A. El-Baz, G. G. Gimel'farb, R. Falk, and S. G. Hushek, "Automatic detection and recognition of lung abnormalities in helical CT images using deformable templates," *Medical Image Computing and Computer-Assisted Intervention - Miccai 2004, Pt 2, Proceedings*, vol. 3217, pp. 856-864, 2004.
- [46] Z. Y. Ge, B. Sahiner, H. P. Chan, L. M. Hadjiiski, P. N. Cascade, N. Bogot, E. A. Kazerooni, J. Wei, and C. A. Zhou, "Computer-aided, detection of lung nodules: False positive reduction using

- a 3D gradient field method and 3D ellipsoid fitting," *Medical Physics*, vol. 32, pp. 2443-2454, Aug 2005.
- [47] D. S. Paik, C. F. Beaulieu, G. D. Rubin, B. Acar, R. B. Jeffrey, J. Yee, J. Dey, and S. Napel, "Surface normal overlap: A computer-aided detection algorithm, with application to colonic polyps and lung nodules in helical CT," *IEEE Transactions on Medical Imaging*, vol. 23, pp. 661-675, Jun 2004.
 - [48] S. G. Armato, M. B. Altman, J. Wilkie, S. Sone, F. Li, K. Doi, and A. S. Roy, "Automated lung nodule classification following automated nodule detection on CT: A serial approach," *Medical Physics*, vol. 30, pp. 1188-1197, Jun 2003.
 - [49] W. J. Kostis, A. P. Reeves, D. F. Yankelevitz, and C. I. Henschke, "Three-dimensional segmentation and growth-rate estimation of small pulmonary nodules in helical CT images," *IEEE Transactions on Medical Imaging*, vol. 22, pp. 1259-1274, Oct 2003.
 - [50] A. P. Reeves, A. B. Chan, D. F. Yankelevitz, C. I. Henschke, B. Kressler, and W. J. Kostis, "On measuring the change in size of pulmonary nodules," *IEEE Transactions on Medical Imaging*, vol. 25, pp. 435-450, 2006.
 - [51] M. Tanino, H. Takizawa, S. Yamamoto, T. Matsumoto, Y. Tateno, and T. Iinuma, "A detection method of ground glass opacities in chest x-ray CT images using automatic clustering techniques," *Medical Imaging 2003: Image Processing, Pts 1-3*, vol. 5032, pp. 1728-1737, 2003.
 - [52] K. Kanazawa, Y. Kawata, N. Niki, H. Satoh, H. Ohmatsu, R. Kakinuma, M. Kaneko, N. Moriyama, and K. Eguchi, "Computer-aided diagnosis for pulmonary nodules based on helical CT images," *Computerized Medical Imaging and Graphics*, vol. 22, pp. 157-167, Mar-Apr 1998.
 - [53] H. Takizawa, S. Yamamoto, T. Nakagawa, T. Matsumoto, Y. Tateno, T. Iinuma, and M. Matsumoto, "Recognition of lung nodule shadows from chest X-ray CT images using 3D Markov random field models," *Systems and Computers in Japan*, vol. 35, pp. 82-95, 2004.
 - [54] H. Arimura, S. Katsuragawa, K. Suzuki, F. Li, J. Shiraishi, S. Sone, and K. Doi, "Computerized scheme for automated detection of lung nodules in low-dose computed tomography images for lung cancer screening," *Academic Radiology*, vol. 11, pp. 617-629, 2004.
 - [55] Q. Li, F. Li, and K. Doi, "Computerized detection of lung nodules in thin-section CT images by use of selective enhancement filters and an automated rule-based classifier," *Academic Radiology*, vol. 15, pp. 165-175, Feb 2008.
 - [56] B. Lessmann, T. W. Nattkemper, V. H. Hans, and A. Degenhard, "A method for linking computed image features to histological semantics in neuropathology," *Journal of Biomedical Informatics*, vol. 40, pp. 631-641, 2007.
 - [57] J. R. Iglesias-Rozas and N. Hopf, "Histological heterogeneity of human glioblastomas investigated with an unsupervised neural network (SOM)," *Histology and Histopathology*, vol. 20, pp. 351-356, Apr 2005.
 - [58] O. Wirjadi, T. Breuel, W. Feiden, and Y. J. Kim, "Automated Feature Selection for the Classification of Meningioma Cell Nuclei," in *Bildverarbeitung für die Medizin*, 2006, pp. 76-80.

- [59] H. Qureshi, O. Sertel, N. Rajpoot, R. Wilson, and M. Gurcan, "Adaptive Discriminant Wavelet Packet Transform and Local Binary Patterns for Meningioma Subtype Classification," *Medical Image Computing and Computer-Assisted Intervention - Miccai 2008, Pt Ii, Proceedings*, vol. 5242, pp. 196-204, 2008.
- [60] H. Qureshi, N. Rajpoot, R. Wilson, T. Nattkemper, and V. H. Hans, "Comparative analysis of Discriminant Wavelet Packet Features and Raw Image Features for Classification of Meningioma Subtypes," in *Medical Image Understanding and Analysis*, Aberystwyth, UK, 2007.
- [61] O. S. Al-Kadi and D. Watson, "Texture measures combination for improved meningioma classification of histopathological images (Submitted for publication)," *Pattern Recognition*, 2009.
- [62] C. Demir, S. H. Gultekin, and B. Yener, "Learning the topological properties of brain tumors," *IEEE-ACM Transactions on Computational Biology and Bioinformatics*, vol. 2, pp. 262-270, 2005.
- [63] O. Sertel, J. Kong, H. Shimada, U. V. Catalyurek, J. H. Saltz, and M. N. Gurcan, "Computer-aided prognosis of neuroblastoma on whole-slide images: Classification of stromal development," *Pattern Recognition*, vol. 42, pp. 1093-1103, Jun 2009.
- [64] D. Glotsos, P. Spyridonos, D. Cavouras, P. Ravazoula, P. A. Dadioti, and G. Nikiforidis, "An image-analysis system based on support vector machines for automatic grade diagnosis of brain-tumour astrocytomas in clinical routine," *Medical Informatics and the Internet in Medicine*, vol. 30, pp. 179-193, 2005.
- [65] D. Glotsos, L. Kalatzis, P. Spyridonos, S. Kostopoulos, A. Daskalakis, E. Athanasiadis, P. Ravazoula, G. Nikiforidis, and D. Cavouras, "Improving accuracy in astrocytomas grading by integrating a robust least squares mapping driven support vector machine classifier into a two level grade classification scheme," *Computer Methods and Programs in Biomedicine*, vol. 90, pp. 251-261, Jun 2008.
- [66] G. K. von Schulthess, H. C. Steinert, and T. F. Hany, "Integrated PET/CT-3: Current applications and future directions," *Radiology*, vol. 238, pp. 405-422, Feb 2006.
- [67] A. P. Meert, M. Paesmans, B. Martin, P. Delmotte, T. Berghmans, J. M. Verdebout, J. J. Lafitte, C. Mascaux, and J. P. Sculier, "The role of microvessel density on the survival of patients with lung cancer: a systematic review of the literature with meta-analysis," *British Journal of Cancer*, vol. 87, pp. 694-701, 2002.
- [68] M. Matsuki, S. Noma, Y. Kuroda, K. Oida, T. Shindo, and Y. Kobashi, "Thin-section CT features of intrapulmonary lymph nodes," *Journal of Computer Assisted Tomography*, vol. 25, pp. 753-756, 2001.
- [69] I. Petkovska, S. K. Shah, M. F. McNitt-Gray, J. G. Goldin, M. S. Brown, H. J. Kim, K. Brown, and D. R. Aberle, "Pulmonary nodule characterization: A comparison of conventional with quantitative and visual semi-quantitative analyses using contrast enhancement maps," *European Journal of Radiology*, vol. 59, pp. 244-252, 2006.

- [70] S. Kido, K. Kuriyama, M. Higashiyama, T. Kasugai, and C. Kuroda, "Fractal analysis of internal and peripheral textures of small peripheral bronchogenic carcinomas in thin-section computed tomography: Comparison of bronchioloalveolar cell carcinomas with nonbronchioloalveolar cell carcinomas," *Journal of Computer Assisted Tomography*, vol. 27, pp. 56-61, 2003.
- [71] S. Kido, K. Kuriyama, M. Higashiyama, T. Kasugai, and C. Kuroda, "Fractal analysis of small peripheral pulmonary nodules in thin-section CT - Evaluation of the lung-nodule interfaces," *Journal of Computer Assisted Tomography*, vol. 26, pp. 573-578, 2002.
- [72] N. Mihara, K. Kuriyama, S. Kido, C. Kuroda, T. Johkoh, H. Naito, and H. Nakamura, "The usefulness of fractal geometry for the diagnosis of small peripheral lung tumors," *Nippon Acta Radiologica*, vol. 58, pp. 148-151, 1998.
- [73] N. F. Vittitoe, J. A. Baker, and C. E. Floyd, "Fractal texture analysis in computer-aided diagnosis of solitary pulmonary nodules," *Academic Radiology*, vol. 4, pp. 96-101, 1997.
- [74] J. Peiss, M. Verlande, W. Ameling, and R. W. Gunther, "Classification of lung tumors on chest radiographs by fractal texture analysis," *Investigative Radiology*, vol. 31, pp. 625-629, 1996.
- [75] Z. C. Chen, F. Tang, Z. Y. Zhou, D. Z. Jiang, and Y. Jiang, "Texture characteristic of CT image for lung parenchyma based on fractal dimension," *Proceedings of the Third International Symposium on Instrumentation Science and Technology*, Vol 3, pp. 716-720, 2004.
- [76] M. Petrou and P. Gacia Sevilla, *Image processing: Dealing with texture*: Wiley, 2006.
- [77] Y. Nakamoto, T. Higashi, H. Sakahara, N. Tamaki, M. Kogire, M. Imamura, and J. Konishi, "Contribution of PET in the detection of liver metastases from pancreatic tumours," *Clinical Radiology*, vol. 54, pp. 248-252, Apr 1999.
- [78] R. Uppaluri, T. Mitsa, and J. R. Galvin, "Fractal analysis of high-resolution CT images as a tool for quantification of lung diseases," *Physiology and Function from Multidimensional Images - Medical Imaging 1995*, vol. 2433, pp. 133-142, 1995.
- [79] C. M. Wu and Y. C. Chen, "Multithreshold Dimension Vector for Texture Analysis and Its Application to Liver-Tissue Classification," *Pattern Recognition*, vol. 26, pp. 137-144, 1993.
- [80] W.-L. Lee, Y. Chen, and K. Hsieh, "Ultrasonic Liver Tissue Classification by Fractal Feature Vector Based on M-Band Wavelet Transform," *IEEE Transactions on Medical Imaging*, vol. 22, pp. 382-392, 2003.
- [81] D. R. Chen, R. F. Chang, C. J. Chen, M. F. Ho, S. J. Kuo, S. T. Chen, S. J. Hung, and W. K. Moon, "Classification of breast ultrasound images using fractal feature," *Clinical Imaging*, vol. 29, pp. 235-245, 2005.
- [82] A. I. Penn, L. Bolinger, M. D. Schnall, and M. H. Loew, "Discrimination of MR images of breast masses with fractal-interpolation function models," *Academic Radiology*, vol. 6, pp. 156-163, 1999.
- [83] M. E. Mavroforakis, H. V. Georgiou, N. Dimitropoulos, D. Cavouras, and S. Theodoridis, "Mammographic masses characterization based on localized texture and dataset fractal analysis

- using linear, neural and support vector machine classifiers," *Artificial Intelligence in Medicine*, vol. 37, pp. 145-162, 2006.
- [84] O. I. Craciunescu, S. K. Das, J. M. Poulson, and T. V. Samulski, "Three-dimensional tumor perfusion reconstruction using fractal interpolation functions," *IEEE Transactions on Biomedical Engineering*, vol. 48, pp. 462-473, 2001.
 - [85] B. B. Mandelbrot, *Fractal Geometry of Nature*. San Francisco, CA: Freeman, 1982.
 - [86] R. C. Gonzales and R. E. Woods, *Digital Image Processing*, 2 ed.: Prentice Hall, 2002.
 - [87] N. Sarkar and B. B. Chaudhuri, "An Efficient Differential Box-Counting Approach to Compute Fractal Dimension of Image," *IEEE Transactions on Systems Man and Cybernetics*, vol. 24, pp. 115-120, 1994.
 - [88] S. Buczkowski, S. Kyriacos, F. Nekka, and L. Cartilier, "The modified box-counting method: Analysis of some characteristic parameters," *Pattern Recognition*, vol. 31, pp. 411-418, 1998.
 - [89] J. M. Keller, S. Chen, and R. M. Crownover, "Texture Description and Segmentation through Fractal Geometry," *Computer Vision Graphics and Image Processing*, vol. 45, pp. 150-166, 1989.
 - [90] J. Feng, W.-C. Lin, and C.-T. Chen, "Functional Box-Counting Approach to Fractal Dimension Estimation," in *13th International Conference on Pattern Recognition (ICPR'96)*, 1996, pp. 854-858.
 - [91] S. S. Chen, J. M. Keller, and R. M. Crownover, "On the Calculation of Fractal Features from Images," *IEEE Transactions on Pattern Analysis and Machine Intelligence*, vol. 15, pp. 1087-1090, 1993.
 - [92] C. J. Traina, A. Traina, L. Wu, and C. Faloutsos, "Fast Feature Selection Using Fractal Dimension," in *XV Brazilian Symposium on Databases*, 2000, pp. 158-71.
 - [93] A. I. Penn and M. H. Loew, "Estimating fractal dimension with fractal interpolation function models," *IEEE Transactions on Medical Imaging*, vol. 16, pp. 930-937, 1997.
 - [94] C. C. Chen, J. S. Daponte, and M. D. Fox, "Fractal Feature Analysis and Classification in Medical Imaging," *IEEE Transactions on Medical Imaging*, vol. 8, pp. 133-142, 1989.
 - [95] R. Uppaluri, T. Mitsa, and J. R. Galvin, "Fractal analysis of high-resolution CT images as a tool for quantification of lung diseases," in *Medical Imaging 1995: Physiology and Function from Multidimensional Images*, 1995, pp. 133-142.
 - [96] P. Gravel, G. Beaudoin, and J. A. De Guise, "A method for modeling noise in medical images," *IEEE Transactions on Medical Imaging*, vol. 23, pp. 1221-1232, 2004.
 - [97] J. Wang, H. B. Lu, J. H. Wen, and Z. R. Liang, "Multiscale penalized weighted least-squares sinogram restoration for low-dose X-ray computed tomography," *IEEE Transactions on Biomedical Engineering*, vol. 55, pp. 1022-1031, 2008.
 - [98] P. J. La Riviere and D. M. Billmire, "Reduction of noise-induced streak artifacts in X-ray computed tomography through spline-based penalized-likelihood sinogram smoothing," *IEEE Transactions on Medical Imaging*, vol. 24, pp. 105-111, Jan 2005.

- [99] J. Hsieh, "Adaptive streak artifact reduction in computed tomography resulting from excessive X-ray photon noise," *Medical Physics*, vol. 25, pp. 2139-2147, Nov 1998.
- [100] A. M. R. Schilham, B. van Ginneken, H. Gietema, and M. Prokop, "Local noise weighted filtering for emphysema scoring of low-dose CT images," *IEEE Transactions on Medical Imaging*, vol. 25, pp. 451-463, 2006.
- [101] O. Demirkaya, "Reduction of noise and image artifacts in computed tomography by nonlinear filtration of the projection images," *Medical Imaging: 2001: Image Processing, Pts 1-3*, vol. 2, pp. 917-923, 2001.
- [102] J. Wang, H. B. Lu, T. F. Li, and Z. R. Liang, "Sinogram noise reduction for low-dose CT by statistics-based nonlinear filters," *Medical Imaging 2005: Image Processing, Pt 1-3*, vol. 5747, pp. 2058-2066, 2005.
- [103] A. Depeursinge, D. Sage, A. Hidki, A. Platon, P. A. Poletti, M. Unser, and H. Muller, "Lung tissue classification using wavelet frames," in *29th Annual International Conference of the IEEE-Engineering-in-Medicine-and-Biology-Society*, Lyon, FRANCE, 2007, pp. 6260-6263.
- [104] A. Tolouee¹, H. Abrishami-Moghaddam¹, R. Garnavi², M. Forouzanfar¹, and M. Giti³, "Texture Analysis in Lung HRCT Images," in *Digital Image Computing: Techniques and Applications*, Australia, 2008, pp. 305-311.
- [105] Y. Mitani, H. Yasuda, S. Kido, K. Ueda, N. Matsunaga, and Y. Hamamoto, "Combining the Gabor and histogram features for classifying diffuse lung opacities in thin-section computed tomography," in *16th International Conference on Pattern Recognition (ICPR)*, Quebec City, Canada, 2002, pp. 53-56.
- [106] M. F. McNitt-Gray, N. Wyckoff, J. W. Sayre, J. G. Goldin, and D. R. Aberle, "The effects of co-occurrence matrix based texture parameters on the classification of solitary pulmonary nodules imaged on computed tomography," *Computerized Medical Imaging and Graphics*, vol. 23, pp. 339-348, Nov-Dec 1999.
- [107] I. Sluimer, A. Schilham, M. Prokop, and B. van Ginneken, "Computer analysis of computed tomography scans of the lung: A survey," *IEEE Transactions on Medical Imaging*, vol. 25, pp. 385-405, Apr 2006.
- [108] T. Osicka, M. T. Freedman, and F. Ahmed, "Characterization of pulmonary nodules on computer tomography (CT) scans: The effect of additive white noise on features selection and classification performance," in *Medical Imaging 2007: Image Processing*, vol. 6512: Spie-Int Society Optical Engineering, 2007, pp. 51245-51245.
- [109] J. Wang, T. Li, H. B. Lu, and Z. R. Liang, "Penalized weighted least-squares approach to sinogram noise reduction and image reconstruction for low-dose X-ray computed tomography," *IEEE Transactions on Medical Imaging*, vol. 25, pp. 1272-1283, 2006.
- [110] D. A. Clausi and H. Deng, "Design-based texture feature fusion using Gabor filters and Co-occurrence probabilities," *IEEE Transactions on Image Processing*, vol. 14, pp. 925-936, 2005.

- [111] S. S. Liu and M. E. Jernigan, "Texture analysis and discrimination in additive noise," *Computer Vision Graphics and Image Processing*, vol. 49, pp. 52-67, Jan 1990.
- [112] J. Sijbers, "Signal and noise estimation from Magnetic Resonance Images," Univesity of Antwerp, Antwerp, Belgium, Ph.D. thesis1999.
- [113] K. Rosenberg, "The Open Source Computed Tomography Simulator ", 2006. Software can be downloaded from <http://www.ctsim.org/download>.
- [114] R. O. Duda, P. E. Hart, and D. G. Stork, *Pattern Classification*, 2 ed.: Wiley, 2001.
- [115] K. J. Morteale, M. R. Oliva, S. Ondategui, P. R. Ros, and S. G. Silverman, "Universal use of nonionic Iodinated contrast medium for CT: Evaluation of safety in a large urban teaching hospital," *American Journal of Roentgenology*, vol. 184, pp. 31-34, Jan 2005.
- [116] H. B. Lu, I. T. Hsiao, X. Li, and Z. G. Liang, "Noise properties of low-dose CT projections and noise treatment by scale transformations," in *2001 IEEE Nuclear Science Symposium*. vol. 1-4, J. A. Seibert, Ed., 2002, pp. 1662-1666.
- [117] D. A. Clausi and B. Yue, "Comparing cooccurrence probabilities and Markov random fields for texture analysis of SAR sea ice imagery," *IEEE Transactions on Geoscience and Remote Sensing*, vol. 42, pp. 215-228, 2004.
- [118] H. T. Morgan, "Dose reduction for CT pediatric imaging," *Pediatric Radiology*, vol. 32, pp. 724-728, Oct 2002.
- [119] H. Imhof, N. Schibany, A. Ba-Ssalamah, C. Czerny, A. Hojreh, F. Kainberger, C. Krestan, H. Kudler, I. Nobauer, and R. Nowotny, "Spiral CT and radiation dose," *European Journal of Radiology*, vol. 47, pp. 29-37, Jul 2003.
- [120] A. Maillo, A. Orfao, A. B. Espinosa, J. M. Sayagues, M. Merino, P. Sousa, M. Lara, and M. D. Tabertero, "Early recurrences in histologically benign/grade I meningiomas are associated with large tumors and coexistence of monosomy 14 and del(1p36) in the ancestral tumor cell clone," *Neuro-Oncology*, vol. 9, pp. 438-446, 2007.
- [121] F. Maiuri, M. D. De Caro, F. Esposito, P. Cappabianca, V. Strazzullo, G. Pettinato, and E. de Divitiis, "Recurrences of meningiomas: predictive value of pathological features and hormonal and growth factors," *Journal of Neuro-Oncology*, vol. 82, pp. 63-68, 2007.
- [122] F. Roser, M. Nakamura, M. Bellinzona, S. K. Rosahl, H. Ostertag, and M. Samii, "The prognostic value of progesterone receptor status in meningiomas," *Journal of Clinical Pathology*, vol. 57, pp. 1033-1037, 2004.
- [123] F. H. Gilles, C. J. Tavaré, L. E. Becker, P. C. Burger, A. J. Yates, I. F. Pollack, and J. L. Finlay, "Pathologist interobserver variability of histologic features in childhood brain tumors: Results from the CCG-945 study," *Pediatric and Developmental Pathology*, vol. 11, pp. 108-117, 2008.
- [124] C. Grootsholten, I. M. Bajema, S. Florquin, E. J. Steenbergen, C. J. Peutz-Kootstra, R. Goldschmeding, M. Bijl, E. C. Hagen, H. C. Van Houwelingen, R. Derksen, and J. H. M. Berden, "Interobserver agreement of scoring of histopathological characteristics and classification of lupus nephritis," *Nephrology Dialysis Transplantation*, vol. 23, pp. 223-230, 2008.

- [125] J. Shuttleworth, A. Todman, M. Norrish, and M. Bennett, "Learning histopathological microscopy," *Pattern Recognition and Image Analysis, Pt 2, Proceedings*, vol. 3687, pp. 764-772, 2005.
- [126] J. S. Duncan and N. Ayache, "Medical image analysis: Progress over two decades and the challenges ahead," *IEEE Transactions on Pattern Analysis and Machine Intelligence*, vol. 22, pp. 85-106, 2000.
- [127] W. Qian, T. Zhukov, D. S. Song, and M. S. Tockman, "Computerized analysis of cellular features and biomarkers for cytologic diagnosis of early lung cancer," *Analytical and Quantitative Cytology and Histology*, vol. 29, pp. 103-111, 2007.
- [128] O. Sertel, J. Kong, H. Shimada, U. Catalyurek, J. H. Saltz, and M. Gurcan, "Computer-aided prognosis of neuroblastoma: Classification of stromal development on whole-slide images - art. no. 69150P," *Medical Imaging 2008: Computer-Aided Diagnosis, Pts 1 and 2*, vol. 6915, pp. P9150-P9150, 2008.
- [129] K. A. Marghani, S. S. Dlay, B. S. Sharif, and A. Sims, "Morphological and texture features for cancers tissues microscopic images," *Medical Imaging 2003: Image Processing, Pts 1-3*, vol. 5032, pp. 1757-1764, 2003.
- [130] E. Alexandratou, D. Yova, D. Gorpas, P. Maragos, G. Agrogiannis, and N. Kavantzias, "Texture analysis of tissues in Gleason grading of prostate cancer - art. no. 685904," in *Imaging, Manipulation, and Analysis of Biomolecules, Cells, and Tissues Vi*, vol. 6859, D. L. Farkas, D. V. Nicolau, and R. C. Leif, Eds., 2008, pp. 85904-85904.
- [131] M. Wiltgen, A. Gerger, C. Wagner, P. Bergthaler, and J. Smolle, "Evaluation of texture features in spatial and frequency domain for automatic discrimination of histologic tissue," *Analytical and Quantitative Cytology and Histology*, vol. 29, pp. 251-263, Aug 2007.
- [132] C. Wittke, J. Mayer, and F. Schweiggert, "On the classification of prostate carcinoma with methods from spatial statistics," *IEEE Transactions on Information Technology in Biomedicine*, vol. 11, pp. 406-414, Jul 2007.
- [133] J. P. Thiran and B. Macq, "Morphological feature extraction for the classification of digital images of cancerous tissues," *IEEE Transactions on Biomedical Engineering*, vol. 43, pp. 1011-1020, 1996.
- [134] H. Seker, M. O. Odetayo, D. Petrovic, and R. N. G. Naguib, "A fuzzy logic based-method for prognostic decision making in breast and prostate cancers," *IEEE Transactions on Information Technology in Biomedicine*, vol. 7, pp. 114-122, 2003.
- [135] J. Estevez, S. Alayon, L. Moreno, J. Sigut, and R. Aguilar, "Cytological image analysis with a genetic fuzzy finite state machine," *Computer Methods and Programs in Biomedicine*, vol. 80, pp. S3-S15, 2005.
- [136] D. N. Louis, H. Ohgaki, O. D. Wiestler, W. K. Cavenee, P. C. Burger, A. Jouvett, B. W. Scheithauer, and P. Kleihues, "The 2007 WHO classification of tumours of the central nervous system," *Acta Neuropathologica*, vol. 114, pp. 97-109, Aug 2007.

- [137] Q. Ji, J. Engel, and E. Craine, "Texture analysis for classification of cervix lesions," *IEEE Transactions on Medical Imaging*, vol. 19, pp. 1144-1149, Nov 2000.
- [138] R. M. Haralick, K. Shanmuga, and I. Dinstein, "Textural Features for Image Classification," *IEEE Transactions on Systems Man and Cybernetics*, vol. SMC3, pp. 610-621, 1973.
- [139] M. M. Galloway, "Texture analysis using gray level run lengths," *Computer Graphics Image Processing*, vol. 4, pp. 172-179, June 1975.
- [140] A. Chu, C. M. Sehgal, and J. F. Greenleaf, "Use of gray value distribution of run lengths for texture analysis," *Pattern Recognition Letters*, vol. 11, pp. 415-419, Jun 1990.
- [141] B. V. Dasarathy and E. B. Holder, "Image characterizations based on joint gray level run length distributions," *Pattern Recognition Letters*, vol. 12, pp. 497-502, Aug 1991.
- [142] Y. Xu, M. Sonka, G. McLennan, J. F. Guo, and E. A. Hoffman, "MDCT-based 3-D texture classification of emphysema and early smoking related lung pathologies," *IEEE Transactions on Medical Imaging*, vol. 25, pp. 464-475, 2006.
- [143] M. Bressan and J. Vitria, "On the selection and classification of independent features," *IEEE Transactions on Pattern Analysis and Machine Intelligence*, vol. 25, pp. 1312-1317, Oct 2003.
- [144] P. Domingos and M. Pazzani, "On the optimality of the simple Bayesian classifier under zero-one loss," *Machine Learning*, vol. 29, pp. 103-130, Nov-Dec 1997.
- [145] A. Tropine, P. D. Dellani, M. Glaser, J. Bohl, T. Ploner, G. Vucurevic, A. Perneczky, and P. Stoeter, "Differentiation of fibroblastic meningiomas from other benign subtypes using diffusion tensor imaging," *Journal of Magnetic Resonance Imaging*, vol. 25, pp. 703-708, 2007.
- [146] R. De Valois and K. De Valois, *Spatial Vision* 1ed.: Oxford University Press, 1990.
- [147] C. Blakemore and F. W. Campbell, "On existence of neurones in human visual system selectively sensitive to orientation and size of retinal images," *Journal of Physiology-London*, vol. 203, pp. 237-&, 1969.
- [148] D. A. Pollen and S. F. Ronner, "Visual cortical-neurons as localized spatial-frequency filters," *IEEE Transactions on Systems Man and Cybernetics*, vol. 13, pp. 907-916, 1983.
- [149] S. Marcelja, "Mathematical-description of the responses of simple cortical-cells," *Journal of the Optical Society of America*, vol. 70, pp. 1297-1300, 1980.
- [150] D. H. Hubel and T. N. Wiesel, "Receptive fields, binocular interaction and functional architecture in cats visual cortex," *Journal of Physiology-London*, vol. 160, pp. 106-&, 1962.
- [151] J. Beck, A. Sutter, and R. Ivry, "Spatial-frequency channels and perceptual grouping in texture segregation," *Computer Vision Graphics and Image Processing*, vol. 37, pp. 299-325, 1987.
- [152] I. Fogel and D. Sagi, "Gabor filters as texture discriminator," *Biological Cybernetics*, vol. 61, pp. 103-113, 1989.
- [153] J. Malik and P. Perona, "Preattentive texture-discrimination with early vision mechanisms," *Journal of the Optical Society of America a-Optics Image Science and Vision*, vol. 7, pp. 923-932, May 1990.

- [154] A. F. Laine, "Wavelets in temporal and spatial processing of biomedical images," *Annual Review of Biomedical Engineering*, vol. 2, pp. 511-550, 2000.
- [155] M. Unser and A. Aldroubi, "A review of wavelets in biomedical applications," *Proceedings of the IEEE*, vol. 84, pp. 626-638, Apr 1996.
- [156] D. D. Feng, *Biomedical Information Technology*, 1 ed.: Academic Press, 2007.
- [157] R. M. Rangayyan, *Biomedical Image Analysis*, 1 ed.: CRC, 2005.
- [158] R. R. Coifman and M. V. Wickerhauser, "Entropy-based algorithms for best basis selection," *IEEE Transactions on Information Theory*, vol. 38, pp. 713-718, Mar 1992.
- [159] R. M. Dansereau, W. Kinsner, and V. Cevher, "Wavelet packet best basis search using generalized Rényi entropy," in *IEEE Canadian Conference on Electrical and Computer Engineering*, Canada, 2002, pp. 1005-1008.
- [160] N. Saito, R. R. Coifman, F. B. Geshwind, and F. Warner, "Discriminant feature extraction using empirical probability density estimation and a local basis library," *Pattern Recognition*, vol. 35, pp. 2841-2852, Dec 2002.
- [161] N. Rajpoot, "Local discriminant wavelet packet basis for texture classification," in *Wavelets - Applications in Signal and Image Processing X Conference*, San Diego, California, 2003, pp. 774-783.
- [162] K. Huang and S. Aviyente, "Information-theoretic wavelet packet subband selection for texture classification," *Signal Processing*, vol. 86, pp. 1410-1420, Jul 2006.
- [163] F. G. Meyer and J. Chinrungrueng, "Analysis of event-related fMRI data using best clustering bases," *IEEE Transactions on Medical Imaging*, vol. 22, pp. 933-939, Aug 2003.
- [164] T. Chang and C. C. J. Kuo, "Texture analysis and classification with tree-structured wavelet transform," *IEEE Transactions on Image Processing*, vol. 2, pp. 429-441, 1993.
- [165] M. Acharyya, R. K. De, and M. K. Kundu, "Extraction of features using M-band wavelet packet frame and their neuro-fuzzy evaluation for multitexture segmentation," *IEEE Transactions on Pattern Analysis and Machine Intelligence*, vol. 25, pp. 1639-1644, Dec 2003.
- [166] S. Barbarossa and L. Parodi, "Tree-structured wavelet decomposition based on the maximization of Fisher's distance," in *1995 International Conference on Acoustics, Speech, and Signal Processing*, Detroit, Mi, 1995, pp. 2523-2526.
- [167] K. M. Iftikharuddin, W. Jia, and R. Marsh, "Fractal analysis of tumor in brain MR images," *Machine Vision and Applications*, vol. 13, pp. 352-362, Mar 2003.
- [168] M. C. Morrone and R. A. Owens, "Feature detection from local energy," *Pattern Recognition Letters*, vol. 6, pp. 303-313, Dec 1987.
- [169] N. Saito and R. R. Coifman, "On local feature extraction for signal classification," in *3rd International Congress on Industrial and Applied Mathematics*, Hamburg, Germany, 1995, pp. 453-456.

- [170] G. Van de Wouwer, P. Scheunders, and D. Van Dyck, "Statistical texture characterization from discrete wavelet representations," *IEEE Transactions on Image Processing*, vol. 8, pp. 592-598, Apr 1999.
- [171] K. S. Thyagarajan, T. Nguyen, and C. E. Persons, "A maximum likelihood approach to texture classification using wavelet transform," in *IEEE International Conference on Image Processing* Austin, Tx, 1994, pp. 640-644.
- [172] S. N. Yu, K. Y. Li, and Y. K. Huang, "Detection of microcalcifications in digital mammograms using wavelet filter and Markov random field model," *Computerized Medical Imaging and Graphics*, vol. 30, pp. 163-173, Apr 2006.
- [173] L. Wang and J. Liu, "Texture classification using multiresolution Markov random field models," *Pattern Recognition Letters*, vol. 20, pp. 171-182, Feb 1999.
- [174] S. G. Mallat, "A theory for multiresolution signal decomposition - the wavelet representation," *IEEE Transactions on Pattern Analysis and Machine Intelligence*, vol. 11, pp. 674-693, Jul 1989.
- [175] C. Burrus, R. Gopinath, and H. Guo, *Introduction to Wavelets and Wavelet Transforms: A Primer* Prentice Hall, 1997.
- [176] I. Daubechies, "The wavelet transform, time-frequency localization and signal analysis," *IEEE Transactions on Information Theory*, vol. 36, pp. 961-1005, 1990.
- [177] S. G. Mallat, *A Wavelet Tour of Signal Processing*, 2 ed.: Academic Press, 1999.
- [178] G. Strang and T. Nguyen, *Wavelets and Filter Banks* 2ed.: Wellesley-Cambridge Press, 1996.
- [179] A. Graps, "An introduction to wavelets," *IEEE Computational Science & Engineering*, vol. 2, pp. 50-61, 1995.
- [180] J. S. Suri, D. L. Wilson, and S. Laxminarayan, *Handbook of Biomedical Image Analysis: Segmentation Models Part A*, 1 ed. vol. 1: Springer, 2005.
- [181] I. Daubechies, *Ten Lectures on Wavelets* Society for Industrial and Applied Mathematics, 1992.
- [182] A. Laine and J. Fan, "Texture classification by wavelet packet signatures," *IEEE Transactions on Pattern Analysis and Machine Intelligence*, vol. 15, pp. 1186-1191, Nov 1993.
- [183] D. Gabor, "Theory of communication," *Journal IEE (London)*, pp. 429-457, 1946.
- [184] J. G. Daugman, "Two-dimensional spectral-analysis of cortical receptive-field profiles," *Vision Research*, vol. 20, pp. 847-856, 1980.
- [185] J. G. Daugman, "Uncertainty relation for resolution in space, spatial-frequency, and orientation optimized by two-dimensional visual cortical filters," *Journal of the Optical Society of America a-Optics Image Science and Vision*, vol. 2, pp. 1160-1169, 1985.
- [186] A. K. Jain and F. Farrokhnia, "Unsupervised texture segmentation using Gabor filters," *Pattern Recognition*, vol. 24, pp. 1167-1186, 1991.
- [187] A. C. Bovik, "Analysis of multichannel narrow-band-filters for image texture segmentation," *IEEE Transactions on Signal Processing*, vol. 39, pp. 2025-2043, 1991.
- [188] D. A. Clausi and T. E. Jernigan, "Designing Gabor filters for optimal texture separability," *Pattern Recognition*, vol. 33, pp. 1835-1849, Nov 2000.